Stability of glass foams : experiments at the bubble scale and on vertical film

Helena Kočárková

To cite this version:

Helena Kočárková. Stability of glass foams : experiments at the bubble scale and on vertical film. Other [cond-mat.other]. Université Paris-Est, 2011. English. NNT : 2011PEST1092 . tel-00664444

HAL Id: tel-00664444

https://theses.hal.science/tel-00664444

Submitted on 30 Jan 2012

Thèse présentée pour obtenir le grande de

Docteur de l'Université Paris-Est

Spécialité: Physique

par

Helena Kočárková

Stabilité des mousses de verre :
Expériences à l'échelle d'une bulle ou d'un film vertical

Soutenue le 14 novembre 2011 devant le jury composé de:

Mme.	M. Adler	Directrice de thèse
M.	C. Clanet	Examinateur
M.	O. Masbernat	Rapporteur
M.	L. Němec	Examinateur
M.	F. Pigeonneau	CoDirecteur de thèse
Mme.	F. Rouyer	CoDirectrice de thèse
M.	B. Scheid	Examinateur
M.	M. Toplis	Rapporteur

Stabilité des mousses de verre :
Expériences à l'échelle d'une bulle ou d'un film vertical

Afin de mieux comprendre la stabilité des mousses de verre, des expériences à l'échelle d'une bulle et d'un film vertical sont réalisées pour différentes composition de verre, viscosité, taille de bulle, et gaz à l'intérieur de la bulle. L'épaisseur du film au-dessus de la bulle est mesurée par interférence optique et décroît exponentiellement avec le temps sous l'effet des forces de pesanteur et capillaires. Le temps de vie de la bulle doit être divisé en deux étapes. En premier, le taux d'amincissement dépend du nombre de Bond. Ensuite, un écoulement contraire est observé aux fortes températures pour les verres silicosodocalcique. Ce phénomène également observé pour des films verticaux et s'explique par des écoulements Marangoni dus à l'évaporation de substances telles que le sodium qui engendre des variations de composition et de tension de surface. Des petites bulles sont crées à la surface libre lors de l'éclatement de grosses bulles à la surface d'un verre fondu faiblement visqueux.

Les mots clés: bulle; drainage; stabilite; évaporation; verre; mousse

Stability of glass foams:
Experiments at the bubble scale and on vertical film

For investigating glass foams stability, experiments with a single bubble rising towards the free surface of molten glass and with vertical films are performed for several values of viscosity, bubble size and various gas nature and glass chemical composition. The glass lamella on top of the bubble is observed by video-recording and its thickness evolution is measured by optical interferometry. The lamella thins as a result of buoyancy and capillary forces and then it ruptures. Actually the lamella thinning occurs in two steps. In the first step, the drainage is regular and the thinning rate depends on Bond number. In the second step a backward flow is observed above 1200°C for ordinary soda-lime-silica glass, which is explained as Marangoni counter flow due to evaporation of volatile species such as sodium. As the lamella ruptures tiny bubbles are created by the rupture of bubble lamella on the free surface for large bubbles and low viscosity of the melt.

Key words: bubble; drainage; stability; evaporation; glass; foam

La thése été préparée dans les laboratoires:

Laboratoire Surface du Verre et Interfaces
UMR 125 Unité mixte CNRS/Saint-Gobain Recherche
39, quai Lucien Lefranc - BP 135
933 03 Aubervilliers, France

Laboratoire de Physique des Matériaux Divisés et des Interfaces (LPMDI)
Université Paris-Est Marne-La-Vallée Cité Descartes
5 boulevard Descartes - Champs sur Marne
77454 Marne La Vallée cedex 2, France

Merci

There were many people, who were helping me with this thesis. At the beginning I would like to thank my two main supervisors, Florence Rouyer and Franck Pigeonneau for three years of endless support, optimism, encouragement and never-ending patience with teaching me fluid dynamics.

I also want to thank to Marie-Helene Chopinet for sharing her knowledge about glass chemistry and for offering various explanations of our results as well as proposing new experimental conditions.

Philippe Baranger and Lorenzo Canova were very helpful during building the experimental set-up, especially their advices regarding optical set-up in difficult steric conditions. I also thank to Catherine Goulas for helpful advices regarding bubble creation.

Joint lab between CNRS and Saint-Gobain Recherche let me work on this PhD in Saint-Gobain Recherche center in Aubervilliers, which was more than well equipped for this work. It also gave me a chance to be closer to industrial issues. I also want to thank the lab for giving me the opportunity to participate at many international conferences.

I thank to my friends and colleagues, to Marion Perrodin for many discussions about bubbles, for redox measurements she performed as well as support and encouragement during my time in SGR. I would like to thank my office colleagues for not only work related discussions but also for so much help in my daily life which I had to face being a foreigner in France.

I would like to thank all members of the jury, especially Mike Toplis and Olivier Masbernat for agreeing to be the "Rapporters" of this PhD work and for their detailed evaluation. I also want to thank to Benoit Scheid, Lubomír Němec and Christophe Clanet for interesting questions and ideas for future work on the subject.

And finally I want to thank to my closest family for so many helpful glass related conver-

sations and their encouragement during the first two years when the planning of the PhD work was changing drastically. I also thank them for being always supportive during the last few months of the PhD when being around me was more and more difficult.

Résumé

Ce travail de thèse est en rapport avec une étape du procédé de fabrication du verre pendant laquelle une mousse de verre peut se former à la surface du verre fondu. Cette mousse est pénalisante pour l'industrielle car elle agit comme un écran thermique et réduit le rendement énergétique de combustion. Ainsi, une mousse de 1 cm d'épaisseur absorbe 30 % de la chaleur émise par rayonnement par le four et une mousse de 5 cm d'épaisseur absorbe près de 60 % de la puissance émise. Afin d'éviter la formation d'une mousse, le temps de vie d'une bulle à la surface d'un bain de verre fondu doit être le plus court possible. L'étude de la stabilité de mousse de verre fondu est complexe et nécessite la prise en compte de la physico-chimie du verre. C'est pourquoi, nous nous sommes intéressés à la genèse de la mousse, en étudiant le cas simplifié d'une bulle unique ou d'un film vertical.

Le premier chapitre explique les différentes étapes de fabrication du verre dans l'industrie pendant lesquelles les bulles sont présentes.
La première étape consiste au mélange des matières premières dans un four à haute température pour obtenir un mélange homogène. La plus abondante des matières premières est le sable (ou SiO_2 est le principal élément). Les autres composants généralement utilisés pour l'élaboration des verres commerciaux sont le calcaire ($CaCO_3$) et le carbonate de sodium (Na_2CO_3). Les premiers liquides apparaissent à 785°C correspondant à la température de fusion eutectique d'un mélange de sable et de calcaire.
Cette première réaction chimique produit une grande quantité de gaz de dioxide de carbone (CO_2). Remarquons que les grosses bulles montent rapidement sous l'effet de la gravité et éclatent à la surface du bain de verre fondu, mais les plus petites bulles montent beaucoup plus lentement. L'élimination des bulles peut durer plusieurs heures sans autres actions (sec. 3.1.2).
C'est pourquoi une deuxième étape est réalisée pendant l'élaboration: c'est l'affinage. Pendant cette période, des composants chimiques dit "d'affinage" réagissent à des températures supérieures à 1200°C afin de produire du gaz (par exemple SO_2, O_2) dans le verre fondu

et d'augmenter la taille des bulles par transfert de masse. Les bulles peuvent également être éliminées par dissolution de leur gaz dans le verre fondu. Deux types de solubilité sont distingués: physique et chimique. La solubilité physique concerne des gaz inertes (azote ou argon) qui remplissent les espaces vides de la structure du verre. La solubilité chimique est liée aux réactions d'oxido-réduction dont les principaux réactifs sont le sulfure et l'oxygene et aux différents niveaux de valences des ions. La solubilité chimique est plus faible aux fortes températures. La dernière phase de la production avant la mise en forme du verre est le conditionnement thermique du verre où ce dernier est progressivement refroidit pour l'amener à une température compatible avec le procédé de formage.

Le deuxième chapitre est consacré aux propriétés du verre fondu qui sont importantes pour la formation d'une mousse de verre. Notamment, la viscosité dynamique et la tension de surface sont des propriétés physiques qui peuvent influencer la formation et/ou le temps de vie d'une mousse. Ce chapitre présente comment ces propriétés changent avec la composition chimique du verre et la température.

La viscosité d'un verre fondu décroît exponentiellement avec la température. Cette décroissante est importante pour la production industrielle. En effet, à haute température (étape d'affinage), une faible viscosité de quelques dizaine de Pa·s, permet le mélange et l'homogénéisation du verre fondu ainsi que la remontée des bulles sous l'effet de la gravité. Quand la température décroît (étape de conditionement), le verre est encore dans un état liquide (très visqueux) et peut être mis en forme. Dans la dernière étape de la production industrielle, le verre est encore plus refroidi et passe d'un état liquide à un état solide. La viscosité dynamique d'un verre peut atteindre près de 10^{20} Pa·s à température ambiante, Fig. 2.1. La variation de la viscosité avec la température peut être décrite par l'équation de Vogel-Fulcher-Tamman, éq.. (2.2). La composition chimique du verre influe sur sa viscosité. Notamment, l'ajout d'élément chimique qui rompt le réseau de la structure du verre abaisse la viscosité (par exemple le sodium). Enfin la viscosité peut également être modifiée par l'atmosphère environante. Il est connu, que la teneur en vapeur d'eau diminue la viscosité.

Les méthodes de mesures de viscosité dépendent de la gamme de viscosité. Des viscosimètres de type Couette cylindrique sont utilisés pour des faibles viscosités. Les analyses des courbures ou élongations de fibres de verre sont utilisées pour des fortes viscosités.

La tension de surface d'un verre est très importante car elle affecte non seulement la création d'une mousse, mais également la fonte, et la corrosion des parois du four. La tension de surface d'un verre fondu est de l'ordre de 300 mN·m^{-1} à 1300°C.

La tension de surface décroît faiblement avec la température (- 4 mN·m^{-1} pour un augmentation de 100°C). Il est connu, que la composition du verre évolue à forte température du

fait de l'évaporation de certaines espèces chimiques volatiles (sec. 2.3). Cette évolution implique un changement de la structure du verre et de ces propriétés physiques en surface et en volume. L'évaporation se décompose en trois étapes : diffusion des espèces volatiles du volume vers la surface, réaction chimique en surface et diffusion des produits de la réaction de la surface vers l'atmosphère environnante. Le taux d'évaporation augmente avec la vitesse dans le fondu et/ou dans l'atmosphère ainsi qu'avec la température.
Un des composant chimiques influençant fortement la tension de surface est le sulfate de sodium, très souvent utilisés comme agents d'affinage, dont le comportement change avec la température. Au-delà d'une concentration de 1 % en masse, ce composé est immiscible avec le verre fondu et forme une "galle". Cette galle a une tension de surface plus faible que le verre et se comporte comme un antimousse. Le sulfate se décompose et s'évapore pour des températures supérieures à 1300°C, cette évaporation s'accompagne de mouvement en surface (sec. 2.4).
La mesure de la tension de surface pour un verre fondu est difficile du fait des températures élevées. Les méthodes classiquement utilisées pour mesurer la tension de surface sont présentées dans ce chapitre : force exercée sur cylindre pendant son retrait du bain liquide, pression maximale d'une bulle, goutte pendante (poids - courbure) et la fonte d'une fibre de verre, sec. 2.2.1.

Le troisième chapitre introduit brièvement les mousses liquides et résume les travaux existants sur les mousses de verre liquide. D'après l'ensemble des chapitres précédents et celui-ci, il apparaît que la création et la stabilité d'une mousse de verre fondu est très complexe. De manière générale, la vie de cette mousse se décompose en trois étapes:

- Un flux de bulles de gaz existe au sein du fondu. Le nombre de bulles créées a fait l'objet d'études précédentes et il est connu qu'il dépend à la fois de la température et de la chimie du verre.

- Le liquide draine au sein de la mousse, et notamment dans le film au-dessus des bulles à la surface du bain de verre fondu. Notons que cette étape a été peu étudiée à l'échelle d'un bulle unique. Les quelques travaux antérieurs ont été réalisés à la surface d'huile de silicon[3]. Seul le drainage de films verticaux a fait l'objet d'étude pour le verre fondu [5]. Enfin il est à noter que d'apres Kumar [6], la courbure d'un film influence le drainage. Des comportements différents peuvent donc être attendu entre drainage d'un film vertical et drainage d'un film au-dessus d'une bulle.

- Les films fins sont meta-tables et rompent au bout d'un certain temps appelé temps de vie [4]. Cette dernière étape est la moins bien comprise. Actuellement, des temps longs de vie sont expliqués par un ralentissement du drainage pour des épaisseurs très fines de film du fait d'un rigidification partielle des interfaces [7].

L'objectif de cette thèse expérimentale est de mieux comprendre le drainage et la stabilité du film au-dessus d'une bulle unique à la surface d'un bain de verre fondu et ainsi pouvoir prédire le temps de vie d'une bulle, pour différentes conditions: de température, de compositions chimiques du verre et de gaz dans la bulle.

Le quatrième chapitre décrit les trois montages expérimentaux qui sont utilisés dans ce travail de thèse.

Le premier montage a été conçu pour mesurer l'épaisseur du film au dessus d'une bulle unique à la surface d'un bain d'huile silicone (PDMS) cf. Fig. 4.1. Une bulle d'air est créée au fond du bain d'huile à la sortie d'une seringue sous l'action d'une impulsion de pression générée à l'aide d'une électrovanne. Une camera placée de côté permet de mesurer la taille de la bulle. Les franges d'interférence générées par une source laser de longueur d'onde 532 nm visibles dans le film sont détectées par une photodiode placée au-dessus du centre de la bulle.

Le deuxième montage est similaire au premier mais adapté à la détermination de l'évolution de l'épaisseur du film au dessus d'une bulle à la surface d'un bain de verre fondu et donc à très haute température dans un four. La bulle est formée grâce à une électrovanne permettant l'émission d'un pulse de pression et connectée à une bouteille de gaz d'azote ou d'oxygene (Fig. 4.6). Ce dispositif de génération de bulle permet une meilleure maîtrise de la pureté du gaz et de la pression afin d'empêcher le verre fondu s'infiltre dans le conduit d'arrivée du gaz (Fig. 4.8). A l'instar de l'expérience faite ? température ambiante, un laser émettant une source lumineuse ? 532 nm est employée et envoyée sur la surface de la bulle. Les interférences sont enregistrées ? l'aide d'une caméra CCD. Afin de supprimer le rayonnement émis par le verre et le four porté ? haute température, un filtre optique ? bande étroite (532 ± 1 nm) est installé au niveau de l'objectif de la caméra. Afin d'éviter les réflexions spéculaires sur les parois du creuset en platine, ces derni?res ont été rendues rugueuses. La caméra permet de suivre l'évolution de la bulle depuis sa création jusqu'? sa rupture ? la surface du liquide.

Le troisième et dernier montage permet l'étude de la stabilité d'un film de verre fondu vertical (Fig. 4.9 et 4.10). Un cadre rectangulaire en platine rhodié (90% de platine et 10% de rhodium) est retiré d'un bain de verre fondu contenu dans un creuset transparent de silice. Le temps de vie du film est déterminé par observation à travers une fenêtre de silice placée sur le côté du four. De plus, cette expérience de film vertical permet d'extraire un film fin de verre fondu qui peut ensuite être soumis à des analyses chimiques afin d'en connaître sa composition dans l'épaisseur.

Le cinquième chapitre présente l'ensemble des fluides visqueux étudiés et les méthodes utilisées dans les expériences.

Nous avons utilisés cinq huiles silicones différentes constituées de polymère à base de siloxanes et de chaînes organiques (PDMS) ayant des viscosités dynamiques variant entre 10 et 100 Pa·s (Tab. 5.1). Ces huiles sont fréquemment utilisées comme des liquides modèles pour le verre fondu car elles sont utilisables à température ambiante et offrent une large gamme de viscosité comparable à celle rencontrée pour le verre. La viscosité de ces huiles dépend de la taille des macromolécules (plus les chaînes sont longues et plus la viscosité est grande).

Enfin nous présentons la détermination des paramètres physiques (viscosité, tension de surface et masse volumique) des verres fondus utilisés. Cette détermination nécessite une parfaite connaissance de la température et de la composition du verre. Malheureusement, la mesure de la température dans le verre fondu n'est pas possible durant l'expérience, aussi un profil de température précis à l'intérieur du four est relevé avant l'expérience pour différentes températures de consigne fixées par l'expérimentateur (Fig. 5.10).

Différents verres silicosodocalcique sont utilisés afin d'étudier l'influence de composants chimiques tels que le fer (deux verres industriels avec respectivement 0,1 % et 0,01 % en masse de Fe_2O_3) et le bore (deux verres préparés au laboratoire avec respectivement 1 % et 10 % en masse de B_2O_3). Enfin un verre très visqueux avec une grande proportion de Al_2O_3, K_2O et MgO est testé (Tab. 5.2).

La composition chimique est établie suivant deux méthodes: chimie humide et microsonde avant et après chaque expérience afin de sonder des possibles variations de la composition au cours de l'expérience pouvant être responsable d'une variation des propriétés physiques. Afin de tester l'homogénéité de la composition au sein du verre fondu, les échantillons de verre sont découpés en différents morceaux et analysés séparément (Fig. 5.6). Aucune variation de la composition au sein de l'échantillon n'est observée et s'explique par le mélange du verre fondu lors de la remontée des bulles dans le bain. Aucune variation de la composition du verre avant et après l'expérience n'est observée, à l'exception du verre contenant 1 % en masse de B_2O_3 et pour lequel le taux de bore diminue légèrement.

L'analyse de la surface du verre révèle la présence de sulfate de sodium. De plus, l'évaporation de sodium et de bore est mise en évidence par la présence de ces espèces chimiques sur les parois sèches du récipient (surface du récipient au dessus du verre), Tab. 5.4 at 5.7.

Du fait de la difficulté de mesurer les propriétés physiques du verre à haute température, de nombreux modèles disponibles dans la littérature permettent le calcul de ces propriétés à

partir de la composition précise du verre et de la température de celui-ci. Nous utilisons ces modèles pour déterminer la tension de surface, la masse volumique, la viscosité et l'indice optique de réfraction sauf pour certains cas ou celles-ci sont mal identifiées, auquel cas, ces propriétés sont déterminées expérimentalement.
Dans l'huile silicone, le diamètre des bulles est mesuré pendant la montée de la bulle (non déformée) sur les images prises de côté et dont l'échelle de longueur dans le plan de la montée est constant et bien identifié (Fig. 5.2 at 5.3). Cependant, dans le four destiné aux expériences de stabilité de bulle dans le verre fondu, nous ne disposons que d'une vue de dessus. Aussi, nous moyennons les échelles de longueur mesurées à la surface du verre et en bas du récipient pour déterminer le diamètre de la bulle. Cette indétermination de l'échelle de longueur entraîne une incertitude de la taille de la bulle, Fig. 5.14 et 5.15.
Enfin, nous présentons le calcul de l'épaisseur du film au-dessus de la bulle à partir de la détermination des minimums et maximums d'intensité des franges d'interférence au cours du temps, Fig. 5.16 at 5.18.

Enfin l'ensemble des résultats est présenté en détail dans le chapitre 6. Nous résumons ici l'essentiel des conclusions apportées par ce travail.
Une décroissance exponentielle de l'épaisseur du film dans le temps est mesurée pour l'ensemble des fluides utilisés - verre à haute température et fluides utilisés à température ambiante. Ces résultats sont en accord avec ceux obtenus par Debregeas et al. avec de l'huile silicone [3] et témoignent d'interfaces mobiles. Cependant, il est observé un drainage relativement plus rapide pour le cas des petites bulles dans le cas du verre (tous les verres, toutes les températures...). Ce comportement n'est pas observé dans le cas de l'huile silicone (pourtant jusqu'à présent considéré comme un fluide modèle pour le verre) mais il est observé pour d'autres fluides tels que le lubrifiant UCON et l'huile de ricin également utilisables à température ambiante. Une augmentation relative du taux d'amincissement du film au dessus d'une bulle à la surface d'un bain de liquide visqueux pour les petits nombres de Bond s'explique par une surface de déformation de l'interface relativement moins importante.
Nous identifions deux étapes distinctes dans la vie d'une bulle à la surface d'un bain liquide. La première étape est appelée “drainage régulier” pendant laquelle le film s'amincit régulièrement. Cette premi?re étape dépend uniquement de la taille de la bulle, des propriétés physiques (viscosité, masse volumique et tension de surface) et bien sur du champ de gravité. La deuxième étape de la vie de la bulle est appelée “drainage irrégulier” pendant laquelle il est observé des écoulements de fluide dans le film dans un sens contraire à la gravité, comparable aux mouvements observées par Conroy [1]. Cette étape est plus

aléatoire et dépend de la température pour un verre donné. Plus la température est élevée et plus la durée de cette étape peut-être longue conduisant a des temps de vie d'une bulle plus grands. Nous pensons que ces mouvements sont responsables de la meta-stabilités des films de verre et qu'ils sont générés par des courants de Marangoni provoqué par l'évaporation de substances volatiles tel que le sodium responsable de gradients de tension de surface dirigés vers le haut de la bulle.

Ce travail apporte ainsi une contribution très utile à la prédiction du temps de vie de la bulle car la premiere étape de drainage régulier est bien souvent dominante aux faibles températures et peut être décrite quantitavement à partir des paramètres physiques caractéristiques du fluide et de la bulle. La deuxieme étape du temps de vie de la bulle n'est pas prédictible, cependant nous pensons avoir identifié l'origine physique de la métastabilité des films de verre. Les expériences de stabilité de film verticaux confirment le précédent scénario: temps de vie longs pour des températures élevées et corrélés à des mouvements de liquide dans le film. De plus des mesures de la composition chimique du verre dans l'épaisseur du film permet d'estimer l'amplitude de variation de la tension de surface entre le sommet d'un bulle et le bain liquide.

Enfin nous reportons l'apparition de petites bulles dite "fille" à la périphérie de grosses bulles à la suite de leur éclatement à la surface de verre peu visqueux. Nous estimons alors un nombre de Reynold pour chaque bulle à partir de la vitesse de Taylor [8] et Culick [2] en supposant des épaisseurs de film de quelques centaines de nanometre. Nous établissons alors un critère d'apparition de ces bulles filles pour des nombres de Reynolds plus grand que 100.

Bibliographie

[1] A. R. Conroy, W. H. Manring, and W. C. Bauer. The Role of Sulfate in the Melting and Fining of Glass Batch. *The Glass Industry*, 47, 1966.

[2] F. E. C. Culick. Comments on a ruptured soap film. *J. Appl. Phys.*, 31:1128–1129, 1960.

[3] G. Debrégeas, P.-G. de Gennes, and F. Brochard-Wyart. The Life and Death of “Bare” Viscous Bubbles. *Science*, 279:1704–1707, 1998.

[4] P. Hrma. Model for a Steady State Foam Blanket. *Journal of Colloid and Interface Science*, 134(1):161–168, 1990.

[5] J. Kappel, R. Conradt, and H. Scholze. Foaming behaviour on glass melts. *Glasstech. Ber.*, 60:189–201, 1987.

[6] K. Kumar, A. D. Nikolov, and D. T. Wasan. Effect of Film Curvature on Drainage of Thin Liquid Films. *Journal of Colloid and Interface Science*, 256:194–200, 2002.

[7] P. Laimböck. *Foaming of Glass Melts*. PhD thesis, 1998.

[8] G. I. Taylor. The dynamics of thin sheets of fluid. III. Disintegration of fluid sheets. *Proc. R. Soc. London, Ser. A*, 253:313–321, 1959.

Contents

Introduction

This work is closely linked to one step in glass manufacturing process. At the beginning, raw material is introduced at one end of a glass furnace. As the raw materials move from one end to another, the temperature in the furnace is increasing and the raw materials start melting. Chemical reactions appear and as a consequence, bubbles are released. Bubbles are removed from the melt at the area of the furnace, where the temperature reaches its highest spot. This step of the glass production is called fining. During glass fining, rising bubbles mix the melt and support homogenization of the molten glass, but on the other hand they can create a layer of foam on the free surface, see Fig. 1. There are two main groups of glass furnaces: pot and continuous tank furnaces. One of the most common continuous furnaces is cross-fired glass furnace, which is used for production of float glass. In this furnace, the melt is heated from the top by burners and therefore, if a layer of foam is created on the surface of the melt, it reduces the heating efficiency of the furnace. When the layer of foam is 1 cm thick, 30 % of the radiation heat is absorbed, but when the thickness of the layer rises to 5 cm, the value of the absorbed heat rises to almost 60 % [2]. More information about the reduced heat transfer can be found in [3, 7, 9]. In order to prevent this unpleasant effect, lifetime of bubbles that rise to the free surface needs to be as short as possible. Study of glass foam stability is a complex process involving physical and chemical processes. Therefore to

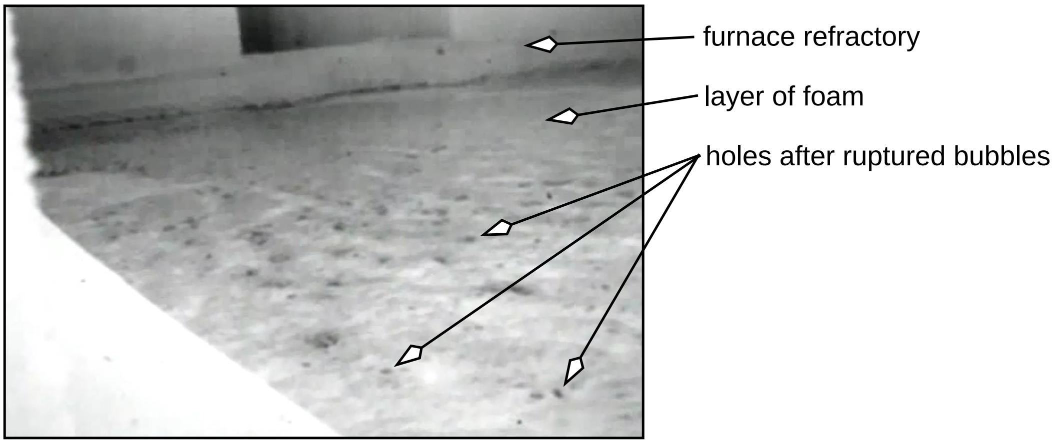

Figure 1: Photo of inner space of a furnace, where the surface of molten glass is covered with foam

understand the basics of the problem, we study a simplified case at the bubble scale and on vertical film.

A study related to the evolution of thickness of a vertical glass film can be found in the work of Laimböck [6] or Kappel *et al.* [5]. Long lasting films were observed in both works. Kappel *et al.* [5] inform about thin metastable films, that can last up to 40 min. This metastable state is not fully understood and has never been studied on a bubble scale. Laimböck [6] observed, that the metastable state occurs after a fast drainage of the film and explains it appears due to the decrease of velocity of the liquid, which is draining out of the film due to partially mobile interfaces. Partially mobile interface can be found in a numerical study by Beerkens and van der Schaaf [1, 8], who predict bubble lifetime as a function of the initial and critical lamella thickness, bubble size and a coefficient describing the rate of interface mobility. Hrma [4] predicts a model of foam blanket based on gravitational drainage and the survival time of a critically thin lamella of the top bubble and not the initial or critical lamella thickness.

The purpose of this work is to describe behavior of a single bubble at the surface. Therefore it is necessary to study the evolution of thickness of the bubble lamella and mobility of the interface, bubble lifetime as well as to observe the behavior after the rupture of the bubble lamella. In order to obtain results, experimental set-up, where evolution of thickness of the bubble lamella is measured using interference method, has been constructed. This experimental set-up enables determination of the lifetime and observation after the bubble rupture. Experiments with molten glass at high temperature range (above 1300°C) are difficult, therefore various model liquids are used to simulate behavior of the melt. In order to verify the reliability of these experiments, behavior of silicon oil is tested in this work and compared to the behavior of molten glass. Another experiment with determination of lifetime of glass vertical film is created to verify if the behavior observed during the experiment at bubble scale is similar to the behavior at the scale of a vertical film.

More details about glass manufacturing, bubble creation and removal will be given in the first chapter of this work. Second chapter will be related to glass foaming, and properties that influence it. Experimental determination of these properties, their variation with temperature and chemical glass composition will be presented. Evaporation of volatile species can influence the foaming and will be discussed in the last section of the second chapter. Third chapter will be related to foam in general. It will contain description of properties that play important role in foaming and summarize terminology, that is used in foaming, as well as describe all steps in foam creation and decay. Last sections will discuss previous studies on glass foaming. Description of the experimental set-ups that were used in this work for a single bubble and a vertical glass film will be presented in the fourth chapter. Fifth chapter will contain description of glasses, their composition and properties, and all chemical analyses, that were used in this work. Chapter 6 will present the obtained results and compare them to previous works. The most important conclusions that were found during this PhD and perspectives for future work will be given in the last chapter.

References

[1] R. G. C. Beerkens and J. van der Schaaf. Gas Release and Foam Formation During Melting and Fining of Glass. *J. Am. Ceram. Soc.*, 89(1):24–35, 2006.

[2] A. G. Fedorov and L. Pilon. Glass foams : formation , transport properties , and heat , mass , and radiation transfer. *Journal of Non-Crystalline Solids*, 311:154–173, 2002.

[3] A. G. Fedorov and R. Viskanta. Radiation Characteristics of Glass Foams. *J. Am. Cer. Soc.*, 83(11):2769–2776, 2000.

[4] P. Hrma. Model for a Steady State Foam Blanket. *Journal of Colloid and Interface Science*, 134(1):161–168, 1990.

[5] J. Kappel, R. Conradt, and H. Scholze. Foaming behaviour on glass melts. *Glasstech. Ber.*, 60:189–201, 1987.

[6] P. Laimböck. *Foaming of Glass Melts*. PhD thesis, 1998.

[7] L. Pilon and R. Viskanta. Radiation Characteristics of Glass Containing Gas Bubbles. *J. Am. Cer. Soc.*, 86(8):1313–1320, 2003.

[8] J. van der Schaaf and R. G. C. Beerkens. A model for foam formation , stability , and breakdown in glass-melting furnaces. *Journal of Colloid and Interface Science*, 295:218–229, 2006.

[9] M. J. Varady and A. G. Fedorov. Combined Radiation and Conduction in Glass Foams. *Journal of Heat Transfer*, 124(December):1103–1109, 2002.

Chapter 1

Glass melting

Glass melting is a complex energetically demanding process, which consists of several stages [1, 2]. First step in glass production is mixing raw materials. For efficient melting and a good quality glass with no cords or stones, it is necessary to prepare a homogeneous medium. The mixture, which is introduced into a furnace for further melting is called a batch. Cullet, which is recycled old or poor quality glass, is often added to the batch to reduce energy expenses during melting. It can comprise up to 90% of the batch for container glass. Glass melting starts when a batch is exposed to a high temperature inside a furnace. More details about raw materials and reactions during the first step of melting are given in section 1.1. Second step of glass melting is called fining. Bubbles, which are created during melting, are being removed in this period. Rising bubbles support homogenization process, but can cause the creation of a layer of foam at the melt surface. This step is the most important for our work and will be discussed in more details in section 1.2. The final step of melting, before the forming process, is cooling, which is briefly presented in sec. 1.3.

1.1 Raw materials and primary foaming

The main component of industrial glass is SiO_2 (silica), which is contained in sand. Apart from SiO_2, an ordinary glass consists of CaO and Na_2O, which are found in limestone and sodium carbonate, respectively. The three main raw materials react together and release a huge amount of CO_2 (approximately 0.2 kg of CO_2 per 1 kg of glass), see eq. below.

$$\mathrm{SiO_2 + CaCO_3 + Na_2CO_3 \rightarrow Na_2O \cdot CaO \cdot SiO_2 + 2CO_2} \tag{1.1}$$

There are several processes, that appear at the same time during the initial melting. When the batch is introduced into a furnace, where temperature rises, dehydration occurs. The size of the grains of raw materials varies from 0.5 to 1 mm, therefore a small amount of water is added to the batch mainly to stick the grains together to eliminate their loss and to prevent segregation. Addition of water also supports reactions and accelerates the melting [3]. Chemical reactions in solid state play an important role during the initial melting. Separately each raw material melts at a high temperature (carbonates above 900°C), but their mutual reactions allow a creation of liquid at much lower temperature. Eutectic melting of the binary mixture of limestone ($CaCO_3$) and sodium carbonate (Na_2CO_3) appears at 785°C forming a double carbonate $Na_2Ca(CO_3)_2$ [19]. The first carbonate liquid phase wets the surface of silica grains and initiates the chemical reactions with silica.

A reaction between sodium carbonate and sand was studied under a microscope by Manring [21], who observed a metasilicate $Na_2O{\cdot}SiO_2$ at temperature around 750°C as a wetting the grains of sand. Cable [7] designed an experiment with a silica rod, which was placed into molten sodium carbonate, and observed a layer of metasilicate crystals that appeared on the surface. Mechanism of this reaction was studied by Guloyan [16].

Limestone does not melt, but it decomposes and reacts in solid state at temperature from 600 to 1000°C. With silica grains it forms $2CaO{\cdot}SiO_2$, which later reacts into substances richer in silica [3].

The dissolving of silica grains is the longest process of the melting [5]. It is necessary to choose a reasonable size of the grains as well as to add melting accelerants to the raw materials to support and shorten the dissolution of the silica grains [17].

A huge amount of CO_2 is released during all of the reactions mentioned above. The gas is entrapped in the batch as well as in a primary melt and creates a primary foam [14]. Large bubbles rise due to buoyancy force and break at the level of the glass, but small bubbles rise slower and are often carried to the glass bath, where they participate in a creation of secondary foam. After the first step of the melting process, glass consists of non-homogeneous liquid silicate with a large quantity of bubbles. Homogenization and removal of the residual gases are achieved in the second step of the melting process, which is called glass fining, and where the temperature reaches its maximum.

1.2 Fining process: Evolution of bubbles in glass and secondary foaming

Molten glass contains a lot of small bubbles at the beginning of fining. Most of them contain CO_2 as a result of the chemical reactions. Other bubbles may contain nitrogen, which was trapped from atmosphere, or oxygen from electrochemical reactions, which will be more discussed in sec. 1.2.1. A summary of gases that mostly occur in glass melts and their origin is given in table 1.1 [3].

Remaining bubbles in the final glass product are undesirable defects. There are two main

Gas	**Origin**	**Gas**	**Origin**
H_2O	inclusion in pores of raw materials dissociation of hydrated raw materials humid batch or cullet furnace atmosphere	CO_2	dissociation product of carbonates oxidation of carbon or organic impurities furnace atmosphere
N_2	air inclusions dissociation product of nitrate furnace atmosphere	O_2	dissociation product of fining agents air inclusions furnace atmosphere
Ar	entrapped air bubbles furnace atmosphere	SO_2	dissociation product of sulfates furnace atmosphere

Table 1.1: Gases in glass and their origin.

principles leading to the removal of bubbles from the molten glass. Either they rise due to the buoyancy force through the melt to the surface, where they burst, see sec. 3.1.2 and 3.3, or they dissolve in the glass. The solubility of gases in glass is discussed in the following section.

1.2.1 Physical and chemical solubility of gases

Gases can be physically or chemically fixed in the glass melt [3].

Physical solubility can be explained by the free volume theory, which says, that the space between atoms in the structure can be filled with physically dissolved elements [12]. It is reasonable to think that elements with smaller atoms will have a higher solubility even though the differences are in hundredths of kg·m^{-3} [23, 22]. This type of solubility is mainly important for noble gases such as Ar, which does not participate in chemical reactions. Physical solubility slightly rises with a rising temperature and is controlled by Henry's law [26]:

$$c_i = L_i p_i \tag{1.2}$$

where:

c_i	concentration of the gas i in the melt (mol·m^{-3})
L_i	solubility constant of the gas i in the melt (mol·Pa^{-1}·m^{-3})
p_i	partial pressure of the gas i (Pa)

A rising content of modifiers, which are alkali and earth alkali oxides, that break the network created by SiO_2 or B_2O_3 as well as GeO_2 or P_2O_5, depending on the glass composition [18], lowers the physical solubility, because the free volume in the structure is filled with the cations of the modifiers [25], see Fig. 1.1, where two-dimensional structures of quartz, vitreous silica and sodium-silicate glass is shown. Apart from noble gases, nitrogen is dissolved physically as well, except for very reduced melts, where it can also exist in chemical forms as nitrides ($-NH_2$ or $=NH$).

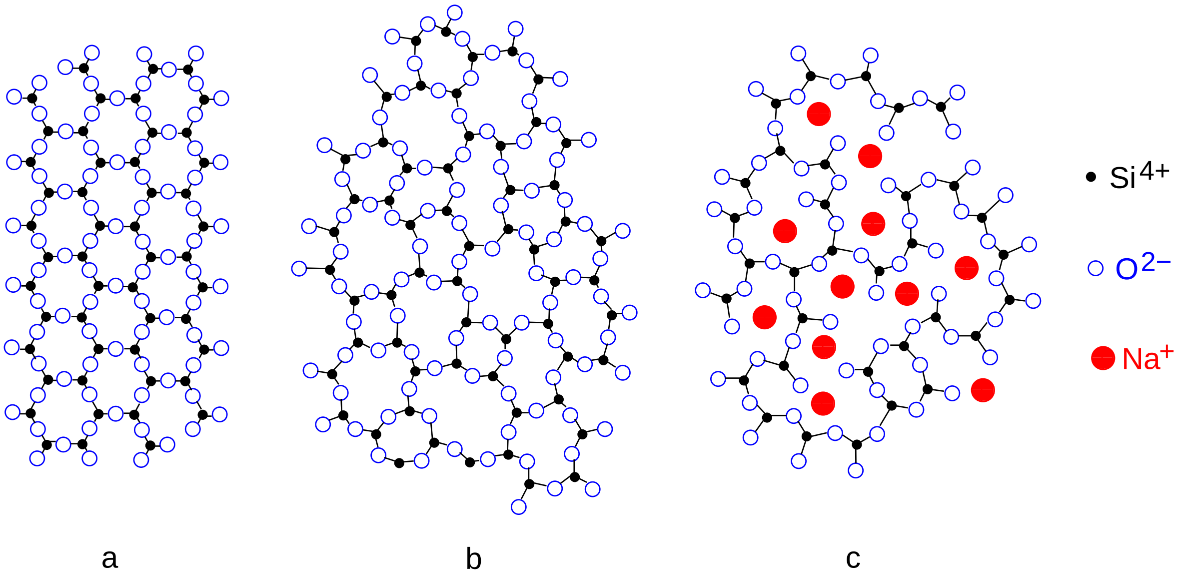

Figure 1.1: Two-dimensional structures of quartz, vitreous silica and sodium-silicate glass [18].

Chemical solubility of gases is closely linked to oxidation-reduction reactions. In the molten glass, many components can be present in multiple valence states. Mutual chemical reactions of these components are called oxidation-reduction reactions and influence many processes during the whole melting as well as final properties of the glass product. Sulfur and oxygen are one of the most common elements that participate in ox.-red. reactions. Their change of valence state can either lead to a huge release of gases or the opposite. Unlike physical solubility, chemical solubility strongly decreases with a rising temperature and increases with a rising content of modifiers. The oxidation-reduction reaction can be expressed by an equilibrium between the valence states of a polyvalent ion (Me):

$$\frac{4}{\mathrm{b}}\mathrm{Me}^{(\mathrm{a+b})+}(\mathrm{l}) + 2\mathrm{O}^{2-}(\mathrm{l}) \leftrightarrow \frac{4}{\mathrm{b}}\mathrm{Me}^{\mathrm{a}+}(\mathrm{l}) + \mathrm{O}_2(\mathrm{l},\mathrm{g}), \tag{1.3}$$

where b is the number of exchanged electrons. One of the most common ox.-red. reaction is due to the couple ($\mathrm{Fe}^{2+}/\mathrm{Fe}^{3+}$), because Fe is contained in most of glasses and strongly influences the color of glass. Fe^{2+} causes a blue tone and Fe^{3+} a yellow one. Glasses containing iron have a green color, which is a consequence of presence of Fe^{2+} and Fe^{3+} and the combination of blue and yellow colors. A ratio between the amount of Fe^{2+} and the total amount of iron is called the redox state of the glass. The higher the Fe^{2+} content, the higher the redox state. The redox state of glass is determined *via* absorption measurement for various wavelengths near infrared range, see sec. 5.2.1 for more details.

Sulfur dioxide can be chemically dissolved in glass as $\mathrm{SO_4}^{2-}$ under oxidizing conditions (eq. (1.4)), or as a sulfide S^{2-} under reducing conditions (eq. (1.5)).

$$\mathrm{SO_2} + \frac{1}{2}\mathrm{O_2} + \mathrm{O}^{2-} \leftrightarrow \mathrm{SO_4}^{2-} \tag{1.4}$$

$$\mathrm{SO_2} + \mathrm{O}^{2-} \leftrightarrow \mathrm{S}^{2-} + \frac{3}{2}\mathrm{O_2} \tag{1.5}$$

Reduced conditions are usually reached by the addition of carbon [4]. Behavior of sulfur in molten glass will be discussed more in sec. 1.2.2 and 2.4. Carbon dioxide can be chemically bounded as carbonates:

$$\mathrm{CO_2} + \mathrm{O}^{2-} \leftrightarrow \mathrm{CO}_3^{2-} \tag{1.6}$$

Chemistry of glass is a very rich field and the above chemical equations are only the main ones, that are important for our work.

1.2.2 Fining agents

Fining agents are chemical compounds that release gases at elevated temperatures (above 1200°C). Released gases diffuse into the bubbles, enlarge their size enhance their rising velocity and hence their removal. Bubbles that rise to the surface create a secondary foam [14]. A layer of foam is created if the flux of bubbles is faster than their decay at the surface, more details will be given in sec. 3.4.

The diffusion of gases through the melt and into bubbles is one of the most important processes in fining. It is increased by temperature. The diffusion coefficient is related to the temperature by Arrhenius relation:

$$D = D_0 \exp\left(-\frac{\Delta E}{RT}\right) \tag{1.7}$$

The size of the bubble is growing if the activity of a certain gas is higher in the melt than inside the bubble. Under these conditions gas diffuses into the bubble and enlarges its size.

The pressure inside the bubble is a function of its size and is given by Laplace law [10]:

$$p = \frac{2\gamma}{r} + p_A + \rho g\,(H - z) \tag{1.8}$$

where:

γ	surface tension of glass (N·m^{-1})
r	bubble radius (m)
p_A	atmospheric pressure (Pa)
ρ	glass density (kg·m^{-3})
H	distance between the bottom and the top of the glass bath (m)
z	distance between the bottom of the bath and the bubble (m)

A larger pressure inside smaller bubbles will cause their disappearance in favor of larger ones if the lamella, that separates them, is thin [24, 11]. This phenomena is very important for bubbles at a scale of a μm, which are not large enough to rise and break at the top of the molten glass in a reasonable time, but they can disappear due to atmospheric pressure. The application of a lower pressure in the surrounding atmosphere during glass melting can be used to support fining. Under these conditions, bubbles can rise faster to the melt surface, because their size increases as a consequence of the law of perfect gas, as well as the diffusion of gases into the bubbles is supported, nevertheless the application of lower pressure is technically complicated in the real furnace, therefore these conditions are mainly achieved under laboratory conditions for the preparation of a small amount of glass.

Sodium sulfate

The most common fining agent for float and container glass is sodium sulfate (Na_2SO_4). It decomposes at temperature around 1300°C [9, 6] and releases SO_2, SO_3 and O_2 (Tab. 1.2) depending on the conditions such as temperature and redox state of the molten glass. SO_3 is very unstable and usually decomposes and forms SO_2 and oxygen. Behavior of sulfur in glass chemistry has been studied by Fincham and Richardson [15], who performed experiments with $CaO:Al_2O_3:SiO_2$ (37:27:36 wt%) melt and observed various sulfur solubility as a

oxidizing conditions	$Na_2SO_4\,(l) \leftrightarrow Na_2O\,(l) + SO_3\,(l)$
less oxidizing conditions	$Na_2SO_4\,(l) \leftrightarrow Na_2O\,(l) + SO_2\,(g) + \frac{1}{2}O_2\,(g)$
reducing conditions	$Na_2SO_4\,(l) + C\,(s) \leftrightarrow Na_2O\,(l) + SO_2\,(g) + CO\,(g)$
more reducing conditions	$Na_2SO_4\,(l) + 2C\,(s) \leftrightarrow Na_2S\,(l) + 2CO_2\,(g)$

Table 1.2: Behavior of sulfate.

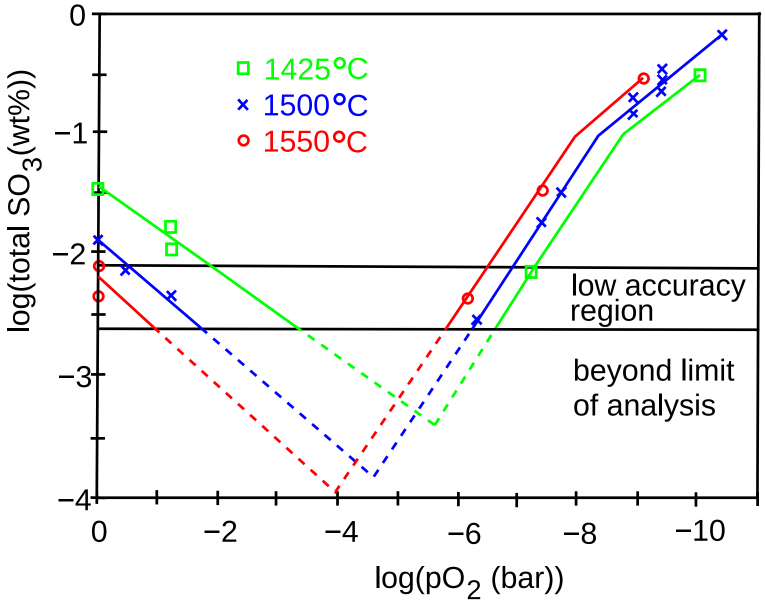

Figure 1.2: Content of sulfur in wt% of SO_3 in glass as a function of the partial pressure of oxygen [15].

function of the partial pressure of oxygen, see Fig. 1.2. The solubility of sulfur was decreasing with a decreasing value of partial pressure until 10^{-4} or 10^{-6}, depending on temperature, and increasing with further decrease of partial pressure. This graph indicates that the solubility of sulfur is high under very oxidizing or very reducing conditions. The minimal value of SO_3 content decreases and is shifted to lower partial pressure as temperature increases. Similar experiment was achieved by Budd [20], who measured the sulfur solubility for soda-lime-silica melts with various values of oxidation state, see Fig. 1.3. The lowest solubility was achieved around 70% of Fe^{2+} content.

In the presence of carbon which causes very reducing conditions, sulfur forms sulfide, see the fourth equation in Tab. 1.2, and reacts with the remaining Fe^{3+} into complex, which causes a typical amber coloration with a maximum absorption above 400 nm [13]. One of the advantages of sodium sulfate as a fining agent is, that the decomposition appears at a narrow temperature interval [27]. More details about glass foaming will be given in the third chapter. Behavior of sulfate changes with temperature and is very important for this work. That is why it will be also discussed in sec. 2.4.

Arsenic oxide

Arsenic oxide is used for fining of lead and lead crystal glasses. It can be added to the batch as As^{3+} or As^{5+}. To support the main reaction which releases oxygen, see eq. (1.9), it is

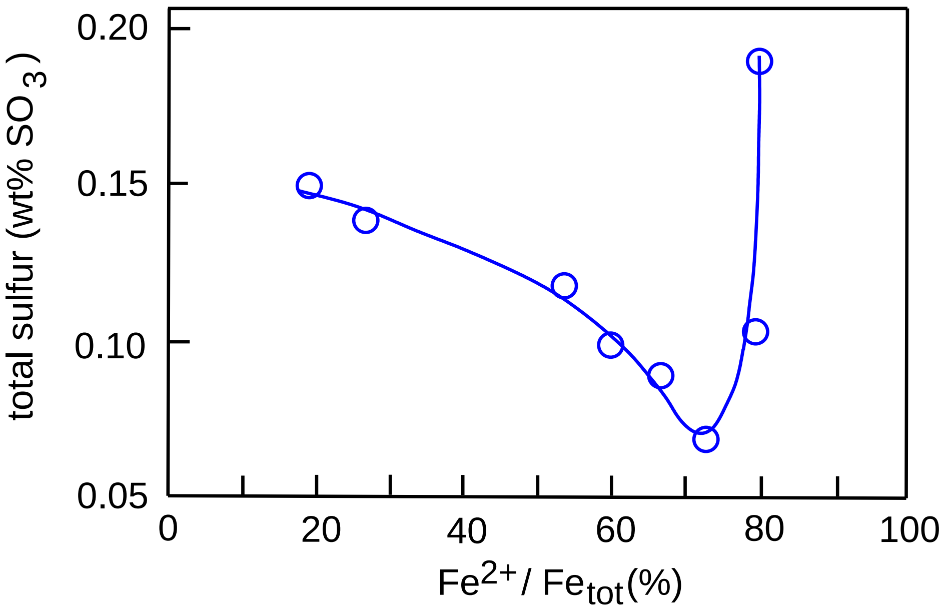

Figure 1.3: Content of sulfur in wt% of SO_3 in glass as a function of the oxidation state [19].

necessary to add oxidizing agents ($NaNO_3$ or KNO_3) to transfer all As^{3+} to As^{5+} (eq. 1.10).

$$As_2O_5 \leftrightarrow As_2O_3 + O_2 \tag{1.9}$$

$$5As_2O_3 + 4NaNO_3 \leftrightarrow 5As_2O_5 + 2Na_2O + 2N_2 \tag{1.10}$$

Arsenic oxide decomposes between 1330 and 1370°C [3]. A disadvantage of this fining agent is an environmental hazard, because the arsenic trioxide is volatile.

Antimony oxide

Antimony oxide reacts similarly to the arsenic oxide, see eq. (1.11). Addition of oxidants is also used. Temperature of the reaction is about 150°C lower [3], than for arsenic oxide, therefore this fining agent is mainly used for glasses with lower melting temperature.

$$Sb_2O_5 \leftrightarrow Sb_2O_3 + O_2 \tag{1.11}$$

Sodium chloride

Sodium chloride is used for glasses with a high temperature of melting, when sodium sulfate is not efficient, because it releases gases at a temperature, where the viscosity of the molten glass is still high, which can lead to the presence of a foam blanket. Sodium chloride does not decompose like other fining agents, but evaporates as NaCl (g) at temperatures above 1440°C [3]. The main disadvantage of this fining agent is the emission of chloride which reacts with gases and humidity in the atmosphere during cooling in the regenerators, as follows:

$$2\mathrm{NaCl} + \mathrm{SO_2} + \mathrm{H_2O} + \frac{1}{2}\mathrm{O_2} \leftrightarrow \mathrm{Na_2SO_4}\,(\mathrm{particles}) + 2\mathrm{HCl}\,(\mathrm{g}) \tag{1.12}$$

Emissions of sodium sulfate particles and vapors of HCl lead to a degradation of regenerators and refractories.

1.3 Last step of melting

The cooling of glass is the last step of the melting process, when temperature decreases after the fining process and small bubbles with a diameter up to 100μm, which are called seeds, are dissolved. Chemical solubility rises in this part, because previously mentioned reactions of fining agents proceed conversely.

A reboil effect may sometimes appear during this part of the melting. It is a creation of small bubbles due to a contact between two parts of the melt with unequal temperatures or redox state. Cable *et al.* [8] observed the reboil effect while temperature of an ordinary soda-lime-silica glass with and without the addition of sulfate was decreasing from 1400 to 1100°C. The gas was mostly oxygen.

References

[1] R. G. C. Beerkens. Modular Melting Industrial Glassmelting Process Analysis. *American Ceramic Society Bulletin*, 83(4):28–32, 2004.

[2] R. G. C. Beerkens. Modular melting Industrial Glassmelting Process Requirements, Part 2. *American Ceramic Society Bulletin*, 83(7):35–37, 2004.

[3] R. G. C. Beerkens and H. de Waal. *Handbook for Glass Technologists*. 1997.

[4] R. G. C. Beerkens and K. Kahl. Chemistry of sulphur in soda-lime-silica glass melts. *Physics and Chemistry of Glasses*, 43(4):189–198, 2002.

[5] R. G. C. Beerkens, H. P. H. Muijsenberg, and T. van der Heijden. Modelling of sand grain dissolution in industrial glass melting tanks. *Glastech. Ber. Glass Sci. Technol.*, 67(7):179–188, 1994.

[6] R. Brückner. Zur Kinetik des Stoffaustausches an den Grenzflächen zwischen Silikatglas- und Salzschmelzen und des Stofftransportes in Silikatglasschmelzen unter besonderer Berücksichtigung des Verhaltens von Na_2SO_4 und seinen Zersetzungsprodukten (Teil I. - III.). *Glastechn. Ber.*, 34; 34; 35.

[7] M. Cable and D. Martlew. Formation of Solid Reaction Products in the Dissolution of Silica in Molten Sodium Carbonate. *Glass Technlogy*, 25(1):24–30, 1984.

[8] M. Cable, C. G. Rasul, and J. Savage. Laboratory investigation of foaming and reboil in soda-lime-silica melts. *Glass Technol.*, 9(2):25–31, 1968.

[9] A. R. Conroy, W. H. Manring, and W. C. Bauer. The Role of Sulfate in the Melting and Fining of Glass Batch. *The Glass Industry*, 47, 1966.

[10] P. G. de Gennes, F. Brochard-Wyart, and D. Quéré. *Capillarity and Wetting Phenomena*. Springer, New York, 2004.

[11] A. J. de Vries. *Foam Stability*. D. B. Centen's uitgeversmaatschappij N. V., Amsterdam, 1957.

[12] R. H. Doremus. *J. Am. Ceram. Soc.*, 49(461), 1966.

[13] R. W. Douglas and M. S. Zaman. The chromophore in iron-sulphur amber glasses. *Phys. Chem. Glasses*, 10(4):125–132, 1969.

[14] A. G. Fedorov and L. Pilon. Glass foams : formation , transport properties , and heat , mass , and radiation transfer. *Journal of Non-Crystalline Solids*, 311:154–173, 2002.

[15] C. J. B. Fincham and F. D. Richardson. The behavior of sulphur in silicate and aluminate melts. *Proc. Roy. Soc. London*, A223:40–63, 1954.

[16] Y. A. Guloyan. Chemical Reactions between Components in the Production of Glass-forming Melt. *Glass and Ceramics*, 60(7-8), 2003.

[17] K. S. Hong, S. W. Lee, and R. E. Speyer. Thermal Analysis of Reactions in soda-lime-silicate Glass Batches Containing Melting accelerators: II, Multicomponent Systeme. *J. Am. Cer. Soc.*, 76(3):605–608, 1993.

[18] G. O. Jones. *Glass*. Methuen and Co. LTD, London, 1956.

[19] N. S. Kham. *Development of Methods for the Characterisation of Melting Batches*. PhD thesis, Technischen Hochschule Aachen, 2005.

[20] P. Laimböck. *Foaming of Glass Melts*. PhD thesis, 1998.

[21] W. H. Manring. Influence of Batch Preparation Process on the Melting and fining of glass. *Glass Industry*, 45(7-8), 1964.

[22] H. O. Mulfinger, A. Dietzel, and J. M. F. Navarro. *Glastechn. Ber.*, 45, 1972.

[23] H. O. Mulfinger and H. Scholze. *Glastechn. Ber.*, 35, 1962.

[24] G. Narsimhan and E. Ruckenstein. Hydrodynamics, enrichment and collapse in foams. *Langmuir*, pages 230–238, 1986.

[25] T. F. Newkirk and F. V. Tooley. Study of the effect of cation concentration and size on helium permeability of alkali-silica glasses. *J.Am.Cer.Soc.*, 32:272–278, 1949.

[26] L. Němec. *Čeření skel (Tavení skla)*. Česká sklářská společnost, 2008.

[27] C. G. Rasul and M. Cable. Spontaneous Bubble Formation in Silicate Melts at High Temperatures. *J. Am. Cer. Soc.*, 49:568–571, 1966.

Chapter 2

Glass properties influencing glass foaming

Glass foaming is a complex process, that includes many chemical (chapter 1) and physical (chapter 3) processes. Viscosity and surface tension are properties of glass that change with chemical composition and temperature and influence the foam formation and its lifetime. Viscosity of glass, its variation with temperature and composition as well as methods of measurement are discussed in sec. 2.1. This chapter gives details about the methods of measurement of surface tension of glass and its variation with composition, see sec. 2.2. Chemical composition of molten glass can change with time due to evaporation, which can lead to a variation of the properties. More details about evaporation of glass and its consequences are given in sec. 2.3. Section 2.4 of this chapter discusses the behavior of sodium sulfate at various temperatures.

2.1 Dynamic viscosity

The dynamic viscosity of glass decreases exponentially with temperature, see Fig. 3.2. A continuous variation of viscosity is very important for glass manufacturing. There are two general symbols for viscosity: μ and η. The second symbol is more common for glass science. SI unit of viscosity is Pa.s but a unit Poise is very commonly used in glass industry. The difference between the two is given by:

$$1\,Poise = 1\,dPa.s = 0.1\,Pa.s \tag{2.1}$$

In the following text, only the symbol μ is used. A variation of viscosity with temperature for ordinary glass with an indication of important steps of the manufacturing process, such as melting or forming, is given in Fig. 2.1. The variation of viscosity with temperature can be

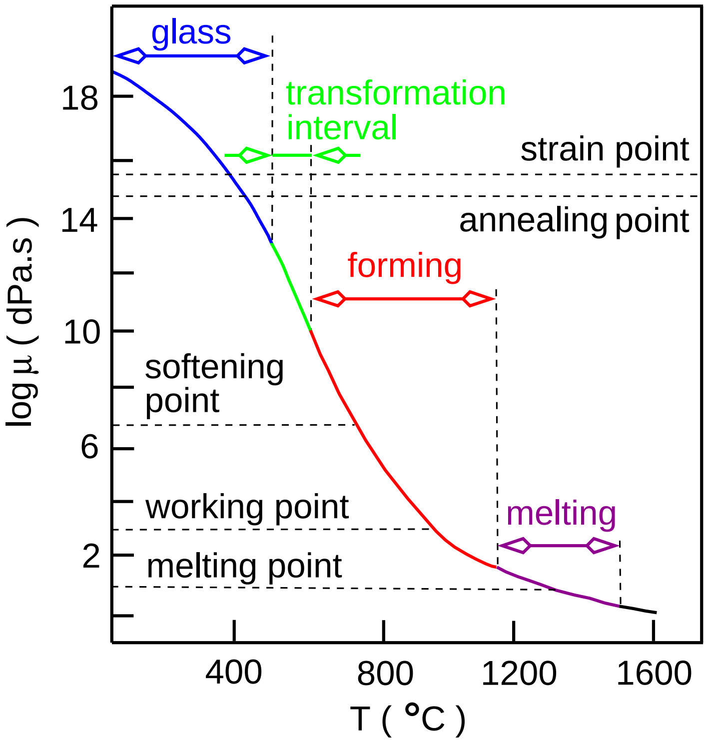

Figure 2.1: The viscosity curve of a glass.

expressed *via* the Vogel-Fulcher-Tamman equation (VFT) [5]:

$$\log \mu = A + \frac{B}{T - T_0}, \tag{2.2}$$

where T is the temperature and A, B and T_0 are coefficients, that change with the glass composition. They can either be determined experimentally or computed, discussed in more details in sec. 5.2.8. The viscosity curve is characterized by several important temperatures that correspond to a value of viscosity at which a certain process is achieved (Fig.2.1). The lowest important value of the viscosity is 10 Pa.s and corresponds to the **melting temperature**. **Working temperature** with μ=10^3 Pa.s is also called a temperature of glass forming and corresponds with the value of viscosity, where various shapes of glass products can be achieved. Glass products can deform due to their own weight at a viscosity 10$^{6.65}$ Pa.s, which is called **softening** or **Littleton** point. An interval during which a transition between the solid and liquid state appears is called the transformation interval with a viscosity in the range from 10^{11} to 10^{12} Pa.s. It is characterized by the **temperature of transformation**. The last two points of the curve are **annealing point** and **strain point**. The glass product is being gradually cooled between these two points in order to remove internal stresses. The value of viscosity changes from 10$^{12.4}$ to 10$^{13.5}$ Pa.s between these two points.

2.1.1 Measurement of viscosity

Since the range of the glass viscosity is so wide, it is impossible to find a method, which will cover the whole region. Methods for low viscosity range are similar to those, that are used for normal liquids. The most frequent are rotational viscometers with various constructions. Either the outer crucible is fixed and the torque which is necessary for a certain constant rotating velocity of the inner part is measured, or the outer crucible is turning and the torque which occurs on the inner rotating element is measured, or neither the crucible, nor the inner element is fixed. From the less common methods a falling-ball or a vibration viscometer can be mentioned. These methods are used for log μ from 2 to 8. Bending of a horizontal glass bar or fiber elongation are used in the range of higher values of viscosity, more details can be found in [30].

2.1.2 Variation of viscosity with glass composition

Viscosity of glass changes with its composition. Elements that cause ruptures in the former network so it becomes more flexible, lower the value of the viscosity. The most common are alkali metals [23] (Fig. 1.1). Bonds in boron glass are weaker than bonds in silica glass and therefore the addition of boron lowers the value of viscosity, more details about bonding will be given in sec. 2.2.2. Addition of 1 wt% of fluoride lowers the viscosity by a factor 10 [5]. A higher content of silica or alumina strengthens the structure of the network and therefore causes an increase of the viscosity. Alkaline earth metals rupture the network of glass at high temperature and lower the viscosity, however at low temperature (until 600°C) they can participate in bridging with anions of oxygen, which causes a higher value of viscosity. A graph in Fig. 2.2 shows viscosity curves for various glass compositions with a notation of the important temperatures, which were mentioned in the previous text. Influence of water vapor contained in the surrounding atmosphere was studied by Cutler [9], who observed a decreasing of the viscosity with a rising partial pressure of H_2O in the surrounding atmosphere. Water can dissolve in glass by creating ruptures in the silica structure as follows:

$$\equiv Si - O - Si \equiv\ + H_2O \rightarrow 2 \equiv Si - OH \tag{2.3}$$

Gaudio *et al.* [10] measured viscosity of water-bearing float glass (0.03-4.87 wt% H_2O) in temperature range from 573 to 1523 K and pressure range from 50 to 500 MPa. Melt viscosity strongly depends on temperature and water content but not on pressure. A new model predicting viscosity as a function of temperature and water content is presented for the range mentioned above.

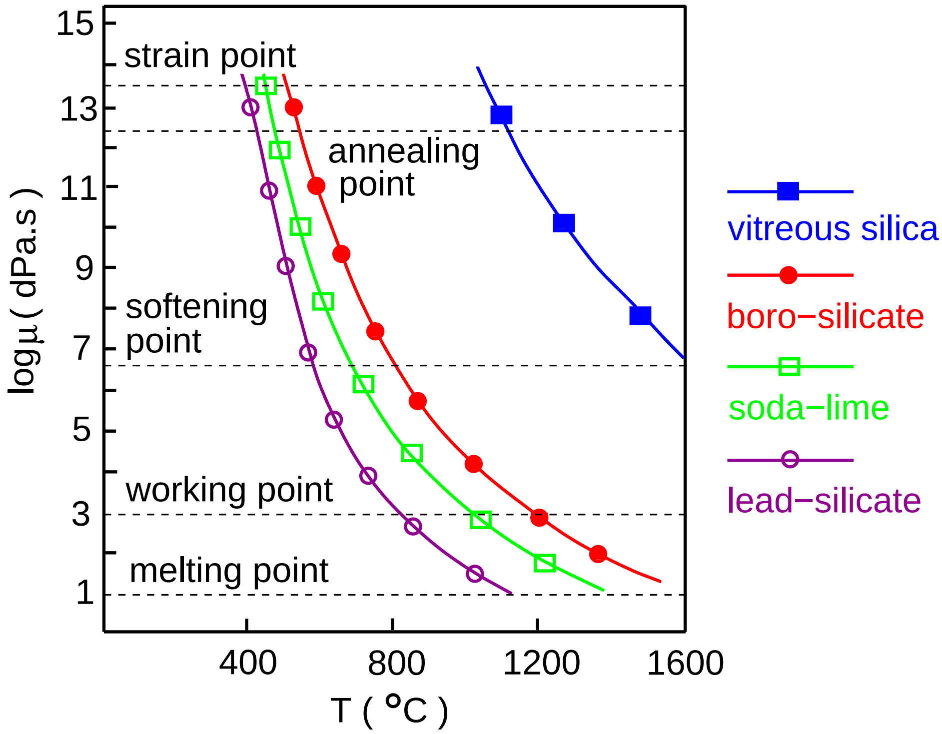

Figure 2.2: The viscosity curve of glasses with various composition.

2.2 Surface tension

Glass surface tension varies with composition and temperature. It is an important property influencing the glass foaming, but apart from that, it also favors melting by wetting the grains surface and participates during corrosion of refractory close to the upper surface of the glass melt, where three phases meet in contact. The surface tension of most glasses is approximately 300 mN·m^{-1} at 1300°C. In comparison, the surface tension of water is around 72 mN·m^{-1}.

2.2.1 Measurement of surface tension

The measurement of the surface tension of molten glass is a difficult process due to the high temperature and high reactivity with surrounding atmosphere. There are five main methods: a pull-on-cylinder method, a maximum bubble pressure method, a drop weight method, determination of a curvature of a glass droplet and melting of a glass fiber. The text below introduces the main principles of these methods, but does not contain all details. All methods exist in slightly modified forms depending on the author. Some references to articles with a precisely described set-up are given in the following text.

The pull-on-cylinder method

This method is usually used for temperatures above 1100°C [2, 31]. A hollow Pt-Rh cylinder is hanged on one side of a balance and its bottom edge is in contact with a level of the molten glass. Weights are being added on the second part of the balance, which leads to a formation of a thin cylindrical shaped glass membrane, which is dragged out of the molten glass until the second part of the balance is heavier and the membrane ruptures, see Fig. 2.3. The optical part, which consists of galvanometer lamp, mirror and scale, supports determination of the moment of rupture. The value of the surface tension is computed from the radius of the cylinder, the weights balance, the thickness of the cylinder wall and the

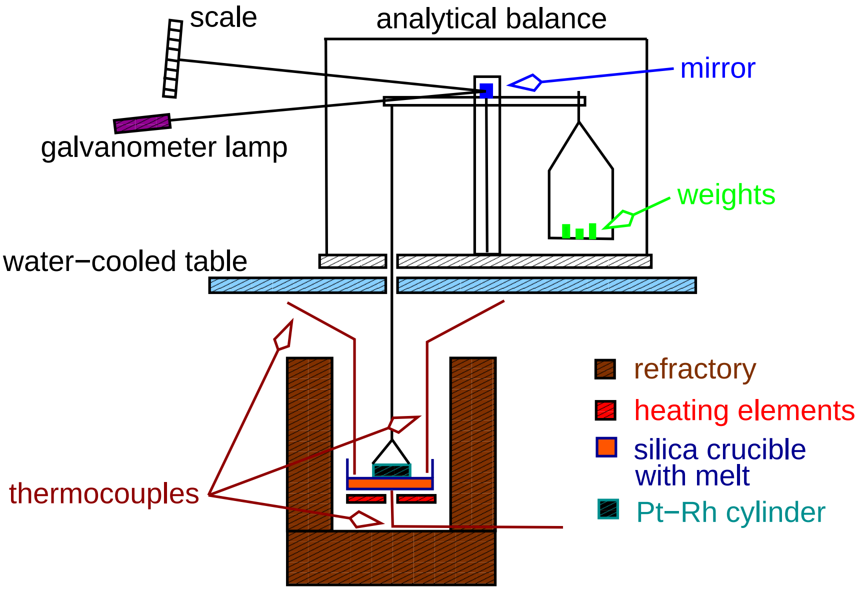

Figure 2.3: Determination of surface tension: pull-on-cylinder method [32].

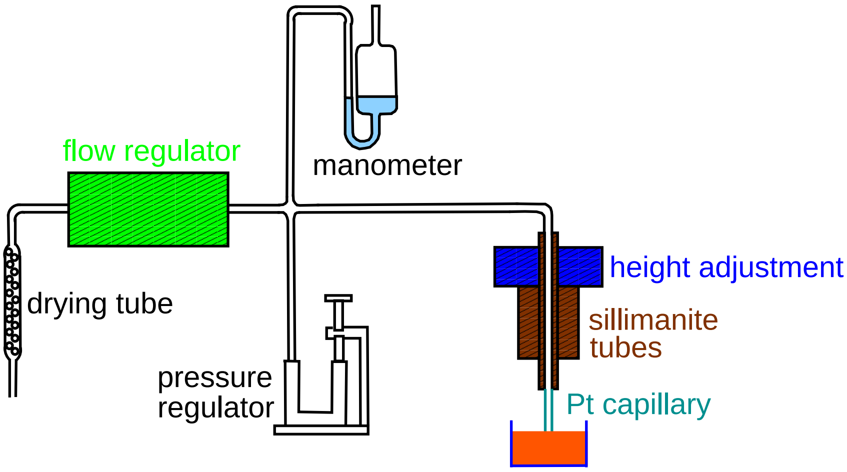

Figure 2.4: Determination of surface tension: maximum bubble pressure method [6].

density of the melt. The whole computation can be found in [32].

The maximum bubble pressure

The maximum bubble pressure is a very commonly used method mainly for low viscosity [6]. Scheme of the experimental set-up is given in Fig. 2.4. Pt-Rh capillary tube is placed in a contact with the level of the molten glass and gas is slowly introduced until the bubble ruptures. The surface tension of glass can be computed when the pressure in the capillary tube reaches the maximum, see eq. below:

$$\gamma = p\frac{r}{2}\left(1-\frac{2}{3}\left(\frac{r}{h}\right)-\frac{1}{6}\left(\frac{r}{h}\right)^2\right) \tag{2.4}$$

where:

p	maximum pressure (Pa)
r	capillary radius (m)
d_1	density of molten glass (kg·m^{-3})
d_2	density of bubble gas (kg·m^{-3})
$h = \frac{p}{(d_1-d_2)g}$	
g	gravitational acceleration (m·s^{-2})

It is necessary to know a precise value of the glass density to obtain correct value of the surface tension. Variation of the density of glass with temperature will be discussed in sec. 5.2.8. More details about the experimental measurement can be found in [6].

The drop weight method

In this experimental measurement glass drips out of a platinum tube and forms a drop. Surface tension of glass is determined from the weight of the drop (m) and radius of the rod (r) [30].

$$\gamma = \frac{mg}{2\pi r} \tag{2.5}$$

This method is similar to pendant-drop technique, which was used in the work of Lihrmann and Haggerty [21] or Kingery [19]. Sketch of arrangement for suspending pendant drop is given in Fig. 2.5. The surface tension is determined from the absolute drop diameter d_m, shape factor d_s and the density of glass using tables prepared by Hauser or Fordham [19].

Determination of the curvature of the pendant drop

A small piece of glass is placed on a refractory and a shape of a droplet, which is formed at high temperature, is determined using a high-temperature microscope [34]. It is neces-

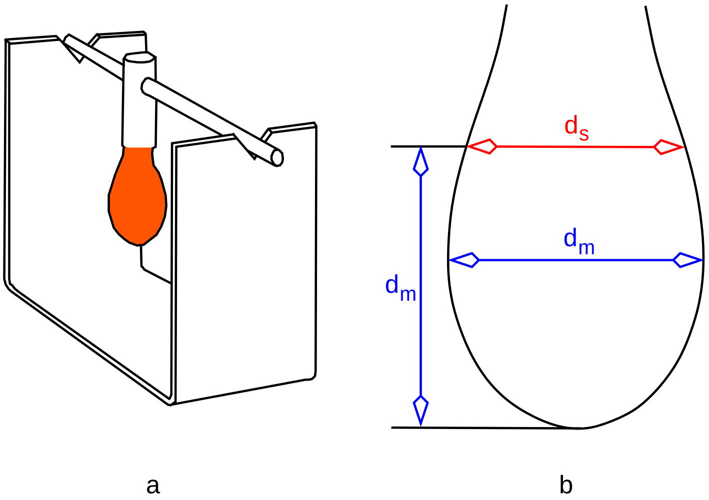

Figure 2.5: Determination of surface tension: pendant-drop method [19].

sary to take into consideration evaporation of spices from the melt during the experiment. Evaporation of glass will be discussed later in sec. 2.3.

Melting of the glass fiber

A competition between gravity and surface force is used during this method, when a glass fiber with a diameter of 0.6 mm is placed in the middle of a Pt heating coil, see Fig. 2.6a. When the heating starts, the middle part of the fiber becomes shorter and wider, which causes a creation of a small droplet (Fig. 2.6b). As the temperature is further rising, the bottom part of the fiber is detached and falls down. The bottom part of the fiber without the wider part is used for the determination of the surface tension, see Fig. 2.6c and eq. (2.6).

$$\gamma = \frac{2\, g\, m_{bot.}}{\pi\, d} \tag{2.6}$$

The last two methods are used for high viscosities. Errors of the measurement are between 1 and 5%, depending on the method, see [11, 29, 36] for more details.

2.2.2 Variation of surface tension with glass composition

The value of surface tension depends on attraction between molecules of the liquid, as it will be mentioned in sec. 3.1.1. For elements contained in glass this can be expressed by a polarizability of atoms and molecules. The higher is their polarizability, the lower is their contribution to the surface tension. The larger is an atom of an element, the easier is to polarize it, therefore the polarizability increases from the top to the bottom and from left to right in a periodic table. Accordingly alkali metals will have much lower contribution than silica. A single Si^{4+} will never occur on the surface of the glass, but it will always exist as a

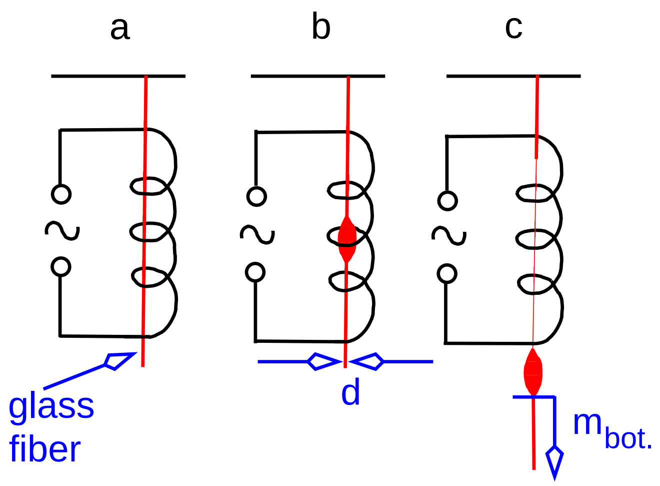

Figure 2.6: Determination of surface tension - melting of a glass fiber.

tetrahedron [SiO_4]. In the contrary, boron glass consists of [BO_3] groups, which form layers, that are connected by a weak binding. This leads to a much lower value of surface tension (80 mN·m^{-1} at 900°C) than for vitreous glass, formed by [SiO_4] tetrahedrons (280 mN·m^{-1} at 1200°C) [25].

Surface tension of glass rises with a rising content of Li [35, 3] due to a low polarizability caused by a small atom radius. Li has the smallest atom out of the alkali metals. Higher polarizability of Na and K leads to a decrease of surface tension with their addition [3]. Based on previous theory about a size of atoms, it can be deduced, that the addition of Rb and Cs lowers the surface tension of glass and even more significantly than potassium [23]. The decrease in surface tension is also initiated by the addition of F [16], V, B and Ti [3]. It is necessary to emphasize, that vanadium lowers the surface tension about 10 times more than boron or titanium.

In a comparison, a rising content of alkaline earth metals causes higher values of surface tension as well as the addition of Zn, Cd [23] or Ce, Zr, Ni, Co, Fe, Al and Mn [3, 26]. Tab. 2.1 summarizes all information above.

Decrease surface tension	**Increase surface tension**
V; B; Ti; F; Na; K; Rb; Cs	Cd; Zn; Ce; Zr; Ni; Co; Fe; Al; Mn; alkaline earth metals; Li

Table 2.1: Decreasing or increasing effect of some elements on the value of the surface tension of soda-lime-silica glasses.

2.2.3 Variation of surface tension with surrounding atmosphere

The influence of water vapor in the surrounding atmosphere was studied by Parikh [25], who determined the value of the surface tension using the fiber elongation method for soda-lime-silica glass in the temperature range from 500 to 700°C and he observed a decrease of the surface tension in wet atmosphere. The lower was the temperature, the higher was the difference between dry and humid atmosphere. The influence of water vapor was less obvious with the increasing temperature and it was predicted that for temperature above 1000°C it would be minor.

Parikh [25] also studied how other gases, which are present in the surrounding atmosphere, influence the value of the surface tension. He observed, that the presence of dry N_2, He and H_2 had no influence on the value of the surface tension, but a presence of SO_2, HCl and NH_3 lowered the value.

Akhtar and Cable [1] made an experiment with oxygen, nitrogen and carbon dioxide in the surrounding atmosphere using a maximum bubble pressure method. When same gas is in the atmosphere as well as in the bubble during the experiment, surface tension remains almost the same for oxygen and nitrogen, but is about 10-20 $mN \cdot m^{-1}$ higher in the atmosphere filled with CO_2.

2.2.4 Variation of surface tension with temperature

The surface tension of glass is decreasing with an increasing temperature [26]. At lower temperatures (up to 1200°C), this variation is more noticeable than at high temperatures (above 1400°C) [23]. It is necessary to emphasize, that the value of surface tension decreases when the temperature of the sample increases continuously, but if a glass sample remains at a high temperature for several hours, its surface tension rises due to variation in glass composition caused by evaporation, more details will be given in the following section.

2.3 Evaporation

It is well known, that glass composition changes at high temperature due to evaporation of volatile species, which leads to different structure and properties in surface layer and glass bulk. Breadly [32] observed a higher value of surface tension for a glass sample, which was exposed to the temperature 1500°C for 5 hours. A similar experiment was performed for various glass compositions by Shartsis and Smock [32]. All glass samples were left at 1350°C for almost 100 hours and the increase of surface tension was observed for all glasses in the first 20 hours.

Evaporation appears in three steps, which are: transport of the volatile substance to the surface, chemical reaction at the surface and transport of the products of the reaction from the surface. Volatilization into bubbles is not as important as from the free surface of the melt.

2.3.1 Evaporation of sodium and potassium

Beerkens [4] reports, that sodium evaporates as a consequence of chemical reaction with water vapor contained in the atmosphere:

$$\mathrm{Na_2O}\,(melt) + \mathrm{H_2O}\,(g) \leftrightarrow 2\mathrm{NaOH}\,(g) \tag{2.7}$$

Activity of Na_2O and partial pressure of water vapor play an important role in the loss of sodium. The activity of Na_2O is very low below 1200°C, but the reaction in eq. (2.7) becomes important above 1300°C. However, the partial pressure of water vapor in the surrounding atmosphere is under industrial conditions more important for the chemical reaction than the activity of Na_2O. Sodium hydroxide, which is the product of the reaction in eq. (2.7), is highly reactive and tends to form sodium sulfate with SO_2 from the atmosphere. Na_2SO_4 appears as droplets below 1100°C and solid inclusions below 884°C. The surface temperature as well as velocity of the convective flow in the surrounding atmosphere play an important role in the total loss of the volatile species, see Fig. 2.7. Much higher loss of sodium oxide in wet atmosphere was observed by Dietzel [12] and Hanke and Scholze [14].

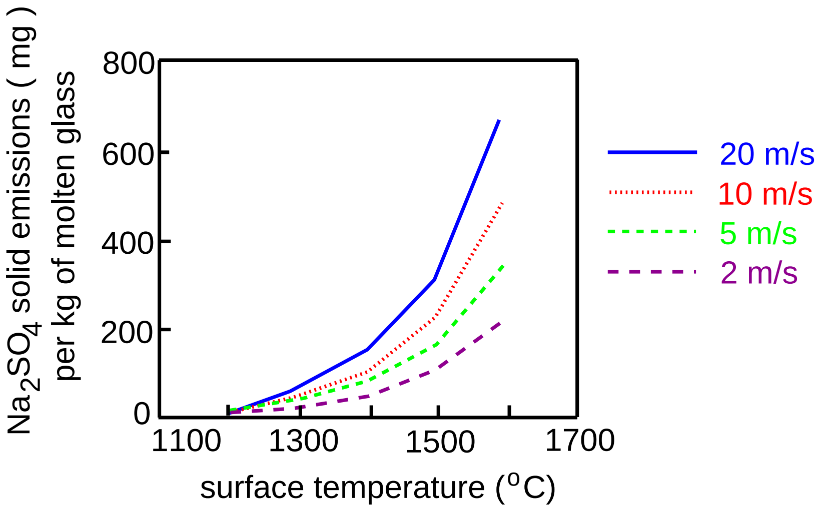

Figure 2.7: Effect of temperature and gas velocity above soda-lime-silica glass melt on sodium sulfate solid emissions due to NaOH volatilization in glass furnace [4].

Preston and Turner [28] performed an experiment, where they observed a loss of potassium at temperature range from 1100 to 1400°C during 200 h. The loss of potassium is increasing with the temperature, the velocity of the nitrogen flow above the glass sample, and with the initial content of K_2O. When the content is above 33 mol%, new structure appears in glass, which leads to a much higher loss of potassium during the experiment.

Kucuk *et al.* [20] studied the evaporation of potassium and sodium by the determination of shape of sessile or pendant drop with a high speed camera. The density and surface tension were determined from the drop shape. Dry argon was flowing in the surrounding atmosphere to eliminate the third step of evaporation, which is the transport of the products of the chemical reaction. Their results show, that potassium and sodium start to volatilize at 1050°C and the volatilization appears at much higher rates above 1300°C. The density for soda-lime-silica and potassium-silica glass is rising in time for all tested temperatures as a consequence of loss of Na_2O and K_2O. On the other hand, surface tension is rising only for soda-lime-silica glass, but remains the same for potassium-silica glass. Same value for potassium glass is explained by a very fast diffusion of potassium from the bulk to the surface, which is as fast as the chemical reaction, and that is why no variation in concentration in the surface layer is observed. Compared to that, diffusion of sodium is slower, than the chemical reaction at the surface, and variation of concentration is observed. The diffusion is slower due to the presence of calcium, which blocks the diffusion paths.

The evolution of the loss of the substance with time can give us an information about the main step in evaporation. If the loss of the substance changes with time linearly (loss = f(t)), then the chemical reaction is the most important step, while if the loss of the substance changes with square root of time (loss = $f(t^{1/2})$), then the driving force is the diffusion. Chemical reaction, as the most important step was observed by Hanke and Scholze [14], while for Cable [20] it was diffusion. The weight loss in the work of Kucuk *et al.* [20] is given in Fig. 2.8. The evolution with time is neither t^1 nor $t^{1/2}$, which indicates, that both steps, chemical

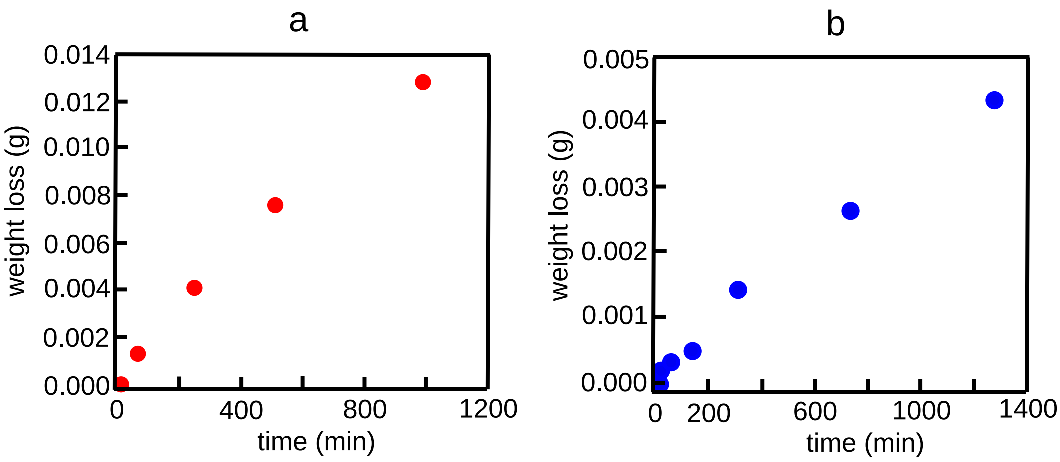

Figure 2.8: Volatilization loss in a: potassium trisilicate melt ($25\,K_2O \cdot 75\,SiO_2$) and b: soda-lime-silica melt ($15\,Na_2O \cdot 10\,CaO \cdot 75\,SiO_2$) at 1400°C [20].

reaction and diffusion participate.

2.3.2 Evaporation of boron

Evaporation of boron appears as a reaction of boron contained in the melt with water vapor in the surrounding atmosphere [33]:

$$\mathrm{B_2O_3}\,(melt)\;+\mathrm{H_2O}\,(g)\;\leftrightarrow\;2\,\mathrm{HBO_2}\,(g) \tag{2.8}$$

In dry atmosphere and in glass melt containing sodium or potassium, boron evaporates as follows:

$$\mathrm{NaBO_2}\,(melt)\;\leftrightarrow\;\mathrm{NaBO_2}\,(g) \tag{2.9}$$

$$\mathrm{KBO_2}\,(melt)\;\leftrightarrow\;\mathrm{KBO_2}\,(g) \tag{2.10}$$

Nevertheless, these reactions appear only in dry atmosphere, the higher is the partial pressure of water vapor, the more probable is the reaction, which is given in eq. (2.8).

In the work of van Limpt *et al.* [33], sample of boron glass with a content of boron between 1 and 10 wt% was placed in a Pt-Rh boat inside a furnace, where the partial pressure of water vapor in the atmosphere varied between 0 and 0.3 bar. Vapors of the glass were collected in gas wash bottles. The rest of the glass composition was: 55-62 wt% $SiO_2 \cdot$ 20-25 wt% CaO $\cdot$ 13-15 wt% Al_2O_3 (depending of the boron concentration) and the temperature of the experiment was between 1400 and 1500°C. More details about the experimental set-up can be found in the work of van Limpt [22].

The higher the initial concentration of boron and the higher the experimental temperature, the higher the evaporation rate is. Two samples with various initial boron concentration were exposed to 1500°C for 6 hours. The concentration profile was determined in the first 8 mm of the sample by SEM-WDX method, see Fig. 2.9. The concentration of boron decreased to 2.8 wt% from the initial 7.6 wt% and no concentration gradient was observed, while for the initial concentration of 2.6 wt%, the concentration gradient appeared. The concentration of B_2O_3 was approximately 0.2 wt% in the surface layer and about 7 times higher in the depth of 4 mm.

According to van Limpt *et al.* [33] diffusion is not the only process, that transports boron to the surface, but convection participates as well. It appears as a consequence of density differences and Marangoni flow caused by temperature gradients. No profile for a higher concentration of boron is observed, because the viscosity is lower, which enables faster diffusion and also convection is probable under these conditions. While for a lower boron content, a silica rich layer with low solubility of boron and lower surface tension slowers diffusion and causes lower convection. A concentration 2.5 wt% of boron is found to be a limiting

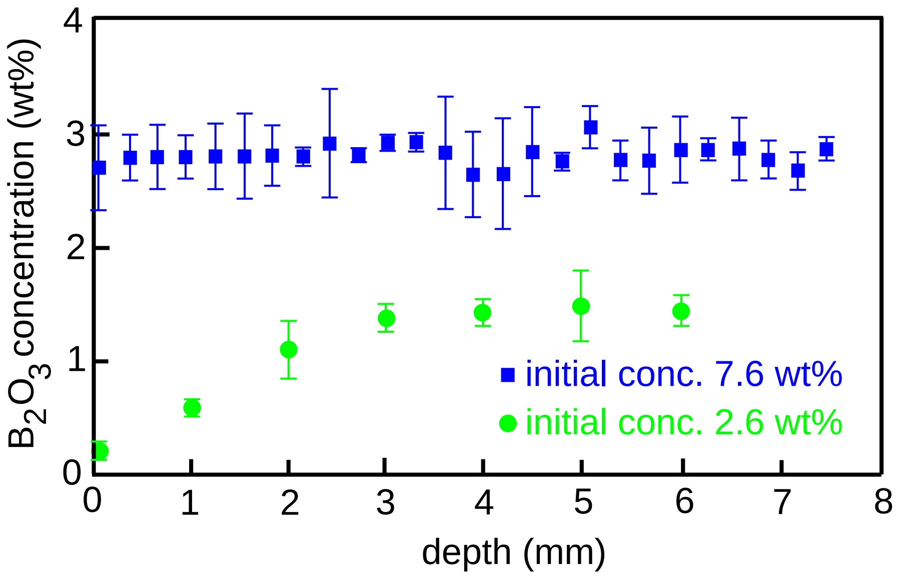

Figure 2.9: Measurement of vertical B_2O_3 concentration profile in the glass sample obtained after 6 hours at 1500°C for two various initial concentrations [33].

concentration over which evaporation rate has much higher value. Actually this limiting concentration is due to changes in the glass structure.

2.4 Behavior of sodium sulfate

The behavior of Na_2SO_4 changes with the temperature and redox state of glass, as it has been mentioned in sec. 1.2.2. Conroy [8] observed the behavior of sodium sulfate under a hot-stage microscope in a wide temperature range. Sodium sulfate appeared as a liquid around 884°C. The liquid phase remained on the interface of grains in the batch and its low viscosity supported bubble release below the temperature 1038°C. When the concentration of sodium sulfate exceeds a certain level (around 1% SO_3 [27, 15]), it becomes immiscible with the silicate melt and forms a sulfate gall on the surface. It behaves as an “anti-foam” substance, because its surface tension is between 194.8 $mN{\cdot}m^{-1}$ at 900°C and 184.7 $mN{\cdot}m^{-1}$ at 1077°C [17]. Anti-foams will be more discussed in the following chapter, see sec. 3.3. Surface tension of an ordinary molten glass is higher, usually between 250 and 350 $mN{\cdot}m^{-1}$, therefore the presence of sulfate gall lowers the value of the apparent surface tension. Dietzel and Wegner [13] observed a lower value of the surface tension for a glass with sulfate, than for a glass with the same composition, but without the addition of SO_3. They measured the surface tension using a fiber elongation method at 850°C and observed a 40 mN·m^{-1} variation with 1 wt% addition of sulfate. Lower value of surface tension was not observed for a glass containing sulfate under reducing conditions, where sulfate is reduced to sulfide, as it has already been shown in sec. 1.2.2, see Tab. 1.2. Similar results were obtained in the work of Jebsen-Marwedel [18], who measured the surface tension of commercial glasses with the addition of sodium sulfate and observed a 22% decrease in the presence of oxidizing atmosphere in comparison with the reduced conditions.

With a rising temperature, Conroy *et al.* [8] observed a decomposition of the sulfate above a temperature 1315°C. The newly created products (Na_2O, SO_2 and O_2) were dissolved in the molten glass, which was accompanied by a motion on the interface. The convective motion supports mixing and accelerates the dissolution of silica grains. Bruckner [7] presented results of an experiment with ether-water interface, where a drop of glacial acetic acid was added. The acid is soluble in both phases and its addition to the system causes a disrupture of the interfacial tension and a Marangoni flow. This is similar to the behavior of sulfate and molten glass, where the products of the decomposition are transported from the sulfate to the molten glass. Merker [24] observed a decrease of surface tension of soda-lime-silica glass with 0.4 wt% of SO_3 around 900°C, which can be explained by the presence of sulfate, but no change of surface tension was observed at 1400°C, where the sulfate was decomposed.

For temperature higher than 1454°C, Conroy *et al.* [8] observed a creation of bubbles, because the products of the decomposition are no longer soluble. They create bubbles and support the mixing and homogenization.

References

[1] S. Akhtar and M. Cable. Some effects of atmosphere and minor constituents on the surface tension of glass melts. *Glass Technology*, 9(5):145–151, 1968.

[2] C. L. Babcock. Surface tension measurements on molten glass by a modified dipping cylinder method. *Journal of The American Ceramic Society*, 23(1):12–17, 1940.

[3] A. E. Badger, C. W. Parmelee, and A. E. Williams. Surface tension of various molten glasses. In *39th Annual Meeting, American Ceramic Society*, pages 325–329, 1937.

[4] R. G. C. Beerkens. The role of gases in glass melting processes. *Glasstech. Ber. Glass Sci. Technol.*, 68(12):369–380, 1995.

[5] R. G. C. Beerkens and H. de Waal. *Handbook for Glass Technologists*. 1997.

[6] C. A. Bradley Jr. Measurement of surface tension of viscous liquids. In *40th Annual Meeting, American Ceramic Society*, pages 339–344, 1938.

[7] R. Brückner. Zur Kinetik des Stoffaustausches an den Grenzflächen zwischen Silikatglas- und Salzschmelzen und des Stofftransportes in Silikatglasschmelzen unter besonderer Berücksichtigung des Verhaltens von Na_2SO_4 und seinen Zersetzungsprodukten (Teil I. - III.). *Glastechn. Ber.*, 34; 34; 35.

[8] A. R. Conroy, W. H. Manring, and W. C. Bauer. The Role of Sulfate in the Melting and Fining of Glass Batch. *The Glass Industry*, 47, 1966.

[9] I. B. Cutler. Effect of Water Vapor on the Sintering of Glass Powder Compacts. *Journal of The American Ceramic Society*, 52(1):11–13, 1969.

[10] P. Del Gaudio, H. Behrens, and J. Deubener. Viscosity and glass transition temperature of hydrous float glass. *Journal of Non-Crystaline Solids*, 353:223–236, 2007.

[11] A. Dietzel. Beobachtungen an chromroten. *Glasuren. Ber. Dtsch. Keram. Ges.*, 26:12–21, 1949.

[12] A. Dietzel and L. Merker. Entstehung von Inhomogenitäten in der Glasschmelze durch Verdampfung einzelner Glasbestandteile. I. *Glastech. Ber.*, 304:134–138, 1957.

[13] A. Dietzel and E. Wegner. Einfluß von SO_3 auf die Oberflächenspannung von Gläsern. *Glastech. Ber.*, 28:166–167, 1955.

[14] K. P. Hanke and H. Scholze. Einfluß der Ofenatmosphäre auf die Verdampfung aus Glasschmelzen. *Glastech. Ber.*, 50:271–275, 1977.

[15] S. Holmquist. Oxygen Ion Activity and the Solubility of Sulfur Trioxide in Sodium Silicate Melts. *J.Am.Cer.Soc.*, 49:467–473, 1966.

[16] P. Hrma. Model for a Steady State Foam Blanket. *Journal of Colloid and Interface Science*, 134(1):161–168, 1990.

[17] F. M. Jaeger. Über die Temperaturabhängigkeit der molekularen treien Oberflächenenergie von Flüsseigkeiten im Temperaturbereich von -80 bis +1650°C. *Anorg. allgem. Chem.*, 101:210, 1917.

[18] H. Jebsen-Marwedel. Abhängigkeit der Oberflächenspannung des Glases von oxydierender und reducierender Atmosphäre - eine Folge “ambulanten” SO_3 - Gehaltes. *Glastechn. Ber.*, 28:161, 1955.

[19] W. D. Kingery. Surface Tension of Some Liquid Oxides and Their Temperature Coefficients. *Journal of The American Ceramic Society*, 42(1):6–10, 1959.

[20] A. Kucuk, A. G. Clare, and L. E. Jones. Differences between surface and bulk properties of glass melts I . Compositional differences and influence of volatilization on composition and other physical properties. *Journal of Non-Crystalline Solids*, 261:28–38, 2000.

[21] J. M. Lihrmann and J. S. Haggerty. Surface Tensions of Alumina-Containing Liquids. *Journal of The American Ceramics Society*, 68(2):81–85, 1985.

[22] H. Limpt. *Modelling of evaporation processes in glass melting furnaces*. PhD thesis, 2007.

[23] O. Mazurin, M. Streltsina, and T. Shvaiko-Shvaikovskaya. *Handbook of glass data Part C Ternary silicate glasses*. Elsevier, 1987.

[24] L. Merker. Der Einfluß von Sulfat in Natron-Kalk-Gläsern auf einige physikalische Eigenschaften. *Glastech. Ber.*, 32:75–76, 1959.

[25] N. M. Parikh. Effect of Atmosphere on Surface Tension of Glass. *Journal of The American Ceramics Society*, 41(1):18–22, 1958.

[26] C. W. Parmelee and C. G. Harman. The effect of alumina on the surface tension of molten glass. *Thirty-Eight Annual Meeting, American Ceramic Society*, pages 224–230, 1936.

[27] M. L. Pearce and J. F. Beisler. Miscibility Gap in the System Sodium Oxid-Silica-Sodium Sulfate at 1200°C. *J.Am.Cer.Soc.*, 48:40–42, 1965.

[28] E. Preston and W. E. S. Turner. *J. Soc. Glass Technol.*, 17:122, 1933.

[29] P. R. Rao and N. Subramanian. Effect of viscosity in the determination of surface tension by the drop-weight method. *J. Sci. Ind. Res.*, 18B:402–404, 1959.

[30] H. Scholze. *Nature, Structure and Properties*. Springer-Verlag, New York, 1991.

[31] L. Shartsis, H. F. Shermer, and A. B. Bestul. Surface Tension of Alkaline-Earth Borates Containing 3 Mole % Potassium Oxide. *Journal of The American Ceramics Society*, 42(5):242–249, 1959.

[32] L. Shartsis and A. W. Smock. Surface tensions of some optical glasses. *Journal of The American Ceramic Society*, 30(4):130–136, 1947.

[33] H. van Limpt, R. Beerkens, S. Cook, R. O'Connor, and J. Simon. Modelling the evaporation of boron species. Part 1. Alkali-free borosilicate glass melts. *European Journal of Glass Science and Technology Part A*, 52(3):77–87, 2011.

[34] D. A. Weirauch Jr. and D. P. Ziegler. Surface tension of calcium aluminosilicate glass using computerized drop shape analysis. *Journal of The American Ceramics Society*, 79(4):920–926, 1996.

[35] R. M. Williams and H. E. Simpson. A Note on the Effect of Lithium Oxide Upon the Surface Tension of Several Silicate Melts. *Journal of The American Ceramics Society*, 34(9):280–283, 1951.

[36] H. Wondratschek. Ein Verfahren zur gleichzeitigen Bestimmung von Zähigkeit und Oberflächenspannung an Gläsern bei relativ niedrigen Temperaturen. *Glastech. Ber.*, 32:276–278, 1959.

Chapter 3

Foam - creation and decay

Foam consists of a gaseous phase dispersed in a continuous phase, that can either be a solid or a liquid, which enables dividing foams into solid and liquid foams [11]. In this study we are interested in liquid foam, where the liquid part is made of molten glass. Creation of foam, its properties and decay depend on the properties of the continuous and gas phase and are discussed in this chapter. At the beginning of foam life, a bubble have to be created in the liquid (sec. 3.1). Then this bubble rise to the surface of the bath (sec. 3.1.2) where it meets others and creates a bubble assembly - foam. If the amount of liquid in the foam is smaller than 1%, we talk about a dry foam, where bubbles have a shape of polyhedral, if the content of liquid is higher than 35%, bubbles remain spherical, move independently and we obtain a wet foam [11, 39]. Dry foam is formed from a wet one due to drainage which is caused by gravity and capillary suction, see sec. 3.2. Capillary suction appears, when a liquid is squeezed between bubbles, which rise due to the buoyancy force. When a bubble lamella reaches a critical thickness as a consequence of drainage, it ruptures. Causes of a lamella rupture are discussed in a section related to foam decay, see sec. 3.3.

Foams are desirable for many applications, such as food industry, cosmetics, fire-fighting foams, or insulation foam which is an example of a solid foam. In the contrary, foam is undesirable during glass melting, as it has already been discussed in the previous text, but also in metallurgy, petrochemical industry or fermentation processes to name a few. Literature related to glass foaming is very rich. The last section of this chapter (sec. 3.4) summarizes the most important conclusions related to the stability of a vertical film, a bubble lamella and foam in general.

3.1 Bubble and a foam creation

Bubbles which are the building units of foam, can appear as a consequence of supersaturation of dissolved gases by decrease of pressure or rising temperature. Variation of temperature is a cause of foaming in glass industry, as it was discussed in previous chapters. Bubbles usually nucleate on walls or some non homogeneous particle in the liquid. Their creation and growth are governed by Laplace pressure and so depend on the surface tension (sec. 1.2). Apart from nucleation, bubbles can be formed mechanically by mixing or whipping. Foam is created, when the amount of bubbles exceeds 50% of the total amount in volume.

3.1.1 Surface tension - key parameter for foam

Deffinition and origin of surface tension

Surface tension is a physical property of a liquid, that informs if foam creation inside this liquid is energetically less or more demanding. Molecules in a liquid attract one another. The molecules inside a liquid volume can interact with all the neighbors, that surround them, but molecules at the surface loose half of the interactions and are considered to be “unhappy” [10]. All liquids are therefore trying to remain in a shape with the smallest possible surface. The higher the value of the surface tension, the smaller surface the liquid is trying to create. The amount of energy, which is needed to enlarge the surface area, is proportional to surface tension. Therefore surface tension can be expressed as the energy needed to increase the surface by one unit:

$$dW = \gamma dS \tag{3.1}$$

Surface tension is related to the chemical structure of liquid. While in oil, the interactions are of van der Waals type, there are hydrogen bonds in water, which are responsible for a larger value of surface tension. That is why a drop of water remains in a spherical shape, when mixed with oil, as far as its diameter is small enough compared to the capillary length, while oil drop spreads on water surface. Chemical composition of the molten glass is responsible for its surface tension (discussed in the previous chapter, see sec. 2.2).

Capillary force is responsible for lowering the total value of free surface energy, by lowering the surface area. An example is given in Fig. 3.1, where a mobile rod is fixed to one end of a thin liquid film with a width l. The mobile rod will move towards the fixed end of the film in order to decrease its surface.

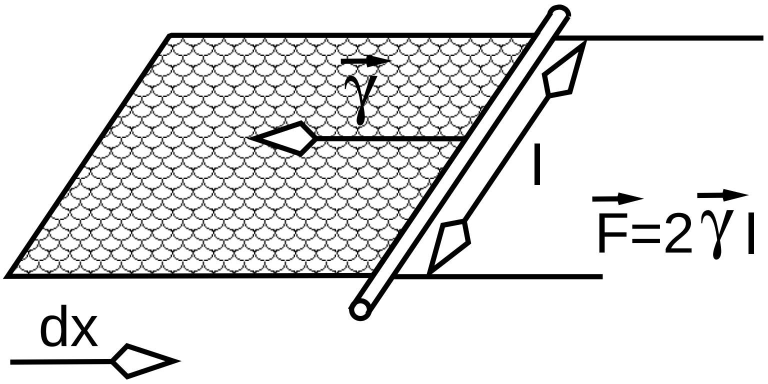

Figure 3.1: Capillary force acting on a thin film.

Foam is in metastable state

The gaseous phase in foam has a much larger volume, than the liquid phase. This leads to a large interfacial area and a large amount of free surface energy, which makes foam unstable from the thermodynamical point of view. Even though Kitchener and Cooper [24] describe foam as unstable from the thermodynamical point of view, they also distinguish foam as metastable and labile. This distinction is related to the lifetime of the foam, which is longer for metastable foam. Stable or metastable foam is a term very often found in the literature in order to express a foam with a long lifetime, but not a stable foam from the thermodynamical point of view.

Following the high surface energy theory, it is easier to create a foam in a liquid having a lower surface tension, because less energy is needed to create a large interfacial area. Nevertheless, no relation was observed between an increasing value of surface tension and a faster decay of glass foam [1, 22].

Surfactant

Surfactants are substances that act on the surface properties of an interface. They consist of a hydrophilic and a hydrophobic part. They can be added to a liquid, where they remain at the surface and lower the free surface energy, which enhances the foam creation in the liquid. The presence of a surfactant prolongs the lifetime of foam, by retarding the drainage (sec. 3.2.2), supports resistance against local deformation and decreases the critical thickness [2, 31, 8, 7, 6, 5, 32].

Marangoni flow

Marangoni flow appears as a consequence of surface tension gradient. It can be observed as tears of wine while drinking alcoholic beverages or in soap films as a consequence of temperature gradient [36]. The flow is initiated from a domain with lower surface tension to a domain with higher. In molten glass, variation of surface tension can appear due to temperature gradient or as a consequence of concentration gradient caused by evaporation. An experiment with sodium-borate glass was done by McNeil *et al.* [30]. A temperature gradient from 10 to 30°C initiates a variation of surface tension causing a motion with velocity from 0.2 to 1.2 mm·s^{-1} in a vertical liquid bridge. The temperature gradient was rising from the bottom to the top and also from the top to the bottom to verify that the motion is not caused by variation of density of molten glass. Absolute values of velocities were comparable, but the direction of the motion was inverse when the temperature gradient was changed. The average temperature of the liquid bridge was varying between 865 and 950°C.

3.1.2 Rising velocity of bubbles in molten glass

A drag and buoyancy forces act on a bubble when it rises through a liquid. The drag force acting on a droplet in an infinite media with a laminar regime and with a pure interface without surfactants, is given in eq. below [40]:

$$\vec{F}_{drag} = -2\pi\mu r \frac{2+3\bar{\mu}}{1+\bar{\mu}} \left(\vec{v} - \vec{u}\right) \tag{3.2}$$

where:

μ	viscosity of the liquid surrounding the droplet (Pa·s)
r	droplet radius (m)
$\bar{\mu}$	ratio of viscosities of a liquid inside and outside of the droplet (-)
$\vec{v}$	velocity of the droplet (m·s^{-1})
$\vec{u}$	velocity of the continuous phase (m·s^{-1})

This formula is considered for a rising bubble in molten glass, because of the absence of surfactants at bubble interface and the high viscosity of molten glass, which ensures the laminar flow and spherical shape of the bubble. Ratio of viscosities is considered to be equal to zero, because the viscosity of glass is much larger than the viscosity of gas inside the bubble. The asymptotic rising velocity is called the Hadamard-Rybczynski velocity and is given in eg. (3.3).

$$v_{HR} = \frac{\rho\, g\, r^2}{3\,\mu} \tag{3.3}$$

Stokes velocity for a solid sphere can be considered only if the surface of the bubble is covered by a non-soluble surfactant, which accumulates at the bottom part of the rising bubble as a result of the combination between a moving bubble interface and buoyancy force. The surface tension gradient between the surfactant poor top and surfactant rich bottom leads to a shear force and immobilization of the bubble interface. Stokes velocity is 1.5 times smaller than the Hadamard-Rybczynski:

$$v_{Stokes} = \frac{2\,\rho\,g\,r^2}{9\,\mu} \tag{3.4}$$

In molten glass, Hadamard-Rybczynski rising velocity was observed during measurements of Jucha *et al.* [21] at temperature range from 800 to 1000°C in borate glass melts as well as by Hornyak and Weinberg [16] at soda-lime-silica glass melt.

The viscosity of glass decreases exponentially with temperature, see Fig. 3.2. The lower the viscosity of glass, the faster the rising velocity, therefore the glass fining is achieved at high temperatures (around 1450°C) as it has already been mentioned in the previous chapters. If we consider a glass density of 2450 kg·m^{-3} and a viscosity 10 Pa.s at 1420°C (graph in Fig. 3.2), the time over which a bubble with a diameter 1 mm rises over 1 m is approximately 83 min, while for a bubble with a diameter 0.1 mm it is more than 138 hours. This computation indicates that it is extremely long to remove small bubbles from the melt and that is why their size is enlarged by diffusion of gases, which are released from fining agents, see sec. 1.2.2.

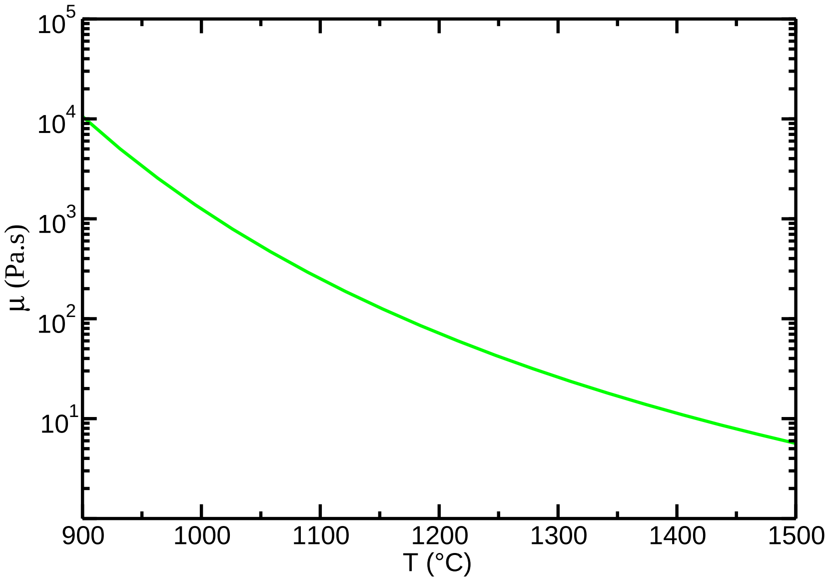

Figure 3.2: Viscosity as a function of the temperature for an ordinary soda-lime-silica glass. (SiO_2:Na_2O:CaO = 75:15:10 wt%)

3.2 Drainage

Bubbles creating foam are separated by lamellas, which meet in Plateau borders. A position of lamellas is controlled by two Plateau laws. First of them says, that for a dry foam, only three lamellas can intersect at one point, which is called a Plateau border, and must do so at an angle 120°. Second rule is valid for Plateau borders in 3D and does not allow more than 4 Plateau borders to meet at one point. Angle between the borders at the point of intersection is about 109° [35]. Channels of Plateau borders form a network filled with liquid and enable drainage of the liquid out of the foam or into it.

3.2.1 The origin of drainage: gravity and capillary forces

There are two important steps of drainage in foam. One of them appears on a large scale, when the liquid drains out of the Plateau borders due to the gravity force, which is opposed by the viscous force. Second drainage appears on a small scale, when the liquid drains from the lamella into the Plateau border due to a variation of pressure caused by a various curvature of the lamella and the border, see Fig. 3.3: This phenomenon, which is called a Plateau border suction, is opposed by the disjoining pressure (Π) consisting of the van der Waals attractive forces, repulsive forces of electric double layer and steric interactions appearing for molecules with long chains, eq. (3.5) and (3.6)[4]:

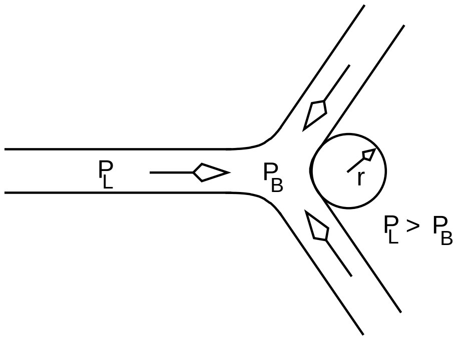

Figure 3.3: Plateau border suction.

$$\Delta P = \frac{\gamma}{r} - \Pi \tag{3.5}$$

$$\Pi = \Pi_{VDW} + \Pi_{DL} + \Pi_{SR} \tag{3.6}$$

where:

ΔP	pressure difference between the middle of the lamella and the Plateau border (Pa)
γ	surface tension (N·m^{-1})
r	radius of the curvature (m)
Π	disjoining pressure (N·m^{-2})
Π_{VDW}	pressure caused by van der Waals attractive forces (N·m^{-2})
Π_{DL}	pressure caused by repulsive forces of electric double layer in case of charged interfaces (N·m^{-2})
Π_{SR}	pressure caused by steric interactions (N·m^{-2})

3.2.2 Mobility of interfaces

As liquid drains out of the bubble lamella, it does so in a certain velocity profile depending on the mobility of the lamella interfaces. The interface can be either fully mobile, partially mobile or fully immobile, see Fig. 3.4. The velocity does not vary inside the lamella with a fully mobile interface and we obtain a plug flow (Fig. 3.4 a). Viscosity of the continuous phase is the limiting factor of the drainage in pure liquid with completely mobile interface. The higher the viscosity, the longer the drainage [14]. This lamella is often called unstable, because it ruptures as soon as the critical thickness is reached.

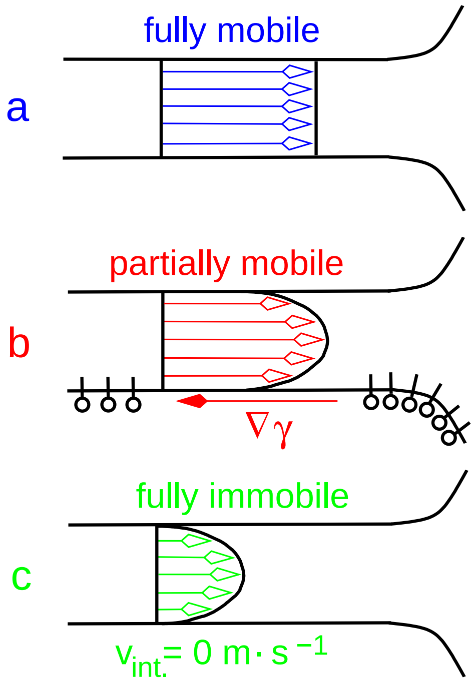

Figure 3.4: Fully mobile, partially mobile and fully immobile interfaces.

When surfactant is contained in the continuous liquid phase, it is swept to the Plateau borders by flow in the lamella causing concentration gradient at the interface (Fig. 3.4 b). The gradient causes Marangoni effect which retards the drainage at the interface. As a consequence, the velocity is lower at the interface than in the center of the lamella [13]. Plateau, cited in [28], talks about a surface viscosity, which is higher close to the interface. The effect of a surface viscosity was studied by Ivanov and Dimitrov [20]. The higher the concentration gradient, the smaller the interface velocity. Limiting case is zero interface velocity at fully immobile interface (rigid wall), see Fig. 3.4 c.

3.3 Decay of foam

Small bubbles can disappear due to diffusion of gas through the lamella into larger bubbles. This phenomena is called Ostwald ripening and was discussed in sec. 1.2.2. Bubbles creating foam can also disappear by a collapse of the lamella when it is sufficiently thin due to drainage. Marginal regeneration also participates in thinning of a lamella. Mysels [15] observed areas with thicker and thinner part on a vertical film. He explains, that the border suction acts differently on the two parts and drags the thicker part to the Plateau border and enhances the drainage in the thin film.

In pure liquids without repulsive forces, a bubble lamella can rupture as a result of spontaneous growth of thermal fluctuation amplified by capillary waves which generate squeezing mode of instability and the attractive van der Waals forces cause the rupture of the film [15]. This was confirmed experimentally by Manev [29]. Fluctuations can lead to a “bending mode” (sinusoidal) or a “squeezing mode” (varicose), see Fig. 3.5. If an interface of a lamella is immobile due to a presence of a surfactant (meta-stable lamella) the collapse of the film is irregular [38] and requires more energy [11]. One of the possibilities to cause a rupture is a presence of an anti-foaming agent. The mechanism is shown in Fig. 3.6. A surface active particle remains on the surface and spreads due to a lower value of the surface tension compared to the remaining liquid. As it is spreading, it drags the liquid below and causes a local thinning, which leads to a rupture of the lamella. Dietzel [22] informs that

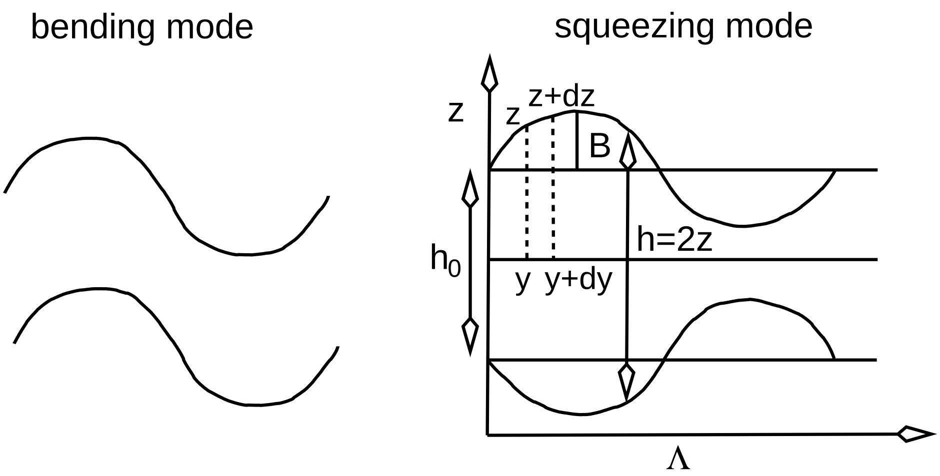

Figure 3.5: Spontaneous growth of capillary waves.

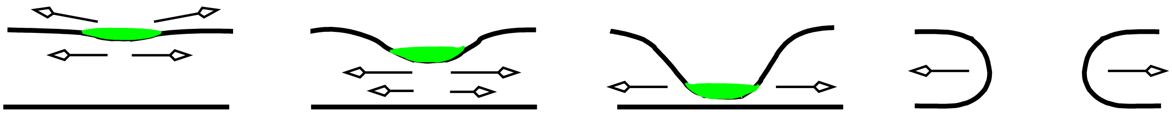

Figure 3.6: Local thinning of a lamella due to a presence of a surface active particle.

sulfide, fluoride or hydroxyl ions can behave like surfactant in the molten glass. Appart from anti-foaming agents, temperature or pressure shocks can initiate a rupture of a meta-stable lamella. Pressure shocks can be achieved by a puff of gas or acoustic vibration. The value of the pressure needs to be local and higher than the activation energy of the hole formation, because lamellas containing a surfactant can be very elastic and deformable. It is necessary to emphasize, that once a first bubble ruptures at an interface (in the top layer of the foam), a destabilization of the ruptured film can appear as it retracts and a liquid jet, which breaks into droplets, can be created. This can cause pressure wave (detonation), which propagates through the foam and cause a propagation reaction of rupture and collapse of foam [35].

3.4 Previous work on glass foaming

Many numerical and experimental studies related to creation and decay of glass foam have been published. The following text summarizes some of the previous work, which is mainly related to the stability of a vertical film, bubble lamella and foam. The influence of glass composition on the temperature of foaming as well as the influence of a surrounding atmosphere on foam stability is discussed at the very end.

3.4.1 Stability of glass vertical film

The experiment with a vertical glass film is very common in glass science and will be described in more details in the next chapter, see sec. 4.3. Kappel *et al.* [22] were interested in the evolution of thickness of the vertical film. When the film was withdrawn from the melt, it was held for a certain time and then rapidly cooled. The thickness at the thinnest part was determined. The thickness decreases exponentially as a function of a draining time and the decreasing constant is a function of temperature. Kappel *et al.* were also interested in the behavior of drainage under various atmospheric conditions. A variation of partial pressure of water vapor in the surrounding atmosphere has no influence on the thinning, but an increasing partial pressure of sodium accelerates the drainage. According to Kappel *et al.* the slower drainage for a lower partial pressure of sodium in the surrounding atmosphere is explained by a higher viscosity at the surface layer caused by the evaporation of sodium. Higher partial pressure of sodium in the surrounding atmosphere eliminates the evaporation and supports the drainage. The rapid drainage of the film stops or significantly decelerates at a thickness around 100 nm, which is determined from an observation with a white light, because it is no longer possible to determine the thickness mechanically. Lifetime of some of these meta-stable films was higher than 40 min. Kappel talks about a meta-stable state of the film due to immobile surfaces caused by a higher viscosity at the surface layers of the film. The lifetime of the films significantly decreases under the conditions of forced drainage caused by a flow of nitrogen blown from one side.

It was later shown in the work of Laimböck [27], that the higher viscosity in the surface layer of the glass vertical film cannot completely explain the retardation in the drainage. Laimböck also studied a lifetime of a glass film for various glass composition and temperature. The first glass sample was sulfur free, the second glass sample contained 0.50 wt% of SO_3 in oxidized state as sulfate, and the last glass contained 0.06 wt% of SO_3 in reduced state as sulfide, see Fig. 3.7. The value of the lifetime is decreasing continuously with increasing temperature for the glass without sulfur and for the glass with sulfide, because with the increasing temperature, the viscosity is decreasing and the drainage is faster. Moving interference patterns, indicating the thicker and thinner parts, are observed during the whole lifetime. Different behavior is observed for glass with content of sulfate. Its lifetime is very short until 1350°C, when the film always ruptured after a fast drainage. Above this temperature, the lifetime increases, which Laimböck explains by the decomposition of sodium sulfate, which is on the surface of the film and acts as an anti-foaming agent below 1350°C. Sodium sulfate has a lower surface tension than glass and behaves as anti-foaming agent, which has already been discussed in sec. 2.4. Laimböck also observes, that blowing a mixture of SO_2 and nitrogen causes a rupture of the sulfate free glass film below 1350°C, while blowing of air has no effect. This is also explained by a creation of the sodium sulfate on the surface of the film, which is responsible for the rupture. Laimböck also measures a thickness of the glass film using electrical resistance and observes a rapid thickness decrease followed by a much slower thickness decrease. The rapid drainage appears during the first 200 s of the experiment. The glass film is stabilized at the thickness of about 100 or 200 nm and ruptures after 5 to 15 min. The meta-stable state is explained by a partial mobility of the interface.

3.4.2 Stability of single bubble in molten glass

There are only a few works dealing with an experiment with a single glass bubble. Kappel *et at.* [22] measured a lifetime of a single bubble. A gas was introduced at the bottom of a crucible and the created bubble rose through the melt to the surface, where it was captured by a Pt ring, which prevented the bubble from drifting to the wall of the crucible. Soda-lime glass with and without the addition of fining agents was tested. Lifetime of the bubble with various gas inside was determined, see Tab. 3.1. In a humid atmosphere, lifetime of bubbles in a glass without a fining agent, filled with various gas is increasing as follows: $SO_2 < N_2 = CO_2 <$ air. The average lifetime of air bubble is approximately 16 times longer than for SO_2 bubble and 8 times longer than for nitrogen bubble. A significantly shorter lifetime in glass with the addition of fining agent was observed for SO_2 bubbles. The lifetime

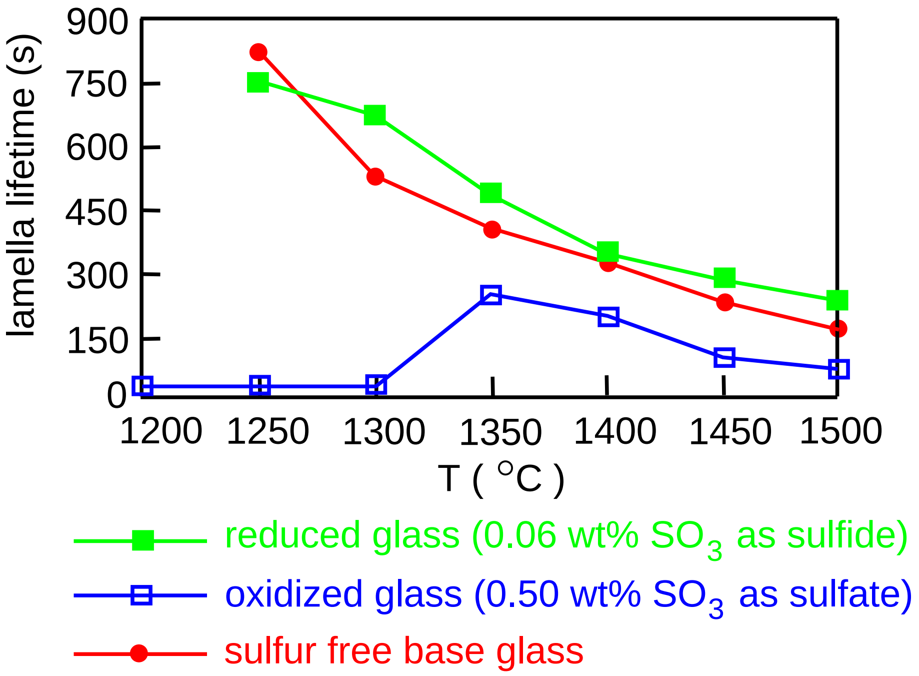

Figure 3.7: Lifetime of glass vertical thin film with various glass composition as a function of rising temperature [27].

glass	bubble lifetime
without fining agent	$SO_2 < N_2 = CO_2 <$ air
with fining agent	$SO_2 < N_2 = CO_2 =$ air

Table 3.1: Lifetime of bubbles containing various gas in glass with and without the addition of fining agent.

of air bubbles is approximately the same as for nitrogen and CO_2 bubbles. Therefore air bubbles have longer lifetime only in glass without a content of a fining agent.

Numerical studies of a bubble lifetime are more numerous than the experimental once. Beerkens [3, 37] proposes a model for the prediction of gas evolution and foam formation in molten glass. According to him, drainage in the bubble lamella is retarded due to partly immobile interface as a consequence of gradient of surface-active components. Vrij [38] found that the critical thickness δ_c at which the lamella ruptures is independent of viscosity. It depends on surface tension σ and Hamaker constant A_H according to the following correlation:

$$\delta_c \approx 0.11 \left(\frac{A_H \cdot R^2}{\sigma} \right)^{0.25}, \tag{3.7}$$

where R is the bubble radius. Surfactants contained in the surface layer of the lamella can be OH^- groups from the atmosphere or dissolved sodium sulfate [25]. Beerkens and van der Schaaf [37] calculated a bubble lifetime for a fully mobile interface:

$$\tau_{mobile} = \frac{\mu}{3\rho g R} ln\left(\frac{\delta_0}{\delta_c}\right) \tag{3.8}$$

and for a fully immobile interface:

$$\tau_{immobile} = \frac{2\mu R}{\rho g \delta_c^2} \tag{3.9}$$

The final lifetime for a bubble, which is given in eq. (3.10), is function of a coefficient Ψ and remains between the lifetimes for mobile and immobile interfaces.

$$\tau_{sb} = \frac{\mu}{3\rho g R}\left(ln\left(\frac{\delta_0}{\delta_c}\right) + \frac{2\Psi R^2}{\frac{\mu}{\delta_c}}\right) \tag{3.10}$$

If Ψ is equal to 0 than we obtain eq. (3.8). On the other hand, a very high value of Ψ results in eq. (3.9). The parameter Ψ represents the surface immobility and expresses the rate of immobility of the surface, which depends on the surface tension gradient along the curved surface. It comes from the balance between the transport of surfactant from the surface to the bulk and from the bulk to the surface. Diffusion, adsorption and desorption are the limiting parameters in the process. The final value of Ψ is function of glass composition, concentration of the surfactant, bubble size and reactions of the surfactant with the furnace atmosphere or gas inside the bubble. The value of Ψ needs to be determined experimentally as well as δ_c and δ_0.

According to Hrma [18] bubble lifetime cannot be predicted from the thickness of the bubble lamella, but two characteristic times, which are drainage time and survival of critically thin lamella, play role in the total lifetime.

3.4.3 Stability and decay of glass foam

Compared to stability of the thin vertical film or the bubble lamella, study of a stability of glass foam under various conditions is a lot richer and many experimental and numerical works can be found.

Kappel *et al.* [22] performed an experiment, where temperature inside a furnace with a glass sample was rising until foam was created and then its decay was determined. The height of the foam decreases exponentially with time. The constant of decay is called k_c and it changes with glass composition. Based on their work with the vertical film and the single bubble lifetime, discussed above, Kappel *et al.* inform, that the coefficient k_c is also function of gas inside the bubble as well as the stability of the bubble lamella.

For glass industry, it is very useful to know a relation, between gas flow and foam creation. A numerical [34] and experimental [35] results of a work of Pilon *et al.* show, that for low gas velocity, the foam linearly reaches a steady state thickness in a short time. For intermediate velocities, the layer of foam oscillates and never reaches a steady state. Finally for a large value of gas velocity a very high layer of foam is created at first. The first foam collapses rapidly and is followed by a steady state lower layer of foam.

Beerkens and van der Schaaf [3, 37] emphasize that lifetime of foam is much longer than lifetime of the sum of bubbles, because the drainage from the lamella placed at the top of the foam influences the drainage of the bubbles below. They propose a critical bubble flux, that will lead to a foam creation, because bubbles will not have enough time to rupture at the surface:

$$J_{incrit} = \frac{\frac{4}{3}\pi R^3 N_S}{\tau_{sb}}, \tag{3.11}$$

where N_S is the number of bubbles per m^{-2}, R is the bubble radius of the spherical shape and τ_{sb} is given in eq. (3.10). Using the critical bubble flux in eq. (3.11) and bubble lifetime in eq. (3.10), they are able to predict the thickness of a foam layer.

A model for foam height can also be found in the work of Hrma [18]. Foam is predicted for specific gas flux and bubble size. Drainage due to gravity and certain time for which the top lamella can survive after reaching a critical thickness are considered in the model.

The number of bubbles, that are rising towards the interface, can be found in the work of Hrma [19], who designed an experiment to study the effect of heating rate on foaming [19]. The value of the heating rate is varying between 5 and 15 °C·min^{-1}. The higher the heating rate, the larger the volume of gas is in the melt. An increased mass-transfer of fining gases from molten glass to gas bubbles is responsible for the increased volume of gas.

Apart from the foam stability study, Hrma [17] proposes a model for behavior of bubbles in the melt. Inside a constant initial volume with a certain distribution of bubble, larger bubbles grow and smaller bubbles shrink as a consequence of Ostwald ripening, see sec. 1.2.2. Bubbles also rise to the level of the molten glass, where they burst. He emphasizes, that behavior of group of bubbles is various from behavior of single bubble presented by Němec [33].

3.4.4 Influence of fining agents and glass composition on temperature of foaming

Cable *et al.* [9] studied a variation of the temperature of the secondary foaming for binary and ternary glass with a content of SO_3, which was rising up to 1%. Higher content of SO_3 lowers the foaming temperature as well as the addition of As, Fe or Al. An increasing content of alumina leads to a more stable foam, which is also observed by Kim and Hrma [23]. On the other hand, a rising content of potassium and sodium as well as the addition of boron causes higher value of the foaming temperature. Kim and Hrma [23] performed a similar experiment with soda-lime-silica glass and varying content of SO_3 between 0.0027 and 0.01 wt%. The higher is the content of SO_3, the larger is the total amount of foam and the lower is the temperature of foaming. With a content of SO_3 rising over 0.01 wt%, the temperature remains the same and the total volume of foam is decreasing. This indicates, that the amount of sodium sulfate, which supports the fining process, does not have to be very high. For the industrial purposes the addition is usually up to 1 wt% of SO_3 in the final glass composition, but mostly it varies from 0.2 to 0.5 wt%.

3.4.5 Influence of surrounding atmosphere

Many studies deal with the effect of water vapor on the foam stability. Water vapor causes lower value of viscosity as well as lower value of the surface tension, as it has been discussed in sec. 2.1.2 and 2.2.3, which can be an explanation, why Kappel *et al.* [22] observe a faster decay of foam, when water vapor is contained in the surrounding atmosphere. Laimböck [27] reports about larger amount of foam under wet conditions, which he explains as a result of “dilution model”. In this model, the water vapor dissolves in the glass and diffuses into bubbles, where it dilutes the concentration of other gases and therefore supports their diffusion into the bubbles. More bubbles of larger sizes are released under these conditions, which agrees with the observation. Results of an experiment done by Dutton and Pilon [12] show a completely different behavior for E-glass compared to soda-lime-silica. For E-glass, water vapor in the surrounding atmosphere leads to smaller amount of less stable foam, which is explained by lower value of viscosity. Another explanation for these results is, that SO_2 volatilizes from the molten glass, which leads to a smaller amount of SO_2, that can create foam. The volatilization of SO_2 is supported by the presence of H_2O in the surrounding atmosphere. They also say, that water vapor in the surrounding atmosphere supports early decomposition of sulfate.

Cable *et al.* [9] studied what happens with a layer of foam, if oxygen is replaced with nitrogen in the surrounding atmosphere. The layer of foam disappears if oxygen is replaced with nitrogen and appears again if nitrogen is replaced with oxygen. This can be repeated several times, but the newly created layer of foam under oxygen atmosphere is always slightly thinner.

References

[1] S. Akhtar and M. Cable. Some effects of atmosphere and minor constituents on the surface tension of glass melts. *Glass Technology*, 9(5):145–151, 1968.

[2] R. S. Allan, G. E. Charles, and S. G. Mason. The Approach of Gas Bubbles to a Gas/Liquid Interface. *J. Colloid. Sci.*, 16(150), 1961.

[3] R. G. C. Beerkens and J. van der Schaaf. Gas Release and Foam Formation During Melting and Fining of Glass. *J. Am. Ceram. Soc.*, 89(1):24–35, 2006.

[4] A. Bhakta and E. Ruckenstein. Decay of standing foams : drainage , coalescence and collapse. *advances in Colloid and Interface Science*, 70:1–124, 1997.

[5] R. J. Braun, S. A. Snow, and S. Naire. Models for gravitationally-driven free-film drainage. *Journal of Engineering Mathematics*, 43:281–314, 2002.

[6] R. J. Braun, S. A. Snow, and U. C. Pernisz. Gravitational Drainage of a Tangentially Immobile Thick Film. *Journal of Colloid and Interface Science*, 219:225–240, 1999.

[7] C. J. W. Breward, R. C. Darton, P. D. Howell, and J. R. Ockendon. Modelling foam drainage. *I Chem E Symposium Series*, 142(2):1009–1019, 2004.

[8] A. G. Brown, W. C. Thuman, and J. W. McBain. The surface viscosity of detergent solutions as a factor in foam stability. *Journal of Colloid Science*, 8(5):491–507, 1953.

[9] M. Cable, C. G. Rasul, and J. Savage. Laboratory investigation of foaming and reboil in soda-lime-silica melts. *Glass Technol.*, 9(2):25–31, 1968.

[10] P. G. de Gennes, F. Brochard-Wyart, and D. Quéré. *Capillarity and Wetting Phenomena*. Springer, New York, 2004.

[11] A. J. de Vries. *Foam Stability*. D. B. Centen’s uitgeversmaatschappij N. V., Amsterdam, 1957.

[12] B. C. Dutton, L. Pilon, D.-S. Kim, and P. R. Hrma. The effect of atmosphere composition on E-glass foaming. In *106th American Ceramic Society Meeting*, pages 1–9, 2004.

[13] D. A. Edwards, H. Brenner, and D. T. Wasan. *Interfacial Transport Processes and Rheology*. Butterworth-Heinemann, 1991.

[14] D. S. Goldman, D. W. Brite, and W. C. Richey. Investigation of Foaming in Liquid-Fed Melting of Simulated Nuclear Waste Glass. *Journal of The American Ceramics Society*, 69(5):413–417, 1986.

[15] C. Hedreul and G. Frens. Foam stability. *Colloids and Surfaces A*, 186:73 – 82, 2001.

[16] E. J. Hornyak and M. C. Wienberg. Velocity of a Freely Rising Gas Bubble in a Soda-Lime-Silicate Glass Melt. *Comm. of the Am. Ceram. Soc.*, pages 244–246, 1984.

[17] P. Hrma. Bubble removal from glass melts: Power-law model. *Glastech. Ber.*, 62(9):301–311, 1989.

[18] P. Hrma. Model for a Steady State Foam Blanket. *Journal of Colloid and Interface Science*, 134(1):161–168, 1990.

[19] P. Hrma. Effect of heating rate on glass foaming : Transition to bulk foam. *Journal of Non-Crystalline Solids*, 355:257–263, 2009.

[20] I. B. Ivanov and D. S. Dimitrov. Hydrodynamics of thin liquid films Effect of surface viscosity on thinning and rupture of foam films. *Colloid Polymer Sci.*, 252:982–990, 1974.

[21] R. B. Jucha, D. Powers, T. McNeil, R. S. Subramanian, and R. Cole. Bubble Rise in Glass melts. *J. Am. Cer. Soc.*, 65(6):289–292, 1982.

[22] J. Kappel, R. Conradt, and H. Scholze. Foaming behaviour on glass melts. *Glasstech. Ber.*, 60:189–201, 1987.

[23] D.-S. Kim and P. Hrma. Foaming in glass melts produced by sodium sulfate decomposition under ramp heating conditions. *J. Am. Ceram. Soc.*, 75:2959–2563, 1992.

[24] J. A. Kitchener and C. F. Cooper. Current concepts in the theory of foaming. *Q.Rev.*, 13:71–97, 1959.

[25] A. Kucuk, A. G. Clare, and L. E. Jones. Influence of various atmospheres on the surface properties of silicate melts. *Glass Science and Technology*, 73(5):123–129, 2000.

[26] K. Kumar, A. D. Nikolov, and D. T. Wasan. Effect of Film Curvature on Drainage of Thin Liquid Films. *Journal of Colloid and Interface Science*, 256:194–200, 2002.

[27] P. Laimböck. *Foaming of Glass Melts*. PhD thesis, 1998.

[28] E. D. Manev and A. V. Nguyen. Critical thickness of microscopic thin liquid films. *Advances in colloid and interface science*, 114-115:133–46, June 2005.

[29] E. D. Manev, S. Sazdanova, and D. T. Wasan. Emulsion and foam stability - the effect of film size on film drainage. *Colloid Interface Sci.*, 97:591–594, 1984.

[30] T. J. McNeil, R. Cole, and R. S. Subramanian. Surface-Tension-Driven Flow in a Glass Melt. *Journal of The American Ceramics Society*, 68(5):254–259, 1985.

[31] S. Naire, R. J. Braun, and S. A. Snow. An Insoluble Surfactant Model for a Vertical Draining Free Film. *Journal of Colloid and Interface Science*, 230:91–106, 2000.

[32] S. Naire, R. J. Braun, and S. A. Snow. A 2+1 dimensional insoluble surfactant model for a vertical draining free film. *Journal of Computational and Applied Mathematics*, 166:385–410, 2004.

[33] L. Němec. The rifining of glass melts. *Glass Technol.*, 15(6):153–156, 1974.

[34] L. Pilon, A. G. Fedorov, and R. Viskanta. Steady-State Thickness of Liquid-Gas Foams. *Journal of Colloid and Interface Science*, 242:425–435, 2001.

[35] L. Pilon, A. G. Fedorov, and R. Viskanta. Analysis of transient thickness of pneumatic foams. *Chemical Engineering Sciences*, 57:977 – 990, 2002.

[36] F. Seychelles, Y. Amarouchene, M. Bessafi, and H. Kellay. Thermal Convection and Emergence of Isolated Vortices in Soap Bubbles. *Physical Review Letters*, 100(144501):1–4, 2008.

[37] J. van der Schaaf and R. G. C. Beerkens. A model for foam formation , stability , and breakdown in glass-melting furnaces. *Journal of Colloid and Interface Science*, 295:218–229, 2006.

[38] A. Vrij. Possible Mechanism for the Spontaneous Rupture of Thin, Free Liquid Films. *Discussion of the Faraday Society*, 42:23–33, 1966.

[39] D. Weaire and S. Hutzler. *The Physics of Foams*. Clarendon Press, Oxford, 1999.

[40] Z. Zapryanov and S. Tabakova. *Dynamics of Bubbles, Drops and Rigid Particles*. Kluwer Academic Publishers, Dordrecht, 1999.

Chapter 4

Experimental set-up

Three different experimental set-ups are used in this work. The first two are designed to measure the evolution of bubble lamella thickness when a bubble is approaching a free interface. First experimental set-up is designed to work with a single bubble in silicon oil at room temperature (sec. 4.1). Second experimental set-up is designed to work with a single bubble in molten glass at high temperatures (sec. 4.2). The third experimental set-up is designed to work with a vertical film. It enables to measure the lifetime of a thin vertical glass film and also to perform chemical analyses of the composition of the thin film before rupture (sec. 4.3).

4.1 Bubble experiment in silicon oil

Sketch of the experimental set-up in silicon oil is given in Fig. 4.1. Compressed air, which is circulating through the pipe system in the laboratory, is introduced through the needle located

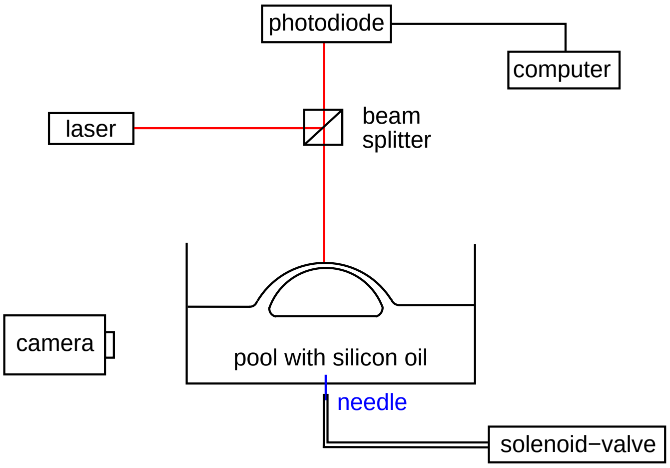

Figure 4.1: Experimental set-up for single bubble in silicon oil.

at the bottom of a pool filled with silicon oil. The diameter of the needle is 150 μm. The created bubble rises through the liquid to the free interface, where the evolution of thickness of the bubble lamella is determined using interference method, more information about the method will be given in the next chapter, see sec. 5.3. A photo of the rising bubble is taken by a camera placed beside the pool to determine the bubble size, which will be discussed in more details in sec. 5.1.2. Bubble creation in highly viscous liquid is a difficult task since the viscous force prevents the rising of the bubble when it is yet kept at the needle at the bottom of the pool [2]. The bubble size must be sufficiently large in order that the buoyancy force exceeds the viscous force. Only single bubble is needed in the experiment and therefore it is not possible to work with constant flow rate. In order to create a bubble with a controlled size, a special device, which is called solenoid-valve, is used. This device enables to switch between low and high pressure as it is shown in Fig. 4.2. The solenoid-valve is off, when the pressure is low, and it is on, when the pressure is high. The bubble size is controlled by changing the pressure level and the duration of the opening of the solenoid-valve.

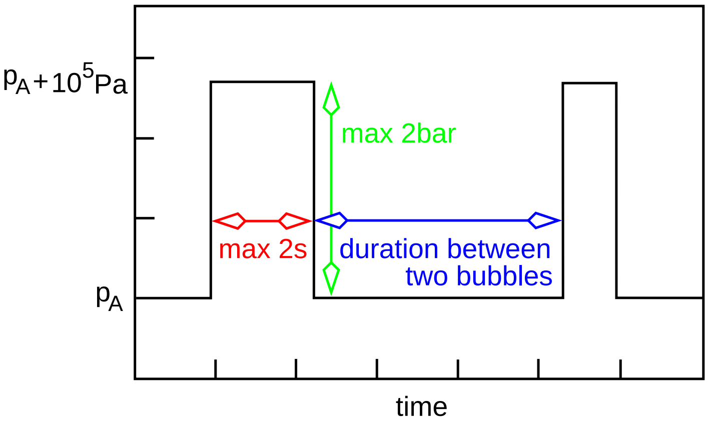

Figure 4.2: Typical signal of the pressure pulse for creation of two bubbles, where the first bubble (left peak) is larger than the second (right peak).

4.2 Bubble experiment in molten glass

The furnace, originally used for measuring the height of foam during melting in a Pt-Rh crucible, required modifications. Therefore it was necessary to design a new crucible, which would enable the bubble creation and rebuild the optical set-up to determine the evolution of film thickness on top of a single bubble. Sketch of the experimental set-up is given in Fig. 4.3. The Pt-Rh crucible with Pt-Rh tube fixed to the crucible bottom is placed at the center of the furnace. 10% of Rh is added to platinum for mechanical strength at high temperatures. The Pt-Rh tube passes through the refractory column and enables inflow of the gas. The middle

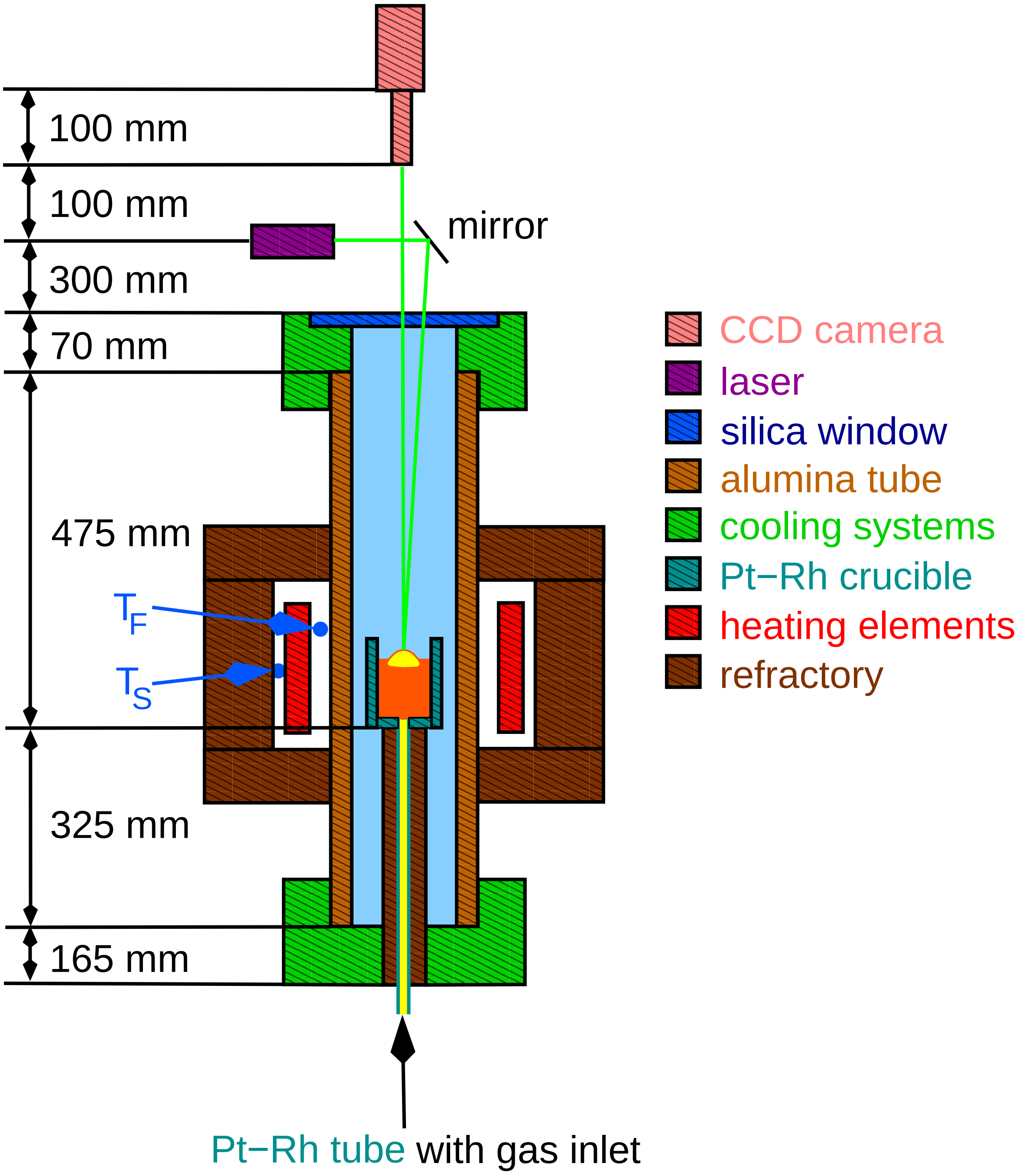

Figure 4.3: Experimental set-up for single bubble in molten glass.

section of the furnace is electrically heated. The heating elements are placed between alumina tube and insulating refractory. Alumina tube is a refractory with content of Al_2O_3 between 99.5-99.9%. It is used in the inner part of the furnace for its high temperature resistance and, compared to refractory bricks consisting of small particles sintered together, alumina is a dense material. This limits the risk of small corroded or mechanically disrupted particles falling into the crucible with glass sample. There are two cooling systems at the top and at the bottom of the furnace. The cooling at the top part is important for the placing the optical equipment. Lower temperature at the bottom part enables the connection with a plastic tube (sec. 4.2.1). The silica window, which is placed at the top part, enables the experimental observation. It is 75 mm long and 35 mm wide (Fig. 4.4). The vision slit is narrowed to 65 x 30 mm when the silica window is placed on the furnace. The optical set-up is placed above the furnace and will be detailed in sec. 4.2.2.

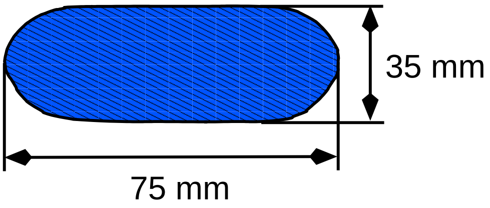

Figure 4.4: Silica window, which closes the furnace at the top.

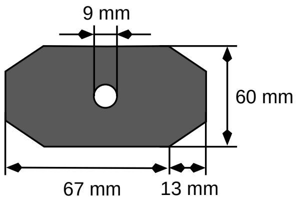

Figure 4.5: Metallic part enabling measurement of temperature field in the furnace.

Two thermocouples enable measurement of the temperature. One of them is placed between the heating element and the alumina tube (T_F), the other is placed further from the alumina tube between the heating element and the refractory (T_S). T_S is called a safety temperature. The system turns off automatically if this temperature exceeds 1000°C. T_F is the furnace temperature, which is adjusted by the experimentator. It is not possible to measure the temperature at the area, where the experiment is taking place. Nevertheless, this information is very important to determine properties of molten glass, as will be shown in the following chapter, see sec. 5.2.8 for more details. To measure the temperature field inside the furnace, it is necessary to remove the silica window from the top of the furnace to introduce another thermocouple. The silica window is replaced by a metallic part with a hole in the middle, which enables insertion of the thermocouple, but preserves the experimental conditions by covering the remaining part of the hole caused by the removal of the silica window, see Fig. 4.5. Results of the temperature field inside the furnace will be discussed in sec. 5.2.7.

4.2.1 Pt-Rh crucible and bubble creation

The gas, which creates the bubble, is brought from a gas bottle (nitrogen or oxygen) through a holder connected to a plastic tube, see Fig. 4.6. One end of Pt-Rh tube, which is 530 mm long, is permanently fixed to the bottom of the crucible. The other end is connected to the plastic tube at the bottom part of the furnace, where the temperature is below 30°C (sec. 5.2.7). The level of the glass in the crucible is around 30 or 40 mm even though the crucible is almost twice as high. The bubble creation increases the total volume inside the crucible, which can cause a leak of glass into the furnace. A smaller crucible, with a height of 35 mm, was used for the very first experiments, but the height of the glass must have been very low, which limited the bubbles sizes, that could have been created during the experiment as well as the determination of their size. The determination of bubble size will be discussed in sec. 5.1.2. The bubbles are created *via* solenoid-valve as well as in the experiment with the silicon oil, but the command of pressure variation had to be improved to prevent glass leak from the crucible to the tube, even if the hole at the bottom of the crucible is around 100 μm, see Fig. 4.7. The molten glass is introducing into the tube and the longer is the duration between two bubbles, the more difficult is the following bubble creation. Proof of the leak of glass into the tube is made when a cleaned crucible is placed into the furnace, heated to 1350°C and gas is introduced into the tube, a certain amount of glass is ejected into the crucible from the tube (Fig. 4.8). It is therefore necessary to control not only the duration of the pulse that influences the creation of the bubble, but also the duration between two bubbles as well. Indeed blowing regularly gas through the tube prevents the glass from entering it. A combination of two pulse generators needs to be used in order to control both. The second pulse generator significantly supports the reproduction and enables creation of sequence of many bubbles with same size. The Pt-Rh crucible is cleaned after each experiment. Glass

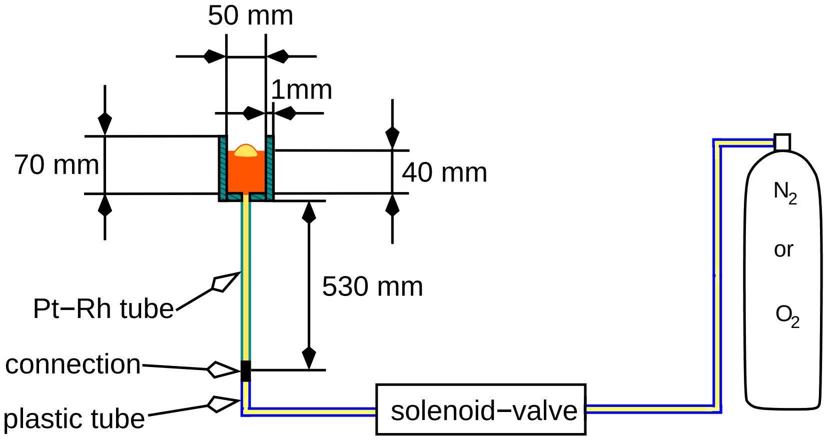

Figure 4.6: Pt-Rh crucible and devices for bubble creation.

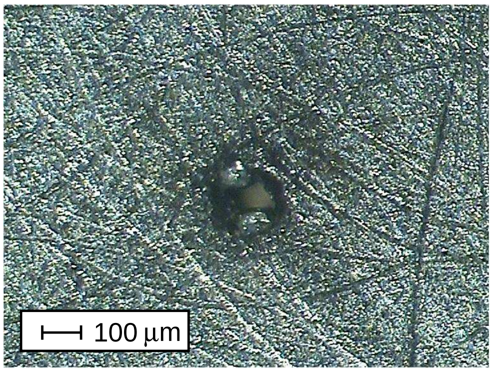

Figure 4.7: Bottom of the Pt-Rh crucible with a hole for a bubble creation.

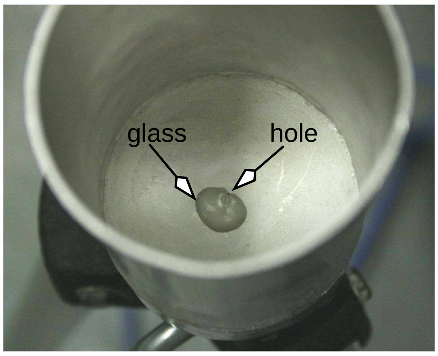

Figure 4.8: The amount of glass, that remained inside the Pt-Rh tube after cleaning (0.063 ml).

is removed and the crucible is left inside hydrofluoric acid for several days. Hydrofluoric acid etch glass, which enables cleaning of curved parts.

4.2.2 Optical set-up

The optical set-up, which is placed above the furnace, consists of laser, silver mirror and CCD camera with very narrow filter (Fig. 4.3). The filter transmits wavelength 532 nm and has a bandwidth of 1 nm. Molten glass as well as the refractory emit light in the red range of the visible light. Therefore green laser [1] with wavelength 532 nm is used in the experiment. The power of the laser can be regulated and its maximum value is 150 mW. At first, no interference pattern was observed with this set-up. A pulse laser with the energy 12 mJ per pulse, frequency up to 50 Hz and wavelength 532 nm was tested in order to solve the problem (computation of the power received by the video-camera is given in appendix A). Nevertheless at the end it was discovered that not the low power of the laser, but a strong reflection of the beam from the bottom of the Pt-Rh crucible was responsible for not detectable interference pattern. The reflection had a much higher intensity, than the interference signal and completely covered it. The problem was solved, when the bottom of the Pt-Rh crucible as well as its walls were roughened to disperse the reflection.

Blue laser with wavelength 408 nm and power 100 mW was tested in order to determine the lamella thickness precisely, see sec. 5.3 for more details. However the intensity of the interference pattern was very low and it was not possible to obtain results. There was not enough time to make more tests and rebuild the optical set-up in order to work with two wavelengths. For the future work it is recommended to use more powerful blue laser, than the one, which was tested, as well as other mirror than silver, which lowers the efficiency of blue laser.

---

[1] SDL-532-150T DPSS laser, where T stands for temperature electric cooling

The resolution of the CCD camera [2] is 1392 x 1040 pixel with a maximal rate 20 full frames per second. This is the maximal recording speed used during the experiment. Other video-cameras with higher frame rates were tested during the work, but their resolution was too low to clearly observe clearly the interference pattern especially for small bubbles. Nevertheless, faster recording video-camera with high resolution would be a significant improvement of the experimental set-up. It will enable observation of drainage of bubbles at higher temperatures and detect the retraction velocity of the film after the bubble rupture. The retraction speed is important in order to determine the critical thickness of the film and will be discussed in sec. 6.6.

4.3 Vertical film experiment in molten glass

The experimental set-up with vertical film was designed in Saint-Gobain Recherche during an internship of Nicolas Champagne [1], who compared the lifetime of a vertical liquid film in silicon oil and in molten glass. A sketch of the experiment is given in Fig. 4.9 and 4.10.

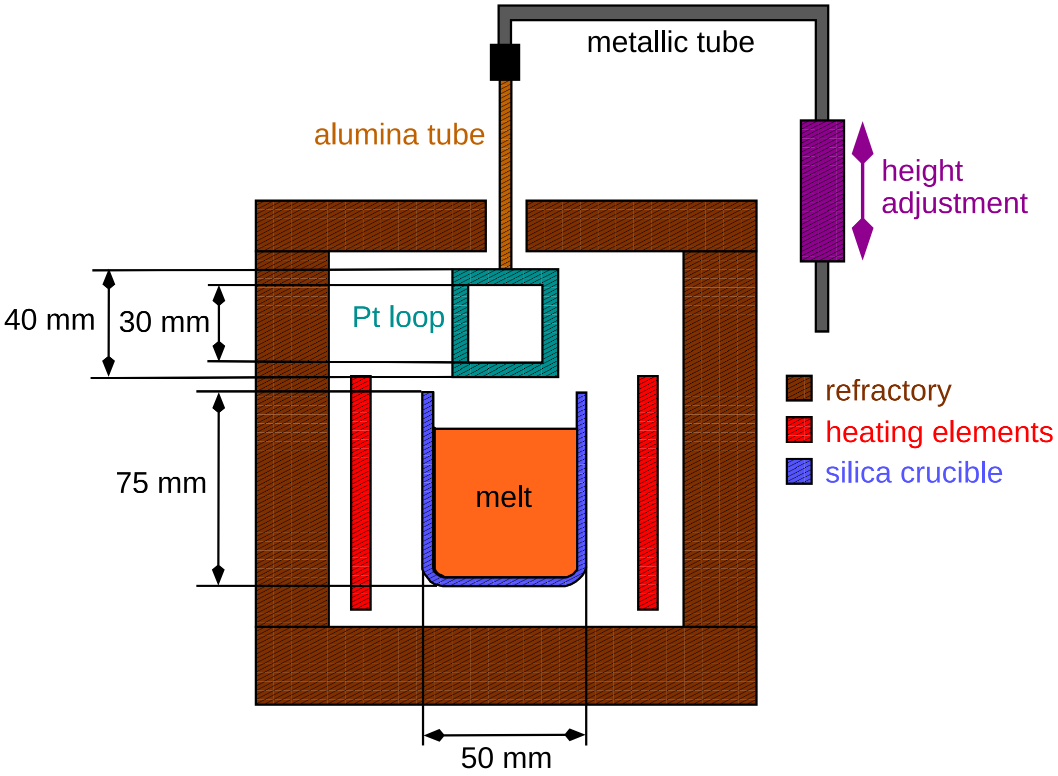

Figure 4.9: Experimental set-up for vertical film in molten glass (front view).

Cullet of glass sample is placed into the silica crucible inside the furnace and the temperature

---

[2] Baumer TXD 13c

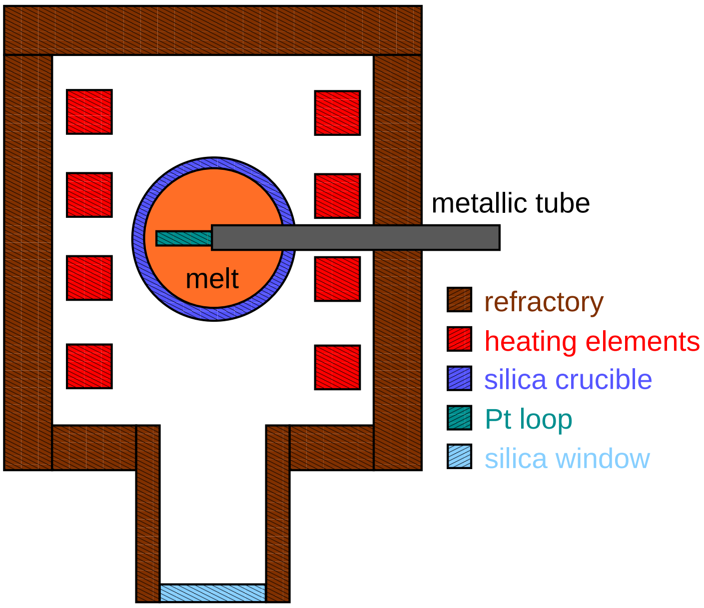

Figure 4.10: Experimental set-up for vertical film in molten glass (top view).

is increased up to 1300°C. It is necessary to wait for 4 or 5 hours in order to remove all bubbles. The Pt-Rh loop is introduced into the silica crucible *via* height adjustment device and withdrawn. Observation of the experiment is enabled *via* silica window, which is placed in the front part of the furnace (Fig. 4.10), as well as the transparency of the silica crucible. The lifetime of the thin film inside the loop is measured.

If the experiments are achieved at various temperature in this furnace, it is recommended to start working at low temperatures and rising it during the experiment, because lowering the temperature may cause crystallization of the silica crucible (Fig. 4.11), which causes opaque wall and disables the observation inside it. After the experiment, it is possible to withdraw

Figure 4.11: Opaque wall of crystallized silica crucible.

the film outside of the furnace in order to preserve the thin film. To avoid rupture of the glass film due to stresses, it is necessary to disjoin the alumina and metallic tubes and insert the alumina tube with the Pt-Rh loop into an annealing chamber and retain the film inside it for several hours at temperature approximately 560°. Further cooling at room temperature is required in order to prepare the sample for analysis.

References

[1] S. Champagne. Etude de la stabilité des films de verre. Master 2, Université Pierre et Marie Curie, Paris VI, 2008.

[2] P. Snabre and F. Magnifotcham. Recirculation flow induced by a bubble stream rising in a viscous liquid. *Eur. Phys. J. B*, 4:379–386, 1998.

Chapter 5

Materials and Methods

This chapter contains description of all materials and methods, that were used during this experimental work. Silicon oil is a liquid with many desirable properties and is often used as a model liquid for molten glass mainly because it enables wide range of viscosities. Chemical composition and properties of silicon oil are discussed in sec. 5.1.

Second section is related to molten glass. It is essential to know the exact temperature of the glass sample and its chemical composition in order to correctly determine the glass properties. Measurement of the temperature field in the furnace is discussed in sec. 5.2.7 and various chemical analyses, that were used before and after experiment are mentioned in sec. 5.2.1. Determination of glass properties is very complex due to elevated temperatures. Therefore many models to compute the glass properties from composition can be found in literature. The models used to determine properties of the experimental glasses used in this work are discussed in sec. 5.2.8. Nevertheless, these models have limitations, and that is why some of the properties had to be determined experimentally as well.

Determination of the bubble size is easier in PDMS (5.1.2), than in molten glass (5.2.9), where only top view of the experiment is available. Last part of this chapter contains the determination of the bubble lamella thickness using interference method in PDMS and molten glass, see sec. 5.3 for more details. This method is a standard one and it was used in many other works [4, 6, 15, 19].

5.1 Silicon oil

Silicon oil is a clear transparent liquid, which is formed by polymerized siloxanes with organic side chains, see Fig. 5.1. PDMS or polydimethylsiloxane, where the two functional groups are methyl groups, is used in this experimental work. The liquid viscosity changes according to the length of PDMS molecules. The higher the number n, the longer the chain and the

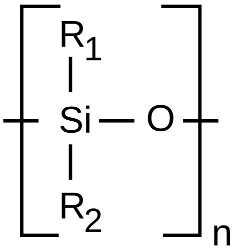

$$\left[\begin{array}{c} R_1 \\ | \\ -\mathrm{Si}-\mathrm{O}- \\ | \\ R_2 \end{array} \right]_n$$

Figure 5.1: Basic formula of silicon oil, where R_1 and R_2 are two functional groups of hydrocarbons.

higher the viscosity is. Viscosity of silicon oil is determined experimentally using rotating viscosimeter. By mixing of two initial commercially available silicon oils, five mixtures with viscosity ranging from 10 to 100 Pa·s, are prepared. The two initial oils have molecular weight 10 thousand times and 100 thousand times higher than water, respectively. The chemical formula of PDMS is $CH_3[Si(CH_3)_2O]_nSi(CH_3)_3$. This enables to determine roughly the number of monomers (n) forming the PDMS molecule. The molecular weight of PDMS with low viscosity can be computed by multiplying the molecular weight of water by 10,000:

$$(2 \cdot \mathrm{H} + \mathrm{O}) \cdot 10,000 = (2 \cdot 1 + 16) \cdot 10,000 \; = \; 180,000 \tag{5.1}$$

The molecular weight of the methyl groups and Si, which are not included in the repeating monomer of the molecule, equals to:

$$\mathrm{C} + 3 \cdot \mathrm{H} + \mathrm{Si} + 3 \cdot (\mathrm{C} + 3 \cdot \mathrm{H}) = (12 + 3 \cdot 1) + 28 + 3 \cdot (12 + 3 \cdot 1) = 88 \tag{5.2}$$

The molecular weight of the repeating monomer of the molecule is:

$$\mathrm{Si} + 2 \cdot (\mathrm{C} + 3 \cdot \mathrm{H} + \mathrm{O} = 28 + 2 \cdot (12 + 3 \cdot 1) + 16 = 74 \tag{5.3}$$

Now we can determine the number of monomers n of the PDMS molecule with molecular weight 10,000 times larger than water:

$$n = \frac{(180,000 - 88)}{74} = 2,431 \tag{5.4}$$

The low viscosity PDMS is characterized by n=2,431. Same method can be used to compute the number of monomers in the high viscosity PDMS resulting in n=24,323.

5.1.1 PDMS properties

Properties of PDMS are given by the supplier. The surface tension is 21 mN·m^{-1}, the density is 970 kg·m^{-3} and the refractive index is 1.4. The viscosity, which was discussed above, is obtained experimentally for all five samples used in the experiment and is given in Tab. 5.1.

M (10,000) : M (100,000)	**μ (Pa·s)**
1:0	10
2:1	23
1:1	51
1:2	74
0:1	100

Table 5.1: Viscosity of PDMS samples, which are bought or prepared as mixture of two commercial liquids with 10,000 and 100,000 times the molecular weight of water.

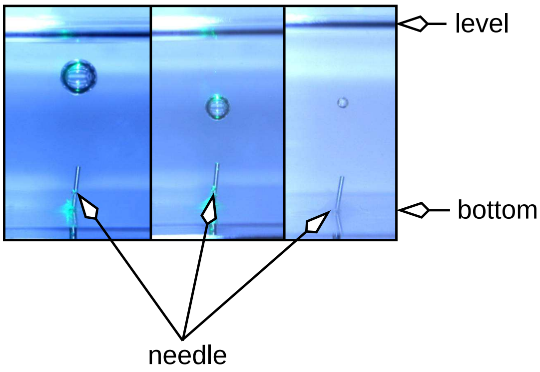

Figure 5.2: Photographs of various bubble sizes inside the pool with PDMS.

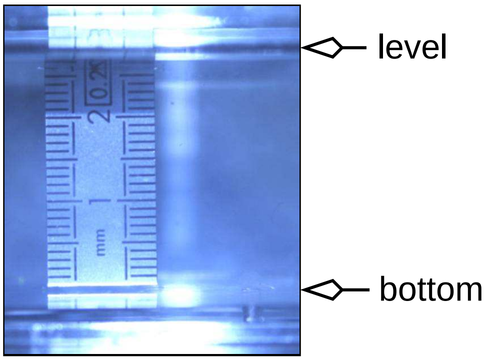

Figure 5.3: Photograph of scale inside the pool with PDMS.

5.1.2 Bubble size determination in PDMS

When a bubble is rising through pool with PDMS towards the interface, a photograph of it is taken by the camera, which is placed beside the pool, see sec. 4.1 for more details about the experimental set-up. A photograph of a scale inside the pool is taken as well and the bubble size is determined precisely by comparing the bubble size (Fig. 5.2) to the scale (Fig. 5.3). As soon as the bubble reaches the free surface, liquid lamella is created and its evolution of thickness is measured using interference method, which will be discussed in sec. 5.3.

5.2 Glass

As presented in chapter 1 and 2, glass is a very complex material, whose properties and structure change with composition and temperature. In this work, experiments are achieved for various glass composition at temperatures higher than the temperature of transformation, above which glass is considered as liquid. In order to understand and describe the behavior of molten glass, its chemical composition and properties need to be precisely determined.

5.2.1 Chemical analyses

Several analyses are used in the work to determine precisely the chemical composition of glass before and after each experiment in order to verify if glass composition changes during the experiment and causes changes in glass properties. Results of all analyses, which are presented below, give composition in weight % (x_i for the species i) and the error of the measurement is given for the vale x_i.

Wet chemistry

Wet chemistry is a quantitative method, that works with liquid phases. Glass sample is mixed with liquid, that either dissolves some substances from the glass or reacts with them and forms chemical substances, that can later be quantitatively determined by titration. The composition of glass is computed from the amount of the reagent, that was added. This analysis is used before the experiments to determine the initial composition. The amount of glass, which is needed for this analysis is 50 g. The error for this method is approximately 1%.

We are mainly interested in the compositions at the surface and bottom of the crucible after experiment. In this case the amount of glass, which can be used for analysis, is much smaller (around 1 g) and other analysis needs to be used.

Microprobe

Microprobe is used to determine the glass compositions after experiment at the top, bulk or bottom of the crucible. Several small pieces of glass (2 mm^3) are taken from the surface, bulk or bottom layer of glass in the crucible. They are put into a plastic mold and preserved in polymer, see Fig. 5.4. The surface of the sample for microprobe needs to be polished. During polishing, the top layer of the glass samples is removed. That is why this method is useful to determine the average bulk concentration in various parts of the glass sample in the crucible, but it is not suitable for the determination of the composition profile in the first few nm of the sample. The composition is obtained in several points in the pieces, which are fixed in the sample. The analyzed area of each point is 20 x 30 μm^2 with a depth of 1 μm. The average value of all determined compositions in the points of one sample gives the final composition.

Microprobe is a quantitative method during which electrons are focused through electromagnetic lenses on a target, which is the sample. Their energy is between 5 and 40 kV. When electrons hit the surface, atoms in the sample excite and electrons are ejected. As a consequence, photons are emitted. Photons are detected and analyzed. Error of this analysis is between 0 and 1% depending on the element. Boron is one of the elements for which this analysis is not very accurate (error close to 1%).

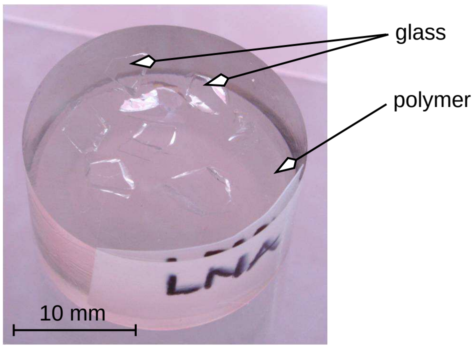

Figure 5.4: An example of polished sample for microprobe.

SIMS - Secondary ion mass spectrometry

SIMS analysis is used to determine the composition in the surface layer of the thin glass film. The depth of the profile is 100 or 150 nm. SIMS is not a quantitative method, however, if we know the bulk composition of the glass and we are sure, that at the deepest point we reach the bulk concentration, it is possible to recompute the concentration profiles from the measured intensities. More details about the recomputation will be given in sec. 6.5.
In this method, oxygen is used to create a hole (200 x 200 μm^2) on the surface of the sample. Smaller area, which is around 30 μm in the middle of the hole, is analyzed using gallium liquid metal ion gun (LMIG). Cations and anions, that are removed from the surface, are detected. That is why, it is necessary to neutralize the surface of the samples before each analysis. Experimental error is mainly related to the fact, that it is not a quantitative method, so we need to be sure that the bulk composition is reached after 100 nm!

5.2.2 Chemical composition of glasses before experiment

Not a binary or ternary glass, but an ordinary industrial soda-lime-silica glass with various iron content is tested in this experimental work. The iron content is 0.01 and 0.1 wt% of Fe_2O_3. A higher concentration of iron, where the content of Fe_2O_3 is 1 wt%, was also tested, but no results were obtained, because several problem occured. The glass had a dark green color and the observation of the bottom of the crucible and the rising bubble was not possible through the silica window. Therefore the bubble size determination, which will be discussed later in sec. 5.2.9, was not possible. Another problem was caused by crystalization, which was observed in the surface layer at lower temperatures, see Fig. 5.5. The glass samples with various content of iron are obtained from industrial production.

Figure 5.5: Captured bubble in glass with 1 wt% Fe_2O_3 with crystals on the surface (a) and without (b).

Glass	SiO_2	Na_2O	CaO	K_2O	MgO	Al_2O_3	SO_3	Fe_2O_3	TiO_2	B_2O_3
0.01 wt% Fe_2O_3	72.3	13.5	9.6	<0.1	4.1	0.6	0.3	0.01	<0.1	-
0.1 wt% Fe_2O_3	72.1	13.3	9.0	0.1	3.6	0.8	0.24	0.07	<0.1	-
1 wt% B_2O_3	70.6	13.0	13.0	<0.1	0.1	2.0	0.24	0.02	<0.1	1.05
10 wt% B_2O_3	62.8	12.4	12.9	<0.1	<0.1	1.9	0.3	0.01	<0.1	9.70
AKM	61.7	12.6	0.5	9.4	7.6	8.1	0.14	0.1	<0.1	-

Table 5.2: Initial chemical composition of all glasses that were used during the experimental work.

Apart from various iron contents, 2 various contents of boron are studied, because boron influences the glass structure and hence its properties. Two soda-lime-silica glasses with 1 and 10 wt% of B_2O_3 are prepared in the laboratory.

Finally we test a glass with a high viscosity, where apart form SiO_2, the contents of Al_2O_3, K_2O and MgO are high. Table 5.2 gives the initial chemical composition of all glasses that are used in this experimental work. Microprobe analysis is used to determine chemical compositions of glasses with iron before the experiment, at least three samples for each glass are analyzed (see details in Tab. B.1, B.2, B.3 and B.4 of the appendix B) and each sample results are average over 5 points.

Wet chemistry is used to determine the composition of glass with 1 and 10 wt% of B_2O_3 as well as for the highly viscous glass (AKM).

5.2.3 Chemical composition of glass with 0.01 wt% of Fe_2O_3 after experiment

Glass samples from various parts of the crucible are analyzed after experiment by microprobe. One sample is taken from the bulk of the crucible in order to compare the composition

Glass	SiO_2	Na_2O	CaO	K_2O	MgO	Al_2O_3	SO_3	Fe_2O_3	TiO_2
0.01 wt% Fe_2O_3 bulk/average	72.6	13.6	9.6	0.0	4.1	0.6	0.3	0.0	0.0
0.01 wt% Fe_2O_3 top/average	72.3	13.4	9.7	0.0	3.7	0.6	0.3	0.0	0.0
0.01 wt% Fe_2O_3 bottom/average	72.9	13.3	9.6	0.0	3.8	0.6	0.2	0.0	0.0

Table 5.3: Average chemical composition of glass with 0.01 wt% Fe_2O_3 in the bulk and on the top and the bottom of the Pt-Rh crucible after experiment, see Tab. B.5, B.6 and B.7 for more details.

to the initial one. Second and third samples are taken from the top and the bottom parts of the glass inside the crucible, see Fig. 5.6, to determine if the composition inside the crucible is homogeneous or if the surface layer is poorer in volatile species. No variation in chemical compositions is found between the initial composition and the compositions reported in Tab. 5.3. The composition in the bulk is determined in three samples and the variation between these measurements is larger than between the average composition in the bulk and the initial concentration, see Tab. 5.3 and B.5. Same conclusion can be made for the top and bottom sample, where also larger variation is found between the 10 measurements at the top or bottom part than between the average values, see Tab. 5.3, B.6 and B.7. The homogeneous composition could be explained by the high mixing rate caused by the bubble creation during the experiment.

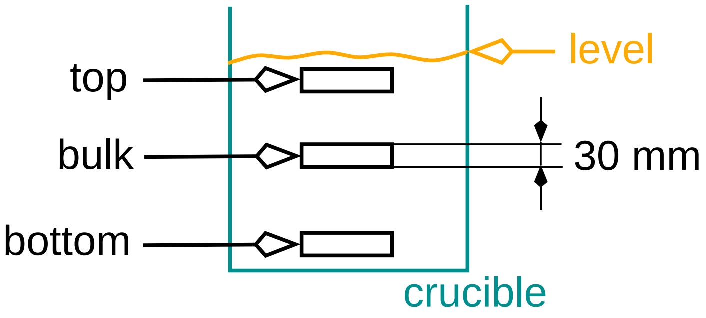

Figure 5.6: Glass samples for analyses inside the Pt-Rh crucible.

Finally, the last analyses of 2 solutions are done in order to determine which species volatilize from the glass and which once remain in the very surface layer of the glass sample. First solution is obtained by pouring distilled water on the surface of the glass inside the crucible after experiment at room temperature. Second solution is obtained by washing the inner wall of the crucible with distilled water. The two solutions are called “surface solution” and

Solution	**Ca**	**Na**	**K**	**Si**	**SO_4 (sulfate)**
wall solution (0.01 wt% Fe_2O_3)	1.85	0.95	$<$1.00	$<$0.10	0.65
surface solution (0.01 wt% Fe_2O_3)	2.15	1.35	$<$1.00	$<$0.10	0.75

Table 5.4: Chemical composition of the "wall solution" and the "surface solution" after experiment with low content of iron.

Glass	**SiO_2**	**Na_2O**	**CaO**	**K_2O**	**MgO**	**Al_2O_3**	**SO_3**	**Fe_2O_3**	**TiO_2**
0.1 wt% Fe_2O_3 sample 1/average	71.5	13.2	9.2	0.1	3.6	0.8	0.23	0.08	0.03
0.1 wt% Fe_2O_3 sample 2/average	71.8	13.3	8.9	0.1	3.7	0.8	0.23	0.08	0.04

Table 5.5: Average chemical composition of glass with 0.1 wt% Fe_2O_3 for two different samples after experiment, see Tab. B.8 and B.9 for more details.

"wall solution" respectively in the following text. Sulfate as well as potassium and sodium are detected on the surface of the glass and also on the walls of the crucible, see Tab. 5.4. It is well known that sodium volatilize from the glass (sec. 2.3.1). Presence of sulfate on the surface of the glass can support the theory of Laimböck [9], that below 1300°C sodium exists as sodium sulfate, which has lower surface tension than glass and can work as anti-foaming agent, which has been discussed in sec. 3.4.1.

5.2.4 Chemical composition of glass with 0.1 wt% of Fe_2O_3 after experiment

Composition of glass with a higher content of iron is determined only in the bulk after experiment, because its composition is very close to the lower iron content and a variation of composition between the bottom and the top of the crucible is unlikely, when it is not observed for lower iron content. The composition after experiment is determined by microprobe in two glass samples, that are obtained after two different experiments. As well as for lower iron content, no variation of composition is observed after experiment compared to the initial composition. The average compositions of the first and second samples are given in Tab. 5.5 and more details can be found in Tab. B.8 and B.9.

5.2.5 Chemical composition of glass with 1 wt% of B_2O_3 after experiment

It is expected, that boron evaporates from the melt during the experiment and therefore more significant changes in composition are expected. It is desirable to test if the composition is homogeneous inside the crucible after experiment. The glass compositions at the top and bottom in the crucible are therefore analyzed. The average compositions of the glass from the top and bottom are determined by the microprobe and are given in Tab. 5.6 and more details can be found in Tab. B.10 and B.11. No variation between the composition of the glass sample obtained from the top and bottom part of the crucible is observed. However, slightly lower contents of boron and sodium are detected in comparison with the initial concentration. As well as for low iron content, for low boron content, solutions from the wall and surface are analyzed. Results are given in Tab. 5.7.

Glass	**SiO_2**	**Na_2O**	**CaO**	**MgO**	**Al_2O_3**	**SO_3**	**B_2O_3**
1 wt% B_2O_3 top/average	70.5	12.8	13.1	0.1	2.1	0.3	0.9
1 wt% B_2O_3 bottom/average	70.5	12.8	13.1	0.1	2.1	0.3	0.9

Table 5.6: Average chemical composition of glass with 1 wt% B_2O_3 at the top and bottom of the Pt-Rh crucible after experiment, see Tab. B.10 and B.11 for more details.

Solution	**B**	**Ca**	**Na**	**K**	**Si**	**SO_4 (sulfate)**
wall solution (1 wt% B_2O_3)	0.08	3.15	1.90	$<$1.0	0.12	1.05
surface solution (1 wt% B_2O_3)	0.11	3.20	2.10	$<$1.0	0.18	1.05

Table 5.7: Chemical composition of the “wall solution” and the “surface solution” after experiment with low content of boron.

5.2.6 Chemical composition of glass with 10 wt% of B_2O_3 after experiment

Since no variation in composition is found between the top and bottom glass sample in the crucible for low content of boron, for higher content of boron only bulk concentration is tested after experiment by microprobe. Tab. 5.8 summarizes the results and more details can be found in Tab. B.12 and B.13. The content of boron is higher after experiment than in the initial composition, but the variation is within the experimental error, which can be close to 1% for boron. Nevertheless, the boron content is suprisingly high considering the glass remained in the furnace for 8 or more hours.

5.2.7 Temperature field inside the furnace

As mentioned above in sec. 4.2, it is not possible to measure the temperature inside the furnace during the experiment, whereas it is necessary to know it for the determination of the in-situ glass properties. Therefore we have measured the temperature field without the crucible in order to estimate the temperature in the experimental part (T_E), see Fig. 5.7. The

Glass	**SiO_2**	**Na_2O**	**CaO**	**B_2O_3**	**MgO**	**Al_2O_3**	**SO_3**
10 wt% B_2O_3 first/average	62.1	12.5	13.1	10.7	0.1	2.0	0.11
10 wt% B_2O_3 second/average	61.6	12.4	13.0	10.8	0.1	2.0	0.11

Table 5.8: Average chemical composition of glass with 10 wt% B_2O_3 for two different samples after experiment, see Tab. B.12 and B.13 for more details.

temperature field is measured for four temperatures adjusted on the furnace (T_F): 1100, 1200, 1300 and 1400°C. The temperature profiles in the middle of the furnace are reported in Fig. 5.8, where y=0 corresponds to the bottom of the crucible, as denoted in Fig. 5.7. To determine the average temperature at the place of the glass sample, linear fitting is applied approximately at the area from y=0 to y=50 mm, where the glass sample is, see Fig. 5.9. The temperature fitted profile for T_F=1100°C is:

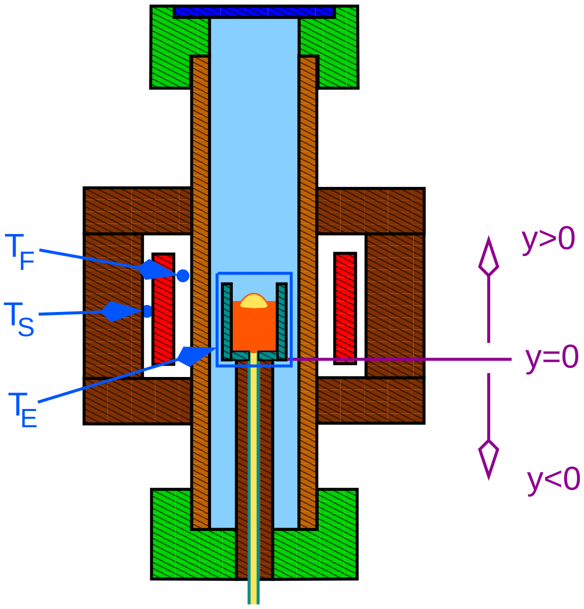

Figure 5.7: Sketch of the furnace showing the locations of the temperature probes and the y-axis orientation of temperature profile.

$$T_E = 1046 - 0.0726 \cdot y \tag{5.5}$$

Temperature is computed for y=0 and y=50 mm:

$$T_{E0} = 1046 \tag{5.6}$$

$$T_{E50} = 1042 \tag{5.7}$$

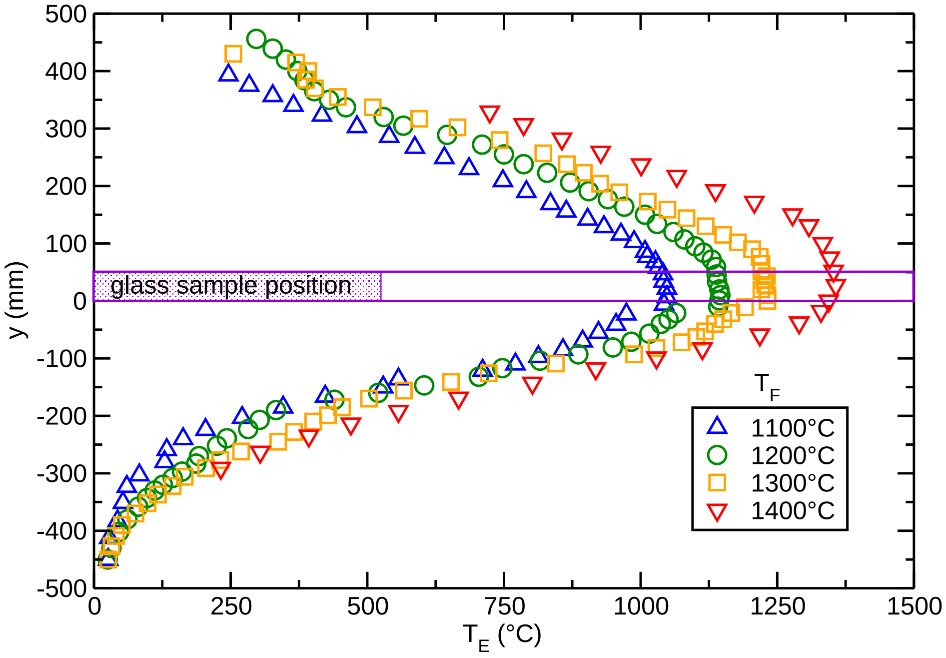

Figure 5.8: Temperature field inside the furnace for various T_F.

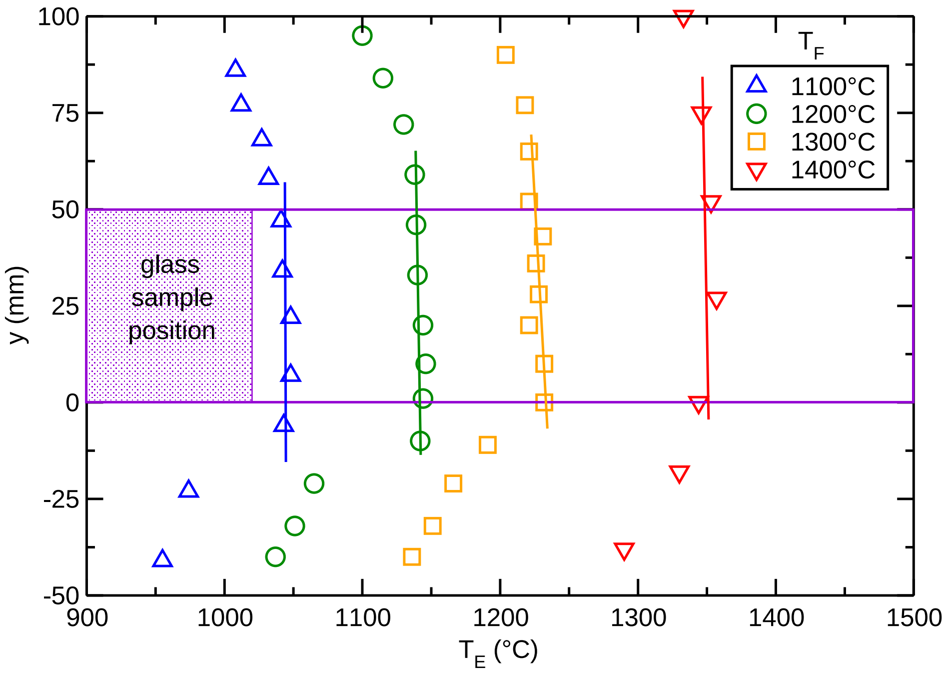

Figure 5.9: Linear fitting of temperature field inside the furnace for various T_F.

T_F (°C)	T_E (°C)	T_{E}_er (°C)	T_{E}_er (%)
1100	1044.09	4.49	0.43
1200	1141.79	3.91	0.34
1300	1227.56	7.19	0.59
1400	1349.76	5.59	0.41

Table 5.9: Experimental temperatures (T$_E$) for various adjusted furnace temperatures (T_F).

These values need to be adjusted in order to include an error caused by the fitting. Error is obtained when the measured values are compared with the computed values as follows:

$$y_{er} = \frac{\sqrt{\frac{1}{N}\sum (dy_i)^2}}{\sqrt{\frac{1}{N}\sum y_i^2}} \tag{5.8}$$

$$T_{E_{er}} = 0.0025642 \tag{5.9}$$

where:

N	number of points (-)
dy_i	difference between the measured and computed temperature (-)
y_i	measured temperature (°C)

It is possible to determine maximal and minimal temperature in the interval:

$$T_{E0_{er}} = 1048.6 \tag{5.10}$$

$$T_{E50_{er}} = 1039.6 \tag{5.11}$$

An average value of the two temperatures is the final temperature (T$_E$) in the furnace. The difference between T$_E$ and the temperature at one of the end points is an absolute error. Tab. 5.9 contains the final experimental temperatures with the error. The temperatures given in Tab. 5.9 are the most used once during the experiments, however, several experiments are achieved at lower or higher temperatures as well. It would be much time consuming to determine the temperature field for every furnace temperature, which is used during the experiment, therefore it is very useful to find an equation which enables the computation of T_E from known adjusted value of T_F. Graph in Fig. 5.10 shows a relation between the two temperatures. A linear fitting relation is obtained as:

$$T_E = 1.0028 \cdot T_F - 62.675 \tag{5.12}$$

The error is determined from the fitting using eq. (5.8) and it is equal to 0.68 %.

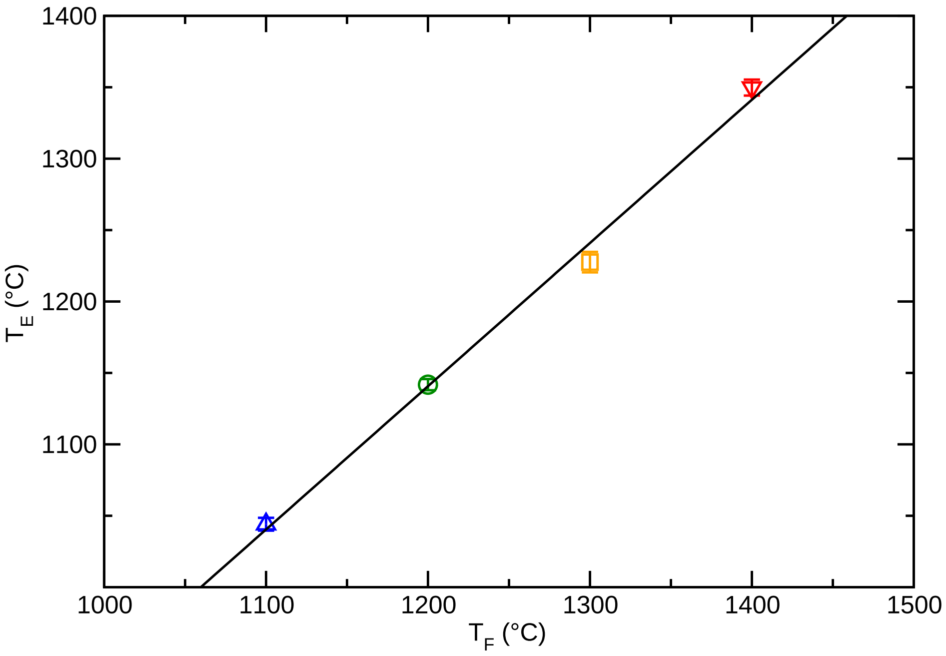

Figure 5.10: Dependence of the experimental temperature T$_E$ on the adjusted furnace temperature T$_F$.

5.2.8 Glass properties

Correct determination of glass properties is a very important part of this experimental work. Measurement of the properties at high temperatures is complex, therefore there are many studies devoted to the prediction of the properties from the chemical composition of glass. They are usually additive methods assuming, that each oxide in the molten glass contributes a certain amount of the property. Nowadays, many of the models are very precise and their error is below 2%. Most of the properties of glasses, which are used in this work, are computed using various models. Error in the composition from analyses is not considered in the computation of properties. Considering various combinations of composition will be very time consuming. It is expected that the error of the computation exceeds the error caused by minor changes in the composition. In the comparison, error caused by the uncertainty in the experimental temperature T$_E$ is taken into consideration for computation of viscosity, where it can lead to a huge error bar at low temperatures, because as it has been already mentioned, the viscosity exponentially changes with temperature.

Surface tension

The surface tension of glass is computed using models proposed by four different authors. The final value is determined as an average of the values obtained from these models. In the computations done by Lyon, Dietzel and Rubenstein, the surface tension is obtained using the additive method, where the glass property is computed as sum of mass or molar fraction of the appropriate glass oxides, which is multiplied by its specific coefficient, see eq. below:

$$\gamma = \sum(x_i \gamma_i), \tag{5.13}$$

where γ is the surface tension of glass, x_i is the molar or mass fraction of glass oxide i and γ_i is the specific coefficient, which describes the importance of the particular oxide on the whole value of the surface tension. The complete computation can be found in [20, 18, 17]. Dietzel's computation is limited in temperature. The given coefficients correspond to the temperature 900°C. When the temperature increases, it is necessary to subtract 4 mN·m^{-1} with every 100°C [18]. Other limitation is the content of Na$_2$O, which must be below 25 wt%. More details about the model of Dietzel can be found in [3]. The computation of Lyon is also limited in temperature. He proposes coefficients for two temperatures: 1200 and 1400°C. Other limitation is the ratio between contents of SiO$_2$ and Na$_2$O, which needs to be approximately 3.5 or higher. In this case the computation is very precise with an error smaller than 1%. If the ratio equals 2, it is necessary to add 30 mN·m^{-1} to the final value and if the rate is close to 1, then it is necessary to add 80 mN·m^{-1} to the final value of the surface tension. More details can be found in [14]. Rubenstein extended Lyon's coefficients from 9 oxides to 30. However his computation is available only at 1200°C. The source does not specify whether it is still necessary to obey the same rules for the ratio as for Lyon's computation. Nevertheless, the ratio for all glasses used in this work is always above 3.5. Mode details about the computation by Rubenstein can be found in [16].
Another determination of surface tension from the glass composition is given by Kucuk *et al.* [8], who propose a formula for the temperature 1400°C and the molar fraction of glass oxides, see eq. below:

$$\begin{aligned}\gamma(mN \cdot m^{-1}) = \;& 271.2 + 1.48 \cdot mol\%Li_2O - 2.22 \cdot mol\%K_2O - 3.43 \cdot Rb_2O \\ & +1.96 \cdot mol\%MgO + 3.34 \cdot mol\%CaO + 1.28 \cdot mol\%BaO \\ & +3.32 \cdot mol\%SrO + 2.68 \cdot mol\%FeO + 2.92 \cdot mol\%MnO \\ & -1.38 \cdot mol\%PbO - 2.86 \cdot B_2O_3 + 3.47 \cdot mol\%Al_2O_3 \\ & -24.5 \cdot mol\%MoO_3\end{aligned} \tag{5.14}$$

Beside the temperature, no other limitations for using this computation are given. In the work by Kucuk *et al.*, the results obtained by this method are compared with experimentally measured values of surface tension for three different glass compositions (sodium trisilicate, soda-lime-silica and commercial TV panel glass) with a disagreement less than 1%. The article of Kucuk *et al.* also gives a comparison between surface tension experimentally determined for the three glasses mentioned above and values computed by the methods of Dietzel, Lyon and Rubenstein. The values obtained by the model of Dietzel are always

T_E (°C)	Dietzel	Lyon	Rubenstein	Kucuk	final
1044	337.2	-	-	-	332
1142	333.3	-	-	-	328
1228	329.9	326.6	326.6	-	324
1350	325.0	322.6	-	317.8	320

Table 5.10: Surface tension of glass with 0.01 wt% Fe_2O_3 for the most tested temperatures.

T_E (°C)	0.01 wt% Fe_2O_3	0.1 wt% Fe_2O_3	1 wt% B_2O_3	10 wt% B_2O_3	AKM
1044	332	328	331	306	-
1142	328	324	327	302	-
1228	324	320	323	298	303
1350	320	316	319	294	299

Table 5.11: Surface tension of all glass compositions and the most tested temperatures, more details are given in Tab. C.1, C.2, C.3, C.4 and C.5.

higher than the real values, but the values obtained with the model by Lyon and Rubenstein remain within the error interval of the experimental measurement. Due to lack of coefficients for oxides in Lyon's computation, values for only two glasses can be compared.

All models mentioned above were used in this work to compute the surface tension of experimental glasses. The computation of glass surface tension using the models of Dietzel, Lyon, Rubenstein and Kucuk can be found in appendix D.1. A chart for each glass for the fourth main tested temperatures is created. An example is given in Tab. 5.10 for the glass with lower iron content. For the temperature 1228°C, coefficients for 1200°C are used and for 1350°C, the coefficients for 1400°C are considered.

The final value for 1400°C is determined as an average value of Kucuk and Lyon, which in this case equals 320 mN·m^{-1}. Then a correction of 4 mN·m^{-1} for every 100°C is applied which gives us values 324, 328 and 332 mN·m^{-1} for temperatures 1228, 1142 and 1044°C respectively. If we compare the final values with those computed by the model of Dietzel, we find, that the surface tension computed by Dietzel is always higher, which corresponds to the observation by Kucuk *et al.* in the experimental work. The final values of surface tension for all tested glasses are given in Tab. 5.11 and more details can be found in Tab. C.1, C.2, C.3, C.4 and C.5. When experiments are achieved at other temperature than the once in Tab. 5.11, 4 mN·m^{-1} are subtracted or added for every 100°C, depending if the new experimental temperature is higher or lower than the main interval.

The error of computation comes from the comparison of measured and computed values in the work of Kucuk and equals 1%, which roughly corresponds to 3 mN·m^{-1} and is considered in this work. This error also includes the error caused by using coefficients for 1200 and 1400°C to compute surface tension at 1228 and 1350°C respectively.

Density

Density of glass is determined by using a computation proposed by Demkina, which can be found in [20, 1, 2]. The model computes the glass density at room temperature and is given in appendix D.2 together with a computation of the refractive index. Error of the computation is between 2 and 3 %, but it can even be lower, which has been tested by a comparison of computed and measured values of density. The density of soda-lime-silica glass with a higher content of iron was determined experimentally and equals to 2,470 kg·m^{-3}, its computed value is 2,489 kg·m^{-3}. The difference between the two values (19 kg·m^{-3}) is less than 1%.

The glass density changes with temperature as a consequence of structural changes. Below the temperature of transformation the variation is linear, not very strong and can be computed, but above the temperature of transformation it decreases strongly with rising temperature (Fig. 5.11). It is necessary to determine the density above Tg experimentally. This is done for soda-lime-silica glasses with high content of iron and for AKM glass, but not for boron glasses. For boron glasses the density is computed for room temperature using the model of Demkina and the temperature variation is not taken into consideration. This can cause an error in the final results and the influence will be discussed in sec. 6.2.4. A model for a computation of density between temperatures 1000 and 1400°C is proposed by Fluegel *et al.* [5]. The model is not valid for high content of boron, but for the glass with 1 wt% of B_2O_3, it proposes the following equation:

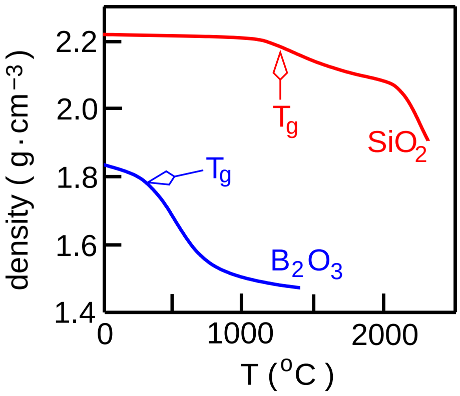

Figure 5.11: Variation of density of glass with temperature [18].

$$\rho = -0.00021651T + 2.6381, \tag{5.15}$$

Glass	density (kg·m^{-3})
1 wt% B_2O_3	2,523.43
10 wt% B_2O_3	2,591.36

Table 5.12: Density at room temperature of glass with 1 and 10 wt% B_2O_3.

where ρ is the density in g·cm^{-3} and T is the temperature between 1000 and 1400°C. The density of soda-lime-silica glass with low content of iron is considered to be the same as for high content, because apart from the minor difference in iron content, the composition remains the same. Results of the experimental measurement of density as function of temperature for soda-lime-silica with 0.1 wt% Fe_2O_3 and AKM glasses are given in Fig. 5.12 and eq. (5.16) and (5.17) respectively, where ρ is the density in g·cm^{-3} and T is the temperature in °C.

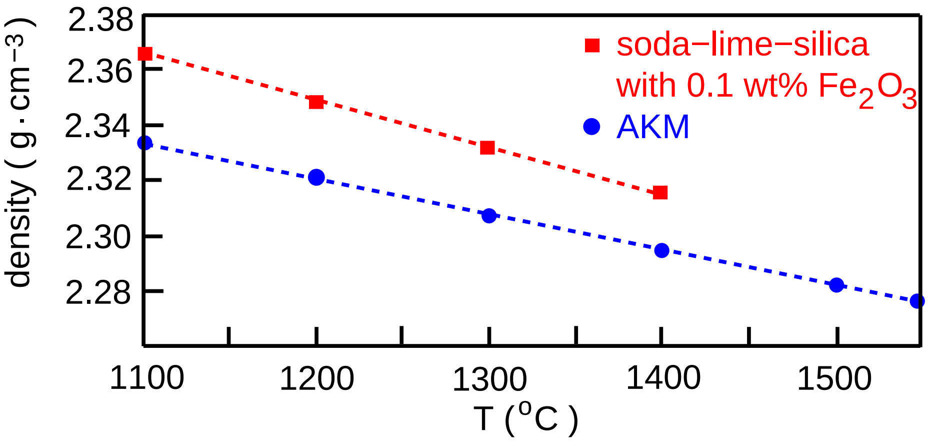

Figure 5.12: Experimental measurement of density as a function of the temperature for soda-lime-silica with 0.1 wt% Fe_2O_3 and AKM glass.

$$\rho_{\mathrm{soda-lime-silica\,with\,0.1\,wt\%\,Fe_2O_3}} = -1.7 \cdot 10^{-4} T + 2,553 \tag{5.16}$$

$$\rho_{\mathrm{AKM}} = -1.272 \cdot 10^{-4} T + 2,474 \tag{5.17}$$

The density of glass with 1 and 10 wt% B_2O_3 is given in Tab. 5.12.

Viscosity

Viscosity is closely linked to drainage. Therefore much attention is paid in order to determine it correctly. A model which is developed in Saint-Gobain Recherche, enables the computation of the viscosity from the glass chemical composition. This program proposes values of viscosity for all important temperatures, that have already been discussed, but does not enable computation of viscosity for any temperature. This is why it is necessary to use a

T_E(°C)	$T_{E_{er}}$(°C)	μ(Pa·s)	μ_{er}(Pa·s)
1044.09	4.49	672.25	49.78
1141.79	3.91	160.41	8.14
1227.56	7.19	58.36	4.50
1349.76	5.59	18.20	0.86

Table 5.13: Computed viscosity of glass with 0.01 wt% Fe_2O_3 for all tested temperatures in the experimental work.

fitting in order to determine the coefficients A, B and T_0 and obtain VFT equation (2.1), which enables computation of viscosity for any temperature. The error of the computation in the program is not known, but it is believed to be lower than the uncertainty from the error known in temperature field inside the furnace. The model has several limitations. One of them is boron content, which needs to be lower than 5% and that is why the viscosity for 10 wt% of boron content is determined experimentally. The fitting of the viscosity curve is achieved in the program, where the initial coefficients of the VFT equation are obtained by the computation of Lakatos [10, 11, 12, 13]. The error comes from the error in the temperature. Viscosities of all temperature and all glasses that are used in this experimental work are given in Fig. 5.13 and Tab. 5.13, 5.14, 5.15, 5.16 and 5.17.

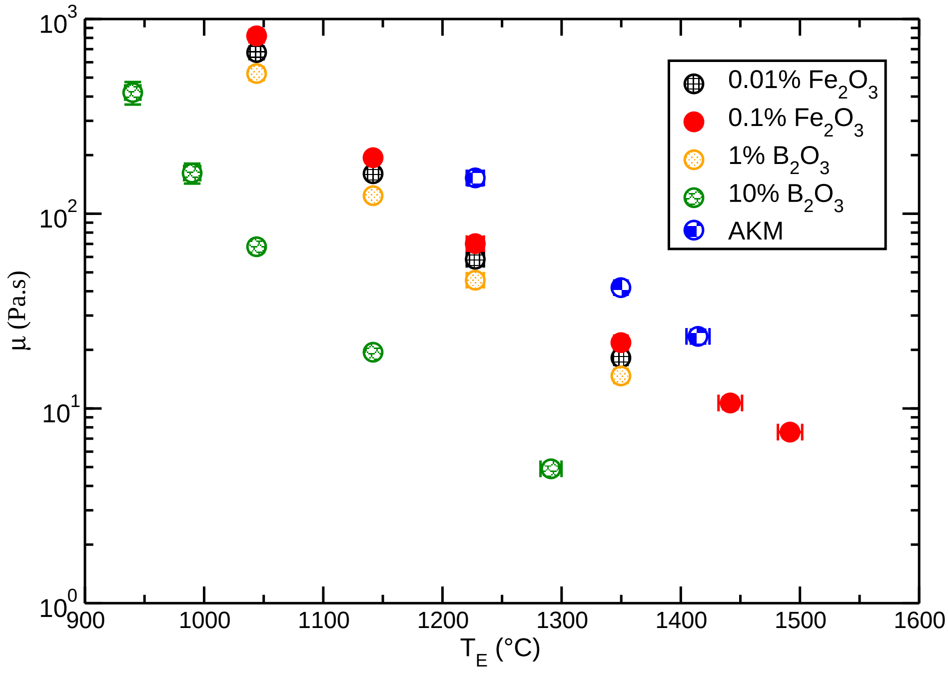

Figure 5.13: Viscosity of all glass compositions tested in the experiment as function of experimental temperature (T_E).

T_E(°C)	$T_{E_{er}}$(°C)	μ(Pa·s)	μ_{er}(Pa·s)
1044.09	4.49	819.47	61.08
1141.79	3.91	193.87	9.89
1227.56	7.19	70.17	5.44
1349.76	5.59	21.78	1.03
1441.53	9.85	10.67	0.75
1491.67	10.91	7.56	0.51

Table 5.14: Computed viscosity of glass with 0.1 wt% Fe_2O_3 for all tested temperatures in the experimental work.

$T_E T_E$(°C)	$T_{E_{er}} T_E$(°C)	μ(Pa·s)	μ_{er}(Pa·s)
1044.09	4.49	524.77	39.61
1141.79	3.91	123.80	6.26
1227.56	7.19	45.56	3.45
1349.76	5.59	14.68	0.67

Table 5.15: Computed viscosity of glass with 1 wt% B_2O_3 for all tested temperatures in the experimental work.

T_E(°C	$T_{E_{er}}$(°C	μ(Pa·s)	μ_{er}(Pa·s)
940.13	6.42	419.14	55.63
989.97	6.75	161.81	18.98
1044.09	4.49	67.66	4.45
1141.79	3.91	19.43	0.84
1291.11	8.82	4.90	0.33

Table 5.16: Measured viscosity of glass with 10 wt% B_2O_3 for all tested temperatures in the experimental work.

T_E(°C	$T_{E_{er}}$(°C	μ(Pa·s)	μ_{er}(Pa·s)
1227.56	7.19	152.74	13.03
1349.76	5.59	41.71	2.20
1414.45	9.66	23.46	1.91

Table 5.17: Computed viscosity of AKM glass for all tested temperatures in the experimental work.

composition	n$_{exp}$	n$_{comp}$	Δ n (%)
SiO_2 79.8 wt% - Na_2O 20.2 wt%	1.4906	1.4840	0.44
SiO_2 74.3 wt% - Na_2O 16.3 wt% CaO 9.4 wt%	1.5168	1.5184	0.11
SiO_2 79.3 wt% - Li_2O 11.3 wt% Al_2O_3 9.4 wt%	1.5118	1.5118	0.00

Table 5.18: Comparison of experimentally determined and computed refractive indexes for three glass compositions.

Glass	n
0.01 wt% Fe_2O_3	1.5196
0.1 wt% Fe_2O_3	1.5179
1 wt% B_2O_3	1.5269
10 wt% B_2O_3	1.5405
AKM	1.5048

Table 5.19: Refractive indexes of all glass compositions used in this experimental work.

Refractive index

The refractive index of glass is computed using the method of Appen, which can be found in [20] or [18] and is given with the computation of the density in appendix D.2. The precision of the method of Appen is obvious from the comparison of experimentally determined and computed values of refractive indexes for three glass compositions in Tab. 5.18. Nevertheless, the computation does not consider variation of refractive index with the wavelength of the light source or the temperature. For silica glasses with a main component of SiO_2, refractive index rises with temperature below the transformation temperature, but for glasses, where B_2O_3 is the main component, the refractive index decreases with the rising temperature below the transformation temperature. Above the transformation temperature the same behavior for all glass compositions is the same and the refractive index decreases with the rising temperature. The variations caused by the light wavelength and the temperature are not considered in this experimental work, because the variation in refractive index influences the absolute value of the thickness of the bubble lamella, but it does not influence the draining rate (evolution of thickness). Since we are using only one wavelength in the experimental set-up, we cannot be certain about the exact determined thickness and that is why the value of refractive index is not studied very precisely. Refractive indexes of all glasses used in this work are computed using the method in appendix D.2 and are given in Tab. 5.19.

5.2.9 Bubble size determination in molten glass

Because the experimental set-up enables only a top view of the experiment, it is more difficult to determine the bubble size in molten glass, than in the experiment with silicon oil. Image of top view of crucible with the glass sample, but without the bubble is given in Fig. 5.14. The bottom and top edges of the crucible are visible. It is also visible, that the level of the glass is between the two, which is indicated by small bubble on the surface close to the crucible wall. The crucible bottom and top have a diameter of 50 mm. It is possible to compute the scale of the level of the glass considering it is between the two. More details about the computation can be found in appendix E. The bright spot in the middle of the crucible is the laser beam. Fig. 5.15 shows an example of a rising bubble in the crucible. When the bubble is created in the crucible, there are several steps that appeared. At the beginning, the bubble is created by gas flow into the crucible, when the flow stops, the bubble is still at the bottom of the crucible and due to over pressure in the bubble, the gas flows from the bubble back to the tube, which corresponds to the shrinkage of the bubble. When the bubble detaches from the bottom thanks to buoyancy force, it rises through the liquid, which can be indicated by constant top view of the bubble and corresponds to spherical shape. When the bubble rises close to the interface, the top view starts to deform. The bubble diameter is measured while the bubble is rising to the surface and its shape is spherical. The diameter is determined by comparing to the two available scales, at the bottom and at the glass level, because it is certain the bubble is between the two. Final bubble size is determined as average value of the two diameters obtained by the two scales. The variation of the average from the two

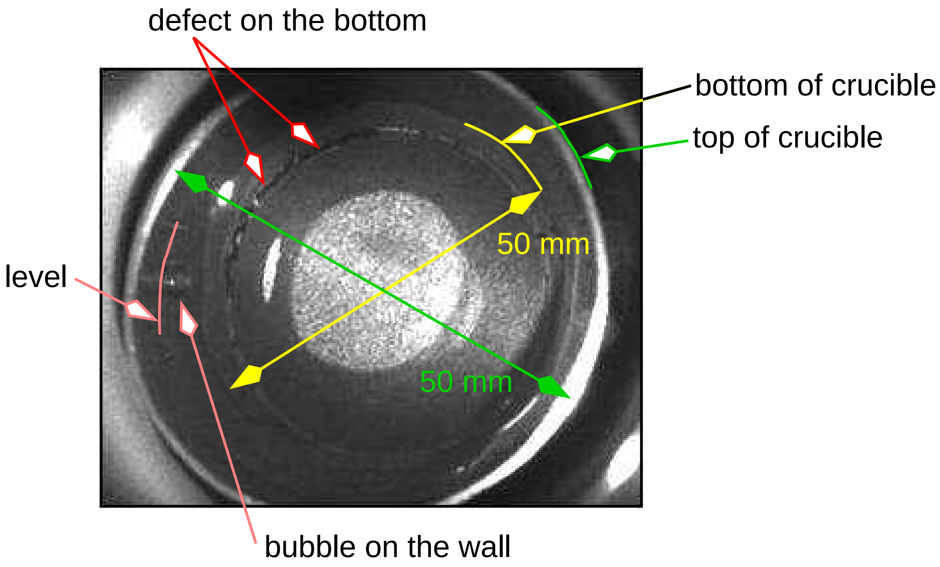

Figure 5.14: Top view of Pt-Rh crucible with dimension of bottom and top part, glass sample and laser beam in the middle.

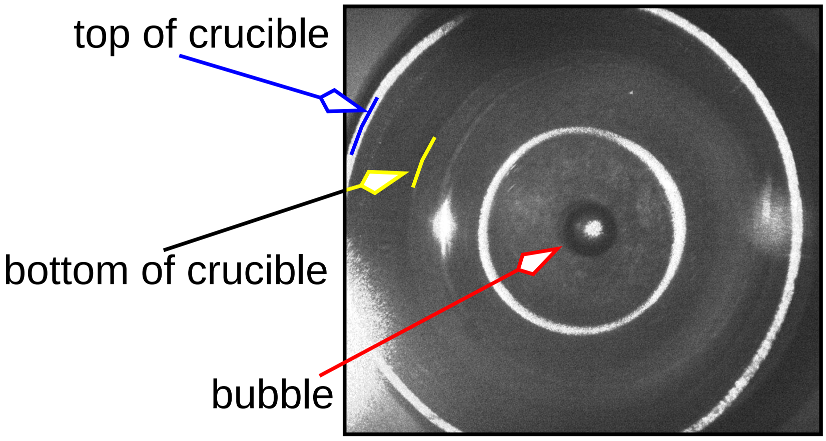

Figure 5.15: Top view on Pt-Rh crucible with rising bubble.

diameters defines the error bar. More details about the behavior of the bubble inside the crucible will be given in the following chapter, see sec. 6.1.1.

5.3 Determination of the thickness

The thickness of the bubble lamella is computed from the signal obtained by the photodiode (PDMS) or the CCD camera (molten glass). In the experiment with PDMS, the intensity of reflected light is translated in electric voltage every 0.2 s (Fig. 5.16). For molten glass,

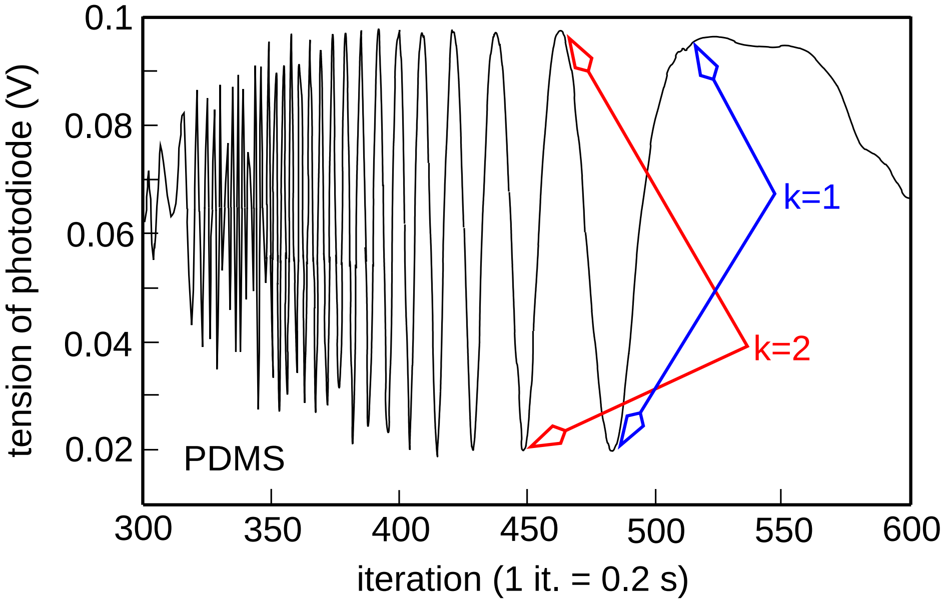

Figure 5.16: Tension of photodiode as a function of time corresponding to light intensity due to interference on bubble lamella.

images are taken by the CCD camera and processed in the program ImageJ, where the intensity of chosen area (Fig. 5.17) is projected through all images (Fig. 5.18). The duration between the images is changing with the glass viscosity. When the viscosity is high, the images are taken every 500 ms, if the viscosity is low, the shortest duration between images is 50 ms. The thickness of the film can be determined at the maximum and minimum of intensity thanks to the classical theory of light interference [7], see eq. below:

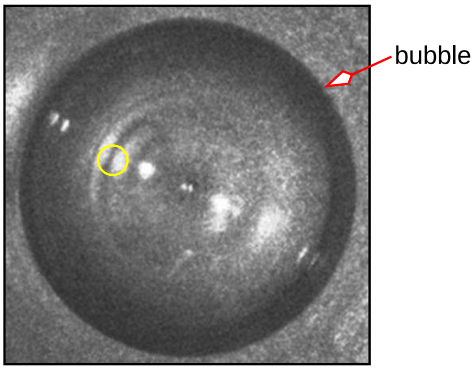

Figure 5.17: Interference signal on bubble in molten glass. Signal in Fig. 5.18 is obtained by plotting average intensity of yellow area as a function of all images in the movie.

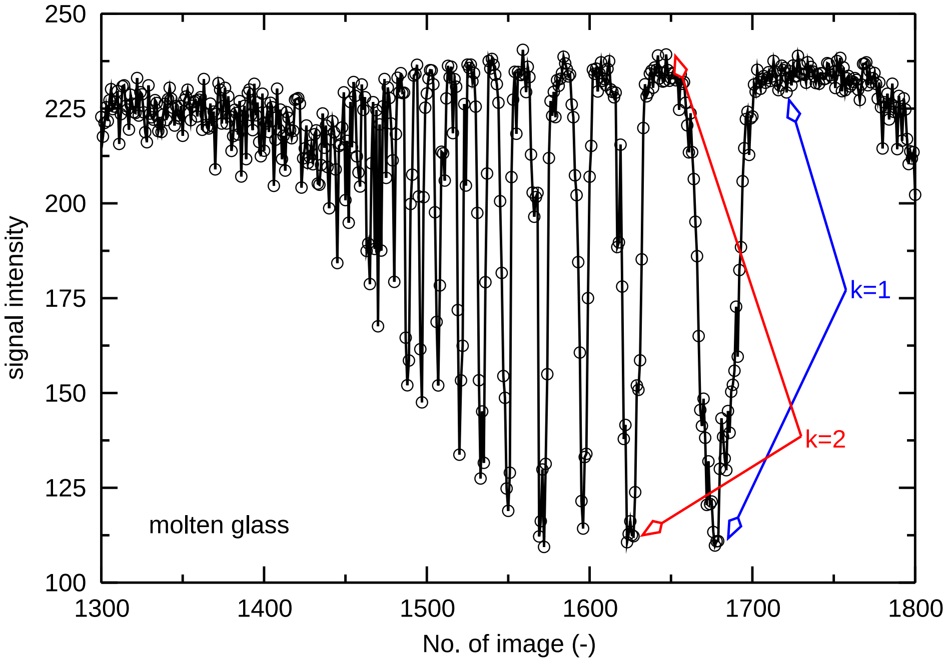

Figure 5.18: Light intensity obtained from images recorded by CCD camera.

$$h_{I_{max}} = \frac{\lambda}{4n} \cdot (2k - 1)\,, \tag{5.18}$$

$$h_{I_{min}} = \frac{\lambda}{2n} \cdot k, \tag{5.19}$$

Glass	**h_{lowest} (nm)**
0.01 wt% Fe_2O_3	87.52
0.1 wt% Fe_2O_3	87.62
1 wt% B_2O_3	87.10
10 wt% B_2O_3	86.34
AKM	88.38

Table 5.20: Lowest determined thicknes of bubble lamella detected by the method.

where h is the thickness of the lamella, λ is the wavelength of the light source, n is the refractive index of the liquid (silicon oil or molten glass) and k is the order of interference. The subscript I_{max} is used for the thickness when the reflecting intensity reaches maximum and I_{min} for the thickness at the minimum intensity. The derivations of eq. (5.18) and (5.19) are given in appendix F. The light intensity is regularly changing between minimum to maximum until the last maximum, after which the signal stops being regular. The lowest thickness is computed at the last determined maximal intensity, where k equals 1. The value of the last thickness is function of the wavelength of the light source and the refractive index of the liquid. The thickness of the rupture of the film cannot be determined using this method. It can only be concluded, that the lamella ruptures below the last determined thickness. The lowest values of thickness for all tested glasses are given in Tab. 5.20. They change slightly for all the compositions due to the variation of the refractive index, which was given in Tab. 5.19. In the experiment by Senée *et al.* [19], who used the same method for the thickness determination, they achieve the experiment using two wavelengths of light source to determine the point, where the first order of interference occurs. In this experiment, only one wavelength is used and the last point of the interference pattern is disrupted. If we establish k=1 at wrong position, where k in reality can equal to a larger value. Using eq. (5.18) and (5.19), the absolute error is then $\lambda/(2n)$. This may lead to an inexact value of the thickness, but relative behavior of the thickness, which is important to determine the thinning rate, remains the same even if the absolute value of the thickness is not correct. In order to determine precisely the thickness, blue laser was tested in the experiment with molten glass, but the improvement of the set-up was not completed as discussed previously in sec, 4.2.2.

References

[1] L. I. Demkina. *Investigation of the Dependence of the Glass Properties on their Composition*. Moscow, 1958.

[2] L. I. Demkina. *Physico-Chemical Principles of the Production of Optical Glass*. Leningrad, 1976.

[3] A. Dietzel. Zusammenhänge zwischen Oberflächenspannung und Struktur von Glasschmelzen. *Kolloid Zeitschrift*, 100(3):368–380, 1942.

[4] L. Doubliez. The drainage and rupture of a non-foaming liquid film formed upon bubble impact with a free surface. *Int. J. Multiphase Flow*, 17(6):783–803, 1991.

[5] A. Fluegel, D. A. Earl, A. K. Varshneya, and T. P. Seward. Density and thermal expansion calculation of silicate glass melts from 1000°C to 1400°C. *Phys. Chem. Glasses: Eur. J. Glass Sci. Technol. B*, 49(5):245–257, 2008.

[6] J. B. M. Hudales and H. N. Stein. Profile of the Plateau Border in a Vertical Free Liquid Film. *Journal of Colloid and Interface Science*, 137(2):512–526, 1990.

[7] C. Isenberg. *The science of soap films and soap bubbles*. Dover Pub., 1992.

[8] A. Kucuk, A. G. Clare, and L. Jones. An Estimation of the surface tension for silicate glass melts at 1400°C using statistical analysis. *Glass Technol.*, 40(5):149–153, 1999.

[9] P. Laimböck. *Foaming of Glass Melts*. PhD thesis, 1998.

[10] T. Lakatos. Viscosity-temperature relations in glasses composed of SiO_2-Al_2O_3-Na_2O-K_2O-Li_2O-CaO-MgO-BaO-ZnO-PbO-B_2O_3. *Glasteknisk Tidskrift*, 31(3):51–54, 1976.

[11] T. Lakatos and L.-G. Johansson. Viscosity and Liquidus Temperature Relations in the Mineral-Wool part of the system SiO_2-Al_2O_3-CaO-MgO-Alkalies-FeO-Fe_2O_3. *Glasteknisk Tidskrift*, 36(4):51–55, 1981.

[12] T. Lakatos, L.-G. Johansson, and B. Simmingsköld. The effect of some glass components on the viscosity of glass. *Glasteknisk Tidskrift*, 27(2):25–28, 1972.

[13] T. Lakatos, L.-G. Johansson, and B. Simmingsköld. Viscosity temperature relations in the glass system SiO_2-Al_2O_3-Na_2O-K_2O-CaO-MgO in the composition range of technical glasses. *Glass Technology*, 13(3):88–94, 1972.

[14] K. C. Lyon. Calculation of surface tension of glasses. *Journal of The American Ceramics Society*, 27(6):186–189, 1944.

[15] W. M. Nozhat. Measurement of liquid-film thickness by laser interferometry. *Applied Optics*, 36(30):7864–7869, 1997.

[16] C. Rubenstein. Factors for the calculation of the surface tension of glasses at 1200°C. *Glass Technology*, 5:36–41, 1964.

[17] H. Scholze. *Le verre*. Institut du Verre, Paris, 1969.

[18] H. Scholze. *Nature, Structure and Properties*. Springer-Verlag, New York, 1991.

[19] J. Senee, B. Robillard, and M. Vignes-Adler. Films and foams of Champagne wines. *Food Hydrocolloids*, 13:15–26, 1999.

[20] M. B. Volf. *Sklo ve výpočtech*. SNTL-Nakladatelství technické literatury, Prague, 1984.

Chapter 6

Results and Discussion

This chapter contains all results that were obtained during this experimental work. Description of bubble creation and a creation of a spatio-temporal image, which is used for bubble size and lifetime determination, is given in sec. 6.1. When a bubble is approaching the liquid interface, its rising velocity (sec. 6.1.1) and shape close to the interface (sec. 6.1.2) are determined. Evolution of thickness of the bubble lamella is discussed for the two tested liquids - silicon oil and molten glass (6.2). This section also presents differences observed in the behavior of silicon oil and molten glass and proposes other liquids, that can be used as model liquids for molten glass (sec. 6.2.6). As it has been already mentioned in the previous chapters, it is not possible to determine precisely the critical thickness of the bubble lamella at the moment of the rupture, nevertheless it is possible to compute the thickness at the moment of the rupture considering evolution of thickness and the bubble lifetime, more details are given in sec. 6.3. This section also specifies two steps of the bubble lifetime: regular and irregular drainage. Determination of the lifetime and its prediction for various glass composition, bubble size and temperature are given in sec. 6.4. Following section discusses the origin of irregular drainage using SIMS analysis of thin glass vertical film. (sec. 6.5.2). The observation during the experiment with vertical film is in a good agreement with the experiment at the bubble scale, sec. 6.5. The role of evaporation on bubble lifetime is discussed in sec. 6.5. Last part of this chapter contains a description of daughter bubble - new source of bubbles, that can appear as a consequence of rupture of large bubbles at low liquid viscosity (sec. 6.6).

6.1 Single bubble approaching liquid interface

As mentioned in sec. 5.2.9, we are able to observe several steps in our experiment, which appear as bubble is inflated. In order to visualize all steps in a unique picture, we create a

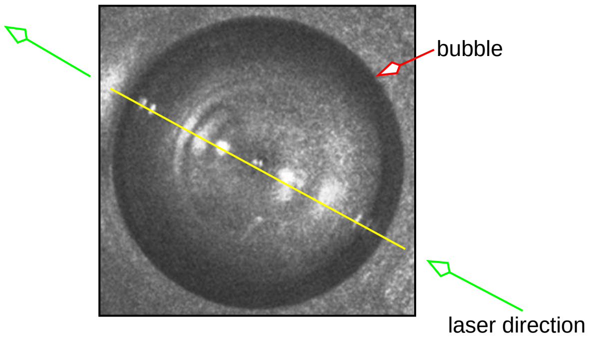

Figure 6.1: Top view of a bubble.

spatio-temporal image or “reslice image”. Top view of a bubble with the direction of incident laser is given in Fig. 6.1. The yellow line in the image indicates the direction of the laser beam and therefore the most interesting region of the image, because all light changes, which correspond to variation of the curvature of the interface during the experiment, are most visible in the direction of the laser beam. The recording of the light along this line during an experiment gives the reslice image corresponding to a spatio-temporal diagram. Example of a reslice image for a small (left) and a large (right) bubble is given in Fig. 6.2. In the reslice image, the direction from left to right indicates the yellow line in Fig. 6.1 and the direction from the top to the bottom indicates time, where one pixel corresponds to one image. At first, bubble is created. During this step, gas is being blown into the Pt-Rh crucible and bubble is growing in size, which is visible in Fig. 6.2 as the growing bubble size. This step duration is very short (max 1 s) and therefore appears as several pixels depending on the recording speed. Second step is bubble shrinkage. During this step, the bubble is still attached to the bottom of the crucible and gas is flowing out of the bubble into the Pt-Rh tube causing the shrinkage of bubble. The higher the viscosity, the longer is the duration of shrinkage. As soon as the buoyancy force dominates and the bubble detaches from the bottom, its diameter is determined. The detachment of the bubble is followed by its rising towards the free surface. This step is indicated by some light changes which correspond to changes of the interface curvature as the bubble is approaching. The end of the rising time of the bubble is considered when the bubble reaches the free surface and its shape starts deforming. It is very difficult to establish this moment in the reslice image. Optical simulation will be necessary in order to understand all light changes visible during the experiment. Nevertheless, two light arcs are visible in the left and right parts of the images and it is assumed that one of them indicates the end of the bubble rising time, so one can measure two rising times. Rising time enables the determination of rising velocity, which will be discussed in the following section (6.1.1). After, the bubble reaches the free surface and remains in a static shape (sec. 6.1.2), no more light changes are observed and all images look approximately the same until the bubble rupture.

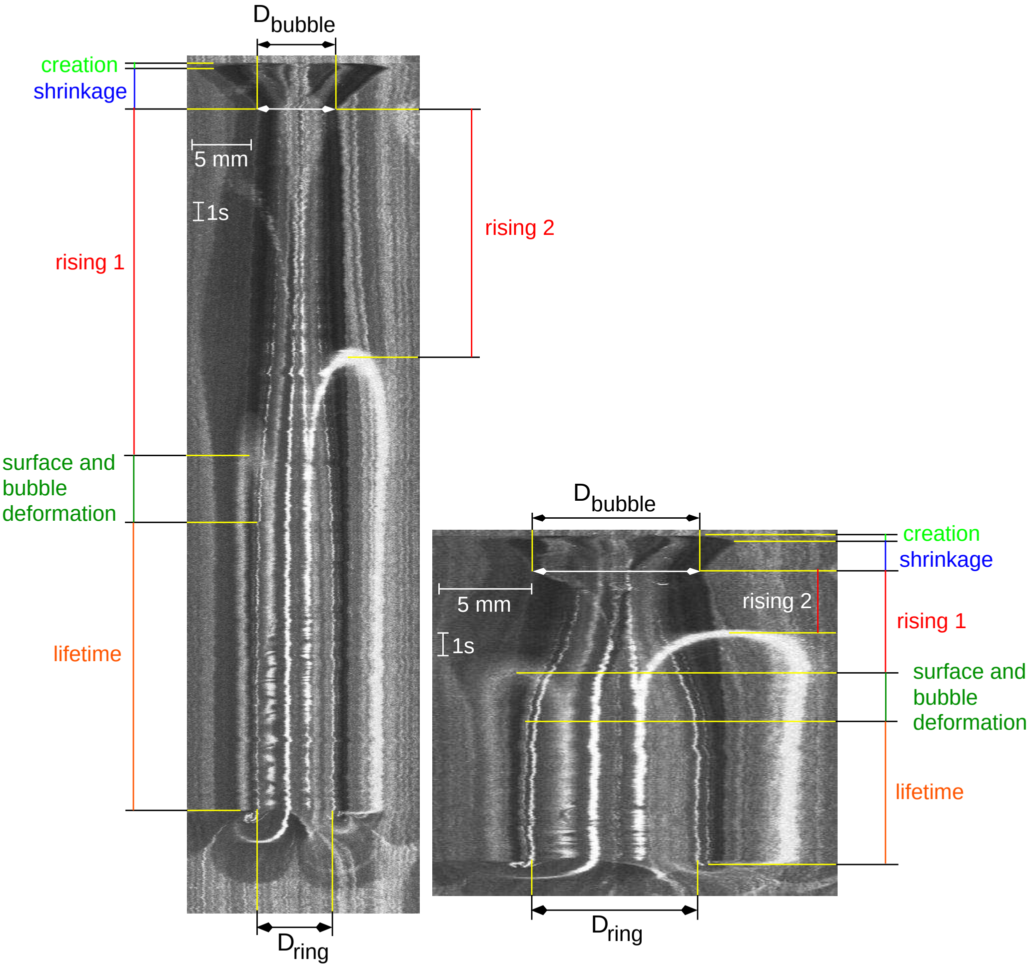

Figure 6.2: Reslice image of small (left) and large (right) bubble.

This step is considered as the bubble lifetime (sec. 6.4). During this step, there appears a variation of intensity in the brightest area, which corresponds to the interference patter discussed in sec. 5.3. A characteristic length noted D$_{ring}$ can be measured as illustrated in Fig. 6.2 and will be discussed in sec.6.1.2.

6.1.1 Bubble rising velocity

Two experimental rising velocities can be determined from the two rising times, as mentioned in the previous paragraph and noted in Fig. 6.2.

Rising velocity is computed as:

$$v_{exp.} = \frac{h - D_{bubble}}{t_r} \tag{6.1}$$

where:

$v_{exp.}$	experimental rising velocity ($m \cdot s^{-1}$)
h	glass height (m)
D_{bubble}	bubble diameter (m)
t_r	rising time (s)

The glass height h is measured after the experiment when glass is removed from the crucible. Bubble diameter and rising time are determined from the reslice image (Fig. 6.2). Error of the rising velocity is a sum of error on the bubble size determination and error on the determination of the rising time. The rising time was determined 3 times and the variation between the three determinations was around 10 pix, therefore 10 pix is considered as the error. The error on the glass height is not taken into account, because it is much smaller in comparison to the one on the bubble diameter. Fig. 6.3 shows the two experimental velocities normalized by theoretical Hadamard-Rybczynski velocity (sec. 3.1.2) as a function of bubble size normalized by the size of the crucible. The coefficient ϕ is the drag correction coefficient for fully mobile bubble rising in a circular tube [22]:

$$\phi = \frac{1 + 1.13785\beta^2}{1 - 1.4034\beta + 1.1378\beta^5 - 0.72603\beta^6}, \tag{6.2}$$

where β is the geometric coefficient given as:

$$\beta = \frac{D_{bubble}}{D_{tube}}. \tag{6.3}$$

It is obvious from graph in Fig. 6.3 that the rising velocity computed using “rising 1” corresponds better to the theoretical velocity, that is why “rising 1” determined in Fig. 6.2 is considered as the correct bubble rising time. Graph in Fig. 6.4 summarizes rising velocities of various bubble sizes in soda-lime-silica glass with 0.01 and 0.1 wt% of Fe_2O_3. Many experimentally determined velocities are below the predicted line corresponding to 1/ϕ. The equation in (6.2) is valid for an infinite tube, while in our experiment, the level of the glass is between 3 and 4 cm far from the bottom, which can be the explanation of the disagreement particularly for high viscosities (low temperature). The rising velocity is not determined in boron glasses or highly viscous AKM glass, because the rising velocity is not a function of chemical glass composition, therefore no variation with composition is expected.

Rising velocity of bubbles in our experiment is in a good agreement with the theoretical Hadamard-Rybczynski velocity corrected by a coefficient that takes into account the presence of the lateral wall of the crucible. This result confirms that interfaces of the bubble

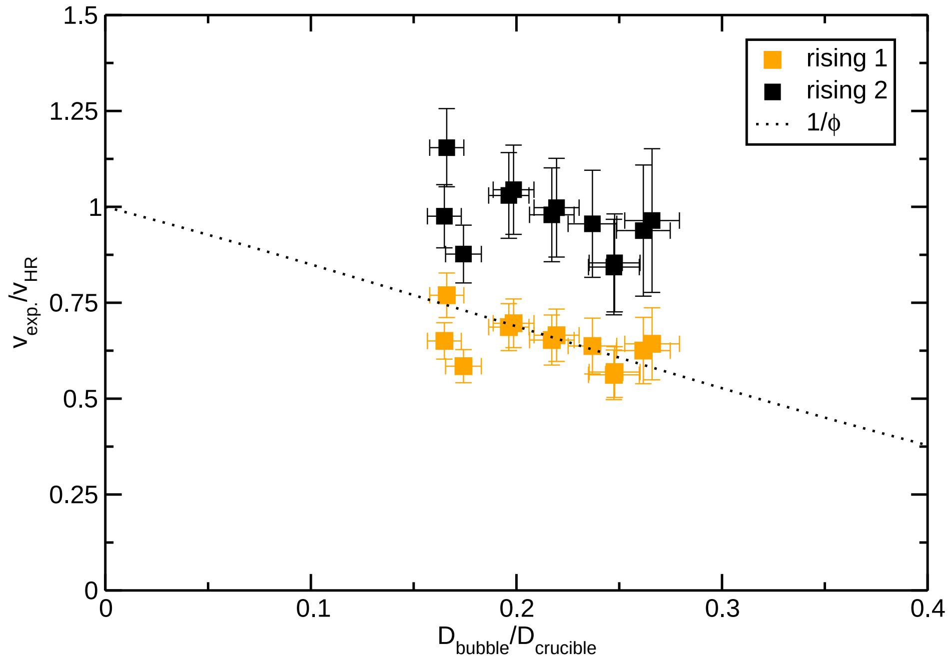

Figure 6.3: Comparison of two experimental rising velocities in glass with 0.1 wt% of Fe_2O_3 at T_E=1228°C.

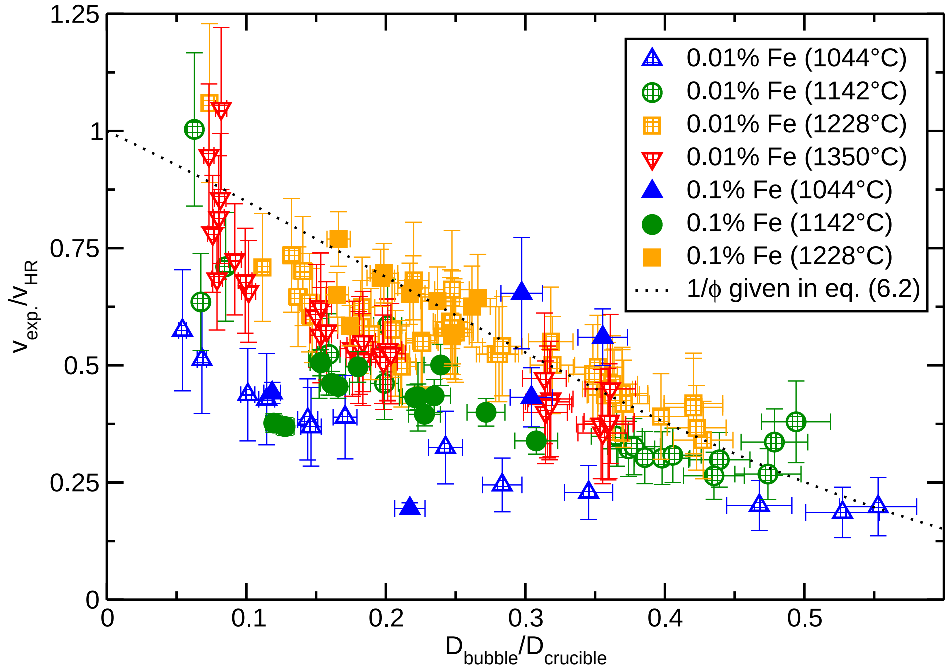

Figure 6.4: Bubble rising velocity for soda-lime-silica glass with 0.01 and 0.1 wt% of Fe_2O_3 and various T_E.

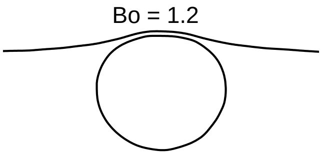

Figure 6.5: Shape of bubble with a small Bo number at the interface.

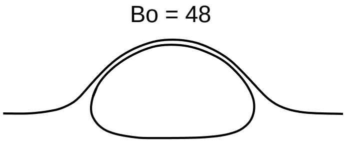

Figure 6.6: Shape of bubble with a large Bo number at the interface.

are mobile (free of surfactants). Slower rising velocity for larger bubbles is observed as a consequence of crucible walls (finite media) and follows a curve proposed for a fully mobile interface.

6.1.2 Bubble static equilibrium at interface

When a bubble approaches near a free surface, its spherical shape deforms and is controlled by the relative importance of the buoyancy forces against the surface tension:

$$D_{bubble}^3 \rho g \approx \sigma D_{bubble}, \tag{6.4}$$

where D_{bubble} is the bubble diameter, ρ is the liquid density (the gas density is neglected) and γ is the surface tension between the two phases. Ratio of these two forces is directly the Bond number:

$$Bo = \frac{\rho D_{\mathrm{bubble}}^2 g}{\sigma} \tag{6.5}$$

Example of bubble shape for small and large Bo number obtained with the boundary element method by Pigeonneau and Sellier [14] is given in Fig. 6.5 and 6.6. Small Bo number can appear as a consequence of a small bubble diameter or a large value of the surface tension. The lower bound of bubble size is characterized by the capillary length which is a particular length beyond which the gravity becomes important. It can be estimated from the comparison of Laplace and hydrostatic pressure and it is given by [5]:

$$\kappa^{-1} = \sqrt{\frac{\sigma}{\rho g}}. \tag{6.6}$$

At small Bo, the free surface is slightly deformed and the bubble remains quasi-spherical. For large Bo number, where the bubble size is larger than the capillary length, the interface is much more deformed. The equilibrium shape of a drop at the liquid-liquid interface (see Fig. 6.7) was studied by Princen [15], who describes the variation of the geometry of the lamella surface on top of the drop (R_{cap}, S_{cap}, h_{cap}, D_{ring}) as a function of the physical parameters (drop size, density and interfacial tension). Distance R$_{ring}$ determines the bounds of the S_{cap} area and creates a sort of ring in top view. In Fig. 6.8, edge of the bubble is dark, but two short bright lines are visible close to the bubble edge in the laser direction. The

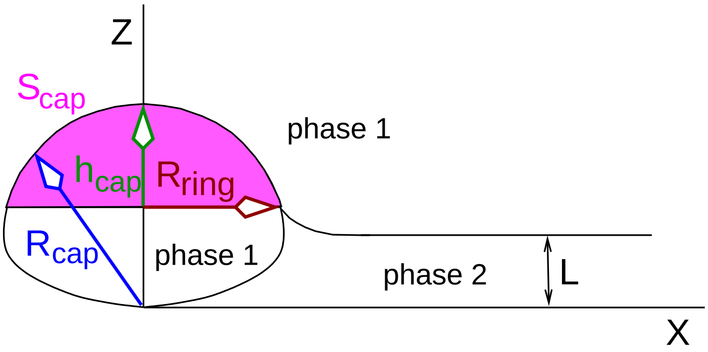

Figure 6.7: General model for the system of a drop at a liquid-liquid interface at equilibrium [15].

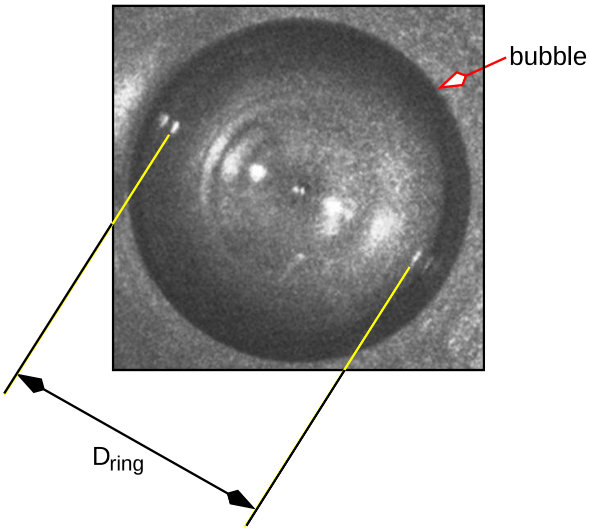

Figure 6.8: Top view of the bubble with indication of the D$_{ring}$.

bright lines are visible in reslice images (Fig. 6.2) as bright lines that appear soon after the determination of the bubble diameter and disappear after the bubble rupture. For larger bubble sizes, two of these lines are visible close to the edge, but for small bubbles only the inner bright lines are observed. The distance of the two inner bright lines is called D$_{ring}$ (Fig. 6.2). Fig. 6.9 compares numerical values given by Princen with our experimental results, where the normalized ring size changes as a function of the Bond number. Normalized size of the ring increases with the Bond number for experimental and numerical values. Nevertheless, compared to the numerical values, the experimental values are higher for smaller bubbles and lower for larger bubbles. The determination of the ring size for very small bubbles is difficult due to low resolution of images. Smaller values for larger bubbles may be influenced by the walls of the crucible, because the theory of Princen is valid for infinite interface. Moreover the determination of bubble diameter might be overestimated by the curved surface of the glass bath, which acts like a loop for large bubbles.

Comparison of the ring on top of the bubble with theoretical work of Princen [15] shows, that

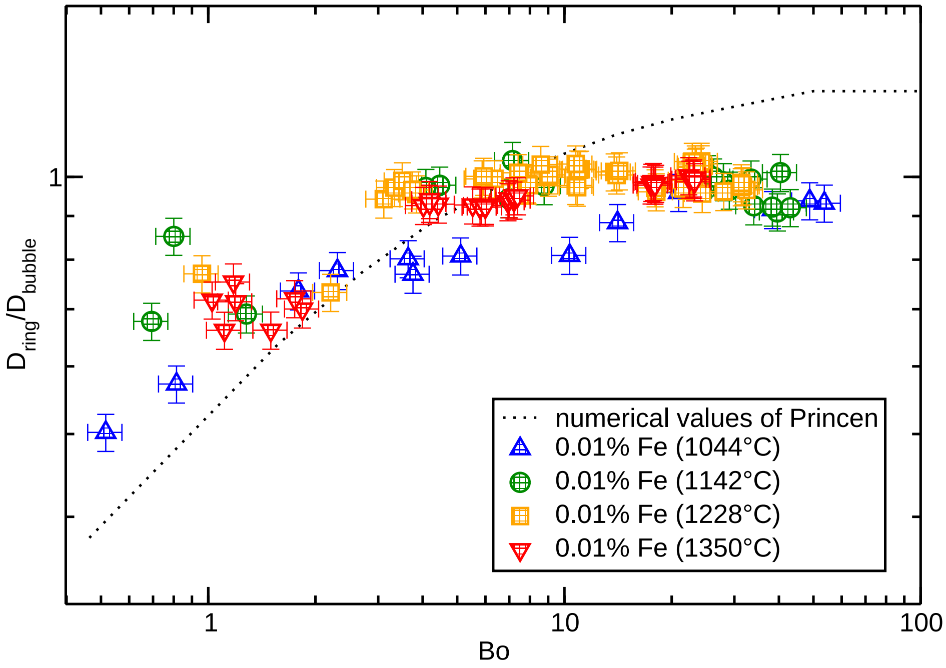

Figure 6.9: Comparison of experimental and theoretical size of ring normalized by the bubble diameter as a function of the Bond number.

when a bubble reaches the liquid interface, its shape is close to the quasi-static one. As a consequence, the ring size normalized by the bubble diameter (D$_{bubble}$), increases with Bond number, as well as, the surface of the cup (S_{cap}).

6.2 Evolution of thickness of a single bubble lamella

Evolution of thickness of a single bubble lamella in silicon oil and molten glass is studied in this work. Liquid drains out of the lamella according to the mobility of the interface (sec. 3.2.2).

6.2.1 Fully immobile interface

The velocity profile is parabolic for fully immobile interface due to no-slip velocity condition at the interface and the drainage is slower than for a fully mobile interface (Fig. 3.4) [21]. The evolution of thickness is algebraic:

$$h(t) \sim \frac{1}{\sqrt{t}} \tag{6.7}$$

6.2.2 Fully mobile interface

The drainage is faster when the interfaces are free of stress. The evolution of thickness is an exponential function of time [6]:

$$h(t) \sim \exp(-\alpha t) \tag{6.8}$$

Rupture of the thin film below h_c prevents an infinite draining time. Exponential decrease of thickness on top of a bubble with mobile interface has been recently confirmed by the numerical study of Pigeonneau and Sellier [14]. Moreover, they point out a slower drainage observed for larger Bond numbers as a consequence of larger deformed interfacial area discussed in sec. 6.1.2. The rupture of the bubble lamella in a finite time is observed for the limit situation when Bo=0, meaning that neither the free surface nor the bubble are deformed.

The characteristic time of drainage for a fully mobile interface can be obtained from the balance between gravity and viscous forces over a length scale (bubble size):

$$\mu \frac{U}{D_{bubble}} \approx \Delta\rho g D_{bubble}, \tag{6.9}$$

where U is the velocity of the liquid in the lamella, D_{bubble} is the bubble diameter and $\Delta\rho$ is the difference of density of the two phases. In the assumption of free shear at the interfaces, the flow in the film is a plug flow [9]. Consequently, the film thickness does not scale the motion and the bubble size is taken as a characteristic length. We obtain for velocity:

$$U = \frac{\Delta\rho g D_{bubble}^2}{\mu}, \tag{6.10}$$

and for time scale:

$$\tau = \frac{\mu}{\Delta\rho g D_{bubble}}. \tag{6.11}$$

Debrégeas *et al.* [6] made an experiment with a single bubble rising through silicon oil towards a liquid interface. An exponential decreasing is observed, which indicates a fully mobile interface. Debrégeas *et al.* propose a characteristic time, where the characteristic length is a size of the static bubble at the free surface, see Fig. 6.10 and eq. (6.12).

$$\tau_{Debr.} = \frac{\mu}{\rho g R_{cap}} \tag{6.12}$$

6.2.3 Silicon oil

A similar experimental set-up of Debrégeas *et al.* [6] is used in this work, however a different range of viscosities and bubble sizes is investigated. Six different bubble sizes are created in

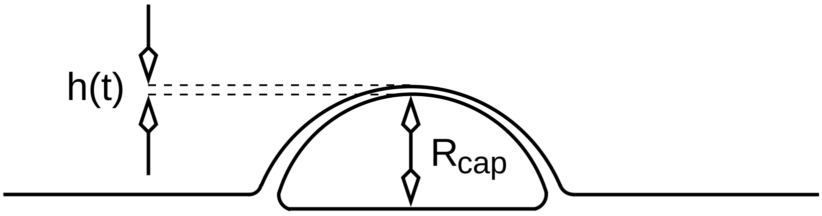

Figure 6.10: Characteristic length in the work of Debrégeas *et al.* [6]

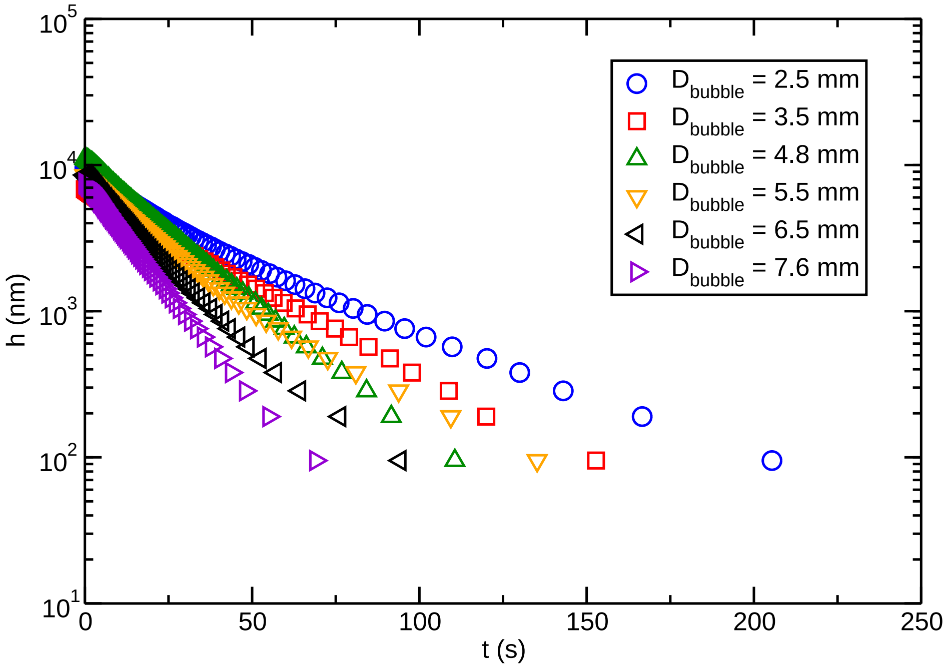

Figure 6.11: Evolution of thickness for various bubble size in silicon oil with viscosity 100 Pa·s.

five viscosities (10 to 100 Pa.s, see sec.5.1.1). The Bond number for this experiment is in the range between 2 and 26, corresponding to a bubble diameter from 2.5 to 7.5 mm. Example of evolution of thickness for various bubble size and viscosity 100 Pa·s is given in Fig. 6.11. Exponential behavior of thickness indicating fully mobile interface is also in agreement with the work of Debrégeas *et al.* [6]. Graph in Fig. 6.12 presents the same results, where thickness is normalized by the maximal determined thickness which corresponds to time zero in Fig. 6.11, and time is normalized by τ, given in (eq. 6.11). This representation allow to superimpose the data. Normalized evolution of thickness can be fit with an equation:

$$\frac{h}{h_{max}} = exp\left(-a\frac{t}{\tau}\right), \tag{6.13}$$

where a is defined as the “thinning rate”, which is in fact dimensionless:

$$a = \frac{\tau}{h}\frac{dh}{dt}. \tag{6.14}$$

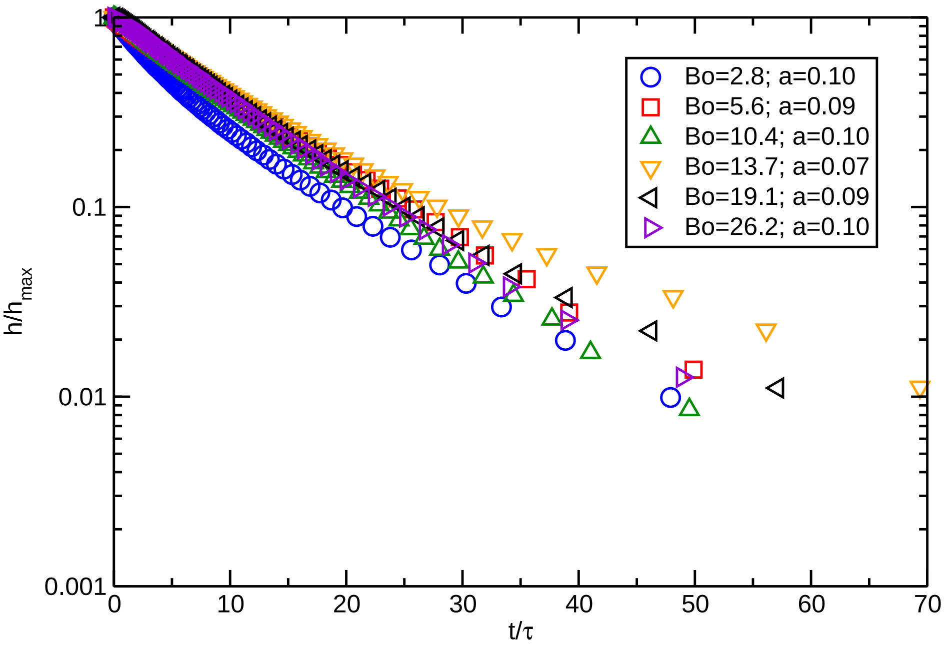

Figure 6.12: Normalized evolution of thickness for various bubble size in silicon oil with viscosity 100 Pa·s.

Same results are obtained for other four viscosities as well, see appendix G for more details. The value of a changes between 0.08 and 0.13 in our work and no evolution with the Bond number is observed. In order to compare the results to the work of Debrégeas *et al.* [6], we need to compute the value of the thinning rate obtained in their work. The evolution of thickness in their work is fit with an equation:

$$\frac{h}{h_{max}} = exp\left(-\frac{t}{\tau_{Debr.}}\right) \tag{6.15}$$

where $\tau_{Debr.}$ is given in eq. (6.12). Comparing to our fit in eq. (6.13), we obtain:

$$\frac{1}{\tau_{Debr.}} = a_{Debr.}\frac{1}{\tau}, \tag{6.16}$$

where $a_{Debr.}$ is the thinning rate, which needs to be compared with our results. Considering volume conservation of the bubble and assuming that D$_{bubble} \gg \kappa^{-1}$, the bubble is hemispherical and we assume for the bubble size:

$$R_{cap} = \frac{D_{bubble}}{2}\sqrt[3]{2}. \tag{6.17}$$

Using Fig. 6.13 and eq. (6.16) and (6.17) and considering that the viscosity in their work equals 10^3 Pa·s and density of silicon oil equals 970 kg·m^{-3} (sec. 5.1.1), we obtain, that $a_{Debr.}$ equals 0.11, which is in a good agreement with our results.

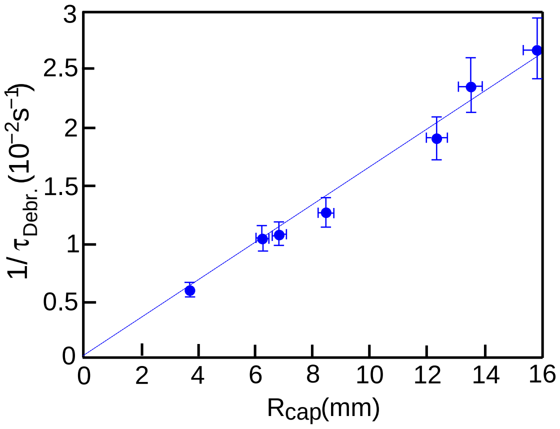

Figure 6.13: Reciprocal characteristic time as a function of a bubble size in the work of Debrégeas *et al.* [6].

6.2.4 Molten glass

Five glass compositions in a temperature range from 990 to 1228°C are investigated. An example of evolution of thickness in soda-lime-silica glass with a lower iron content for various bubble sizes is given in Fig. 6.14. Data are obtained at temperature T_E=1044°C when the glass viscosity is approximately 819 Pa·s. Results for other temperatures are given in appendix G. The film thickness decreases exponentially with time, which indicates a fully mobile interface. Normalized evolution of thickness (Fig. 6.15) is obtained using the same method as for silicon oil. Unlike in the experiment with silicon oil, the thinning rate a changes with the Bond number. Graph in Fig. 6.16 gives the evolution of the thinning rate a as a function of the Bond number for soda-lime-silica glass with a lower content of iron for three experimental temperatures in a comparison with the numerical simulation of Pigeonneau and Sellier [14]. The error of the thinning rate is a sum of error obtained from the fitting of the evolution of thickness (Fig. 6.15 and eq. (5.8)), error of the bubble size and uncertainty caused by determination of glass density and viscosity. The uncertainty of viscosity determination is more important at low temperature, while the uncertainty caused by the fitting of the experimental data is more significant at high temperature where less points of the evolution of thickness are measured (Fig. G.12, G.18 or G.22).

The value of the thinning rate increases as the Bond number decreases for all temperatures. Nevertheless, for higher temperature (1228°C), the absolute values of the thinning rate a are higher than for lower temperature (1044°C). For the moment this disagreement is not understood and possible explanations will be discussed in the following chapter. Fig. 6.17 summarizes the results of the thinning rate as a function of the Bond number for soda-lime-silica glass with 0.1 wt% of Fe_2O_3. For this glass composition, as well as for soda-lime-silica glass with lower content of iron, faster drainage appears for smaller Bond numbers and dif-

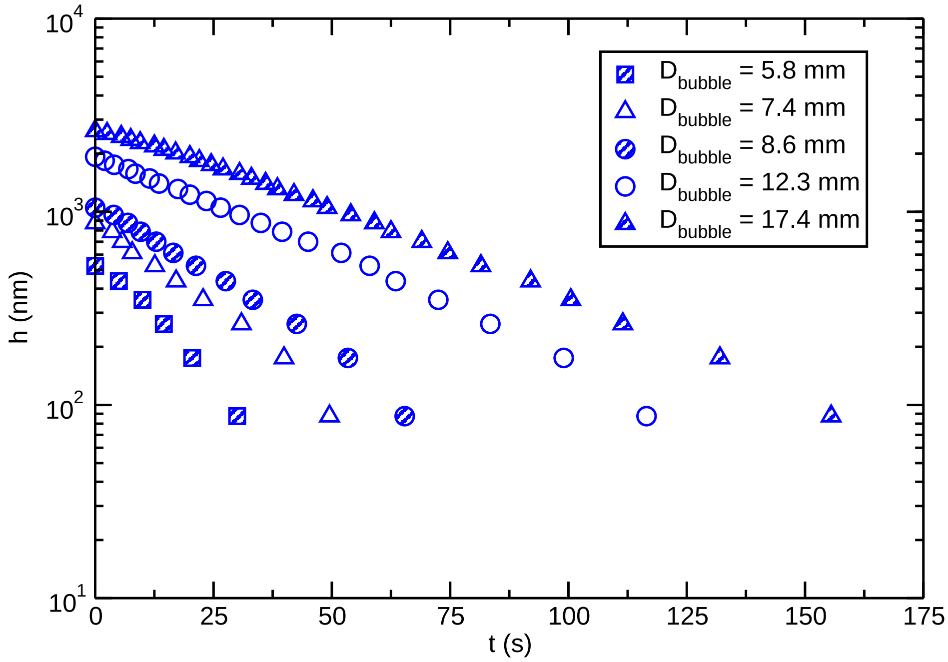

Figure 6.14: Evolution of thickness for various bubble size in soda-lime-silica glass with 0.01 wt% of Fe_2O_3 and temperature 1044°C.

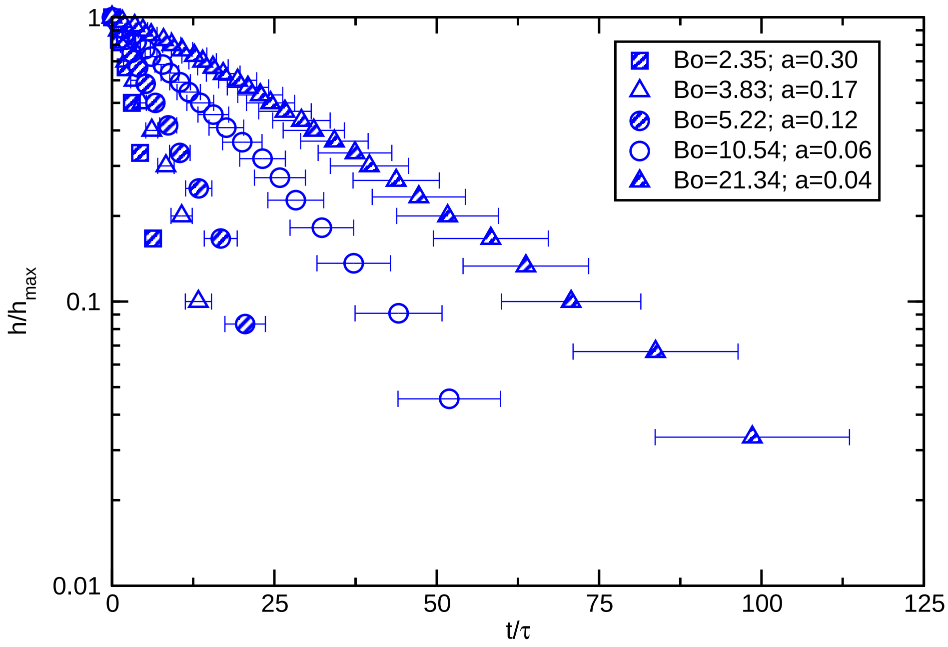

Figure 6.15: Normalized evolution of thickness for various bubble size in soda-lime-silica glass with 0.01 wt% of Fe_2O_3 and temperature 1044°C.

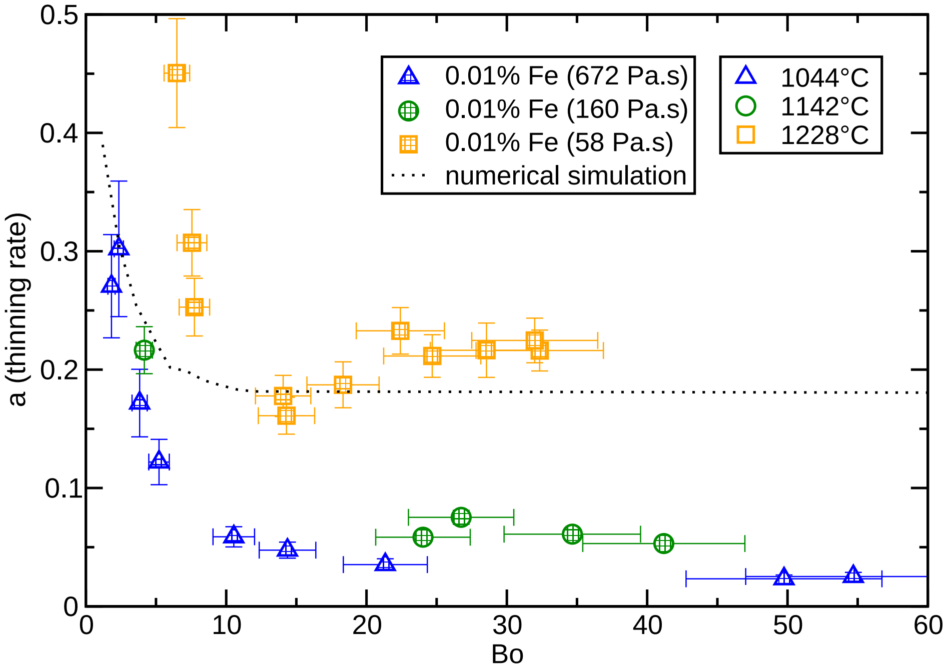

Figure 6.16: Thinning rate a as a function of the Bond number for glass with 0.01 wt% of Fe_2O_3.

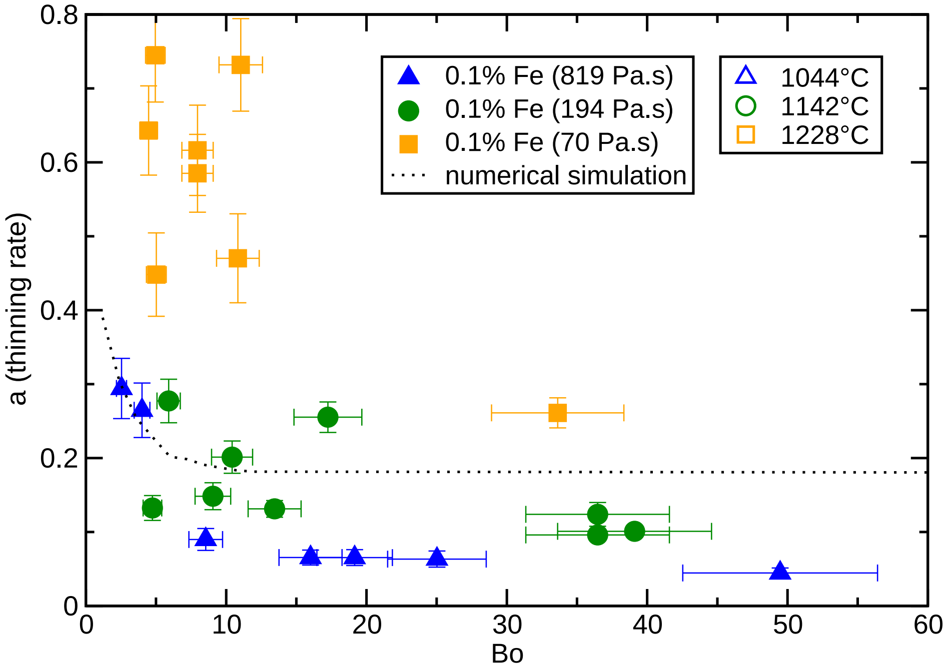

Figure 6.17: Thinning rate a as a function of the Bond number for glass with 0.1 wt% of Fe_2O_3.

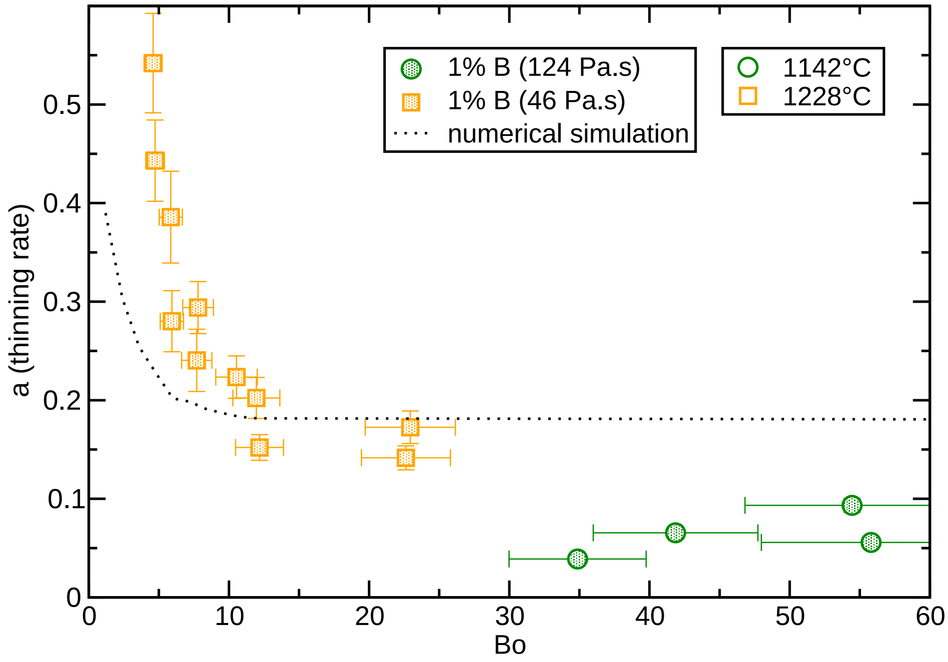

Figure 6.18: Thinning rate a as a function of the Bond number for glass with 1 wt% of B_2O_3.

ferent absolute value of the thinning rate at high and low temperature is observed.

Graph in Fig. 6.18 summarize data obtained for soda-lime-silica glass with 1 wt% of B_2O_3. Only large bubbles were created at T_E=1142°C, because, at this temperature, it is extremely difficult to control the device for bubble creation in order to obtain a bubble with a small diameter. Either the bubble is too large and detaches very fast from the bottom of the crucible or the amount of air blowing into the tube is not sufficiently large and the bubble disappears completely back into the Pt-Rh tube during the "shrinkage" period (Fig. 6.2). It is reasonable to think, that the absolute values of the thinning rate are in reality slightly higher than in the graph in Fig. 6.18. As discussed in previous chapter, glass density is a function of temperature (sec. 5.2.8). However, density determined at room temperature (T_{room}) is used in the computation of τ for this glass composition. It is possible to compute the correct value of the thinning rate considering temperature dependence of density and eq. (6.11) and (6.13). The new thinning rate a_{new} is expressed as a ratio of the density at room and experimental temperature:

$$a_{new} = a_{old} \frac{\rho_{T_{room}}}{\rho_{T_E}} \tag{6.18}$$

The ρ_{T_E} will be smaller compared to the density at room temperature and therefore the new thinning rate will be higher than a_{old}. ρ_{T_E} can be computed using eq. (5.15) and $\rho_{T_{room}}$ given in Tab. 5.12. The new thinning rate will be 1.056 and 1.065 times higher for temperatures 1142 and 1228°C, respectively.

Not many small bubbles were created during the experiment with 10 wt% of B_2O_3 (Fig.

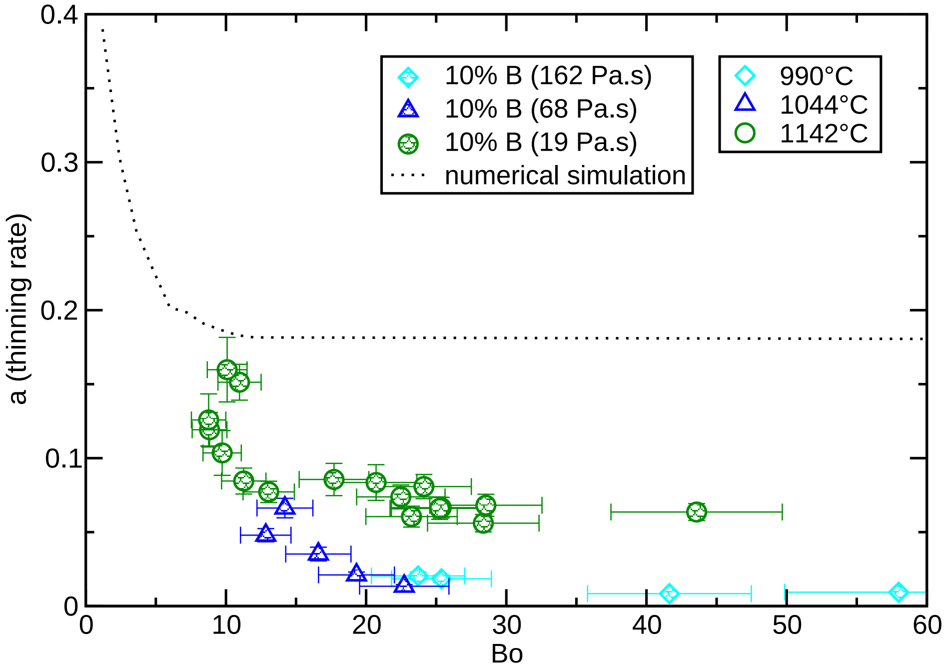

Figure 6.19: Thinning rate a as a function of the Bond number for glass with 10 wt% of B_2O_3.

6.19). Nevertheless, as well as for all other tested glass compositions, the values of the thinning rate start to rise around Bo=10. Unlike results presented above, the absolute value of the thinning rate a is smaller for the glass with 10 wt% of B_2O_3. This can be explained by an incorrect value of density and viscosity. The density for a room temperature is used while obtaining the results and therefore all values of the thinning rate should have higher values as it was presented above for the glass with 1 wt% of B_2O_3. The variation of density with temperature is not determined experimentally and no model computing density at various temperatures is valid for this high content of boron, therefore the shift of the data is not determined for this glass composition. Slower drainage can appear as a consequence of higher viscosity caused by boron evaporation. We can assume from the graph, that the value of the thinning rate is approximately two or three times smaller compared to the numerical simulation. In order to obtain the correct value, the viscosity of the glass would have to be two or three times higher. Tab. 6.1 summarizes values of viscosity for glass with various boron content. Viscosity of the glass with 10 wt% of boron is measured experimentally, two and three times higher viscosity correspond to the viscosity which is necessary in order to obtain a value of the thinning rate which is in the agreement with the numerical simulation and viscosity of glass with 1 and 5 wt% of boron is predicted by a model (sec. 5.2.8). It is obvious, that the content of boron needs to be between 10 and 5 wt%, because the viscosity for 5 wt% of boron is lower than for 1 wt%, but not low enough to correspond to the two or three times higher original viscosity. Since the model is valid only for boron content below

glass	μ **(Pa·s)** **at 1000°C**	μ **(Pa·s)** **at 1100°C**	μ **(Pa·s)** **at 1200°C**
10 wt% B_2O_3 original	137.1	31.8	10.6
10 wt% B_2O_3 two times higher	274.2	63.5	21.3
10 wt% B_2O_3 three times higher	411.3	95.3	31.9
1 wt% B_2O_3 computed	1100.3	203.0	59.6
5 wt% B_2O_3 computed	658.0	126.1	39.8

Table 6.1: Measured viscosity for soda-lime-silica glass with 10 wt% of B_2O_3, expected viscosity for glass with 10 wt% of boron to obtain higher absolut value of thinning rate and computed viscosity for glass with 1 and 5 wt% of boron using model described in sec. 5.2.8.

5 wt%, it is impossible to predict exactly the amount of boron which needs to be lost due to evaporation to explain the slower drainage. Experimental measurement of several glasses with various boron content would be necessary. One last explanation for the observation of slower drainage can be related to the fact, that for this glass composition, the experiment is performed at low temperatures only, compared the other glass compositions, where the experiment was performed at temperature 1228°C. As mentioned in the previous text, for all glass compositions, the values of the thinning rate have lower absolut values at lower temperatures compared to results collected at the temperature 1228°. The evolution of thickness is determined at only one temperature for highly viscous AKM glass, see Fig. 6.20. As well as for all other glass compositions, faster drainage appears for smaller bubbles (lower Bond number).

Slower drainage is observed at lower temperature during the experiment with molten glass. For the moment, the different behavior at low and high temperature is not understood. The absolute value of the thinning rate is influenced by the glass properties: density and viscosity. These values are determined experimentally or they are computed using models. They depend on temperature (glass viscosity strongly changes at low temperature). The whole experiment is very complex and even though high attention was paid to the determination of temperature field and glass properties, it is possible, that the disagreement is caused by some experimental artifacts.

Slower drainage is observed during the experiment with glass with 10 wt% of B_2O_3. Glass with a content of boron is known to cause problem with foaming during melting. It can be found in the literature, that boron behaves like surface-active solution and shows slower drainage due to partial mobility of the interface. In the contrary, exponential evolution of thickness in our experiment confirms a completely mobile interface. Therefore the slower drainage is not caused by surface-active behavior of boron, but due to lower absolute values

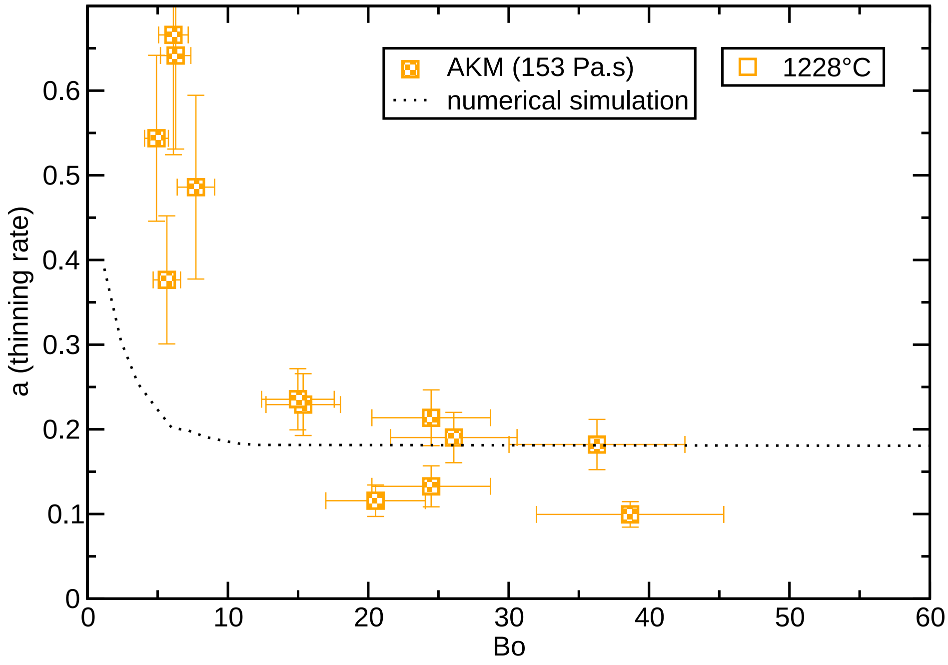

Figure 6.20: Thinning rate a as a function of the Bond number for highly viscous AKM glass.

of the thinning rate, which can be explained by evaporation of boron and change in viscosity.

6.2.5 Extensional flow model

The film thinning appears as a consequence of the buoyancy force expressed by pressure which is imposed by rising bubble and by the top interface which resists against the deformation once it has reached a stationary shape. Capillary force acts on the interface and causes squeezing of the film. This can be approximated by a squeeze between two discs with area:

$$S_{cap} = 2\pi R_{cap} h_{cap}, \tag{6.19}$$

where R_{cap} and S_{cap} are given in Fig. 6.7. Than assuming the interfaces are fully mobile, the flow is performed through the lubricated squeezing experiment and its tensile stress [13] can be written as follows:

$$\sigma_T = 6\mu \frac{d\epsilon}{dt}, \tag{6.20}$$

where $d\epsilon/dt$ is the extensional rate of strain. According to [11]:

$$\frac{d\epsilon}{dt} = -\frac{1}{2h}\frac{dh}{dt}. \tag{6.21}$$

The stress is opposed to the pressure imposed by the buoyancy force of the bubble that applies on the cap area:

$$3\mu \frac{1}{h}\frac{dh}{dt} = -\frac{\Delta\rho g \frac{4}{3}\pi R^3}{S_{cap}}. \tag{6.22}$$

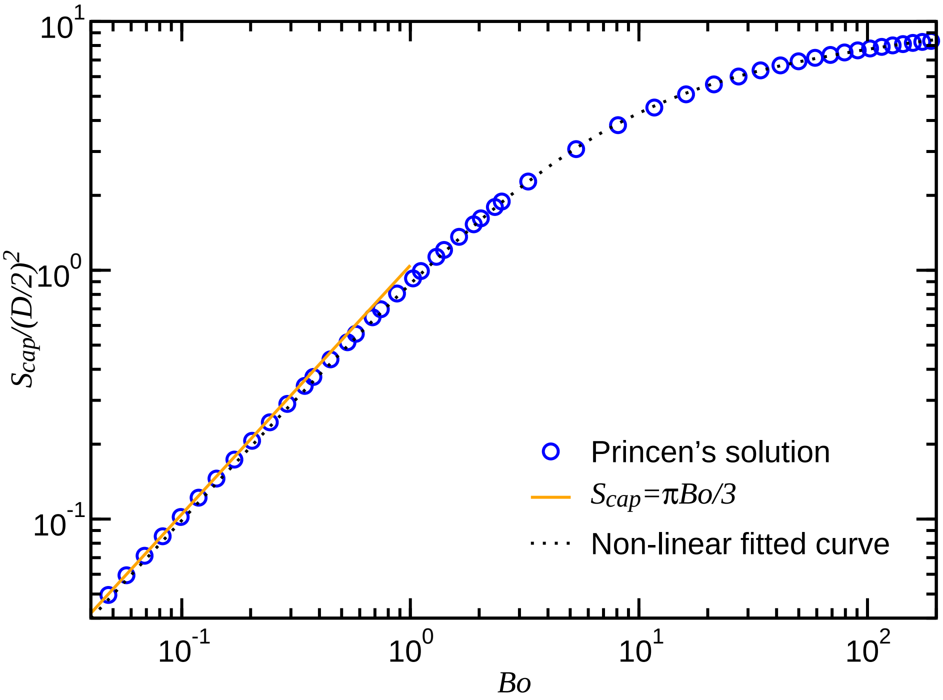

Figure 6.21: $S_{cap}/(D/2)^2$ versus Bo: circle points are determined according to the Princen's model [15] and dashed line is the fit corresponding to equation 6.24. The solid line is the asymptotic behavior at small Bond number according to Howell's model [9].

From this we can obtain the thinning rate as a function of bubble size and S_{cap}:

$$a_{efm} \approx \frac{2\pi}{9}\frac{(D_{bubble}/2)^2}{S_{cap}}. \tag{6.23}$$

It is possible to obtain a variation of the deformed interface area as a function of the Bond number from the work of Princen [15], see Fig. 6.21. Using a non-linear fitting with a rational function we obtain:

$$\frac{S_{\text{cap}}}{(D_{bubble}/2)^2} = 2^{5/3}\pi\frac{94.7\,Bo + Bo^2}{901.96 + 142.46\,Bo + Bo^2}, \tag{6.24}$$

From eq. (6.23) and (6.24) we obtain a final formula for thinning rate a_{efm} as a function of Bond number:

$$a_{efm} = \frac{1}{9 \cdot 2^{2/3}} \cdot \frac{902 + 142Bo + Bo^2}{95Bo + Bo^2} \tag{6.25}$$

Howell [9] studied the bubble shape when the Bond number is small. Using the asymptotic solution given in [9], the area of the spherical cap divided by the radius squared is given by

$$\frac{S_{\text{cap}}}{(D_{bubble}/2)^2} = \frac{\pi}{3}Bo + \mathcal{O}(Bo^2). \tag{6.26}$$

Conversely, at large Bond number observed for a bubble size larger than the capillary length, the free surface is strongly deformed and the shape of bubble as well. In the limit of very

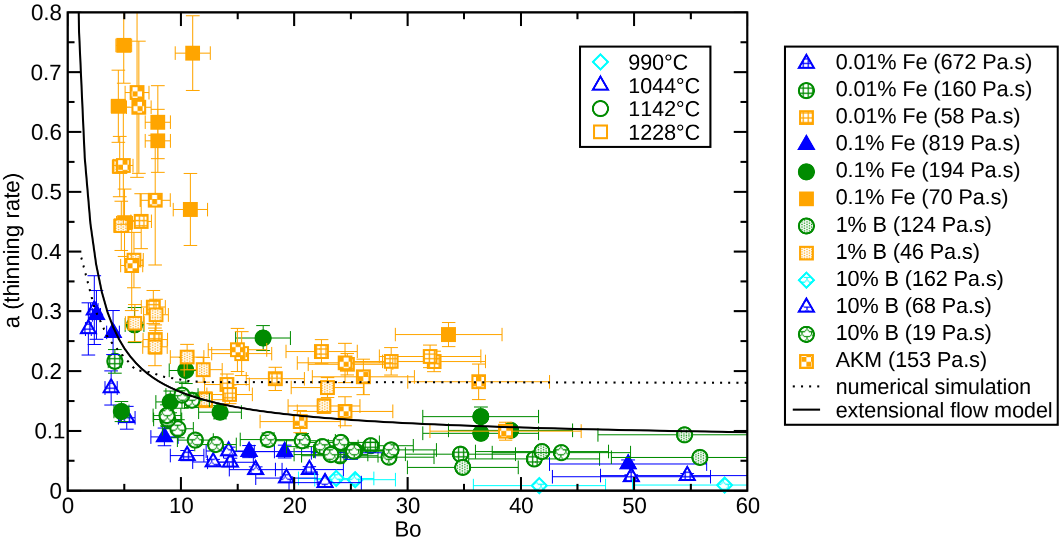

Figure 6.22: Thinning rate as a function of the Bond number - comparison of experimental data with numerical simulation (dotted line) and extensional flow model (continuous line).

high Bond number, the bubble at the free surface is just a hemispherical cap leading to the following bound

$$\lim_{Bo\to\infty} \frac{S_{\mathrm{cap}}}{(D_{bubble}/2)^2} = 2^{5/3}\pi \approx 9.974. \tag{6.27}$$

Both limits are given in Fig. 6.21 The eq. 6.25 is in a good agreement with all presented experimental results and the numerical simulation, see Fig. 6.22. It is obvious from the experimental data in Fig. 6.22 that the thinning rate of the film is not scaling with the characteristic time obtained from the balance by gravity and viscosity at the scale of bubble diameter, given in eq. (6.11). For this scaling, the thinning rate is higher for small Bo, which does not correspond with the experimental observation. It is necessary to use S_{cap} for scaling, because it corresponds to the deformed area and increases with the rising Bond number. The model of extensional flow shows, that the experimental results can be explained by a theory of squeezed elongation flow of the liquid within the cap.

6.2.6 Model liquids for molten glass

Similar experiment with the determination of the evolution of thickness was made by Metallaoui [12] for three liquids: Castor oil, UCON and polymer [1]. Graph in Fig. 6.23 shows the thinning rate a as a function of the Bond number for all three liquids in the comparison with the data obtained for silicon oil (6.2.3), the numerical simulation by Pigeonneau and Sellier [14] and extensional flow model (EFM). Unlike for molten glass, results for silicon oil are not in an agreement with the numerical simulation and the EFM. The value of the thinning rate

---

[1] Poly(ethylene glycol-ran-propylene glycol) monobutyl ether: $CH_3(CH_2)_3(OCH_2CH_2)_x[OCH_2CH(CH_3)]_yOH$

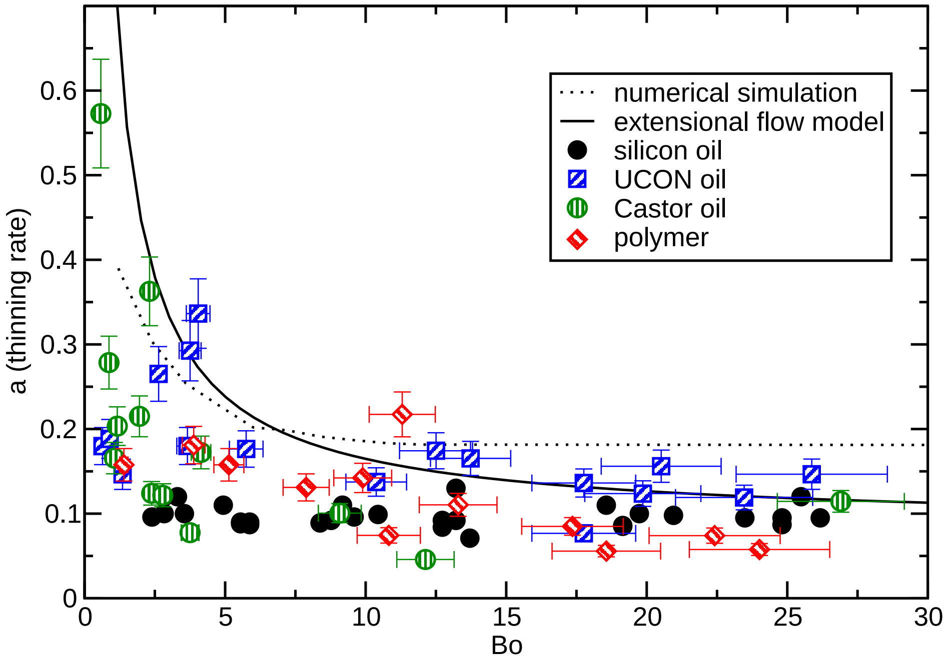

Figure 6.23: Thinning rate a as a function of the Bond number for various liquids.

is insensitive to the Bond number, but remains approximately constant. Kumar *et al.* [11] observed an influence of micelles at a thickness lower than 100 μm, while studying drainage of vertical and curved film. Below this thickness, sizes of molecules play a role and decelerate the drainage. This theory could explain the results observed for silicon oil, where for the smallest bubble size in viscosity 100 Pa·s, we can determine two slopes, see Fig. 6.24. First slope is determined when the thickness of the lamella is larger than 10^3 nm. Above this thickness, drainage is faster than at smaller thickness. One can suspect that the size of the macromolecules of high number of monomers (high viscosity) can influence the drainage of the liquid for small thickness of the film. To confirm the theory, we should observe smaller or no decrease in the drainage for the lowest viscosity, where the number of monomers of molecules is lower. Unfortunately it is not possible to determine the slope at high thickness for the lowest viscosity, because the thickest bubble lamella determined at this viscosity is slightly above 10^3 nm (Fig. G.1) and it is difficult to predict if above this thickness we can observe faster drainage. In the comparison, higher value of a for smaller Bond number is observed for the other three liquids. Especially results for Castor and UCON oils are in a good agreement with the numerical simulation, EFM and experimental results of molten glass. Therefore using these two liquids as model liquids for molten glass is advisable.

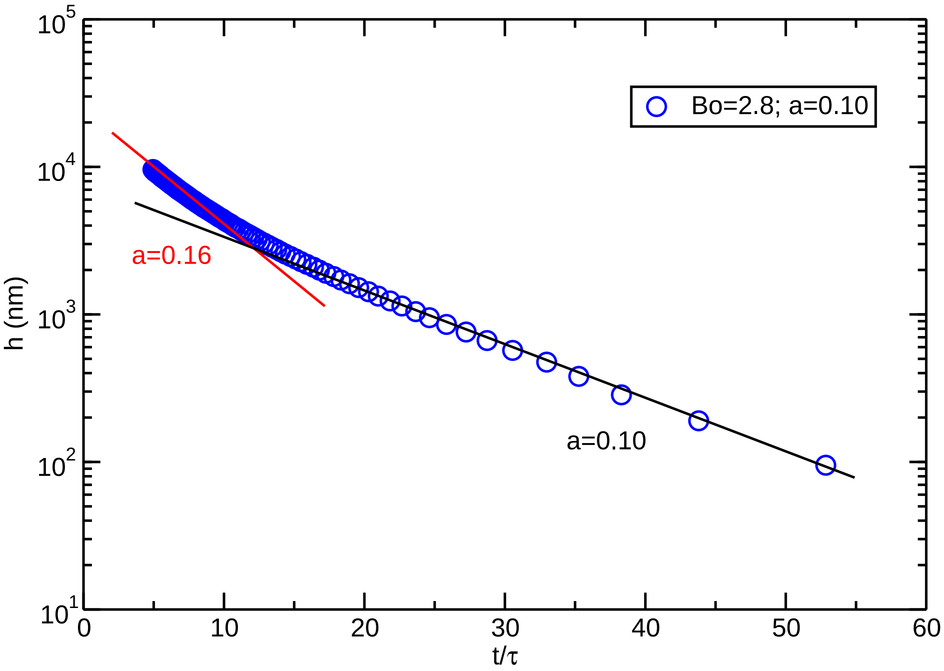

Figure 6.24: Two thinning rates for thicker and thinner lemella in silicon oil with viscosity 100 Pa·s.

6.3 Critical thickness - Regular and Irregular drainage

As mentioned in the previous text, it is not possible to measure precisely the thickness of the bubble lamella at the moment of the rupture (h_c). We only observe the lowest determined thickness (Tab. 5.20). Nevertheless, we can determine the time of the rupture of the bubble lamella (reslice image in Fig. 6.2) and using graph in Fig. 6.14 and expecting the evolution of thickness continues after the last determined thickness, we can estimate the critical thickness.

The value of the critical thickness remains approximately between 1 and 20 nm for temperatures 1044 and 1142°C, but this interval exceeds significantly at temperature 1228°C. The highest values of h_c are around 10 nm at this temperature, but the lowest values are below 1 Å for soda-lime-silica glass with 0.01 wt% of Fe_2O_3, see Fig. 6.25. A chaotic motion is observed in the bubble lamella at this temperature and therefore it is necessary to divide the bubble lifetime into two steps. During the first step, drainage in the bubble lamella is observed, which is indicated by interference fringes moving from the middle of the bubble lamella to the side. During the second step, thickness can no longer be determined experimentally, but it is observed, that the interference fringes start moving backwards, which indicates that the liquid is draining back to the lamella and the thickness is increasing. This backward flow is followed by a chaotic motion during which interference fringes move in various directions. While the duration of the first step is approximately the same for all created

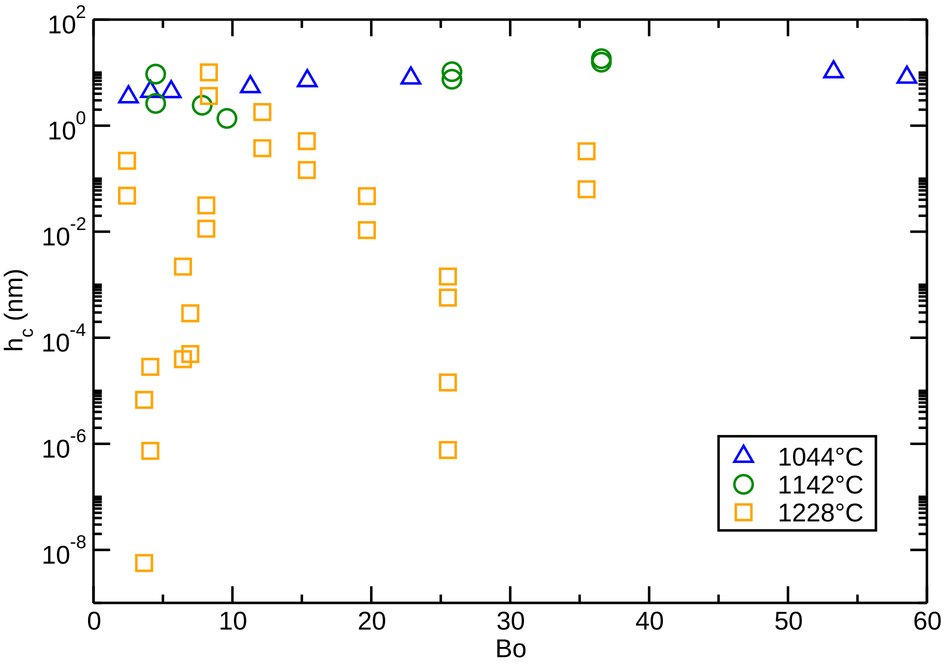

Figure 6.25: Theoretical critical thickness of bubble lamella at the moment of the rupture.

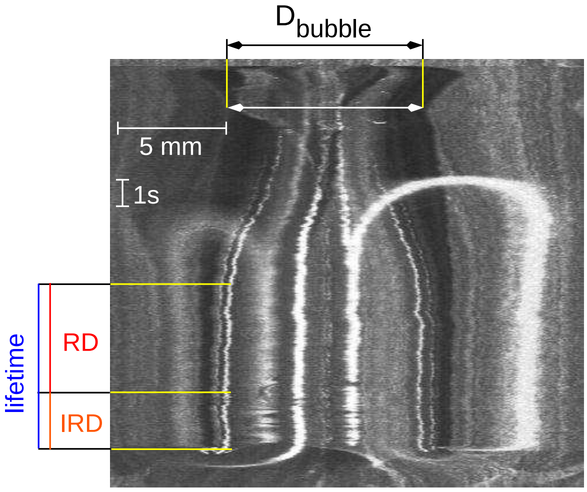

Figure 6.26: Example of the reslice image, where lifetime is divided into two steps - regular and irregular drainage.

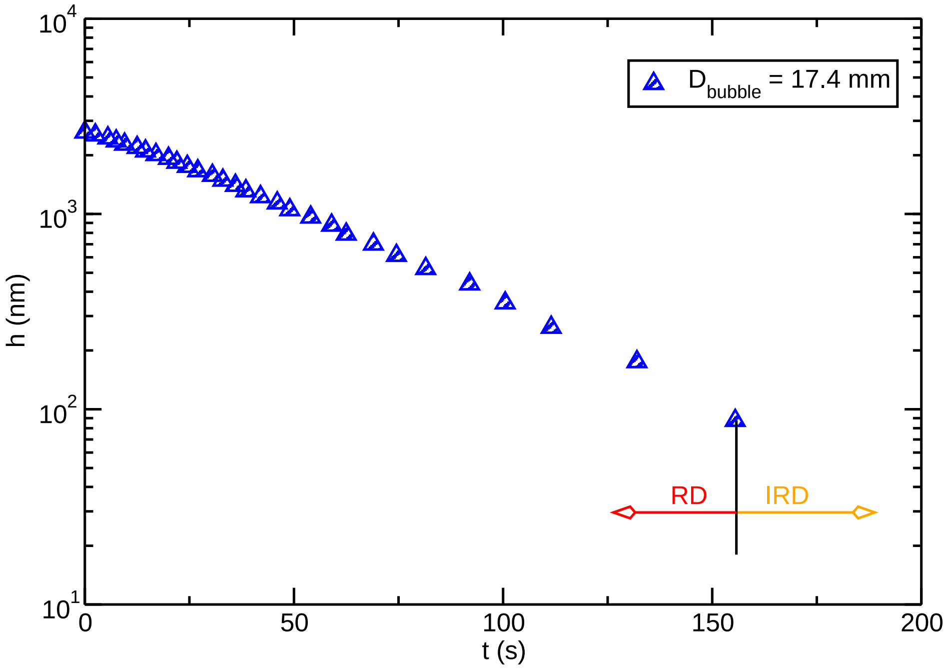

Figure 6.27: Example of evolution of thickness of the bubble lamella, where lifetime is divided into two steps - regular and irregular drainage.

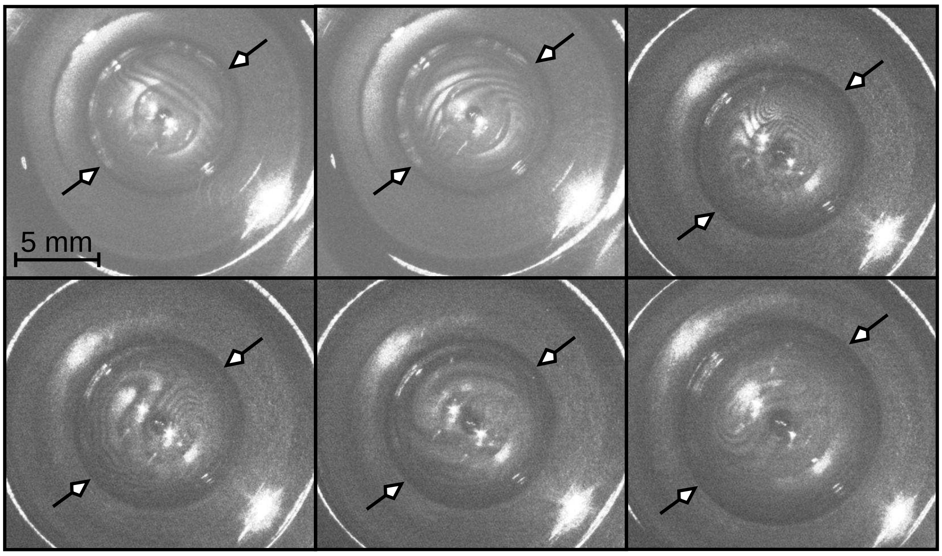

Figure 6.28: Examples of chaotic motion in the bubble lamella for soda-lime-silica glass with 0.1 wt% of Fe_2O_3 (first two images) and with 1 wt% of B_2O_3 (remaining images) at 1350°C. The white arrows indicate the edge of the bubble at the surface.

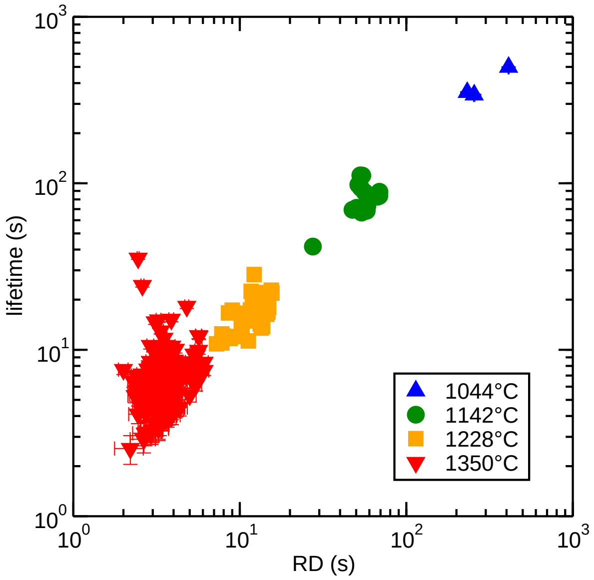

Figure 6.29: Lifetime of nitrogen bubbles for glass with 0.1 wt% of Fe_2O_3 as a function of RD.

bubbles, the duration of the second step is completely random. In the following text, the first step of the bubble lifetime is called regular drainage and the second step is called irregular drainage. The time of the last determined thickness is considered as the beginning of the second step, see Fig. 6.26 and 6.27. From now on, RD denotes the duration of regular drainage and IRD the one of irregular drainage. Images in Fig. 6.28 show examples of the chaotic motion of interference fringes in the bubble lamella for two glass compositions.

6.4 Bubble lifetime

6.4.1 Correlation of lifetime with drainage

For every created bubble, its lifetime is determined from the reslice image (Fig. 6.2). Graph in Fig. 6.29 shows the bubble lifetime as a function of RD for soda-lime-silica glass with 0.1 wt% of Fe_2O_3. This graph contains data for temperature 1350°C eventhough the evolution of thickness of the bubble lamella for this temperature was not discussed in the previous section. At this high temperature, the viscosity of the glass is below 20 Pa·s and the drainage is very fast. With our maximal recording speed, it is not possible to obtain enough points to determine the evolution of thickness and the value of the thinning rate, however, it is possible to divide the lifetime into the two steps (RD and IRD) and observe motion during the second step. For temperatures 1044 and 1142°C, the lifetime changes linearly with RD, but at higher temperatures, the lifetime is for some bubbles significantly longer than RD and at the temperature 1350°C, the lifetime of several bubbles is even longer than the lifetime of bubbles

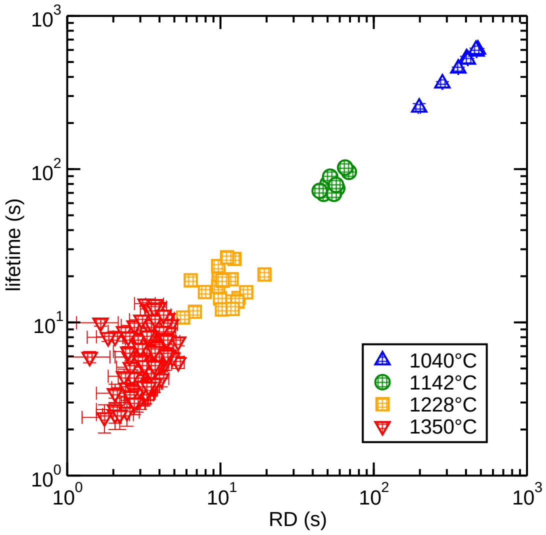

Figure 6.30: Lifetime of nitrogen bubbles for glass with 0.01 wt% of Fe_2O_3 as a function of RD.

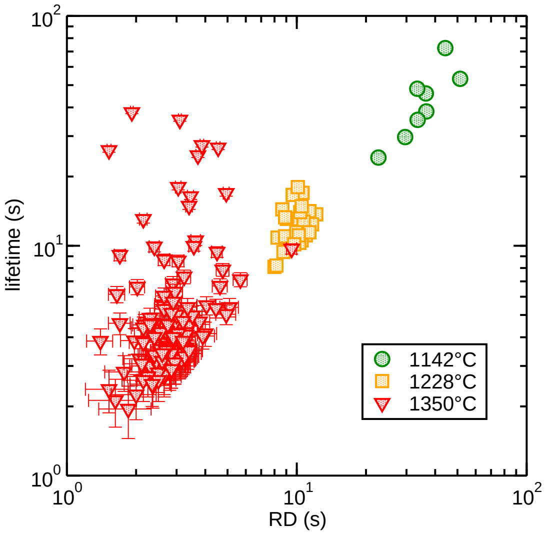

Figure 6.31: Lifetime of nitrogen bubbles for glass with 1 wt% of B_2O_3 as a function of RD.

created at lower temperature. The longer lifetime is caused by a longer IRD for temperatures above 1200°C. Similar behavior was observed for soda-lime-silica glass with lower content of iron, see Fig. 6.30. For glass with 1 wt% of boron (Fig. 6.31), linear evolution of the bubble lifetime with RD is disrupted even at temperature 1142°C. This temperature is the first one, where we observe the motion. Why do we observed the motion at lower temperature for this glass composition compared to soda-lime-silica glass without boron will be discussed in sec. 6.5. During the experiment with glass with 10 wt% of B_2O_3, the motion is observed at 1142°C and it is obvious from the graph in Fig. 6.32 that once the motion appears, longer lasting bubbles appear. For highly viscous AKM glass, the lowest experimental temperature was 1228°C, where the motion is already observed and therefore, the linear evolution of lifetime as a function of RD is disturbed for all tested temperatures, see Fig. 6.33. It is very important to emphasize, that the lifetime of some bubbles at temperature 1414°C is longer than the lifetime of bubbles created at 1350°C and even at 1228°C. This observation confirms, that bubble lifetime is not only function of viscosity, but temperature as well. The importance of the second step of the bubble lifetime is obvious from the graph in Fig. 6.34 where the IRD is normalized by the total bubble lifetime and expressed in % as a function of rising experimental temperature. The higher the temperature, the more important IRD is. At 1044°C IRD creates only 20 % of the total lifetime, but at 1350°C, it can create up to 90 %. However, it can be very short as well in case the bubble ruptures as soon as it reaches the last determined thickness and no motion is observed. When the motion appears, strong perturbation is necessary to cause a rupture of the bubble lamella. In order to predict the bubble

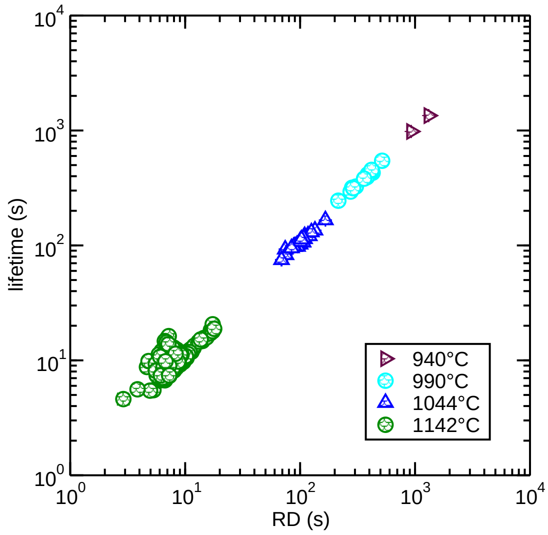

Figure 6.32: Lifetime of nitrogen bubbles for glass with 10 wt% of B_2O_3 as a function of RD.

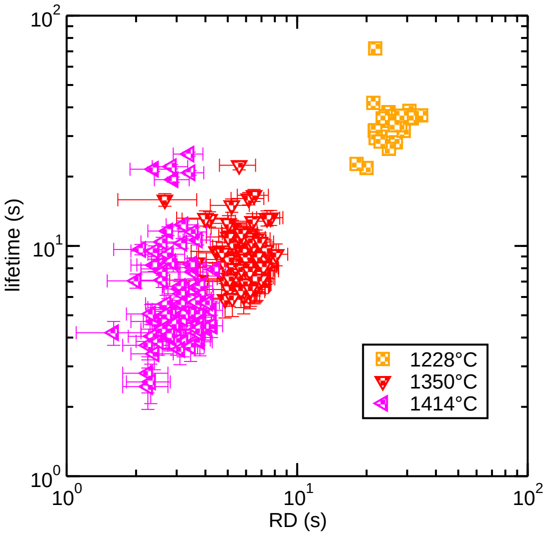

Figure 6.33: Lifetime of nitrogen bubbles for highly viscous AKM glass as a function of RD.

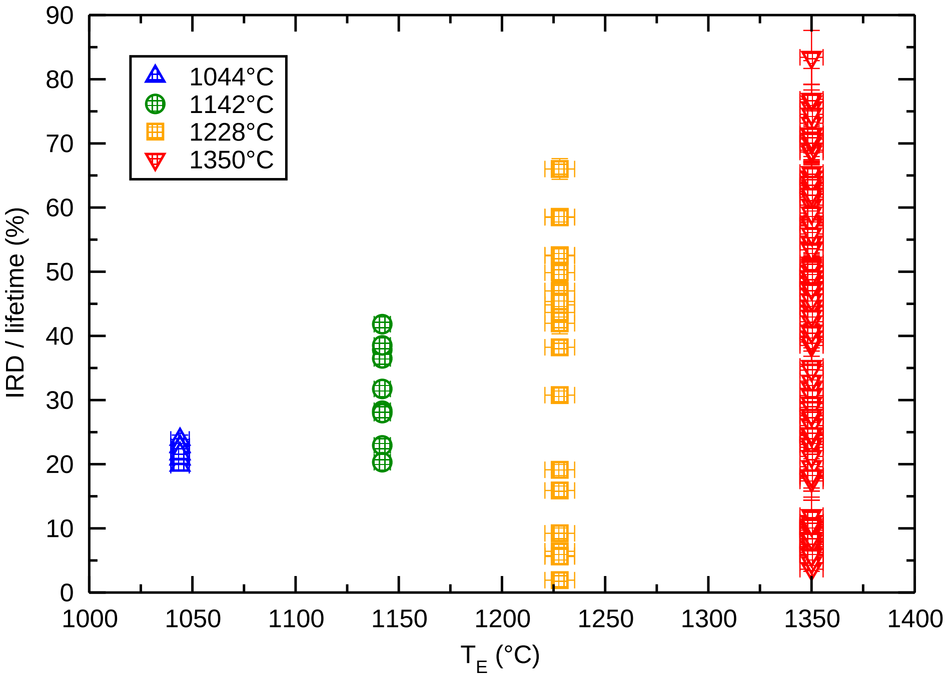

Figure 6.34: Importance of IRD of nitrogen bubbles for glass with 0.01 wt% of Fe_2O_3 as a function of T_E.

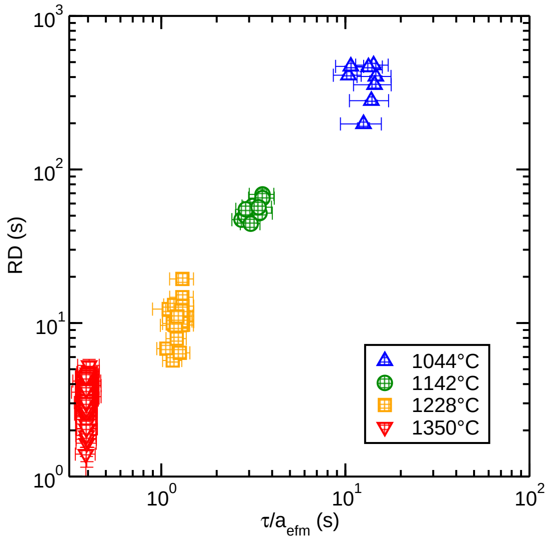

Figure 6.35: RD of nitrogen bubbles for glass with 0.01 wt% of Fe_2O_3 as a function of τ/a_{efm}.

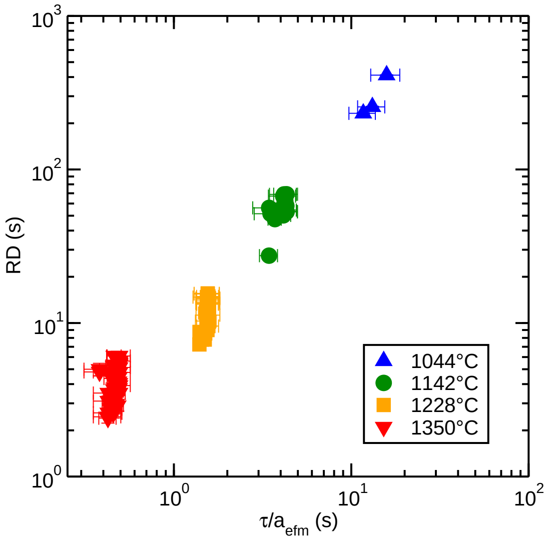

Figure 6.36: RD of nitrogen bubbles for glass with 0.1 wt% of Fe_2O_3 as a function of τ/a_{efm}.

lifetime, it is necessary to predict RD. To eliminate the influence of viscosity and bubble size, RD is plotted as a function of the characteristic time τ (eq. (6.11))normalized by the thinning rate a_{efm} (eq. (6.25)), see Fig. 6.35 - 6.39 for all tested glass compositions. As it has been mentioned in the previous section (6.2.4), the value of the thinning rate decreases with rising Bond number, which is respected by the EFM model, nevertheless, the absolute value of the thinning rate is changing for various temperatures or compositions. If we plot RD for all glass compositions in the same graph (Fig. 6.40), we see that glass with 10 wt% of boron has longer RD compared to the other glass compositions. This appears as a consequence of lower absolute experimental values of the thinning rate a, which were discussed in sec. 6.2.4. Similar graphs can be created for the evolution of IRD and total bubble lifetime as well, see graphs in appendix H. Graph in Fig. 6.41 shows lifetime of all bubbles for all tested glass compositions and temperatures as a function of characteristic time (eq. (6.11)) normalized by the thinning rate obtained from extensional flow model (6.25). If we assume that glass with 10% of boron behaves differently compared to other tested glass compositions, it is possible to propose an empirical fit of the rest of our experimental data and predict the bubble lifetime as follows:

$$lifetime = 28 \cdot \frac{\tau}{a_{efm}} \tag{6.28}$$

By a combination of eq. (6.28) and eq. (6.25) we obtain a formula, where the bubble lifetime is a function of characteristic time (6.11) and Bond number (6.5), which enables us to predict

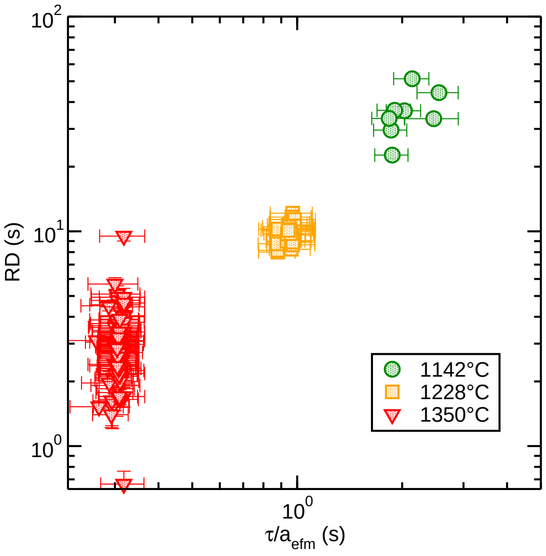

Figure 6.37: RD of nitrogen bubbles for glass with 1 wt% of B_2O_3 as a function of τ/a_{efm}.

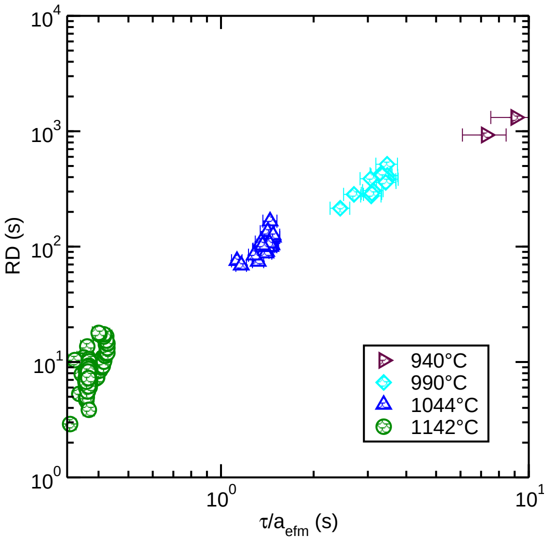

Figure 6.38: RD of nitrogen bubbles for glass with 10 wt% of B_2O_3 as a function of τ/a_{efm}.

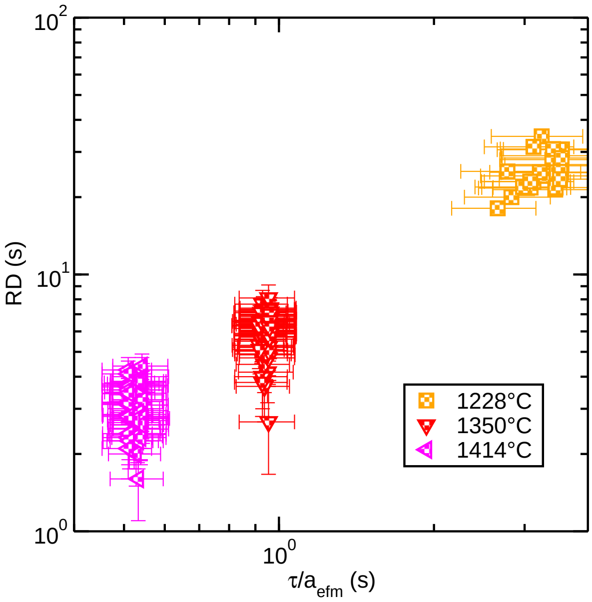

Figure 6.39: RD of nitrogen bubbles for highly viscous AKM glass as a function of τ/a_{efm}.

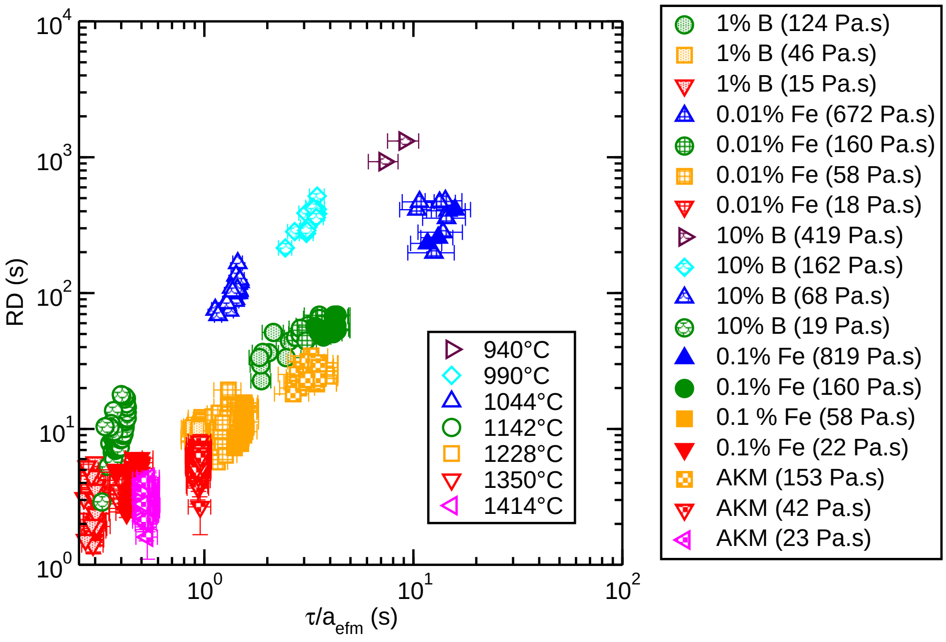

Figure 6.40: RD of nitrogen bubbles for all tested glass compositions as a function of τ/a_{efm}.

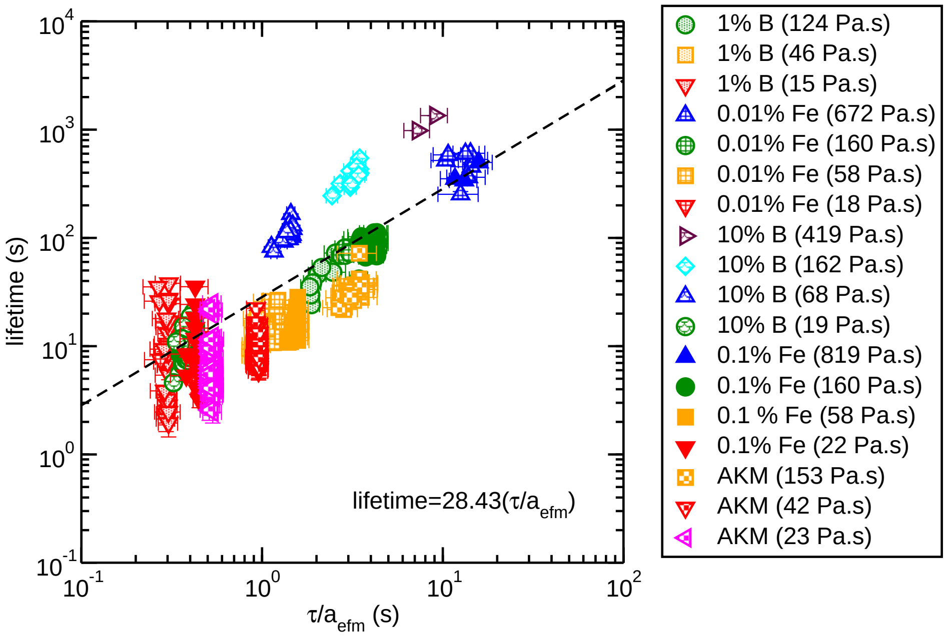

Figure 6.41: Lifetime of nitrogen bubbles for all tested glass compositions as a function of τ/a_{efm}.

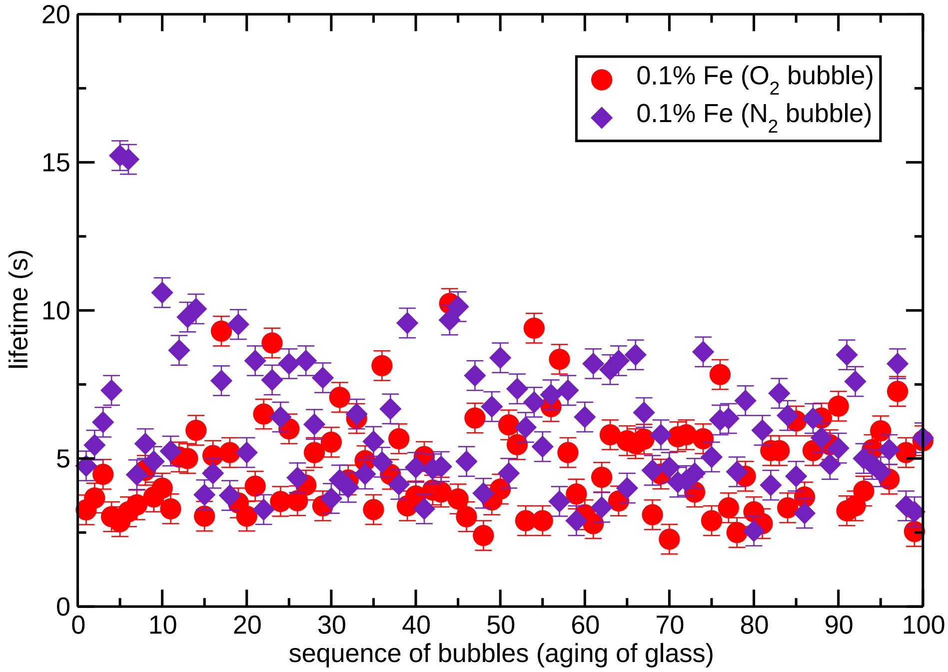

Figure 6.42: Lifetime of sequence of 100 bubbles for glass with 0.1 wt% of Fe_2O_3 and various bubble gas.

the bubble lifetime knowing only the physical properties of glass and the bubble size:

$$lifetime = \tau \cdot 406 \cdot \frac{95Bo + Bo^2}{902 + 142Bo + Bo^2} \tag{6.29}$$

This prediction is very reliable at low temperature, where no motion is observed and bubble ruptures fast after reaching the last determined thickness. The prediction is less precise at high temperatures (above 1200°C for ordinary soda-lime-silica glass), where appearing motion can prolong the IRD and therefore the total bubble lifetime, which leads to a stochastic collapse of the bubble.

6.4.2 Influence of gas inside bubble

In order to verify if the bubble lifetime is influenced by aging of glass or by the gas inside the bubble, experiment with a sequence of 100 bubbles (approximately the same size, see Fig. H.12) filled with nitrogen or oxygen under the same conditions is created. The experiment is performed in soda-lime-silica glass with 0.1 % of Fe_2O_3 at T_E=1350°C during approximately 42 min (frequency = 0.04). Results of the lifetime as a function of the sequence of bubbles are given in Fig. 6.42. No effect of glass aging is observed during the experiment. Tab. 6.2 summarizes the average, min and max values of the lifetime for nitrogen and oxygen bubble. Even though the mean value of the lifetime for oxygen bubble is slightly smaller compared to nitrogen bubble, it can be concluded, that the gas inside the bubble has no

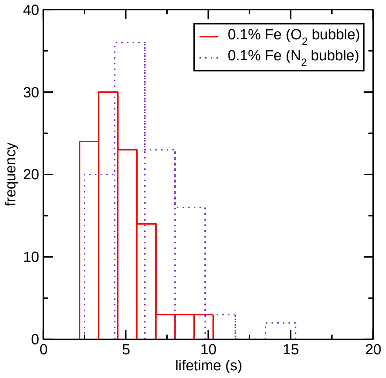

Figure 6.43: Histogram of lifetime of sequence of 100 bubbles for glass with 0.1 wt% of Fe_2O_3 and various gas bubble.

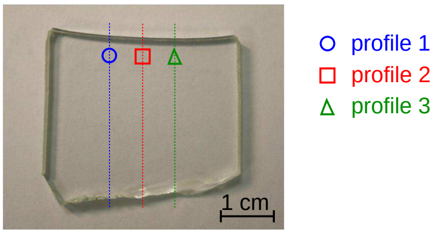

Figure 6.44: Polished slice of glass sample with three measured profiles.

significant effect on the bubble lifetime at the surface. Frequency of the lifetime is given in Fig. 6.43. It is obvious, that the distribution of the data is not Gaussian. Majority of the bubbles break soon after reaching the last determined thickness and that is why the distribution more corresponds with Poisson or exponential distribution. While bubbling oxygen through the glass sample containing iron, oxidation-reduction reaction occurs and Fe^{2+} changes into Fe^{3+} (sec. 1.2.1) according to the reaction:

Gas	mean (s)	st. dev. (s)	min (s)	max (s)
oxygen	4.72	1.68	2.28	10.23
nitrogen	6.13	2.31	2.55	15.23

Table 6.2: Average and minimal and maximal values of lifetime of sequence of 100 bubbles for glass with 0.1 wt% of Fe_2O_3 and various gas in the bubble.

$$4\mathrm{FeO} + \mathrm{O}_2 \rightarrow 2\mathrm{Fe}_2\mathrm{O}_3. \qquad (6.30)$$

As it has been mentioned in the previous text, the ratio of Fe^{2+} and Fe^{3+} changes the glass color. It is possible to determine the amount of FeO in the glass sample by the measurement of transmission, see appendix I for more details about the computation. After the experiment is finished, the glass sample is removed from the crucible and cut in order to preserve a thin glass slice (approximately 4 mm) from the middle of the removed glass. The slice is polished from both sides and the transmission is measured from the top to the bottom of the sample as three profiles, see Fig. 6.44. Profile from the top to the bottom is measured in order to establish if the sample is homogeneous or if the surface layer is influenced by surrounding atmosphere. If the top layer reacts with oxygen from atmosphere, the redox should have

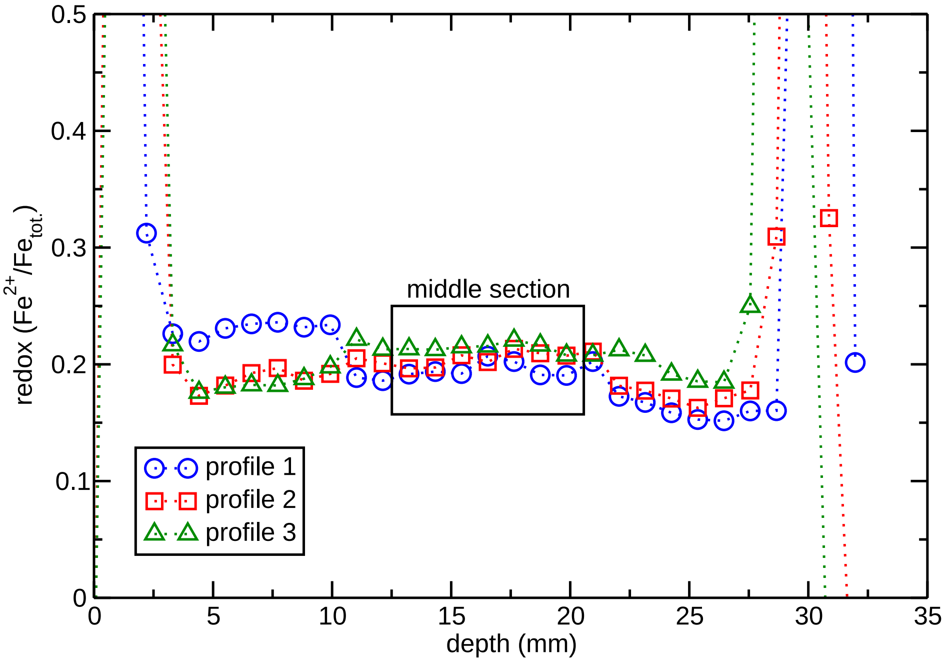

Figure 6.45: Three redox profiles in one glass sample which is obtained after the experiment.

a lower value in the surface layer. The redox of glass can be computed by normalizing the content of FeO by the total iron content, which was given in Tab. 5.2. Graph in Fig. 6.45 shows the redox state as a function of the depth of the sample. In order to measure the very surface layer of the sample, the transmission is measured in several point above and below the glass sample, therefore the first several points as well as the last points give incorrect values, because they are measured outside of the sample. In average over the profiles, no redox variation is observed from the top to the bottom of the sample. The bubble creation during the experiment mix the volume of the molten glass inside it, which leads to a homogeneous redox profile. Same effect was already mentioned for homogeneous glass composition inside the crucible after the experiment (sec. 5.2.3).

It is possible to determine the amount of oxygen absorbed in the glass during the experiment using eq. (6.30), the difference in the content of FeO in the glass before and after the experiment and the assumption that oxygen behaves as an ideal gas:

$$V_{O_2} = \frac{(n_{FeO}/4)\, RT_E}{p}, \tag{6.31}$$

where n_{FeO} is determined from the difference in the content of FeO in the glass before and after the experiment, R is the ideal gas constant and equals 8.314 J·mol^{-1}·K^{-1} and T_E is the experimental temperature (1350°C). For n_{FeO} we can write:

$$n_{FeO} = \frac{\left([FeO_{before}(wt\%) - FeO_{after}(wt\%)]\,/100\right) V\rho}{M_{FeO}}, \tag{6.32}$$

where $FeO(wt\%)$ is computed by eq. (I.1), V is the total volume of the glass sample, ρ is the glass density at room temperature and equals 2.49 g·cm^{-3} (D.2) and M_{FeO} is the molar weight of FeO (71.85 g·mol^{-1}). The difference of the average content of FeO in the middle section of the sample before and after the experiment, deduced from Fig. 6.45 and appendix I, is 2.69·10^{-3} wt%, the diameter of the crucible is 5 cm and height of the glass sample is approximately 3 cm. The total volume of oxygen which reacted during the experiment is approximately 1.8 cm^3. No variation in the lifetime of 100 bubbles filled with oxygen proves that the lifetime of the bubble lamella on the surface is independent of the redox state of the glass. RD remains approximately constant (within the error bar) for the sequence of nitrogen and oxygen bubbles, see Fig. H.13. This confirms that RD is only a function of bubble size and glass physical properties and does not depend on the gas inside the bubble or the redox state of the glass. The experiment with nitrogen and oxygen bubble is performed in the same glass composition and at the same temperature, therefore similar value of IRD is expected (Fig. H.14). More details about regular and irregular drainage are given in Tab H.2 and H.3.

6.4.3 Influence of viscosity and temperature

According to the results mentioned above, bubble lifetime is mainly a function of viscosity (influences RD) and temperature (influences IRD). In order to verify this hypothesis, an experiment with a sequence of 100 bubbles of approximately the same size (Fig. H.15) is created for all glass compositions and similar viscosity. Same value of viscosity should result in similar RD, but various temperature should give various values of IRD. Graph in Fig. 6.46 summarizes results of lifetime of a sequence of 100 bubbles and various glass composition. Histogram of the lifetime is divided into two graphs for better orientation, see Fig. 6.47 and 6.48. For the soda-lime-silica glass with lower and higher content of iron as well as for the lower content of boron, the experiment lasted approximately 42 min. For the AKM glass, only 75 bubbles were created and measured. Several bubbles remained on the surface in the crucible for a very long time and after several minutes moved to the wall and remained up to 30 min. In order to shorten the time of the experiment, less than 100 bubbles were created. The whole experiment lasted around 5 hours for AKM glass. Boron evaporated from the glass with 10 wt% of B_2O_3 and therefore the silica window placed at the top of the furnace had to be cleaned after each 10 bubbles. This prolonged the duration of the experiment to 1 hour. For glass with 10 wt% of B_2O_3, slightly longer lifetime is observed, compared to other glass compositions, see Tab. 6.3. This can be a consequence of slightly larger bubble (Fig. H.15), that can cause longer draining time, but more probable explanation is slower drainage due to higher viscosity than expected, that appears for this glass composition and has already been mentioned in the previous text. Longer draining time for glass with high content of boron is

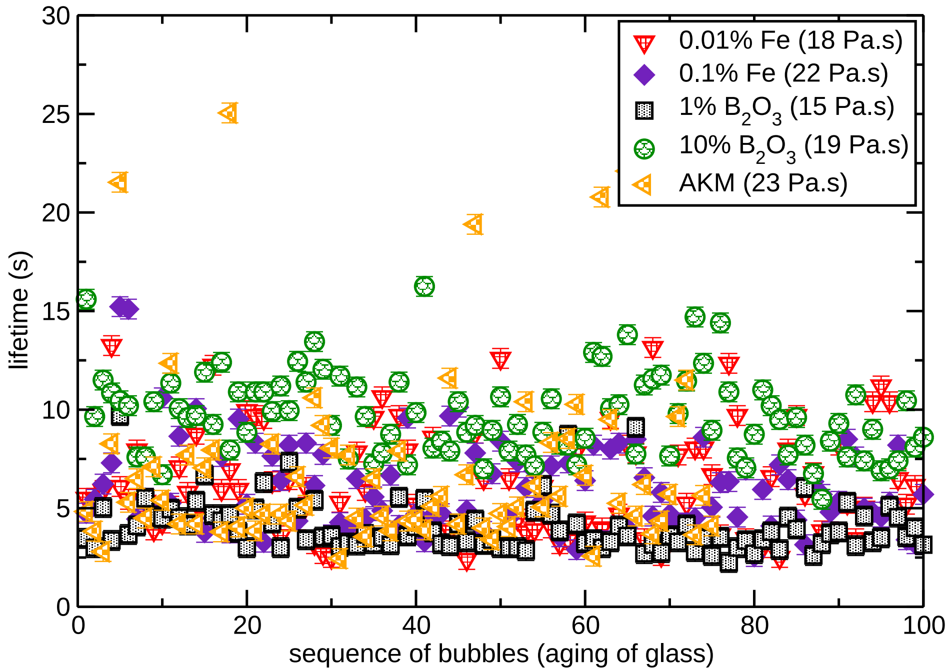

Figure 6.46: Lifetime of sequence of 100 nitrogen bubbles for various glass composition and similar viscosity.

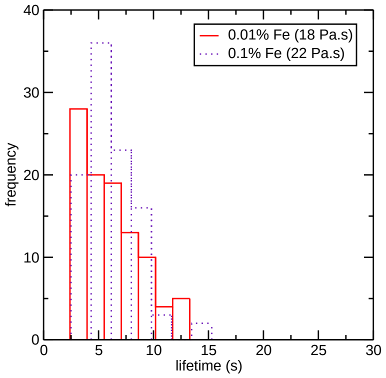

Figure 6.47: Histogram of lifetime of sequence of 100 bubbles for glass with 0.01 and 0.1 wt% of Fe_2O_3.

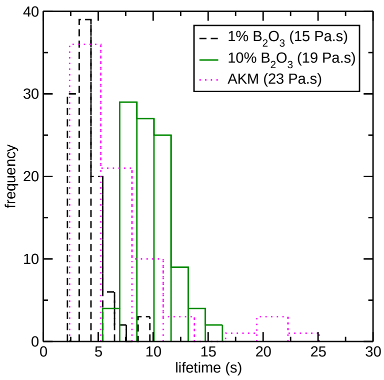

Figure 6.48: Histogram of lifetime of sequence of 100 bubbles for glass with 1 and 10 wt% of B_2O_3 and highly viscous AKM glass.

Glass	T_E (°C)	mean (s)	st. dev. (s)	min (s)	max (s)
0.01 wt% Fe_2O_3	1350	6.20	2.72	2.40	13.25
0.1 wt% Fe_2O_3	1350	6.13	2.31	2.55	15.23
1 wt% B_2O_3	1350	4.06	1.33	2.25	9.70
10 wt% B_2O_3	1142	9.70	2.09	5.45	16.25
AKM	1414	7.00	4.60	2.45	25.05

Table 6.3: Average, minimal and maximal values of lifetime of sequence of 100 nitrogen bubbles for various glass composition and similar viscosity.

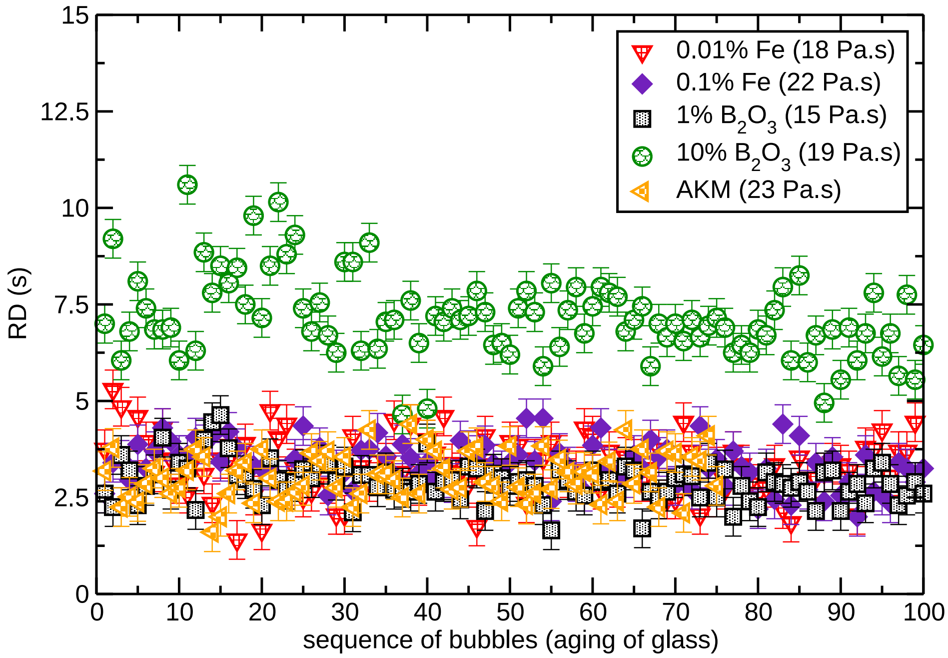

Figure 6.49: RD of sequence of 100 nitrogen bubbles for various glass composition and similar viscosity.

obvious from the graph in Fig. 6.49, where RD is plot as a function of glass aging. The standard deviation of RD of the glass with higher content of boron is almost two times higher than the standard deviation of the other glass compositions, see Tab. 6.4. RD is approximately the same for all bubbles for all glass compositions, except for the glass with high content of boron. One reason, why do we observe different drainage for each bubble can be caused by non-homogeneous evaporation, which leads to variation of the glass viscosity during the experiment, but for the moment, there is no prove to support this hypothesis. Moreover, the bubble diameter vary from one bubble to another, which influences the RD in the same way. This result suggests different behavior of glass with high content of boron, which is not fully understood and will be discussed in more details in sec. 6.5. The average value of IRD (Fig.

Glass	T_E (°C)	mean (s)	st. dev. (s)	min (s)	max (s)
0.01 wt% Fe_2O_3	1350	3.31	0.76	1.40	5.30
0.1 wt% Fe_2O_3	1350	3.35	0.56	2.00	4.55
1 wt% B_2O_3	1350	2.90	0.50	1.65	4.64
10 wt% B_2O_3	1142	7.16	1.06	4.65	10.60
AKM	1414	3.06	0.60	1.60	4.40

Table 6.4: Average, minimal and maximal values of RD of sequence of 100 nitrogen bubbles for various glass composition and similar viscosity.

6.50) for AKM glass is 3.93 s, which is approximately 1.4 times higher compared to the ones of other glass compositions, see Tab. 6.5. To obtain the same viscosity, the experimental temperature during the experiment with AKM glass had to be approximately 64°C higher compared to the other experiments, which are performed at 1350°C. As it has been mentioned in the previous text, the higher the temperature, the more probable the appearance of motion and the longer the IRD. In the comparison, the temperature during the experiment with the glass with high content of boron was 1142°, which is 208°C lower than for the three other compositions. Even though the temperature for this glass composition is lower compared to the others, the IRD has approximately the same duration, see Tab. 6.5. As above mentioned, the motion appears at lower temperature for glass with boron, which can explain the similar duration of the IRD. Long duration of irregular drainage for glass with high content of boron at 1142°C is also obvious from Fig. H.11.

Glass	T_E (°C)	mean (s)	st. dev. (s)	min (s)	max (s)
0.01 wt% Fe_2O_3	1350	2.89	2.60	0.15	10.00
0.1 wt% Fe_2O_3	1350	2.78	2.23	0.10	11.85
1 wt% B_2O_3	1350	1.20	1.42	0.05	7.40
10 wt% B_2O_3	1142	2.55	2.07	0.05	9.05
AKM	1414	3.93	4.64	0.05	21.65

Table 6.5: Average, minimal and maximal values of IRD of sequence of 100 nitrogen bubbles for various glass composition and similar viscosity.

Last experiment with a sequence of bubbles compares behavior of lifetime for bubbles created at the same temperature, but various viscosity. The comparison is performed for soda-lime-silica glass with 0.1 wt% of Fe_2O_3 and highly viscous AKM glass at T_E=1350°C, see Fig. 6.51 for the results of the lifetime and Fig. 6.52 for the frequency of the lifetime. Only 86 bubbles are created in the highly viscous glass due to long lasting bubbles mentioned above. Therefore the experiment was interrupted several times, which led to a small vari-

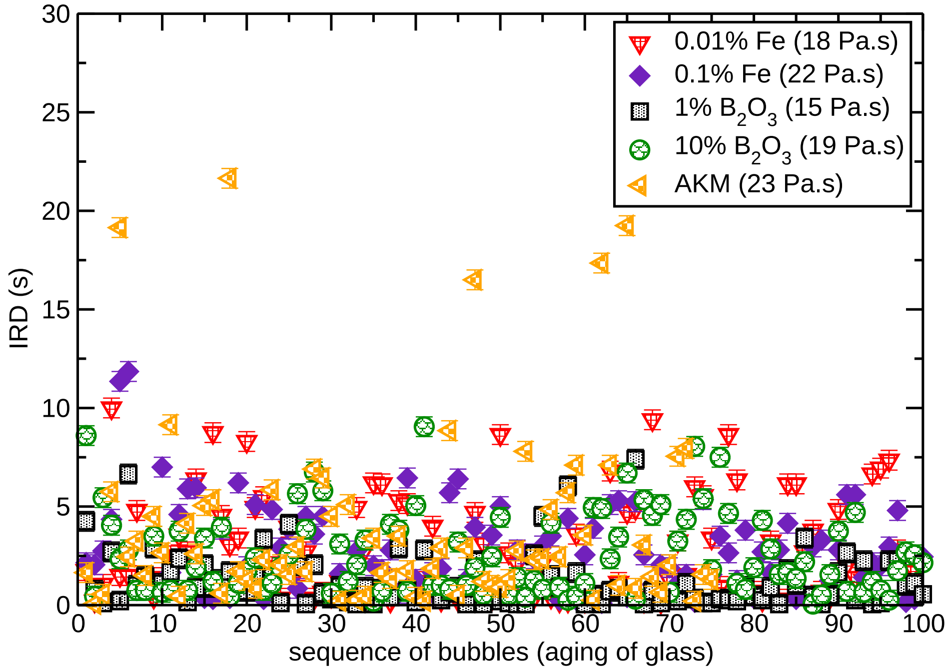

Figure 6.50: IRD of sequence of 100 nitrogen bubbles for various glass composition and similar viscosity.

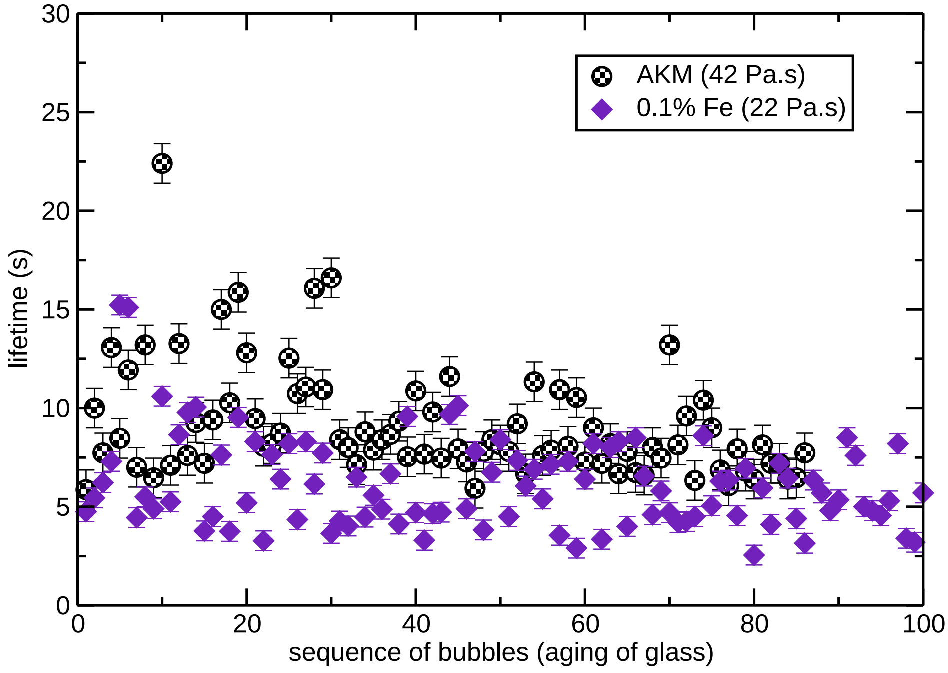

Figure 6.51: Lifetime of sequence of 100 nitrogen bubbles for glass with 0.1 wt% of Fe_2O_3 and highly viscous AKM glass at temperature T_E=1350°C.

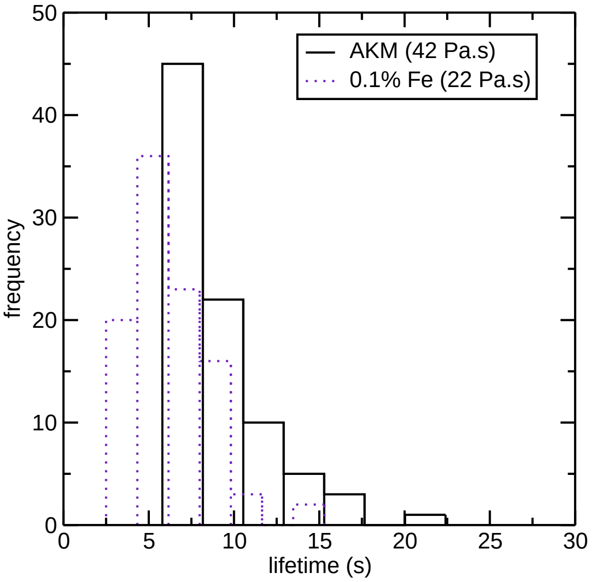

Figure 6.52: Histogram of lifetime of sequence of 100 nitrogen bubbles for glass with 0.1 wt% of Fe_2O_3 and highly viscous AKM glass at temperature T_E=1350°C.

ation in the bubble size during the experiment, see Fig. H.16. It might be misleading that the lifetime for AKM glass decreases as a function of time (aging of glass), but the very long lasting bubbles, that were observed during the whole experiment, are missing in this graph, because they could not have been considered. Duration of the experiment with AKM glass was approximately 5 hours, compared to 42 min for glass with 0.1 wt% of iron. Longer lifetime for AKM glass appears as a consequence of approximately two times higher viscosity, which is confirmed in the graph of RD in Fig. 6.53. As a consequence of the same experimental temperature, the duration of the IRD is approximately the same for both glass compositions, see Fig. 6.54. Summary of all mean values of lifetime, regular and irregular drainage for all glass compositions and all viscosities is given in appendix H in Tab. H.1, H.2 and H.3, respectively.

6.5 Origin of the liquid motion observed in the lamella at the second step of the bubble lifetime

It has been shown in the previous section, that the second step of the bubble lifetime during which motion is observed in the bubble lamella, prolongs the bubble lifetime at higher temperatures. In order to shorten the bubble lifetime on the surface, it is necessary to understand the origin of the motion and find options how to eliminate it. During this motion, we observe a backward flow into the bubble lamella against gravity. The observation of the motion is very similar to Marangoni flow (sec. 3.1.1). If we see a backward flow, the surface tension in

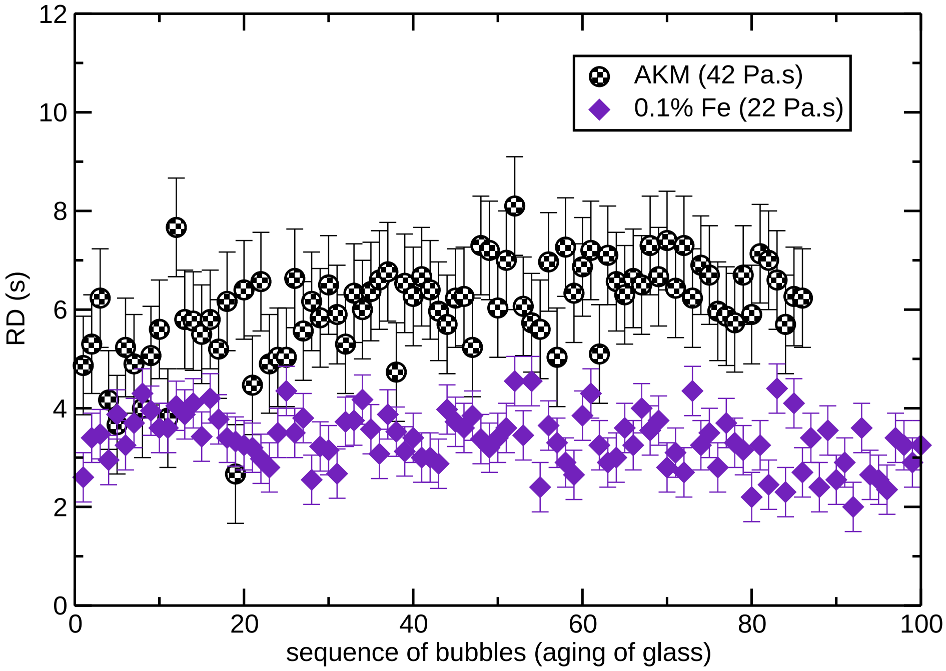

Figure 6.53: RD of sequence of 100 nitrogen bubbles for glass with 0.1 wt% of Fe_2O_3 and highly viscous AKM glass at temperature T_E=1350°C.

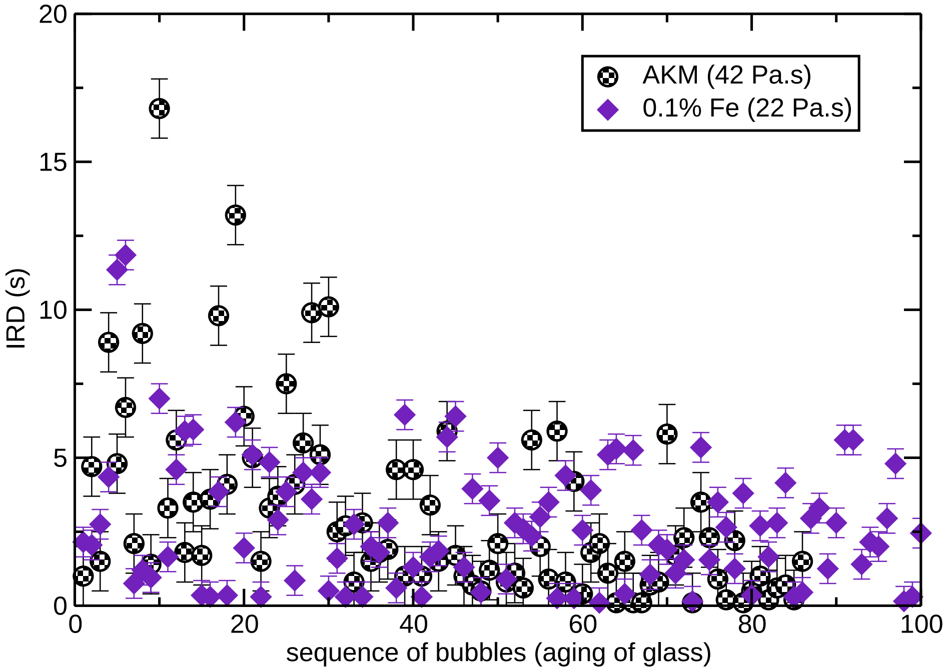

Figure 6.54: IRD of sequence of 100 nitrogen bubbles for glass with 0.1 wt% of Fe_2O_3 and highly viscous AKM glass at temperature T_E=1350°C.

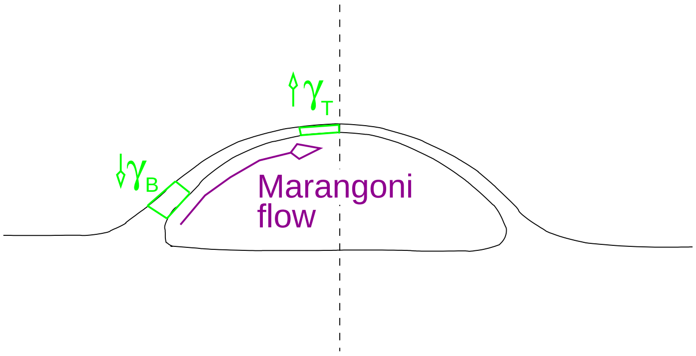

Figure 6.55: Sketch of a bubble at the surface - Marangoni flow.

the top part of the bubble needs to have higher value, than the surface tension at the bottom part of the bubble, see Fig. 6.55. As discussed in sec. 2.3, glass composition changes at high temperature due to evaporation of volatile species. Loss of sodium, potassium and boron was discussed in sec. 2.3 and as it was mentioned in sec. 2.2, surface tension of glass is a function of its chemical composition. Therefore it will be interesting to determine the chemical composition in various parts of the bubble lamella. During the experiment with a single bubble, the crucible with the bubble at the surface was removed from the furnace in order to preserve the bubble lamella for analyses. Unfortunately this experiment was not successful. Either the bubble broke sooner than removed from the furnace or the preserved bubble lamella vanished in the furnace atmosphere due to high convection that broke the cooled lamella. In order to understand better chemical changes that can occur at low and high temperature, experiment with a thin vertical film was performed.

6.5.1 Lifetime of vertical film

Experimental set-up for determination of lifetime of a vertical film was described in sec. 4.3. Lifetimes of vertical films for soda-lime-silica glass with 0.01 and 0.1 wt% of Fe_2O_3 as a function of temperature are given in Fig. 6.56 and 6.57, respectively. Observation of this experiment is similar to the experiment with a single bubble. The lifetime is decreasing with rising temperature, because viscosity is decreasing. But as soon as liquid motion is observed in the film (Fig. 6.58), the lifetime of the film increases, see Fig. 6.56 and 6.57. For glass with lower iron content, the motion is first observed at 1300°C and for the glass with higher iron content, the motion is observed already at 1200°C. The exact experimental temperature might be slightly different, because inside this furnace, the temperature is not measured at the area of the vertical film. Even though the real experimental temperature is not expected to be very different from the temperature set on the furnace, it is important to emphasize, that the exact temperature field inside the furnace at the area of the vertical film was not

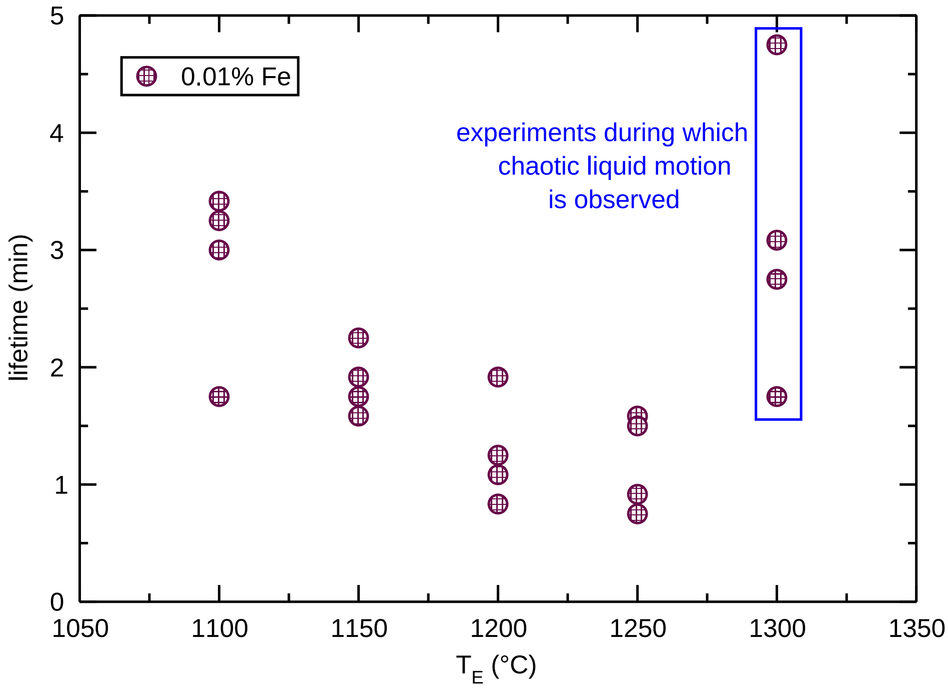

Figure 6.56: Lifetime of vertical film for glass with 0.01 wt% of Fe_2O_3 at various temperature.

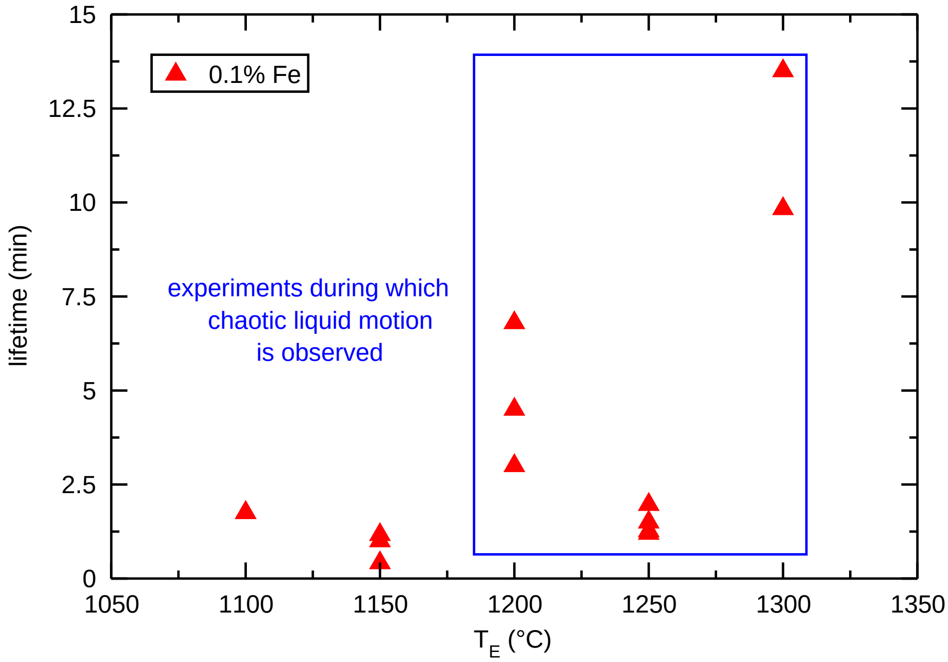

Figure 6.57: Lifetime of vertical film for glass with 0.1 wt% of Fe_2O_3 at various temperature.

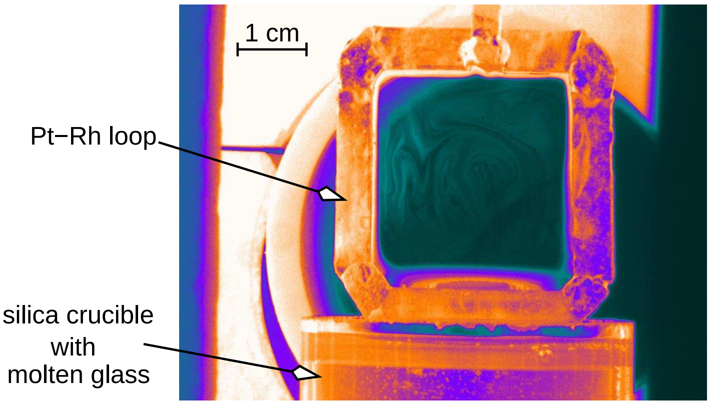

Figure 6.58: Example of motion observed in the vertical film for glass with higher content of iron at 1300°C.

determined experimentally. It is also necessary to emphasize, that only four experiments were performed at each temperature. The main purpose of the experiment was not to collect data related to the film lifetime, but to verify if the motion is observed at high temperatures and to preserve the film for chemical analyses.

6.5.2 SIMS analyses of vertical film

As discussed in sec. 2.4, a motion, described as Marangoni flow, was observed in glass long time ago by Conroy [3]. He observed motion at temperature above 1315°C and associates the motion with sodium sulfate decomposition. In order to verify if this motion is related to this decomposition, we performed an experiment with soda-lime-silica glass free of sulfate. Chemical composition of the glass is given in Tab. 6.6. The experiment is performed at temperatures 1200 and 1400°C. The motion is not observed at the lower temperature, but it is observed at the higher temperature. This experimental observation proves that the motion we observe in this work is not related to sodium sulfate decomposition. The created film of this glass composition was preserved after the experiment, placed into the annealing chamber and cooled to room temperature. In order to determine concentration profile as a function of the film depth at both temperatures, chemical composition was determined perpendicularly to the film using SIMS analysis. Intensity of the signals as a function of the depth of the sample is given in Fig. 6.59 and 6.60. It is obvious that the intensity of sodium decreases close to the surface. The evaporation of sodium can explain this result.

Na_2O_3	MgO	Al_2O_3	SiO_2	K_2O	CaO	Fe_2O_3	TiO_2	SO_3
13.20	3.80	0.74	72.7	0.19	9.17	0.09	0.02	<0.01

Table 6.6: Chemical composition of soda-lime-silica sulfate free glass.

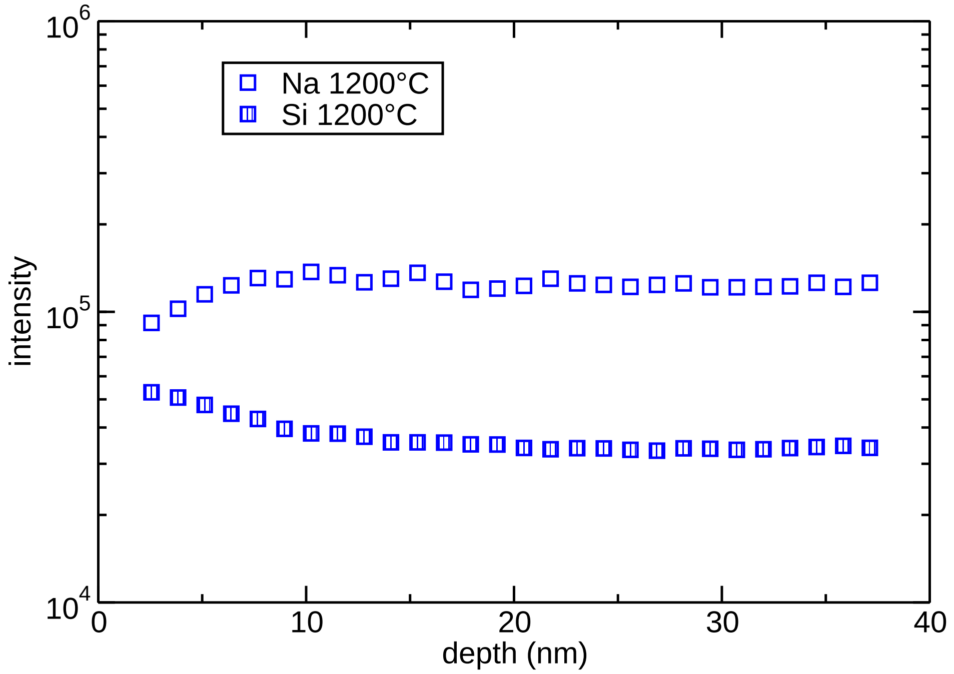

Figure 6.59: Intensity obtained by SIMS analysis as a function of the depth of the thin vertical film at 1200°C.

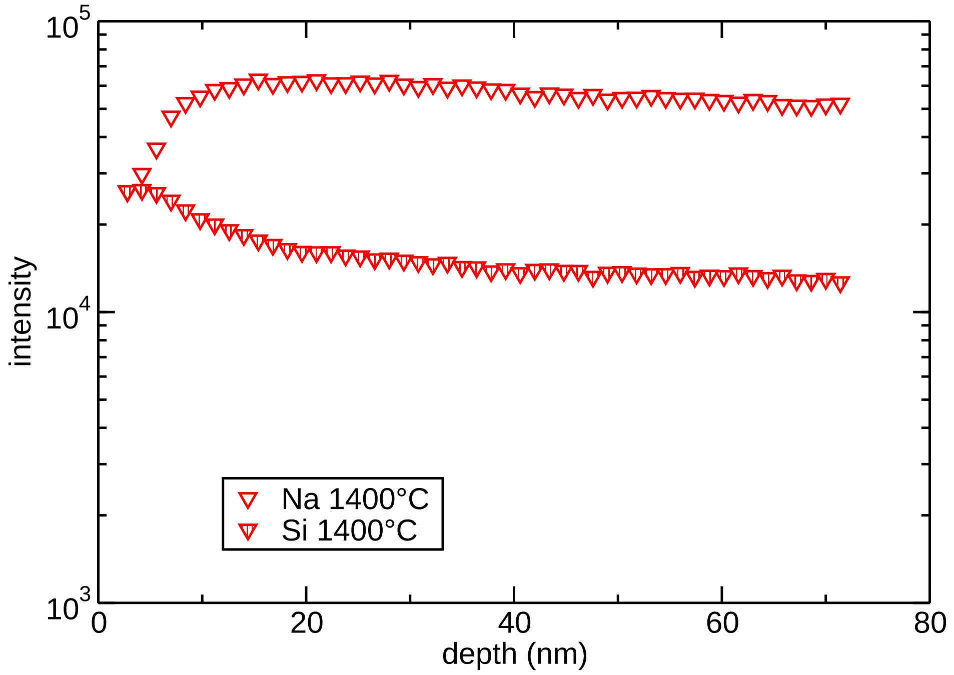

Figure 6.60: Intensity obtained by SIMS analysis as a function of the depth of the thin vertical film at 1400°C.

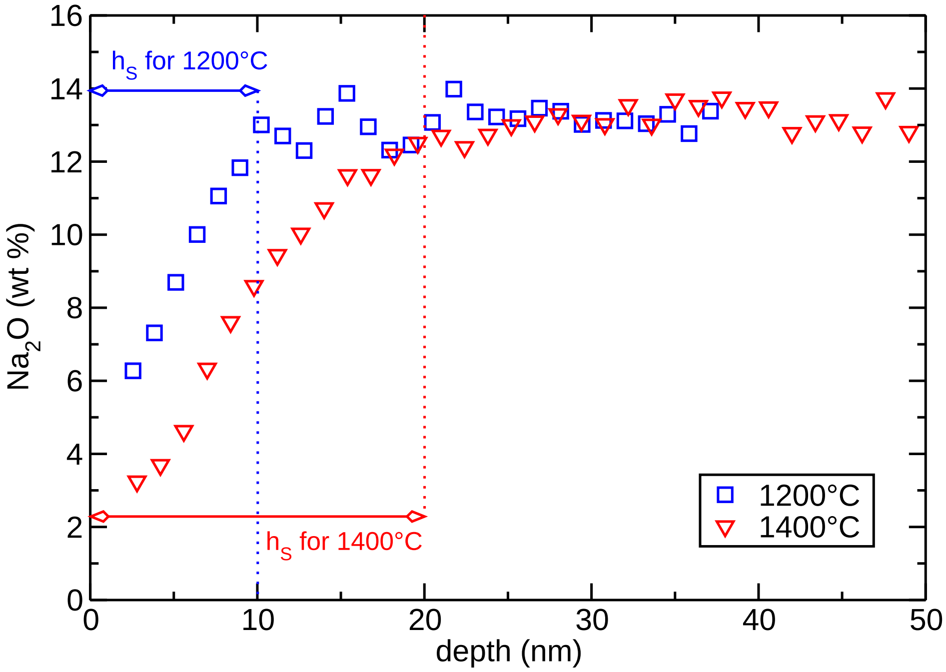

Figure 6.61: Content of sodium oxide as a function of depth of vertical film, computed from intensity obtained by SIMS analysis and expecting that composition at 150 nm is the initial composition of glass given in Tab. 6.6.

The deficiency of sodium is compensated by an increase in silicon content. The decrease in intensity is more significant at higher temperature, where we expect higher evaporation. It is possible to recompute the intensity from SIMS analysis into concentration considering that at the deepest point of the analysis, we reach the bulk composition, as discussed previously in sec. 5.2.1. Fig. 6.61 shows content of sodium oxide as a function of the depth in the sample. The concentration decreases from 13 to 6 wt% in the first 10 nm at temperature 1200°C and from 13 to 3 wt% in the first 20 nm at the higher temperature. Considering sketch of a bubble at the surface, which was given in Fig. 6.55, and assuming evaporation from both interfaces of the bubble lamella, the total amount of sodium will be lower at the top of the bubble and higher at the bottom due to the variation of lamella thickness. This will cause higher value of surface tension in the top part of the bubble, compared to the bottom, see Fig. 6.62. Concentration at the top part (w_T) of the bubble lamella can be written as:

$$w_T = \frac{2w_S V_S \rho + w_M V_M \rho}{(2V_S V_M)\,\rho}, \tag{6.33}$$

where w_S is an average concentration in the surface layer and V_S is a specific volume, accordingly w_M and V_M are concentration and specific volume in the middle of the lamella. Considering h_S is the thickness in which the concentration decreases and h_T is the thickness

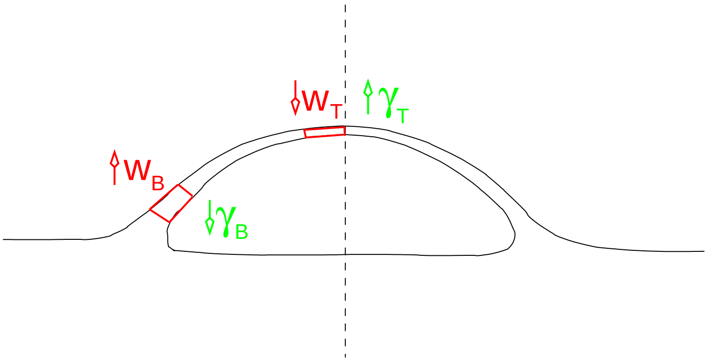

Figure 6.62: Sketch of a bubble, where the thickness of the bubble lamella is smaller at the top, than at the bottom, which leads to lower concentration of sodium at the top part and as a consequence to higher surface tension at the top part.

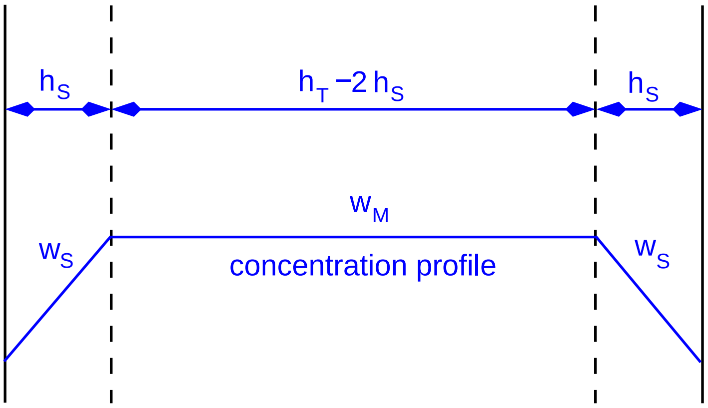

Figure 6.63: Sketch of the top part of the lamella, where all parameters from eq. (6.34) are given.

of the bubble lamella at the top part of the bubble, we can write (Fig. 6.63):

$$w_T = \frac{2w_S h_S + w_M h_T - 2w_M h_S}{h_T}. \tag{6.34}$$

Using data in Tab. 6.7, we obtain that for 1200°C, the difference in concentration between top and bottom of the bubble is 0.7 wt% and for temperature 1400°C, it is 2.0 wt%. Thickness 100 nm at the top part of the bubble approximately corresponds with the last determined thickness in our experiment. Thickness 1 mm at the bottom of the bubble is an assumption. We can compute the difference in surface tension considering model in appendix D.1 and modified initial composition, which is in Tab. 6.6. Surface tension at the bottom of the bubble is computed as an average value obtained by the model of Lyon and Rubenstein and equals approximately 324.76 mN·m^{-1}. Considering the loss in sodium is compensated by an increase in the content of silicon, we obtain, that the difference in surface tension between the bottom and top is 1.39 mN·m^{-1} at lower temperature and almost three times higher at high temperature, where the surface tension at the top equals to 328.72 mN·m^{-1}, see Tab. 6.8. For the moment it is not possible to conclude if this difference in surface tension is sufficient

variable	1200°C	1400°C
w_S	9.5 wt%	8 wt%
w_M	13 wt%	13 wt%
h_S	10 nm	20 nm
h_T	100 nm	100 nm
h_B	1 mm	1 mm

Table 6.7: Data for computation of concentration difference between top and bottom of a bubble.

surface tension	1200°C	1400°C
γ_B	324.76 mN·m^{-1}	324.76 mN·m^{-1}
γ_T	326.15 mN·m^{-1}	328.72 mN·m^{-1}
$\Delta\gamma$	1.39 mN·m^{-1}	3.96 mN·m^{-1}

Table 6.8: Surface tension at the bottom and top of the bubble for various temperature.

to cause Marangoni flow against gravity or even how precise the value is. In order to have exact value, it will be necessary to determine the composition by a quantitative analysis and determine the surface tension experimentally. To have an information if the surface tension difference can cause Marangoni flow, numerical simulation will be necessary. Nevertheless it can be concluded, that the surface tension difference is higher at higher temperature, therefore the appearance of Marangoni flow is more probable at higher temperature.

6.5.3 Evaporation experiment

In order to better understand the loss of sodium at various temperatures and glass compositions, an experiment studying evaporation was performed. Approximately 13 g of three various glass compositions were put into small crucibles and left inside a furnace for eight hours at 1200 and 1400°C. After this time, glass composition was established as a function of the depth in the glass sample using SIMS analysis. The profiles in the first 150 nm did not give very interesting results. However, the chemical composition in the deepest point of the sample was different for various temperature and initial glass compositions, see Tab. 6.9. For glass with 0.1 wt% of Fe_2O_3, the content of sodium decreased from original 13.3 wt% to 11.9 wt% at 1200°C and 10.6 wt% at 1400°C. Even higher loss in sodium is observed for the glass with 10 wt% of B_2O_3, where the content decreased from 12.4 to 10.4 wt% at lower temperature and 4.7 wt% at higher temperature. Evaporation of boron, which decreased for this glass from 9.7 to 7.7 and 3.1 wt% at lower or higher experimental temperature, can support the evaporation of sodium and explain the higher loss for this glass. Supported evapora-

Glass and T_E (°C)	**B_2O_3**	**Na_2O_3**	**MgO**	**Al_2O_3**	**SiO_2**	**K_2O**	**CaO**	Fe_2O_3
0.1 wt% Fe_2O_3 1200	0	11.9	3.5	0.7	75.7	0.1	8.1	0.1
0.1 wt% Fe_2O_3 1400	0	10.6	3.2	0.6	77.8	0.1	7.6	0.1
without Na_2SO_4 1200	0	9.9	3.8	0.7	76.2	0.2	9.1	0.2
without Na_2SO_4 1400	0	11.0	3.5	0.6	76.4	0.2	8.3	0.1
10 wt% B_2O_3 1200	7.7	10.4	0.1	2.1	67.5	0.1	12.1	0.0
10 wt% B_2O_3 1400	3.1	4.7	0.1	2.0	82.3	0.2	7.6	0.0

Table 6.9: Chemical composition of various glasses after the evaporation experiment.

tion of sodium may be the explanation, why for boron glass we observe the motion at lower temperature than for ordinary soda-lime-silica glass. The content of sodium for sulfate free glass decreased from original 13.2 to 9.9 wt% at lower temperature and 11.0 wt% at higher temperature, it is not understood, why the sodium loss is lower at higher temperature for this glass composition. The loss of sodium during this experiment is evident, nevertheless, in order to determine precisely the decrease in the sodium content, a quantitative analysis would be necessary. Apart from temperature, convection in the surrounding atmosphere influences evaporation and therefore one part of this work was to model temperature and velocity field inside the furnace. Unfortunately, this work has not been finished, see appendix J.

6.6 Daughter bubble

The bubble formation in liquid can have various origins, such as supersaturation of dissolved gases, mixing or whipping (sec. 3.1). Recently, another source of bubbles was pointed out by Bird *et al.* [1]. The formation of tiny bubbles, called “daughter bubbles”, appears as the consequence of bursting of a bubble on a free liquid surface. In the framework of glass melting, this phenomenon is important since it can explain the huge quantity of small bubbles (smaller than 1 mm in diameter) observed in the submerged burner furnaces or during bubbling (Fig. 6.64). The formation of these tiny bubbles appears as a consequence of the rupture of the thin film.

6.6.1 Film rupture and opening velocity

Film rupture has been studied since long time ago. One of the first work has been done by Dupré in 1867 (cited in [7]). The opening velocity has been investigated by Taylor [18] and Culick [4]. When the inertia and the surface tension are the main driving forces, the opening velocity is a constant depending only on the surface tension, the liquid density and the film

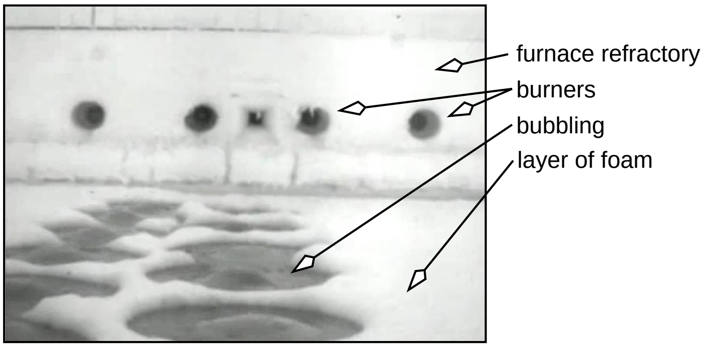

Figure 6.64: Example of bubbling in continuous cross-fired furnace.

thickness. In the case of a highly viscous liquid, Debrégeas *et al.* [8, 6] studied the bursting of a bubble at a free surface. Two important points have been observed in their work. The first point is, that the opening velocity grows exponentially with time and the second point is, that the retracting film is not collected into a rim as it is observed in the case of a non-viscous film [18, 4]. The absence of the rim has been explained by the viscoelasticity behavior, see [8, 6]. The bursting of the viscous film has been studied numerically thanks to a lubrication equation by Brenner and Gueyffier [2]. They showed that the absence of the rim can be also explained by a purely viscous effect. Savva and Bush [17] pointed out that the rim depends on the Ohnesorge number, that compares viscous and capillary effect, based on the film thickness. They presented a model to study the retraction of circular hole, they confirm the absence of rim in pure viscous regime (large Oh) and that the opening velocity grows exponentially at short time and tends to Taylor - Culick velocity at long time.
More recently, Bird *et al.* [1] studied how does the ruptured thin film create bubbles at a free surface of water. They pointed out that the bubble bursting provided a creation of smaller bubbles called “daughter bubbles”. The origin of the daughter bubbles seems to appear due to the folding of the film during the retraction. The film bends and entraps a torus of gas which is destabilized in small bubbles.

6.6.2 Mechanism of daughter bubble creation

Before the bubble ruptures, there is a balance between bubble pressure and capillary stresses. When a hole is created at the top of the bubble, the film liquid retracts and inner and outer pressures are balanced. Due to a pressure balance, capillary forces, which are directed inward, compete with inertia or viscous force, which is directed outward of the moving rim. As it is shown by Taylor [18] and Culick [4], when the capillary forces are balanced with inertia, the retraction velocity is constant and given by the following relationship:

$$U = \sqrt{\frac{2\gamma}{\rho h}}, \tag{6.35}$$

where γ is the surface tension, ρ the liquid density and h the film thickness which is assumed constant. Even if the velocity given by (6.35) is established by the balance of inertia and capillary forces, this velocity remains valid when the viscosity effect exists. This result, pointed out by Savva and Bush [17], exists due to the viscous energy dissipating in the liquid film.

As pointed out by Brenner and Gueyffier [2], the film does not bend when the Reynolds number

$$Re = \frac{\rho R U}{\mu}, \tag{6.36}$$

stays smaller than one. In the definition of the Reynolds number, Eq. (6.36), R is the radius of the bubble on the free surface and μ the dynamic viscosity. Bird *et al.* [1] studied experimentally the rupture of hemispherical bubbles using a high speed video-camera. The hole was performed artificially thanks to a pine at the top of the bubble. The authors observed that the film bended during the retraction and formed one or two concentric ring(s) of gas. When the bended film is unstable (Plateau-Rayleigh instability), it traps only one torus of air. The destabilization of these torus leads to a formation of daughter bubbles. The number of rings is controlled by a capillary number:

$$Ca = \frac{U\mu}{\gamma}. \tag{6.37}$$

Remark that using the Taylor-Culick velocity, Eq. (6.35), the product of Re and Ca, which is usually known as the Weber number, is equal to:

$$ReCa = \frac{2R}{h}. \tag{6.38}$$

6.6.3 Experimental observation

Daughter bubbles are observed for a glass with 10 wt% of B_2O_3 at T_E=1291°C and for soda-lime-silica glass with 0.1 wt% of Fe_2O_3 above 1440°C when the value of viscosity is around 10 Pa·s or lower. All of the presented Figures are top views of the bubble inside the crucible with glass containing 10 wt% of B_2O_3. The edge of the crucible is far from the bubble and is not visible in the Figures. The slightly lighter ring surrounding the bubble about 1.5 cm far from the bubble edge is the laser beam. Fig. 6.65 and 6.66 show a bubble before and right after bursting. As mentioned above, creation of two rings of gas is possible. If we look closely at the two pairs of bubbles in the top part of the image in Fig. 6.66, the bubble on the right in each pair seems to be placed slightly further away from the middle of the bubble than the bubble on the left. The right bubble might be part of an outer ring of daughter bubbles and the bubble on the left might be part of the inner ring. However, the resolution of the image is not sufficient to make this conclusion. The bubble diameter (D_{bubble}) is approximately 2 cm. Considering a hemispherical shape of the bubble at the

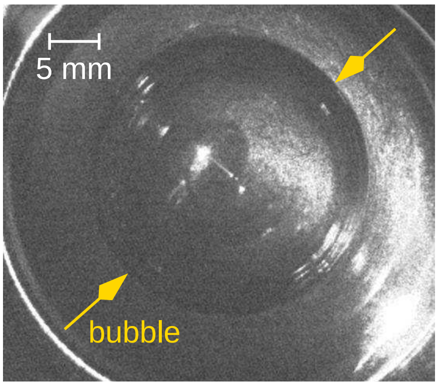

Figure 6.65: Glass bubble with a diameter 2 cm before bursting.

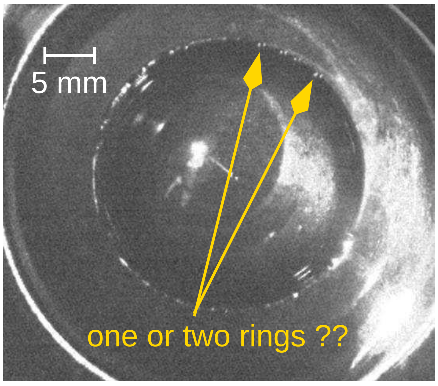

Figure 6.66: Gas bubble right after bursting.

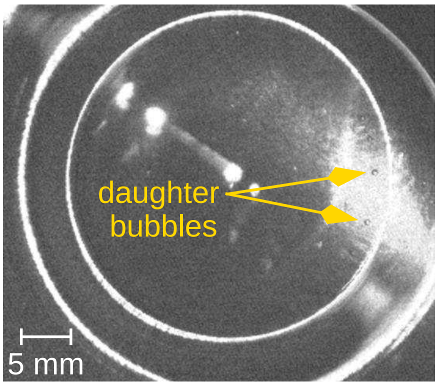

Figure 6.67: Daughter bubble with a diameter 0.6 mm.

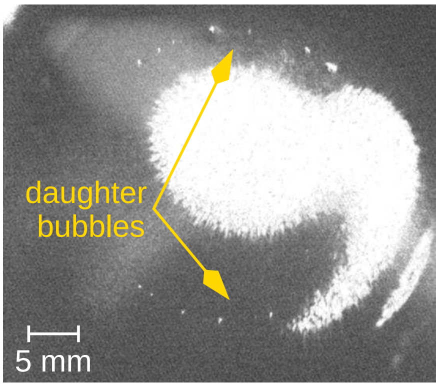

Figure 6.68: Ring of daughter bubbles.

surface, we can compute its D_{cap} using eq. (6.17) and obtain 25 mm, which corresponds to the measurement of the bubble at the surface, see Fig. 6.65. A daughter bubble with a diameter 0.7 mm is visible in Figure 6.67. The original bubble in the work of Bird *et al.* [1] had a radius 4 cm and created a daughter bubble with a 40 times smaller radius around 1 mm. This size relation approximately corresponds with our experiment. Fig. 6.68 shows a ring of several daughter bubbles. According to the prediction, daughter bubbles can be formed for $Re \gg 1$. The determination of Re and Ca is difficult in our experiment due to uncertainty of the retraction speed of the thin film. We are not able to observe the evolution of the film retraction during our experiment (duration between two images taken during the experiment is 0.05 s). Consequently, we cannot determine the retraction speed experimentally. Since we are not able to observe the rupture of the bubble, the value of the retraction speed has to be larger than 0.26 m/s:

$$v > \frac{0.013}{0.05} = 0.26 \text{ m/s}. \tag{6.39}$$

Debrégeas *et al.* [8, 6] proposed a relationship of the retraction speed, which can be in the case where the viscosity is high given by

$$v = \frac{\gamma}{\mu}. \tag{6.40}$$

For the given glass composition (10 wt% of B_2O_3), the surface tension equals 296 mN·m^{-1} and the viscosity is 4.9 Pa·s (Tab. C.4 and 5.16). The retraction speed proposed by Debrégeas *et al.* [8, 6] would equal to 0.06 m·s^{-1}, which is too small compare to the frequence of our video-camera. Indeed, if the velocity was given by (6.40), we would be able to see the film retraction with our equipment.

Another formula for the determination of the retraction speed is given in eq. (6.35). The only unknown in the formula is h, which is the film thickness at the bursting. Experimentally, the film thickness is unknown. Nevertheless, we can estimate minimal and maximal values of h. On one hand, spontaneous rupture due to the van der Waal forces [16, 20] can be considered: the value of the critical thickness h_c can be evaluated using a formula found in [16, 20] and used by van der Schaaf and Beerkens [19]:

$$h_c = 0.11 \cdot \left(\frac{A_H R^2}{\gamma}\right)^{1/4}, \tag{6.41}$$

where A_H is the Hamaker constant, which is approximately 7·10^{-20} J for glass (see [10]). Remark that equation (6.41) has been obtained for a flat film. Considering R_{cap} is equal to 1.3 cm, h_c is equal to 276 nm. Using eq. (6.41) in (6.35), the value of the Taylor-Culick retraction speed is approximately equal to 29 m·s^{-1}. On the other hand, we can consider the minimal thickness given in Tab. 5.20, but round the value for all glass compositions to 100 nm for the computation. If we take this value of thickness, the retraction velocity given by (6.35) is equal to 48 m·s^{-1}. Both values of velocity are larger than 0.26 m·s^{-1} so they fulfill the condition coming from the experimental observation. Using both values of the velocity and the glass properties, minimal and maximal values for Re and Ca numbers can be computed. Reynolds number for glass with 10 wt% of B_2O_3 and T_E=1291°C is between 193 and 319 and its capillary number is in the range from 480 to 791.

Maximal and minimal values of Re and Ca numbers for all temperatures and all glass samples are computed using the method above and are given in Tables 6.10 to 6.13. The formation of daughter bubbles is observed for two highest temperatures for soda-lime-silica glass with 0.1 wt% of Fe_2O_3 and the highest temperature for the glass with 10 wt% of B_2O_3. These situations are pointed out in bold character in Tables 6.10 to 6.13. The min and max values of Re and Ca are plotted in Fig. 6.69. The two lines separate the points into two groups, where a formation of daughter bubbles is or is not observed. The dotted line divides the min values and the solid line divides the max values. According to Bird *et al.* [1], the limit for a formation

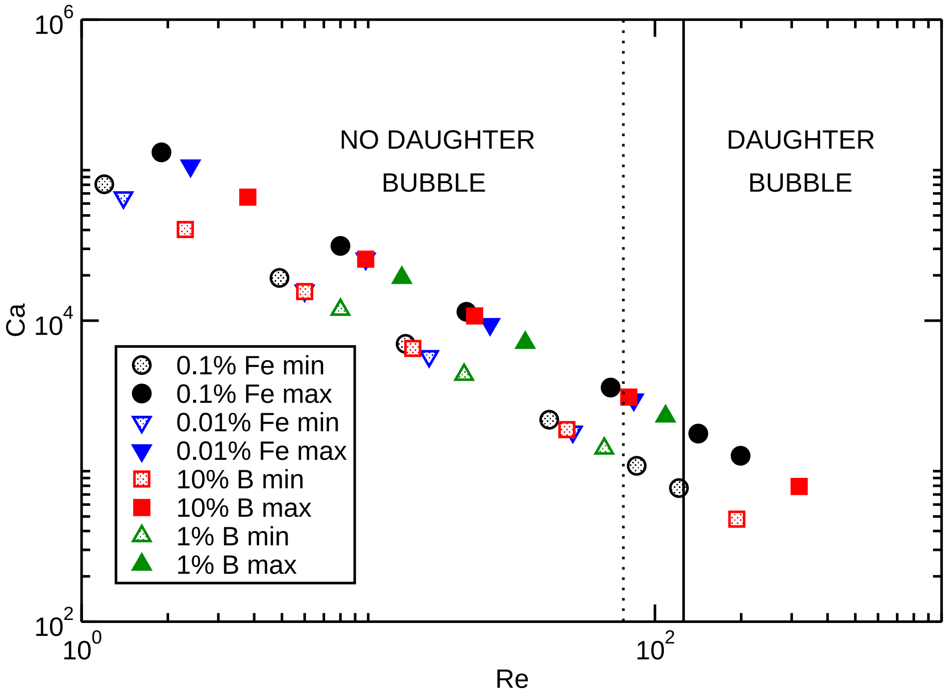

Figure 6.69: Dynamical characterization of the formation of daughter bubbles.

of daughter bubbles is $Re \gg 1$. A higher value of Re corresponds to our experimental results. This disagreement can be explained by an overestimation of the retraction speed estimated in our computations.

If we would like to have an accurate value of the capillary and Reynolds numbers, we have to use a high speed video-camera to determine the retraction speed experimentally. However if we know properties of a glass sample we can compute Re and Ca using the same method as described above and the diagram in Figure 6.69 should give us an idea if we can expect a formation of daughter bubbles or not. It is impossible to precisely determine if we observe

	Re		Ca	
T_E (°C)	min	max	min	max
1044	1.2	1.9	80593	131291
1142	4.9	8.0	19222	31361
1228	13.5	22.0	7011	11457
1350	42.8	70.1	2196	3595
1442	**86.4**	**141.7**	**1085**	**1778**
1492	**121.3**	**199.0**	**772**	**1266**

Table 6.10: Values of Re and Ca for glass with 0.1 wt% of Fe_2O_3.

	Re		Ca	
T_E (°C)	min	max	min	max
1044	1.4	2.4	65815	107053
1142	6.0	9.8	15831	25790
1228	16.3	26.6	5804	9470
1350	51.7	84.4	1827	2985

Table 6.11: Values of Re and Ca for glass with 0.01 wt% of Fe_2O_3

	Re		Ca	
T$_E$ (°C)	min	max	min	max
1142	8.0	13.1	11827	19274
1228	21.6	35.3	4373	7137
1350	66.6	108.9	1415	2314

Table 6.12: Values of Re and Ca for glass with 1 wt% of B_2O_3.

	Re		Ca	
T$_E$ (°C)	min	max	min	max
940	2.3	3.8	40312	66135
990	6.0	9.8	15600	25614
1044	14.3	23.5	6539	10745
1142	49.3	81.1	1887	3106
1291	**193.0**	**318.5**	**480**	**791**

Table 6.13: Values of Re and Ca for glass with 10 wt% of B_2O_3.

one or two rings of daughter bubbles in our experiment. Better resolution and a high speed video-camera will be necessary to make a conclusion about this point.

References

[1] J. C. Bird, R. de Ruiter, L. Courbin, and H. A. Stone. Daughter bubble cascades produced by folding of ruptured thin films. *Nature*, 465(June):759–762, 2010.

[2] M. P. Brenner and D. Gueyffier. On the bursting of viscous film. *Phys. Fluids*, 11:737–739, 1999.

[3] A. R. Conroy, W. H. Manring, and W. C. Bauer. The Role of Sulfate in the Melting and Fining of Glass Batch. *The Glass Industry*, 47, 1966.

[4] F. E. C. Culick. Comments on a ruptured soap film. *J. Appl. Phys.*, 31:1128–1129, 1960.

[5] P. G. de Gennes, F. Brochard-Wyart, and D. Quéré. *Capillarity and Wetting Phenomena*. Springer, New York, 2004.

[6] G. Debrégeas, P.-G. de Gennes, and F. Brochard-Wyart. The Life and Death of “Bare” Viscous Bubbles. *Science*, 279:1704–1707, 1998.

[7] G. Debrégeas, P. Martin, and F. Brochard-Wyart. Viscous bursting of suspended films. *Phys. Rev. Lett.*, 75:3886–3889, 1995.

[8] G. Debrégeas, P. Martin, and F. Brochard-Wyart. Viscous bursting of suspended films. *Phys. Rev. Lett.*, 75:3886–3889, 1995.

[9] P. D. Howell. The draining of a two-dimensional bubble. *Journal of Engineering Mathematics*, 35:251–272, 1999.

[10] J. N. Israelachvili. *Intermolecular and surface forces*. Academic Press, London, 1992.

[11] K. Kumar, A. D. Nikolov, and D. T. Wasan. Effect of Film Curvature on Drainage of Thin Liquid Films. *Journal of Colloid and Interface Science*, 256:194–200, 2002.

[12] S. Metallaoui. Drainage d’un film liquide au-dessus d’une bulle: influence de sa géométrie. Master 1, Université Pierre et Marie Curie (UPMC) Paris VI, 2011.

[13] C. J. S. Petrie. Extensional viscosity: A critical discussions. *Journal of Non-Newtonian Fluid Mechanics*, 137:15–23, 2006.

[14] F. Pigeonneau and A. Sellier. Low-Reynolds-Number gravity-driven migration and deformation of bubbles near a free surface. *Phys.Fluids*, accepted for publication, 2011.

[15] H. M. Princen. Shape of a fluid drop at a liquid-liquid interface. *Journal of Colloid Science*, 18:178–195, 1963.

[16] E. Ruckenstein and R. K. Jain. Spontaneous rupture of thin liquid films. *J. Chem. Soc., Faraday Trans. 2*, 70:132–147, 1974.

[17] N. Savva and J. W. M. Bush. Viscous sheet retraction. *J. Fluid Mech.*, 626:211–240, 2009.

[18] G. I. Taylor. The dynamics of thin sheets of fluid. III. Disintegration of fluid sheets. *Proc. R. Soc. London, Ser. A*, 253:313–321, 1959.

[19] J. van der Schaaf and R. G. C. Beerkens. A model for foam formation, stability, and breakdown in glass-melting furnaces. *Journal of Colloid Interface Sci.*, pages 218–229, 2005.

[20] A. Vrij. Possible Mechanism for the Spontaneous Rupture of Thin, Free Liquid Films. *Discussion of the Faraday Society*, 42:23–33, 1966.

[21] D. Weaire and S. Hutzler. *The Physics of Foams*. Clarendon Press, Oxford, 1999.

[22] Z. Zapryanov and S. Tabakova. *Dynamics of Bubbles, Drops and Rigid Particles*. Kluwer Academic Publishers, Dordrecht, 1999.

Conclusion and Perspectives

In order to better understand the stability of glass foam, an experimental study at the bubble scale and on vertical film has been presented. There are several steps that appear as a single bubble is created in a liquid. At first it rises towards the free surface and its shape deforms. When it arrives at the surface and its quasi-static shape is reached, drainage appears in the bubbles lamella and evolution of thickness of the lamella can be determined until the rupture of the lamella - end of bubble lifetime. When the bubble lamella ruptures, it can disappear in the liquid or it can generate new bubbles. All of these steps were closely studied in this work and the main observations are presented in the summary below.

Exponential evolution of thickness of bubble lamella is observed for all viscosities and all bubble sizes investigated in silicon oil, which indicates a fully mobile interface. The results are in a good agreement with previous similar work of Debrégeas *et al.* [2]. Exponential decreasing of thickness is observed for all chemical compositions and all bubble sizes in molten glass as well and confirms a fully mobile interface of the bubble lamella under all tested conditions. Faster relative drainage is observed for smaller bubbles as a consequence of smaller deformed interfacial area during the experiment with molten glass. When a bubble reaches the free surface, its shape is close to quasi-static and the surface of the cup (S_{cap}) increases with Bond number. In the comparison, slower relative drainage for larger bubbles is not observed during the experiment with silicon oil. This liquid is often used as model liquid for molten glass. Based on the presented results, we can conclude, that the behavior of silicon oil is very different from molten glass. Silicon oil viscosity can be easily changed, which makes it a good model liquid for simulation of flow of melt, but the behavior of drainage of bubble lamella is very different, which makes silicon oil less applicable as a model liquid for bubble studies such as bubble lifetime or coalescence measurement. In the comparison, it was tested, that Castor or UCON oils have the same behavior than molten glass and can substitute silicon oil as the model liquid.

It has been shown, that bubble lifetime needs to be divided into two steps. First step is regular drainage during which decrease in thickness of the bubble lamella is observed. Duration of this step is influenced by glass properties, mainly viscosity, and bubble size. The second step of the bubble lifetime is irregular drainage and it is a function of temperature. The higher the temperature, the more probable is a long duration of irregular drainage. Backward flow of the molten glass into the bubble lamella, followed by a liquid motion, is observed during this period. Similar motion was observed long time ago by Conroy [1] at temperature above 1315°C, when sodium sulfate decompose, see sec. 2.4. In our work, we believe, that the motion appears as a consequence of variation of surface tension on the bubble surface (Marangoni flow). Variation of surface tension is a consequence of evaporation of sodium and hence non-homogeneous chemical surface composition of glass. Chemical analyses of the thin film confirms that sodium evaporation creates a decrease of Na close to the interface over a layer which thickness increases with temperature. Moreover, the liquid motion is observed for boron glasses below 1200°C and during the experiment with thin vertical film created in sulfate free glass, which confirms it cannot appear due to sodium decomposition. Hrma [3] presents, that bubble lifetime consists of two characteristic times. One of them is the drainage time and the second is a survival time of critically thin lamella, see sec. 3.4.2. This results are in a good agreement with our work, where we call the first characteristic time regular drainage and the second one irregular drainage. We can also complement this information, that while the first step is predictable, the second characteristic time is stochastic and its duration is influenced by temperature.

Our experimental results show, that the bubble lifetime is not a function of the nature of the gas or the redox state of the glass.

For the moment, only one formula for the bubble lifetime prediction can be found in the literature (eq. (3.10) in sec. 3.4.2). Nevertheless this formula contains the initial and critical thickness of the bubble lamella as well as a coefficient which corresponds to partial mobility. The coefficient is specific for various glass compositions and needs to be determined experimentally. The formula does not consider various draining speed for various bubble size. In the comparison, results obtained in our experimental work enable prediction of the bubble lifetime using glass properties and bubble size. However, it is important to emphasize, that bubble lifetime variation appears at high temperature, the stochastic irregular time can represent the major part of the lifetime, and therefore its prediction under these conditions is extremely difficult.

Lifetime of a vertical film was studied by Laimböck [5] and results of his work were already discussed in sec. 3.4.1. According to him, sodium sulfate behaves as an anti-foaming agent below 1350°C. The presence of sodium sulfate at low temperature is confirmed in our experiment, where the content of sulfate was determined in a solution of distilled water, which was poured on the surface of the cooled glass in the crucible, see sec. 5.2.3,5.2.5. At high temperature, Laimböck [5] observes longer lifetime, which according to him appears as a consequence of meta-stable lamella. We also observe longer lifetime of the vertical film and explain it as a consequence of Marangoni flow which appears at high temperature and forces the liquid to flow back into the film and increases the thickness, which is observed as a liquid motion in the film and corresponds with the observation at the bubble scale. It can be found in the work of Kappel *et al.* [4] (sec. 3.4.1), who measured evolution of thickness on a vertical film, that the draining process is accelerated when partial pressure of sodium is increased in the surrounding atmosphere. He explains, that viscosity of the glass can increase due to evaporation of sodium and therefore if partial pressure of sodium is increased in the surrounding atmosphere, it eliminates the evaporation and the viscosity remains low. Based on our observation, we can also think that the increased partial pressure in the surrounding atmosphere prevents the Marangoni flow from appearing.

Daughter bubbles appear as a new source of bubbles, which are formed out of a larger one after its rupture. The occurrence of daughter bubbles can be summed-up in a graph plotting a Reynolds number versus a capillary number based on the Taylor-Culick velocity. Daughter bubbles can appear as a cascade meaning that it is possible to obtain secondary daughter bubbles out of a ring of daughter bubbles. This process can create numerous small bubbles out of an original much larger bubble, which can be important during bubbling in furnace or glass melting in furnace with submerged burners. The graph proposed in Fig. 6.69 can be in reality different, because in order to determine the precise values of Reynolds and capillary numbers, we need to know the retraction velocity of the film. We will have to improve the experimental set-up with a fast recording video-camera to obtain this data. Nevertheless, the diagram and the described method can be used as a tool for prediction of the daughter bubble creation.

The behavior of a single bubble has been described in many details in this work. Nevertheless, it will be very interesting to verify the theory about evaporation of sodium and its influence on liquid motion appearance and irregular drainage duration. As it has been presented in the previous chapter, lifetime of a sequence of 100 bubbles can be divided into two steps. If this experiment is repeated under the same conditions but with increased partial pressure of sodium, according to the presented theory, the duration of regular drainage should remain constant, but the duration of the irregular drainage should be shorter. In order to determine if the backward liquid motion can be caused by the presented difference in surface tension, numerical simulation that studies drainage against gravity in the bubble lamella or vertical film should be done. Next steps in the study should be observation of two bubbles rising one after another and the influence on the evolution of the bubble lamella thickness.

References

[1] A. R. Conroy, W. H. Manring, and W. C. Bauer. The Role of Sulfate in the Melting and Fining of Glass Batch. *The Glass Industry*, 47, 1966.

[2] G. Debrégeas, P.-G. de Gennes, and F. Brochard-Wyart. The Life and Death of "Bare" Viscous Bubbles. *Science*, 279:1704–1707, 1998.

[3] P. Hrma. Model for a Steady State Foam Blanket. *Journal of Colloid and Interface Science*, 134(1):161–168, 1990.

[4] J. Kappel, R. Conradt, and H. Scholze. Foaming behaviour on glass melts. *Glasstech. Ber.*, 60:189–201, 1987.

[5] P. Laimböck. *Foaming of Glass Melts*. PhD thesis, 1998.

Appendices

Appendix A

Power received by the video-camera

Introduction

The radiation coming from the furnace perturbs the interferometry measurement of the film thickness. One of the solutions to remove the radiation of the furnace is to use a pulse laser. In order to know what kind of laser do we need, we must know the energy received by the video-camera filtered by the wavelength of the laser. The calculation of this energy is given in this appendix.

Power received by the video-camera

Fig. A.1 is a sketch of the radiation emission sent by the furnace. We consider that the radiation emission comes from the surface of glass depending directly on the absolute temperature of the furnace. The circular surface of the crucible, S_1 in Fig. A.1 is characterized by its radius r_1. The optical objective is also a circle with radius r_2. The distance between these two surfaces is equal to L. The power emitted by an elementary surface of S_1 in an elementary solid angle $d\Omega_{12}$ is given by

$$d^3Q_\lambda = L(\lambda, T)\cos\theta_1 dS_1 d\Omega_{12} d\lambda, \tag{A.1}$$

where $d\Omega_{12}$ is defined by

$$d\Omega_{12} = \frac{\cos\theta_2 dS_2}{r_{12}^2}. \tag{A.2}$$

We assume in this relationship that the furnace emits as black body. All geometrical parameters are defined in Fig. A.1. $L(\lambda, T)$ is the emittance of the black body given by the Planck's law:

$$L(\lambda, T) = \frac{2c^2h}{\lambda^5\left[e^{ch/k\lambda T} - 1\right]}, \tag{A.3}$$

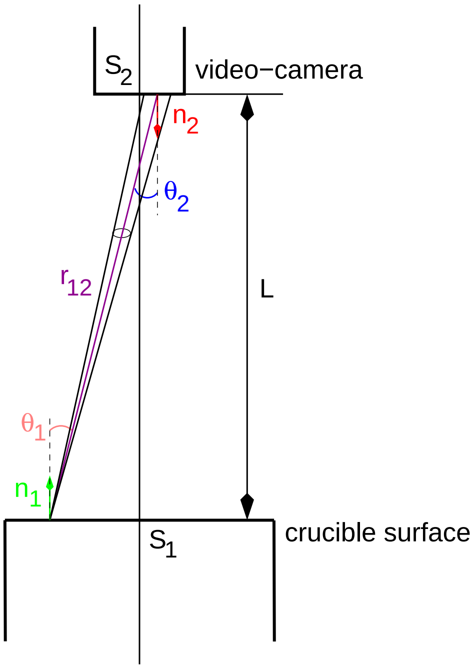

Figure A.1: Sketch of the radiation emission from the surface of the crucible received by the video camera.

in which, c is the light velocity, h the Planck's constant and k the Boltzmann's constant. The double integral over S_1 and S_2 gives the following power:

$$dQ_\lambda = \pi L(\lambda, T) S_1 F_{12} d\lambda, \tag{A.4}$$

where F_{12} is the form factor defined by

$$F_{12} = \frac{1}{S_1} \int_{S_1} \int_{S_2} \frac{\cos\theta_1 \cos\theta_2 dS_1 dS_2}{\pi r_{12}^2}. \tag{A.5}$$

For the two circular surfaces centered in the same axis, F_{12} is given by [1]:

$$F_{12} = \frac{1}{2} \left[X - \sqrt{X^2 - 4\left(\frac{r_2}{r_1}\right)^2} \right], \tag{A.6}$$

where X is defined by

$$X = 1 + \frac{L^2 + r_2^2}{r_1^2}. \tag{A.7}$$

dQ_λ is the power by unity of wavelength. This quantity has to be integrated by taking into account the filter fixed just in front of the video-camera centered in the wavelength of the laser. So, if we write the absorption spectrum of the filter, $f(\lambda)$, the power emitted by the furnace filtered at the wavelength of the laser is:

$$Q = \pi S_1 F_{12} \int_0^\infty L(\lambda, T) f(\lambda) d\lambda. \tag{A.8}$$

For a filter centered on green color, 532 nm, the range where the filter is transparent is $[531; 533]$ nm. From the experimental set-up, we have the geometrical data:

$$\begin{aligned} r_1 &= 2.5 \cdot 10^{-2} \text{ m}, && \text{(A.9)} \\ r_2 &= 1 \cdot 10^{-2} \text{ m}, && \text{(A.10)} \\ L &= 0.8 \text{ m}. && \text{(A.11)} \end{aligned}$$

So, F_{12} is equal to $1.561 \cdot 10^{-4}$. Finally, by an estimation of the integral in the range of $[531; 533]$ nm, eq. (A.8) gives

$$Q = 1.2 \cdot 10^{-3} \text{ mW}. \tag{A.12}$$

The density of power, Q/S_1 is therefore equal to

$$\frac{Q}{S_1} = 0.64 \cdot 10^{-4} \text{ mW/cm}^2. \tag{A.13}$$

References

[1] J. Taine, E. Iaconna, and J.-P. Petit. *Transferts thermiques. Introduction aux transferts d'énergie*. Dunod, Paris, 2008.

Appendix B

Chemical analyses

Glass	SiO_2	Na_2O	CaO	MgO	Al_2O_3	SO_3
0.01 wt% Fe_2O_3 sample 1	72.4	13.5	9.6	4.1	0.6	0.3
0.01 wt% Fe_2O_3 sample 2	72.2	13.5	9.6	4.1	0.6	0.3
0.01 wt% Fe_2O_3 sample 3	72.4	13.6	9.6	4.2	0.6	0.3

Table B.1: Initial chemical composition of glass with 0.01 wt% Fe_2O_3 in 3 samples before experiment.

Glass	SiO_2	Na_2O	CaO	K_2O	MgO	Al_2O_3	SO_3	Fe_2O_3	TiO_2
0.1 wt% Fe_2O_3 sample 1/1	71.8	13.2	8.6	0.1	3.6	0.8	0.24	0.08	0.04
0.1 wt% Fe_2O_3 sample 1/2	72.1	13.3	8.8	0.0	3.6	0.7	0.25	0.07	0.04
0.1 wt% Fe_2O_3 sample 1/3	72.1	13.5	9.1	0.1	3.5	0.8	0.23	0.06	0.05
0.1 wt% Fe_2O_3 sample 1/4	72.4	13.7	9.0	0.1	3.7	0.8	0.24	0.07	0.06
0.1 wt% Fe_2O_3 sample 1/5	72.0	13.4	8.8	0.1	3.7	0.9	0.24	0.08	0.04
0.1 wt% Fe_2O_3 sample 1/average	72.1	13.4	8.9	0.1	3.6	0.8	0.24	0.07	0.05

Table B.2: Initial chemical composition of glass with 0.1 wt% Fe_2O_3 at 5 points in the first sample.

Glass	SiO_2	Na_2O	CaO	K_2O	MgO	Al_2O_3	SO_3	Fe_2O_3	TiO_2
0.1 wt% Fe_2O_3 sample 2/1	72.1	13.1	9.2	0.1	3.6	0.8	0.25	0.10	0.04
0.1 wt% Fe_2O_3 sample 2/2	71.9	13.2	9.2	0.1	3.7	0.8	0.24	0.07	0.05
0.1 wt% Fe_2O_3 sample 2/3	72.0	13.3	9.0	0.1	3.7	0.8	0.23	0.08	0.05
0.1 wt% Fe_2O_3 sample 2/4	72.7	13.8	9.3	0.1	3.6	0.8	0.21	0.07	0.05
0.1 wt% Fe_2O_3 sample 2/5	72.8	12.9	9.0	0.1	3.7	0.8	0.26	0.06	0.04
0.1 wt% Fe_2O_3 sample 2/average	72.3	13.3	9.1	0.1	3.7	0.8	0.24	0.08	0.05

Table B.3: Initial chemical composition of glass with 0.1 wt% Fe_2O_3 at 5 points in the second sample.

Glass	SiO_2	Na_2O	CaO	K_2O	MgO	Al_2O_3	SO_3	Fe_2O_3	TiO_2
0.1 wt% Fe_2O_3 sample 3/1	72.2	13.2	8.9	0.1	3.7	0.8	0.24	0.07	0.04
0.1 wt% Fe_2O_3 sample 3/2	71.6	13.2	9.0	0.1	3.5	0.8	0.23	0.07	0.04
0.1 wt% Fe_2O_3 sample 3/3	71.8	13.1	9.0	0.1	3.6	0.8	0.23	0.05	0.03
0.1 wt% Fe_2O_3 sample 3/4	71.9	13.6	9.0	0.1	3.6	0.8	0.24	0.08	0.05
0.1 wt% Fe_2O_3 sample 3/5	72.3	12.9	9.0	0.1	3.7	0.7	0.24	0.08	0.03
0.1 wt% Fe_2O_3 sample 3/average	72.0	13.2	9.0	0.1	3.6	0.8	0.24	0.07	0.04

Table B.4: Initial chemical composition of glass with 0.1 wt% Fe_2O_3 at 5 points in the third sample.

Glass	SiO_2	Na_2O	CaO	MgO	Al_2O_3	SO_3
0.01 wt% Fe_2O_3 sample 1	72.4	13.6	9.7	4.2	0.6	0.3
0.01 wt% Fe_2O_3 sample 2	72.6	13.6	9.5	4.1	0.6	0.3
0.01 wt% Fe_2O_3 sample 3	72.7	13.7	9.5	4.1	0.6	0.3

Table B.5: Chemical composition of glass with 0.01 wt% Fe_2O_3 in 3 samples obtained from the bulk after experiment.

Glass	**SiO_2**	**Na_2O**	**CaO**	**MgO**	**Al_2O_3**	**SO_3**
0.01 wt% Fe_2O_3 TOP 1	71.8	13.5	10.0	3.7	0.6	0.3
0.01 wt% Fe_2O_3 TOP 2	72.6	13.4	9.7	3.6	0.6	0.3
0.01 wt% Fe_2O_3 TOP 3	72.5	13.3	9.6	3.8	0.5	0.3
0.01 wt% Fe_2O_3 TOP 4	72.1	13.4	9.5	3.9	0.6	0.3
0.01 wt% Fe_2O_3 TOP 5	72.4	13.3	9.7	3.8	0.6	0.3
0.01 wt% Fe_2O_3 TOP 6	72.6	13.5	9.8	3.8	0.6	0.3
0.01 wt% Fe_2O_3 TOP 7	72.4	13.5	9.7	3.7	0.6	0.3
0.01 wt% Fe_2O_3 TOP 8	72.1	13.4	9.6	3.6	0.6	0.3
0.01 wt% Fe_2O_3 TOP 9	72.2	13.2	9.7	3.9	0.5	0.3
0.01 wt% Fe_2O_3 TOP 10	72.2	13.2	9.6	3.6	0.6	0.3

Table B.6: Chemical composition of glass with 0.01 wt% Fe_2O_3 at 10 points in 5 samples from the top of the platinum crucible after experiment.

Glass	**SiO_2**	**Na_2O**	**CaO**	**MgO**	**Al_2O_3**	**SO_3**
0.01 wt% Fe_2O_3 BOTTOM 1	73.4	13.5	9.8	3.9	0.5	0.3
0.01 wt% Fe_2O_3 BOTTOM 2	73.2	13.2	9.5	4.0	0.6	0.2
0.01 wt% Fe_2O_3 BOTTOM 3	72.6	13.2	9.4	3.7	0.7	0.2
0.01 wt% Fe_2O_3 BOTTOM 4	73.1	13.2	9.6	3.8	0.6	0.2
0.01 wt% Fe_2O_3 BOTTOM 5	73.5	13.3	9.3	3.8	0.5	0.2
0.01 wt% Fe_2O_3 BOTTOM 6	72.5	13.6	9.5	3.6	0.6	0.3
0.01 wt% Fe_2O_3 BOTTOM 7	72.6	13.7	9.7	3.9	0.6	0.3
0.01 wt% Fe_2O_3 BOTTOM 8	73.0	13.3	9.8	3.7	0.5	0.3
0.01 wt% Fe_2O_3 BOTTOM 9	72.4	13.1	9.7	3.9	0.6	0.3
0.01 wt% Fe_2O_3 BOTTOM 10	72.8	13.3	9.7	3.5	0.6	0.3

Table B.7: Chemical composition of glass with 0.01 wt% Fe_2O_3 at 10 points in 5 samples from the bottom of the platinum crucible after experiment.

Glass	**SiO_2**	**Na_2O**	**CaO**	**K_2O**	**MgO**	**Al_2O_3**	**SO_3**	**Fe_2O_3**	**TiO_2**
0.1 wt% Fe_2O_3 sample 1/1	71.7	13.2	9.5	0.1	3.7	0.7	0.22	0.07	0.04
0.1 wt% Fe_2O_3 sample 1/2	71.2	13.3	9.3	0.0	3.7	0.8	0.26	0.09	0.02
0.1 wt% Fe_2O_3 sample 1/3	71.4	13.0	9.0	0.0	3.7	0.8	0.23	0.08	0.03
0.1 wt% Fe_2O_3 sample 1/4	71.6	13.3	9.0	0.1	3.6	0.8	0.20	0.07	0.04
0.1 wt% Fe_2O_3 sample 1/5	71.5	13.1	9.3	0.1	3.5	0.8	0.24	0.08	0.03

Table B.8: Chemical composition of glass with 0.1 wt% Fe_2O_3 at 5 points in the first sample after experiment.

Glass	**SiO_2**	**Na_2O**	**CaO**	**K_2O**	**MgO**	**Al_2O_3**	**SO_3**	**Fe_2O_3**	**TiO_2**
0.1 wt% Fe_2O_3 sample 2/1	71.5	13.2	9.1	0.1	3.8	0.8	0.22	0.05	0.04
0.1 wt% Fe_2O_3 sample 2/2	72.1	13.3	9.3	0.1	3.6	0.7	0.24	0.08	0.04
0.1 wt% Fe_2O_3 sample 2/3	71.7	13.3	8.7	0.1	3.6	0.7	0.23	0.09	0.03
0.1 wt% Fe_2O_3 sample 2/4	71.9	13.4	9.0	0.1	3.7	0.8	0.22	0.09	0.05
0.1 wt% Fe_2O_3 sample 2/5	71.5	13.5	8.6	0.1	3.8	0.7	0.22	0.08	0.05

Table B.9: Chemical composition of glass with 0.1 wt% Fe_2O_3 at 5 points in the second sample after experiment.

Glass	**SiO_2**	**Na_2O**	**CaO**	**B_2O_3**	**Al_2O_3**	**SO_3**
1 wt% B_2O_3 top 1	70.6	12.7	13.2	0.9	2.1	0.2
1 wt% B_2O_3 top 2	70.4	12.8	13.1	0.9	2.1	0.2
1 wt% B_2O_3 top 3	70.4	12.8	13.1	0.9	2.0	0.3
1 wt% B_2O_3 top 4	70.8	12.9	13.1	0.9	2.1	0.3
1 wt% B_2O_3 top 5	70.4	12.8	13.1	0.8	2.1	0.3
1 wt% B_2O_3 top 6	70.3	12.8	13.1	0.8	2.1	0.3

Table B.10: Chemical composition of glass with 1 wt% B_2O_3 at 6 points in the sample from the top of the platinum crucible after experiment.

Glass	**SiO_2**	**Na_2O**	**CaO**	**B_2O_3**	**Al_2O_3**	**SO_3**
1 wt% B_2O_3 bottom 1	70.7	12.9	13.2	0.9	2.1	0.3
1 wt% B_2O_3 bottom 2	70.4	12.7	13.0	0.9	2.1	0.3
1 wt% B_2O_3 bottom 3	70.5	12.8	13.1	0.9	2.1	0.3
1 wt% B_2O_3 bottom 4	70.5	12.8	13.2	0.9	2.0	0.3
1 wt% B_2O_3 bottom 5	70.5	12.7	13.1	0.9	2.1	0.3

Table B.11: Chemical composition of glass with 1 wt% B_2O_3 at 5 points in the sample from the bottom of the platinum crucible after experiment.

Glass	**SiO_2**	**Na_2O**	**CaO**	**B_2O_3**	**Al_2O_3**	**SO_3**
10 wt% B_2O_3 first 1	62.2	12.5	13.1	11.0	2.1	0.1
10 wt% B_2O_3 first 2	62.0	12.5	13.1	10.6	1.9	0.1
10 wt% B_2O_3 first 3	62.6	12.3	13.1	10.5	2.1	0.1
10 wt% B_2O_3 first 4	62.1	12.5	12.8	10.9	1.9	0.1
10 wt% B_2O_3 first 5	61.9	12.7	13.1	10.7	2.0	0.1

Table B.12: Chemical composition of glass with 10 wt% B_2O_3 at 5 points in a sample from the bulk of the platinum crucible after first experiment.

Glass	**SiO_2**	**Na_2O**	**CaO**	**B_2O_3**	**Al_2O_3**	**SO_3**
10 wt% B_2O_3 second 1	61.7	12.5	12.9	10.8	2.0	0.1
10 wt% B_2O_3 second 2	61.9	12.5	13.1	10.9	2.0	0.1
10 wt% B_2O_3 second 3	62.0	12.6	12.9	10.8	2.0	0.1
10 wt% B_2O_3 second 4	61.1	12.3	12.9	10.9	2.0	0.1
10 wt% B_2O_3 second 5	61.1	12.3	12.9	10.6	2.0	0.1

Table B.13: Chemical composition of glass with 10 wt% B_2O_3 at 5 points in a sample from the bulk of the platinum crucible after second experiment.

Appendix C

Surface tension of experimental glasses

T_F (°C)	T_E (°C)	Dietzel	Lyon	Rubenstein	Kucuk	final
1100	1044	337.2	-	-	-	332
1200	1142	333.3	-	-	-	328
1300	1228	329.9	326.6	326.6	-	324
1400	1350	325.0	322.6	-	317.8	320

Table C.1: Surface tension of glass with 0.01 wt% Fe_2O_3 for all tested temperatures.

T_F (°C)	T_E (°C)	Dietzel	Lyon	Rubenstein	Kucuk	final
1100	1044	331.7	-	-	-	328
1200	1142	327.8	-	-	-	324
1300	1228	324.4	321.1	321.6	-	320
1400	1350	319.5	317.1	-	315.2	316
1500	1442	-	-	-	-	312
1550	1492	-	-	-	-	310

Table C.2: Surface tension of glass with 0.1 wt% Fe_2O_3 for all tested temperatures.

T_F (°C)	T_E (°C)	Dietzel	Lyon	Rubenstein	Kucuk	final
1100	1044	330.2	-	-	-	331
1200	1142	326.4	-	-	-	327
1300	1228	322.9	322.7	322.9	-	323
1400	1350	317.9	319.3	-	319.8	319

Table C.3: Surface tension of glass with 1 wt% B_2O_3 for all tested temperatures.

T_F (°C)	T_E (°C)	Dietzel	Lyon	Rubenstein	Kucuk	final
1000	940	-	-	-	-	310
1050	990	-	-	-	-	308
1100	1044	308.7	-	-	-	306
1200	1142	304.8	-	-	-	302
1300	1228	301.3	297.3	297.7	-	298
1350	1291	-	-	-	-	296
1400	1350	296.4	290.1	-	298.0	294

Table C.4: Surface tension of glass with 10 wt% B_2O_3 for all tested temperatures.

T_F (°C)	T_E (°C)	Dietzel	Lyon	Rubenstein	Kucuk	final
1300	1228	318.6	310.7	310.7	-	303
1400	1350	313.7	-	-	-	299
1473	1414	311.1	298.1	-	298.9	297

Table C.5: Surface tension of AKM glass for the most tested temperatures. The coefficients for 1400°C in the computation by Lyon and Kucuk were used for T_E=1414°C and not 1350°C like for other glass compositions.

Appendix D

Computation of glass properties

D.1 Computation of surface tension

```
//DATA INPUT
//temperature of glass
T = ?;
//composition of glass in weight percentage
SiO2hm = ?;
GeO2hm = ?;
TiO2hm = ?;
ZrO2hm = ?;
ThO2hm = ?;
SnO2hm = ?;
Al2O3hm = ?;
Fe2O3hm = ?;
BeOhm = ?;
MgOhm = ?;
CaOhm = ?;
SrOhm = ?;
BaOhm = ?;
ZnOhm = ?;
CdOhm = ?;
MnOhm = ?;
CoOhm = ?;
NiOhm = ?;
Li2Ohm = ?;
```

```
Na2Ohm = ?;
CaF2hm =?;
K2Ohm = ?;
PbOhm = ?;
B2O3hm = ?;
Sb2O3hm = ?;
P2O5hm = ?;
V2O5hm = ?;
WO3hm = ?;
MoO3hm = ?;
Cr2O3hm = ?;
Rb2Ohm = ?;
FeOhm = ?;
//END OF DATA INPUT - DO NOT CHANGE WHAT IS BELOW!!!

//computation from Volf (Miloš B. Volf, Sklo ve výpočtech, Praha 1984)
S=[SiO2hm,GeO2hm,TiO2hm,ZrO2hm,ThO2hm,SnO2hm,Al2O3hm,Fe2O3hm,
BeOhm,MgOhm,CaOhm,SrOhm,BaOhm,ZnOhm,CdOhm,MnOhm,CoOhm,NiOhm,
Li2Ohm,Na2Ohm,CaF2hm,K2Ohm,PbOhm,B2O3hm,Sb2O3hm,P2O5hm,
V2O5hm,WO3hm,MoO3hm,Cr2O3hm];
D900 = [3.4,0,3,4.1,0,0,6.2,4.5,0,6.6,4.8,0,3.7,4.7,0,4.5,4.5,4.5,4.6,1.5,3.7,0.1,
1.2,0.8,0,0,-6.1,0,0,-5.9];
L1200 = [3.25,0,0,4.1,0,0,5.98,0,0,5.77,4.92,0,3.7,0,0,0,0,0,0,1.27,0,0,0,0.23,0,
0,0,0,0,0];
L1400 = [3.24,0,0,6.5,0,0,5.85,0,0,5.49,4.92,0,3.8,0,0,0,0,0,0,1.12,0,-0.75,0,-0.23,
0,0,0,0,0,0];
R1200 = [3.25,2.6,3,4.1,0.5,0.5,5.98,5,11,5.77,4.92,3.8,3.5,4.7,3,0,4.5,0,3,1.27,0,0,
1.2,0.23,1.5,1.5,2.5,4,0,0];

Dietzel_900 = sum(S .*D900);
Dietzel_temp_correction = Dietzel_900-4*((T-900)/100);
Lyon_1200 = sum(S .*L1200);
Lyon_1400 = sum(S .*L1400);

Lyon_correction_1200 = 1;
Lyon_correction_1400 = 1;
rate = SiO2hm/Na2Ohm;
```

```
if rate==3.5 then
Lyon_correction_1200 = Lyon_1200+0;
Lyon_correction_1400 = Lyon_1400+0;
else
if rate==2 then
Lyon_correction_1200 = Lyon_1200+30;
Lyon_correction_1400 = Lyon_1400+30;
else if rate==1 then
Lyon_correction_1200 = Lyon_1200+80;
Lyon_correction_1400 = Lyon_1400+80;
else
Lyon_correction_1200 = Lyon_1200+0;
Lyon_correction_1400 = Lyon_1400+0;
end;
end;
end;

Rubenstein_1200 = sum(S .*R1200);

//computation given by Kucuk et al. (Kucuk, Clare, Jones, Glass Technol. 40, 1999)
SiO2Mi = 60.0843;
PbOMi = 223.1994;
ZnOMi = 81.3894;
CaOMi = 56.0774;
MgOMi = 40.3044;
BaOMi = 153.3264;
Na2OMi = 61.97894;
Al2O3Mi = 101.961276;
K2OMi = 94.196;
Li2OMi = 29.8814;
B2O3Mi = 69.6202;
Rb2OMi = 186.935;
SrOMi = 103.6194;
FeOMi = 71.8444;
MnOMi = 70.937449;
MoO3Mi = 143.9382;
```

```
SiO2molpod = SiO2hm/SiO2Mi;
PbOmolpod = PbOhm/PbOMi;
ZnOmolpod = ZnOhm/ZnOMi;
CaOmolpod = CaOhm/CaOMi;
MgOmolpod = MgOhm/MgOMi;
BaOmolpod = BaOhm/BaOMi;
Na2Omolpod = Na2Ohm/Na2OMi;
Al2O3molpod = Al2O3hm/Al2O3Mi;
K2Omolpod = K2Ohm/K2OMi;
Li2Omolpod = Li2Ohm/Li2OMi;
B2O3molpod = B2O3hm/B2O3Mi;
Rb2Omolpod = Rb2Ohm/Rb2OMi;
SrOmolpod = SrOhm/SrOMi;
FeOmolpod = FeOhm/FeOMi;
MnOmolpod = MnOhm/MnOMi;
MoO3molpod = MoO3hm/MoO3Mi;

suma=SiO2molpod+PbOmolpod+ZnOmolpod+CaOmolpod+MgOmolpod+BaOmolpod+
K2Omolpod+Na2Omolpod+Al2O3molpod+Li2Omolpod+B2O3molpod+Rb2Omolpod+
SrOmolpod+FeOmolpod+MnOmolpod+MoO3molpod;

//computation of mol% composition
SiO2 = SiO2molpod/suma;
PbO = PbOmolpod/suma;
ZnO = ZnOmolpod/suma;
CaO = CaOmolpod/suma;
MgO = MgOmolpod/suma;
BaO = BaOmolpod/suma;
K2O = K2Omolpod/suma;
Na2O = Na2Omolpod/suma;
Al2O3 = Al2O3molpod/suma;
Li2O = Li2Omolpod/suma;
B2O3 = B2O3molpod/suma;
Rb2O = Rb2Omolpod/suma;
SrO = SrOmolpod/suma;
FeO = FeOmolpod/suma;
MnO = MnOmolpod/suma;
```

```
MoO3 = MoO3molpod/suma;

SiO2mol = SiO2*100;
PbOmol = PbO*100;
ZnOmol = ZnO*100;
CaOmol = CaO*100;
MgOmol = MgO*100;
BaOmol = BaO*100;
K2Omol = K2O*100;
Na2Omol = Na2O*100;
Al2O3mol = Al2O3*100;
Li2Omol = Li2O*100;
B2O3mol = B2O3*100;
Rb2Omol = Rb2O*100;
SrOmol = SrO*100;
FeOmol = FeO*100;
MnOmol = MnO*100;
MoO3mol = MoO3*100;

Kucuk_1400=271.2+1.48*Li2Omol-2.22*K2Omol-3.43*Rb2Omol+1.96*MgOmol+
3.34*CaOmol+1.28*BaOmol+3.32*SrOmol+2.68*FeOmol+2.92*MnOmol-
1.38*PbOmol-2.86*B2O3mol+3.47*Al2O3mol-24.5*MoO3mol;

//OUTPUT
T
Dietzel_900
Dietzel_temp_correction
rate
Lyon_1200
Lyon_correction_1200
Lyon_1400
Lyon_correction_1400
Rubenstein_1200
Kucuk_1400
```

D.2 Computation of density and refractive index

```
//computation of density and refractive index of glass by Demkina
//only for content of PbO below 45 weight percentage

//DATA INPUT
//composition of glass in weight percentage
SiO2hm = ?;
PbOhm = ?;
ZnOhm = ?;
CaOhm = ?;
MgOhm = ?;
BaOhm = ?;
K2Ohm = ?;
Na2Ohm = ?;
Al2O3hm = ?;
Li2Ohm = ?;
B2O3hm = ?;
//END OF DATA INPUT - DO NOT CHANGE WHAT IS BELOW!!!

//computation of molar weight
SiO2Mi = 60.0843;
PbOMi = 223.1994;
ZnOMi = 81.3894;
CaOMi = 56.0774;
MgOMi = 40.3044;
BaOMi = 153.3264;
K2OMi = 94.196;
Na2OMi = 61.97894;
Al2O3Mi = 101.961276;
Li2OMi = 29.8814;
B2O3Mi = 69.6202;

SiO2molpod = SiO2hm/SiO2Mi;
PbOmolpod = PbOhm/PbOMi;
ZnOmolpod = ZnOhm/ZnOMi;
CaOmolpod = CaOhm/CaOMi;
```

```
MgOmolpod = MgOhm/MgOMi;
BaOmolpod = BaOhm/BaOMi;
K2Omolpod = K2Ohm/K2OMi;
Na2Omolpod = Na2Ohm/Na2OMi;
Al2O3molpod = Al2O3hm/Al2O3Mi;
Li2Omolpod = Li2Ohm/Li2OMi;
B2O3molpod = B2O3hm/B2O3Mi;

suma = SiO2molpod+PbOmolpod+ZnOmolpod+CaOmolpod+MgOmolpod+BaOmolpod+
K2Omolpod+Na2Omolpod+Al2O3molpod+Li2Omolpod+B2O3molpod;

//computation of glass composition in mol percentage
SiO2 = SiO2molpod/suma;
PbO = PbOmolpod/suma;
ZnO = ZnOmolpod/suma;
CaO = CaOmolpod/suma;
MgO = MgOmolpod/suma;
BaO = BaOmolpod/suma;
K2O = K2Omolpod/suma;
Na2O = Na2Omolpod/suma;
Al2O3 = Al2O3molpod/suma;
Li2O = Li2Omolpod/suma;
B2O3 = B2O3molpod/suma;

SiO2mol = SiO2*100;
PbOmol = PbO*100;
ZnOmol = ZnO*100;
CaOmol = CaO*100;
MgOmol = MgO*100;
BaOmol = BaO*100;
K2Omol = K2O*100;
Na2Omol = Na2O*100;
Al2O3mol = Al2O3*100;
Li2Omol = Li2O*100;
B2O3mol = B2O3*100;

siSiO2l = 60;
```

```
siSiO2II = 60;
diSiO2I = 2.27;
diSiO2II = 2.2;
niSiO2I = 1.475;
niSiO2II = 1.458;

if SiO2mol>80 then
siSiO2 = siSiO2II;
diSiO2 = diSiO2II;
niSiO2 = niSiO2II;
else
siSiO2 = siSiO2I;
diSiO2 = diSiO2I;
niSiO2 = niSiO2I;
end;

if B2O3mol==0 then
b4 = 0;
else
No = (PbOmol+BaOmol+CaOmol+K2Omol+Na2Omol-Al2O3mol)/B2O3mol;
deltaSiO2 = SiO2mol-(0.5*(ZnOmol+MgOmol)+BaOmol+CaOmol+
2*(B2O3mol+PbOmol+Na2Omol)+4*K2Omol);
if No<1.2 then
b4 = No-0.2;
else if deltaSiO2>0 then
b4 = 1;
else deltaSiO2<0;
b4 = 2/3;
end;
end;
end;

b3 = 1-b4;
siB2O3 = b4*43+b3*70;
diB2O3 = b4*2.95+b3*1.85;
niB2O3 = b4*1.61+b3*1.464;
```

```
siPbO = 343;
diPbO = 11.7;
niPbO = 2.46;
siZnO = 223;
diZnO = 6.8;
niZnO = 1.96;
siCaO = 84;
diCaO = 3.7;
niCaO = 1.83;
siMgO = 140;
diMgO = 2.9;
niMgO = 1.63;
siBaO = 213;
diBaO = 8;
niBaO = 2.025;
siK2O = 94;
diK2O = 2.92;
niK2O = 1.58;
siNa2O = 62;
diNa2O = 3.03;
niNa2O = 1.59;
siAl2O3 = 59;
diAl2O3 = 2.5;
niAl2O3 = 1.49;
siLi2O = 30;
diLi2O = 2.5;
niLi2O = 1.65;

numerator_mass = (SiO2hm*diSiO2)/siSiO2+(PbOhm*diPbO)/siPbO+(ZnOhm*diZnO)/siZnO+
(CaOhm*diCaO)/siCaO+(MgOhm*diMgO)/siMgO+(BaOhm*diBaO)/siBaO+
(K2Ohm*diK2O)/siK2O+(Na2Ohm*diNa2O)/siNa2O+(Al2O3hm*diAl2O3)/siAl2O3
+(Li2Ohm*diLi2O)/siLi2O+(B2O3hm*diB2O3)/siB2O3;
denominator_mass = SiO2hm/siSiO2+PbOhm/siPbO+ZnOhm/siZnO+CaOhm/siCaO
+MgOhm/siMgO+BaOhm/siBaO+K2Ohm/siK2O+Na2Ohm/siNa2O+Al2O3hm/siAl2O3+
Li2Ohm/siLi2O+B2O3hm/siB2O3; mass = numerator_mass/denominator_mass;
mass_in_kg_m3=mass*1000;
```

```
numerator_n = (SiO2hm*niSiO2)/siSiO2+(PbOhm*niPbO)/siPbO+(ZnOhm*niZnO)/siZnO
+(CaOhm*niCaO)/siCaO+(MgOhm*niMgO)/siMgO+(BaOhm*niBaO)/siBaO+
(K2Ohm*niK2O)/siK2O+(Na2Ohm*niNa2O)/siNa2O+(Al2O3hm*niAl2O3)/siAl2O3+
(Li2Ohm*niLi2O)/siLi2O+(B2O3hm*niB2O3)/siB2O3;
denominator_n = SiO2hm/siSiO2+PbOhm/siPbO+ZnOhm/siZnO+CaOhm/siCaO
+MgOhm/siMgO+BaOhm/siBaO+K2Ohm/siK2O+Na2Ohm/siNa2O+Al2O3hm/siAl2O3+
Li2Ohm/siLi2O+B2O3hm/siB2O3; n = numerator_n/denominator_n;

//RESULTS
mass_in_kg_m3
n
```

Appendix E

Computation of the scale on the level

The scale can be determined at the top and at the bottom of the crucible from Fig. E.1. The level of the glass is between the bottom and the top at distance 30 mm far from the bottom, see Fig. E.2. Linear approximation can be applied to compute the scale at the level of the glass. If the scale is 820 pix at the bottom of the crucible, so at the zero height, and 1050 pix at the top, which is 80 mm far from the bottom, than the scale for the level of the glass, which

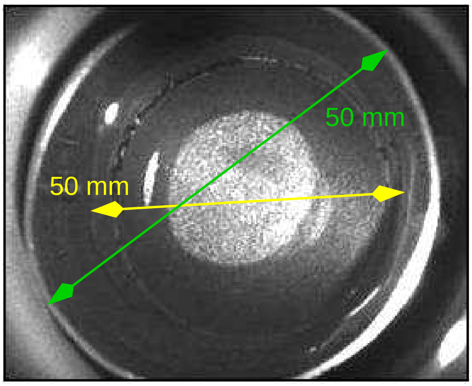

Figure E.1: Scale at the bottom and at the top of platinum crucible.

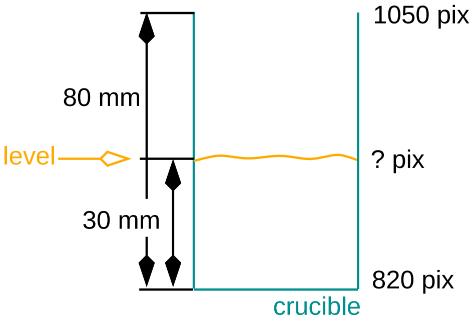

Figure E.2: Sketch of a platinum crucible and its scale at the top and bottom part.

is 30 mm far from the bottom, can be computed as follows:

$$y = Ax + B \tag{E.1}$$

$$1050 = A \cdot 80 + B \tag{E.2}$$

$$820 = A \cdot 0 + B \tag{E.3}$$

$$B = 820 \tag{E.4}$$

$$A = 2.875 \tag{E.5}$$

$$\mathrm{level} = 2.875 \cdot 30 + 820 = 906.25\,\mathrm{pix} \tag{E.6}$$

Appendix F

Computation of thickness

Light reflection by two interfaces of liquid film with thickness h is given in Fig. F.1. Ray r is reflected by the first interface as r_1 and by the second interface as r_2. The thickness of the film can be computed thank to the path differences between rays one and two. While the ray r_1 moves in media with a refractive index n_1 between points A and B, ray r_2 moves in media with a refractive index n_2 from point A to E and to C. The difference in these trajectories is the path difference (PD):

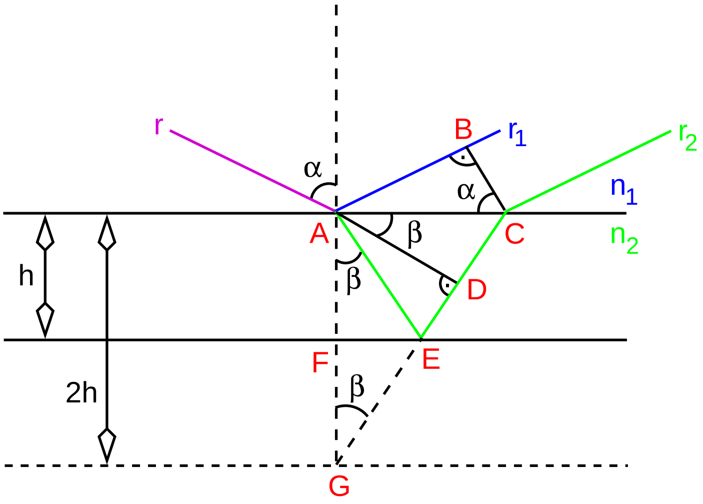

Figure F.1: Light reflection by two interfaces of liquid film with thickness h.

$$PD = n_2(|AE| + |EC|) - n_1|AB| \tag{F.1}$$

If we consider, that $|AE| = |EG|$ and $|GC| = |GD| + |DC|$, we can write:

$$PD = n_2(|GD| + |DC|) - n_1|AB| \tag{F.2}$$

Thanks to Snell's law:

$$\frac{\sin\alpha}{\sin\beta} = \frac{n_2}{n_1} \tag{F.3}$$

It is obvious from Fig. F.1 that:

$$\sin\beta = \frac{|DC|}{|AC|} \tag{F.4}$$

as well as:

$$\sin\alpha = \frac{|AB|}{|AC|} \tag{F.5}$$

Using eq. (F.2), (F.3), (F.4) and (F.5), we obtain for the path difference:

$$PD \;=\; n_2\left(|GD| + |AB|\frac{n_1}{n_2}\right) - n_1|AB| \;=\; n_2|GD| \tag{F.6}$$

$|GD|$ can be written as:

$$|GD| = |AG|\cos\beta = 2h\cos\beta \tag{F.7}$$

Using eq. (F.6) and (F.7), the path difference can be written as:

$$PD \;=\; n_2 \cdot 2h\cos\beta + \frac{1}{2}\lambda, \tag{F.8}$$

where λ is the wavelength of the reflected light and $\frac{1}{2}\lambda$ needs to be added, because the light is reflected by a medium of a higher refractive index [1]. $\cos\beta$ is considered to be one, because β is a very small angle close to zero for normal incidence. The intensity of the reflected light reaches maximum if the path difference is a multiple of an integer k (eq. (F.9)) and it reaches a minimum if the path difference is a multiple of integer k plus one half (eq. (F.10)). This is also called a constructive or destructive interference.

$$PD \;=\; n_2 \cdot 2h + \frac{1}{2}\lambda = k\lambda \tag{F.9}$$

$$PD \;=\; n_2 \cdot 2h + \frac{1}{2}\lambda = \left(k + \frac{1}{2}\right)\lambda \tag{F.10}$$

The final formula for the thickness computed in minimum and maximum intensity of the light is given as follows:

$$h_{max} = \frac{\lambda}{4 \cdot n_2}(2k - 1) \tag{F.11}$$

$$h_{min} = \frac{\lambda}{2 \cdot n_2}k \tag{F.12}$$

References

[1] C. Isenberg. *The science of soap films and soap bubbles*. Dover Pub., 1992.

Appendix G

Evolution of thickness

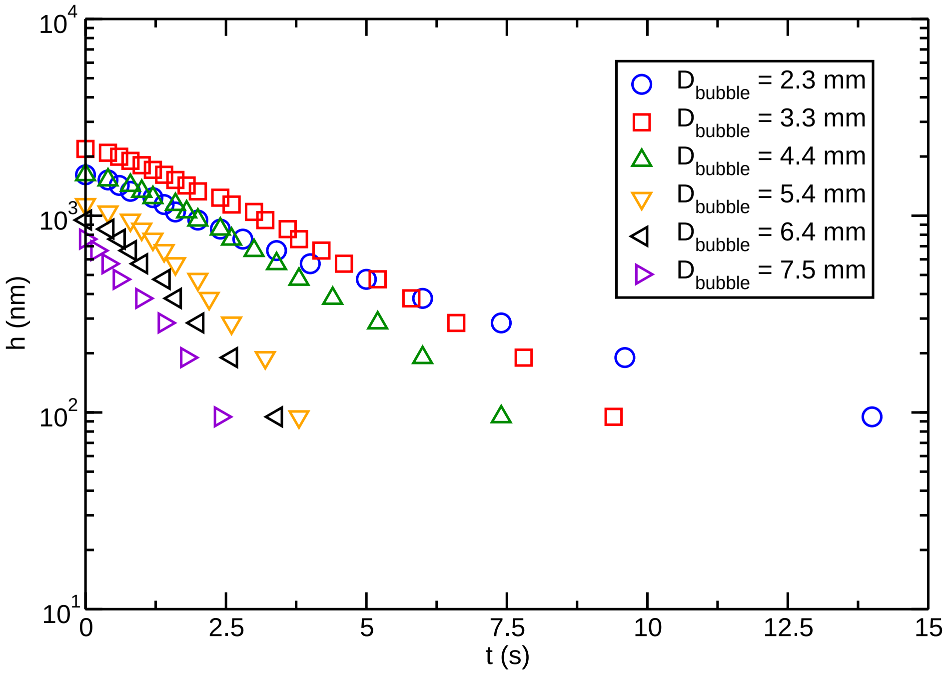

Figure G.1: Evolution of thickness for various bubble size in silicon oil with viscosity 10 Pa·s.

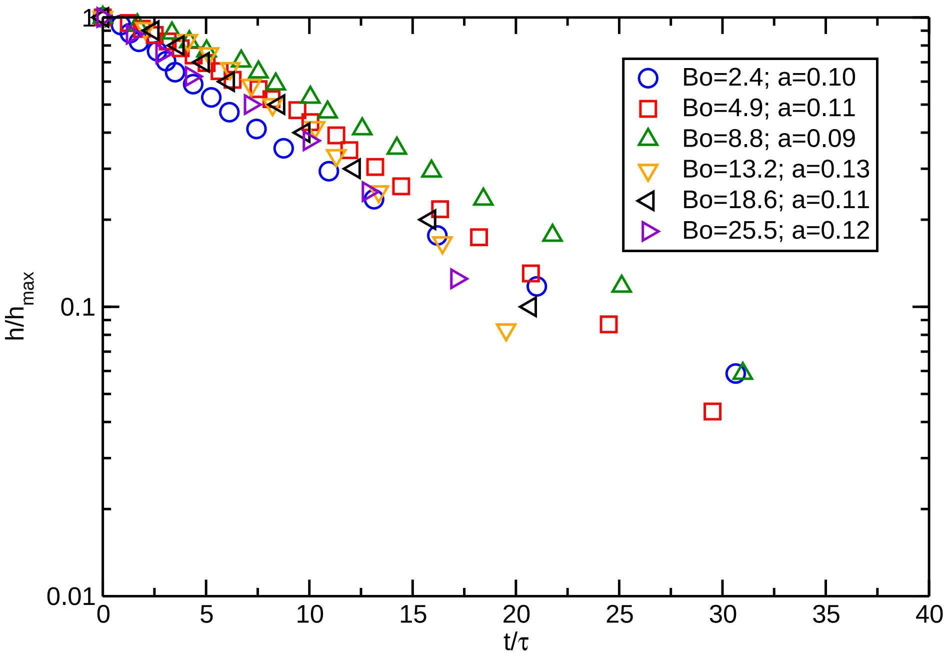

Figure G.2: Normalized evolution of thickness for various bubble size in silicon oil with viscosity 10 Pa·s.

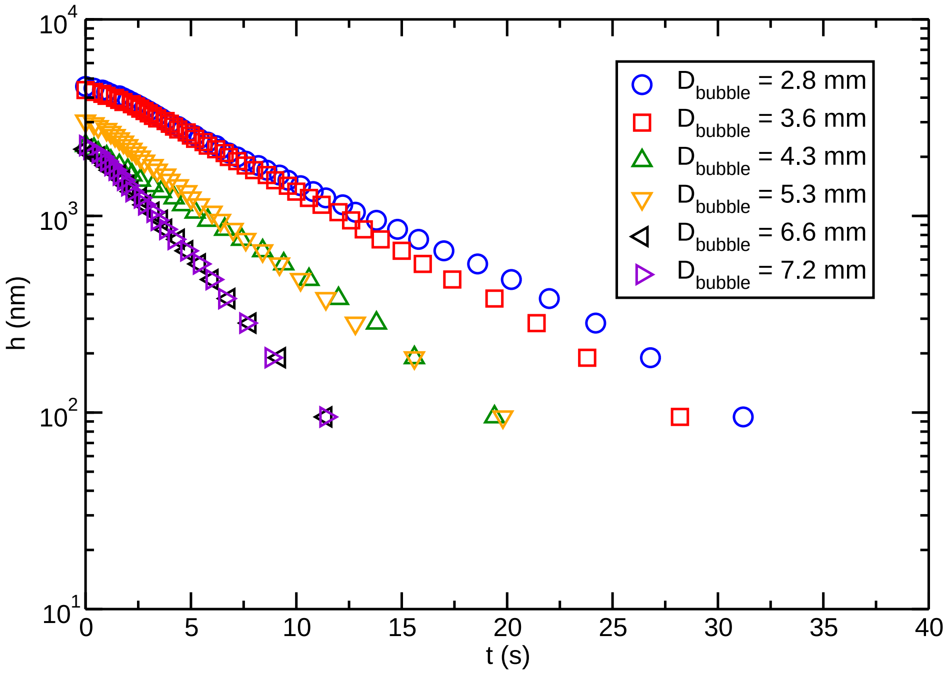

Figure G.3: Evolution of thickness for various bubble size in silicon oil with viscosity 23 Pa·s.

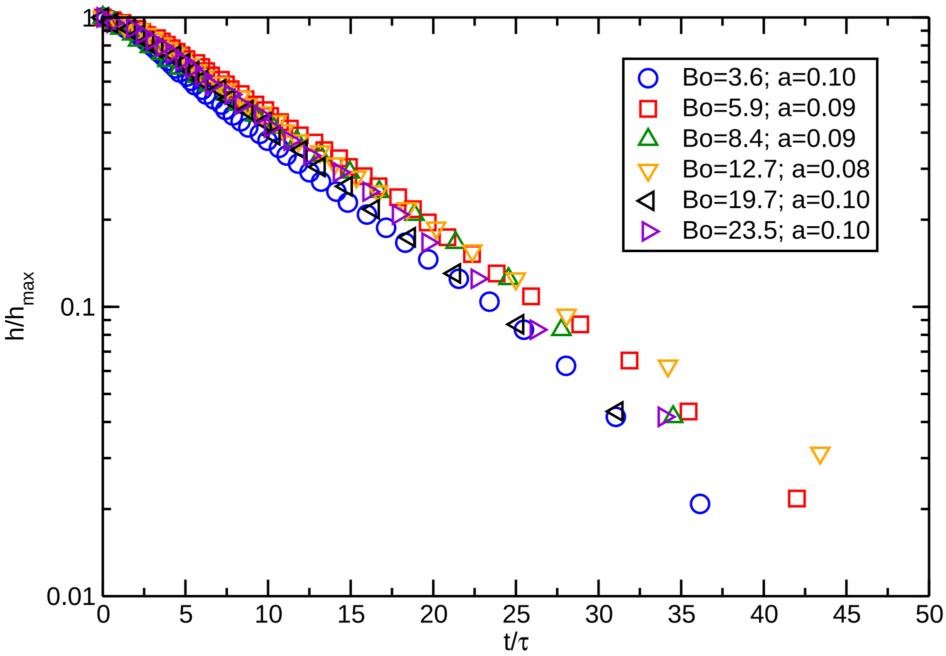

Figure G.4: Normalized evolution of thickness for various bubble size in silicon oil with viscosity 23 Pa·s.

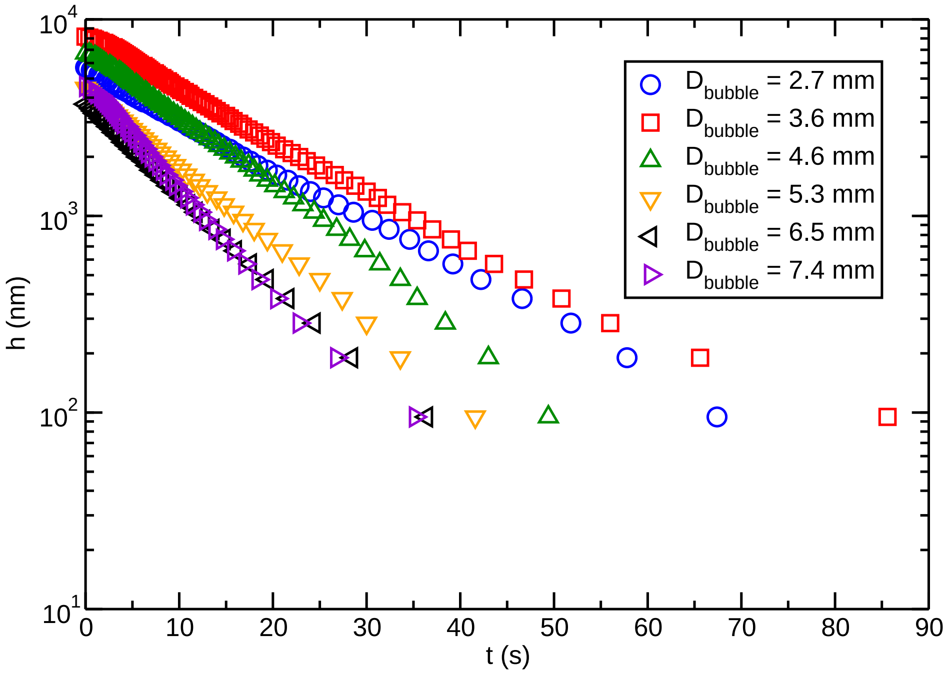

Figure G.5: Evolution of thickness for various bubble size in silicon oil with viscosity 51 Pa·s.

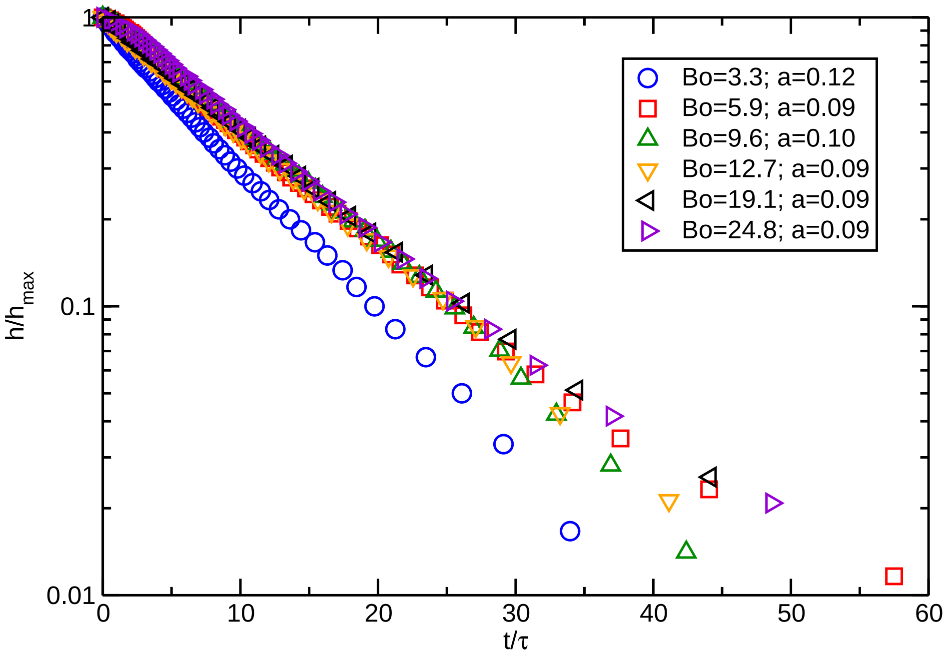

Figure G.6: Normalized evolution of thickness for various bubble size in silicon oil with viscosity 51 Pa·s.

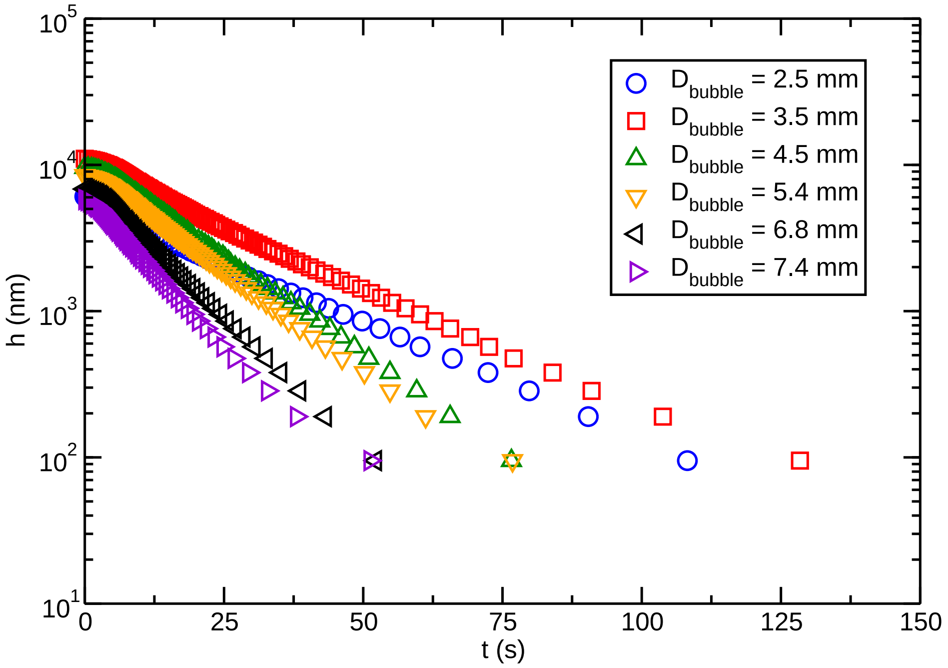

Figure G.7: Evolution of thickness for various bubble size in silicon oil with viscosity 74 Pa·s.

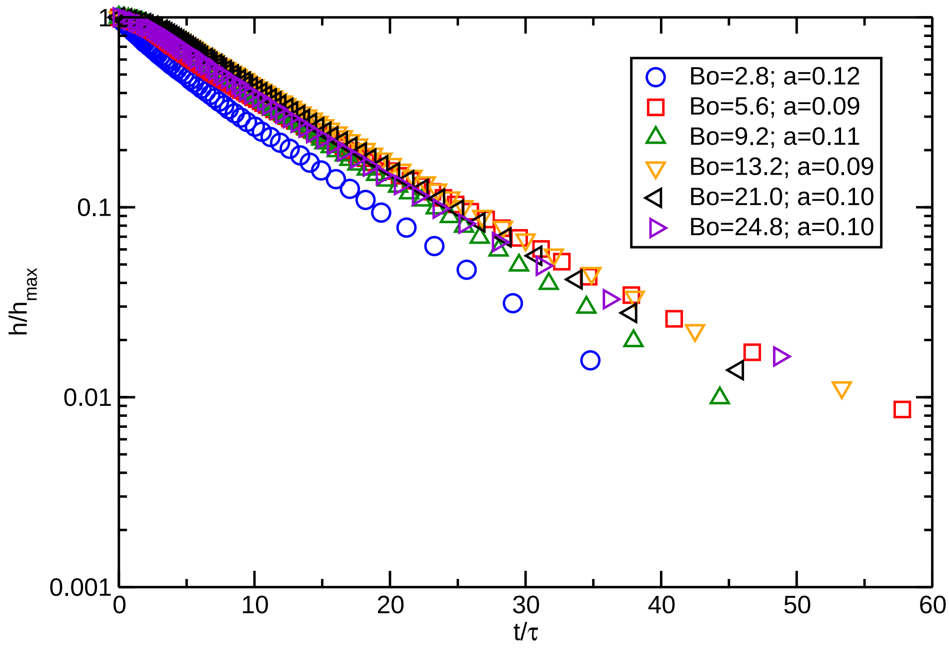

Figure G.8: Normalized evolution of thickness for various bubble size in silicon oil with viscosity 74 Pa·s.

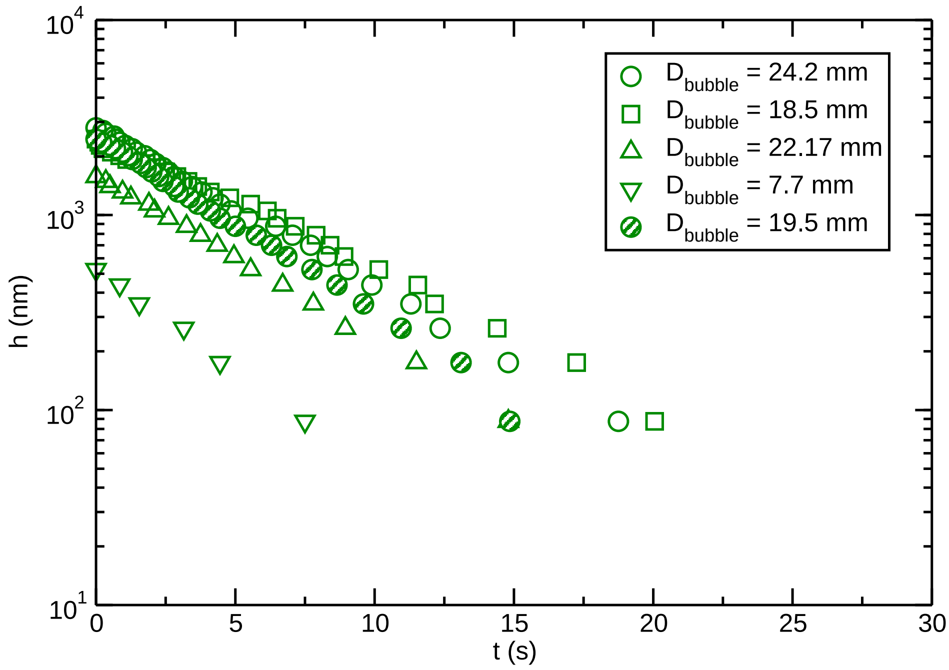

Figure G.9: Evolution of thickness for various bubble size in soda-lime-silica glass with 0.01 wt% of Fe_2O_3 and temperature 1142°C.

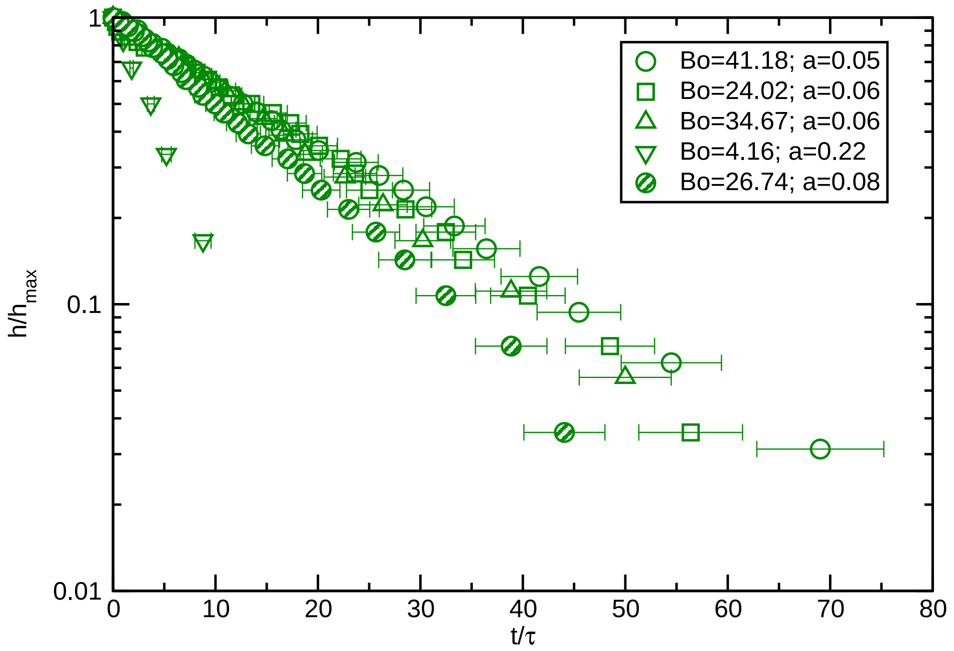

Figure G.10: Normalized evolution of thickness for various bubble size in soda-lime-silica glass with 0.01 wt% of Fe_2O_3 and temperature 1142°C.

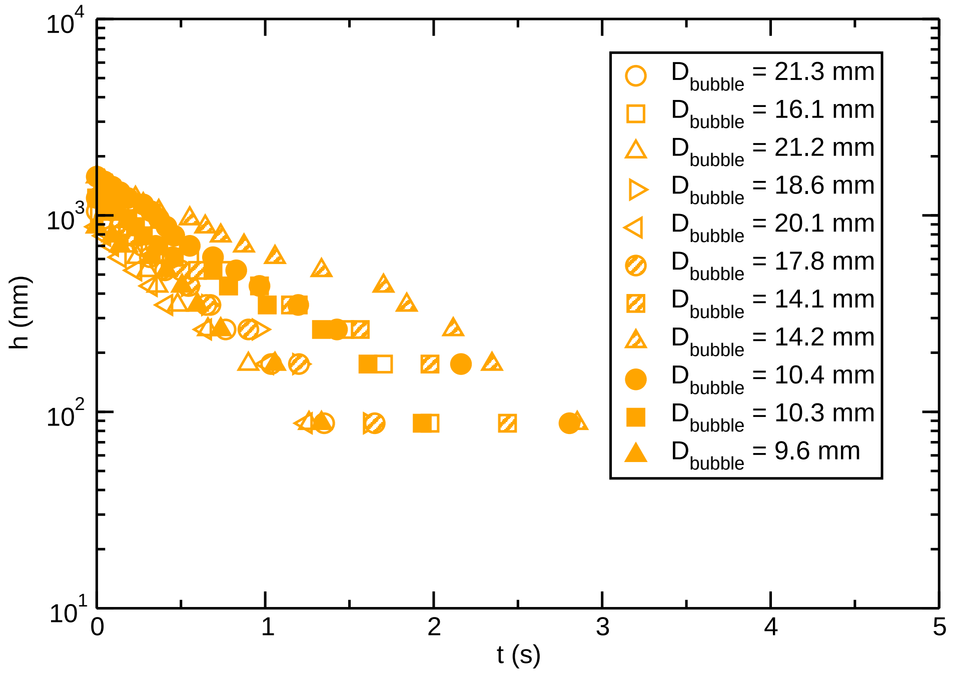

Figure G.11: Evolution of thickness for various bubble size in soda-lime-silica glass with 0.01 wt% of Fe_2O_3 and temperature 1228°C.

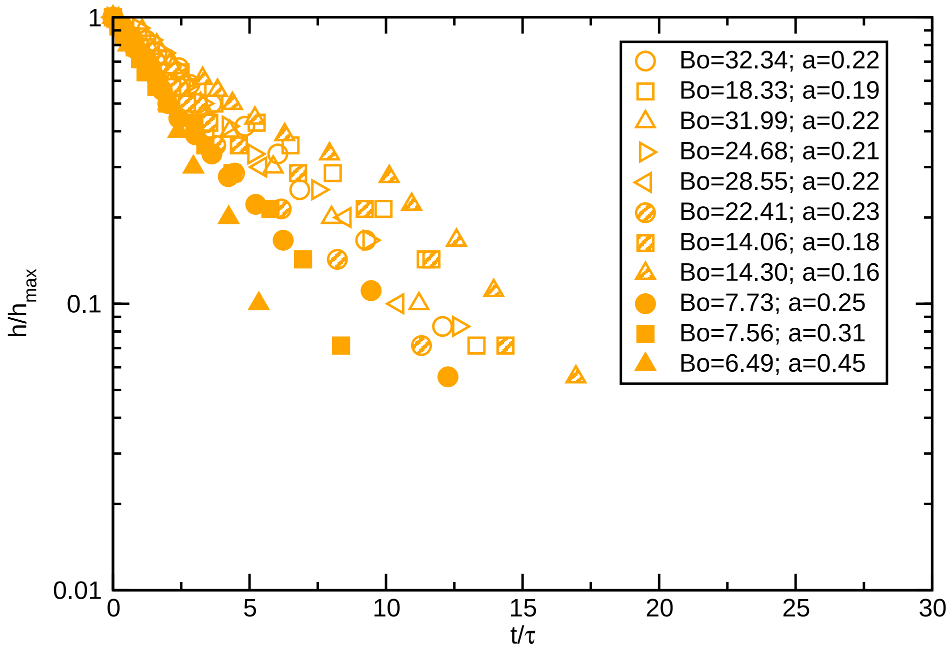

Figure G.12: Normalized evolution of thickness for various bubble size in soda-lime-silica glass with 0.01 wt% of Fe_2O_3 and temperature 1228°C.

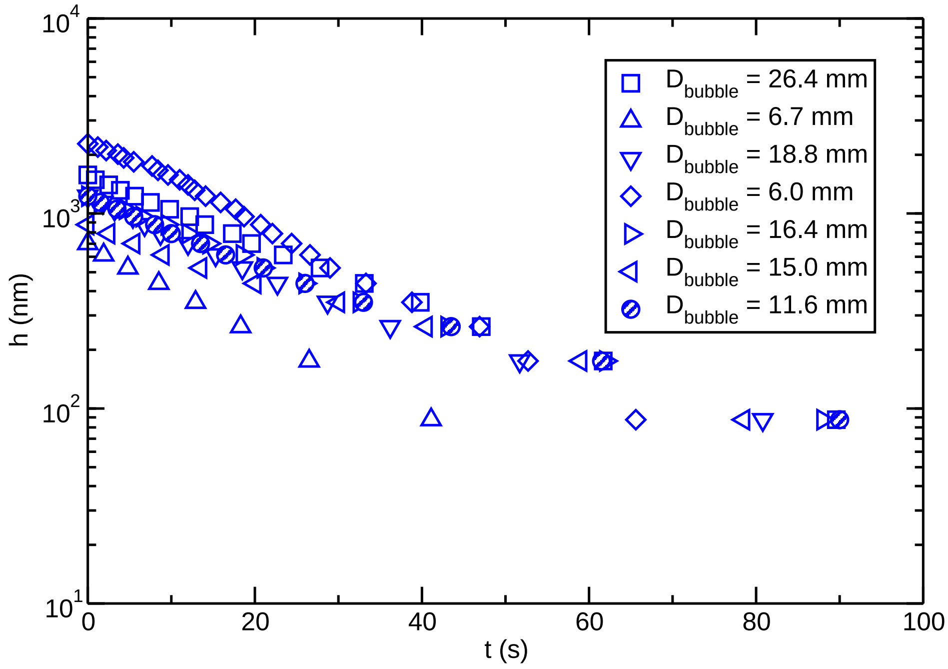

Figure G.13: Evolution of thickness for various bubble size in soda-lime-silica glass with 0.1 wt% of Fe_2O_3 and temperature 1044°C.

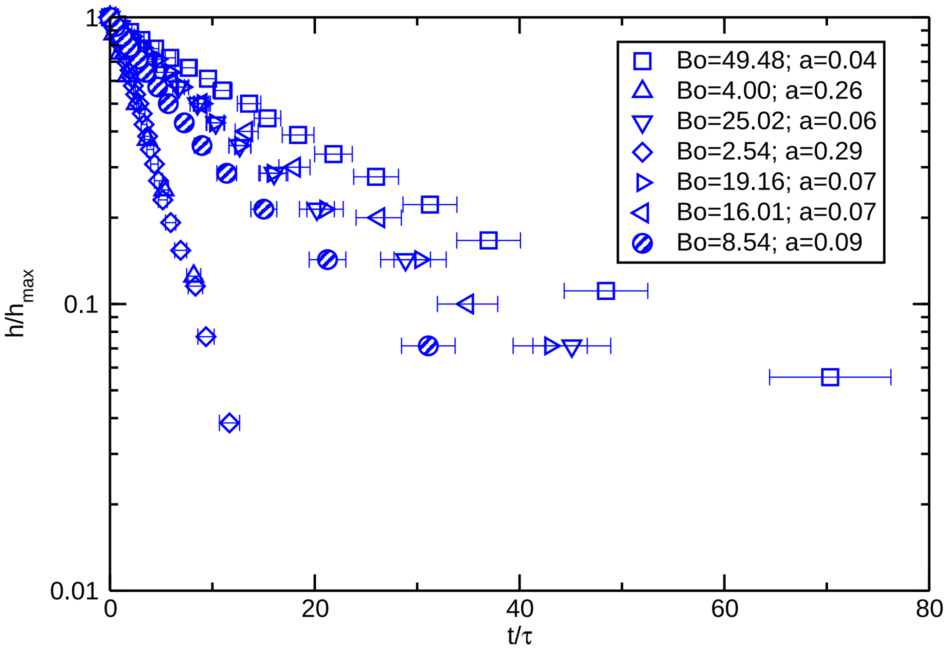

Figure G.14: Normalized evolution of thickness for various bubble size in soda-lime-silica glass with 0.1 wt% of Fe_2O_3 and temperature 1044°C.

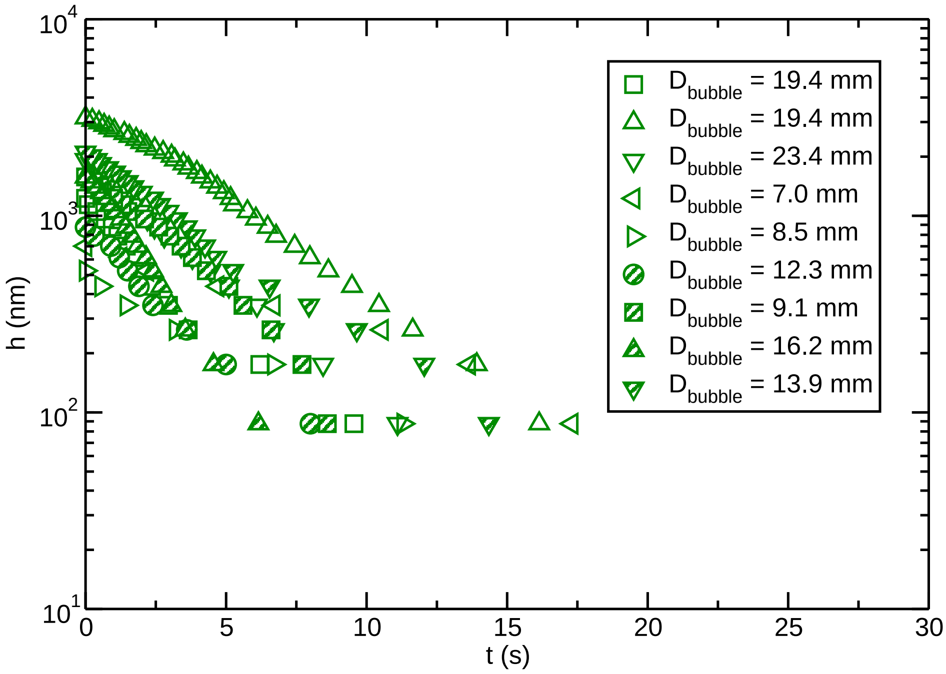

Figure G.15: Evolution of thickness for various bubble size in soda-lime-silica glass with 0.1 wt% of Fe_2O_3 and temperature 1142°C.

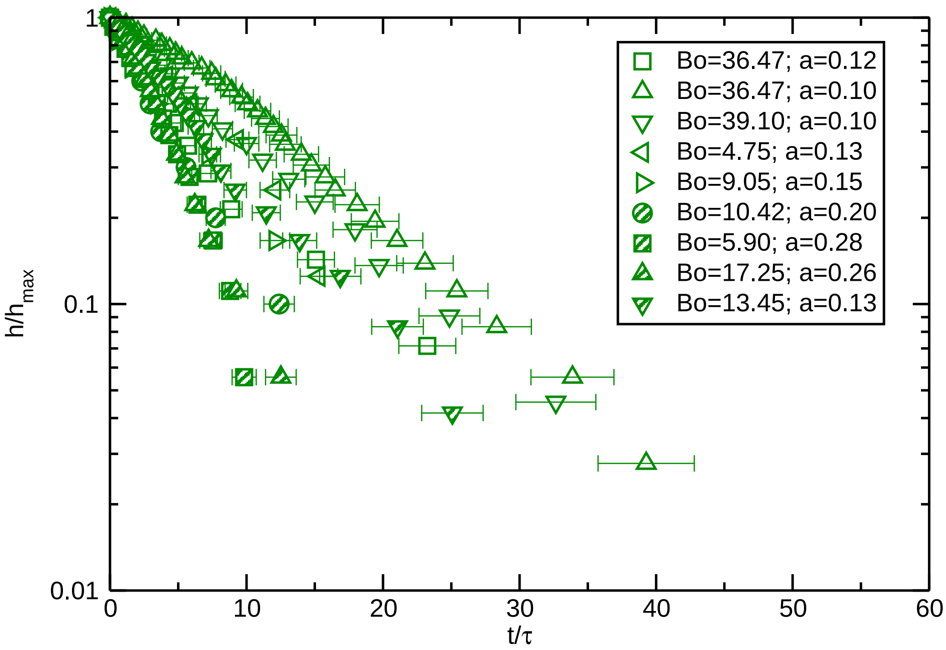

Figure G.16: Normalized evolution of thickness for various bubble size in soda-lime-silica glass with 0.1 wt% of Fe_2O_3 and temperature 1142°C.

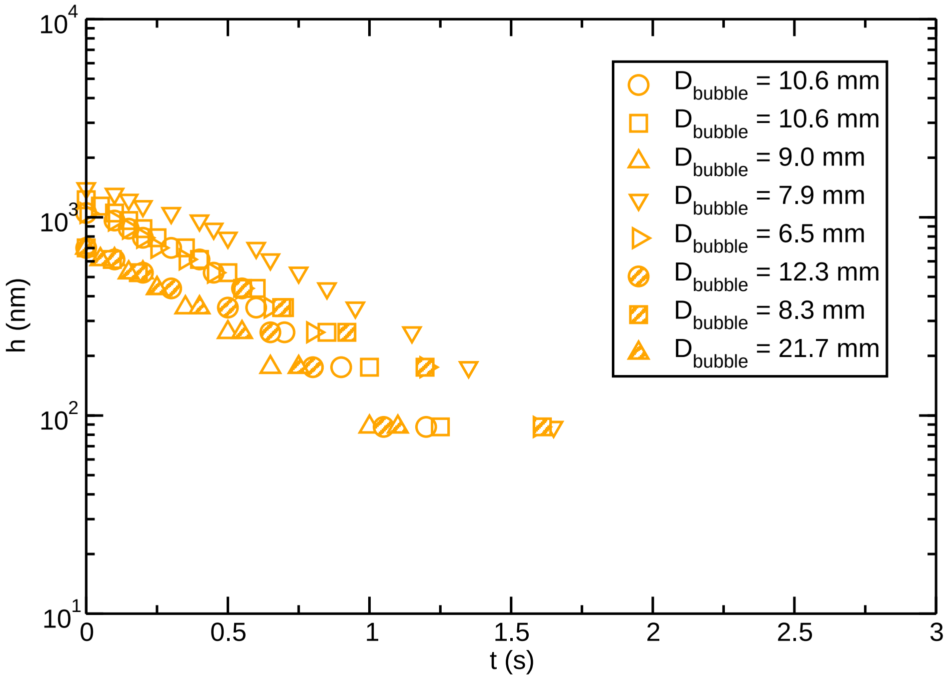

Figure G.17: Evolution of thickness for various bubble size in soda-lime-silica glass with 0.1 wt% of Fe_2O_3 and temperature 1228°C.

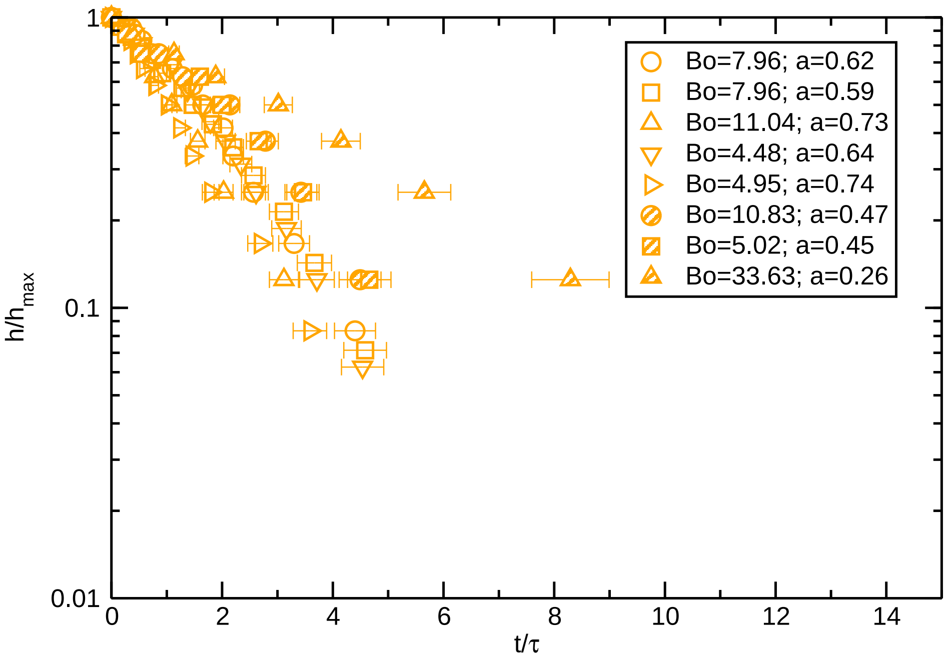

Figure G.18: Normalized evolution of thickness for various bubble size in soda-lime-silica glass with 0.1 wt% of Fe_2O_3 and temperature 1228°C.

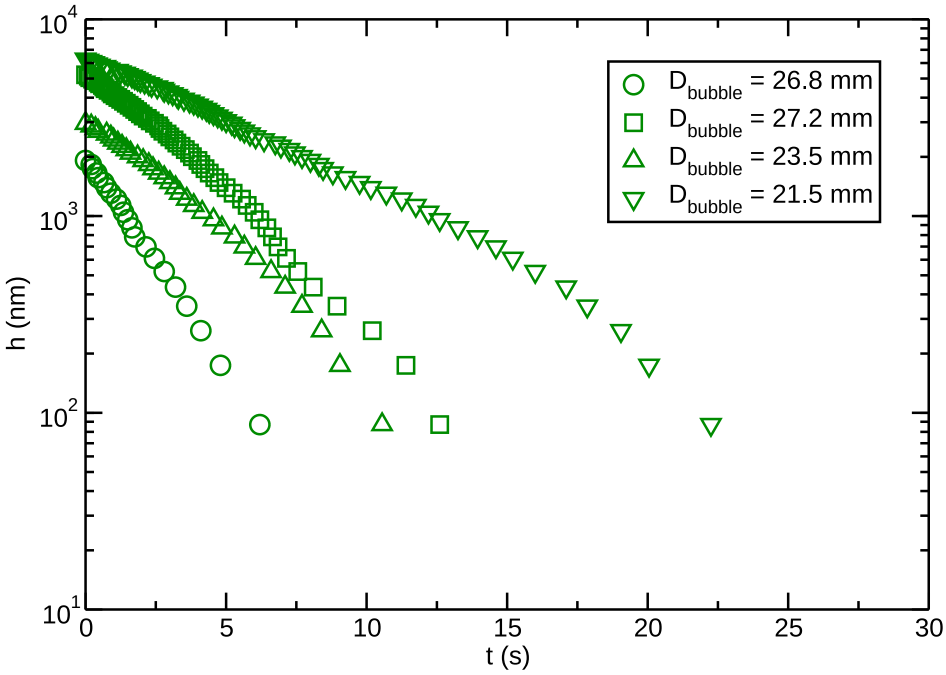

Figure G.19: Evolution of thickness for various bubble size in soda-lime-silica glass with 1 wt% of B_2O_3 and temperature 1142°C.

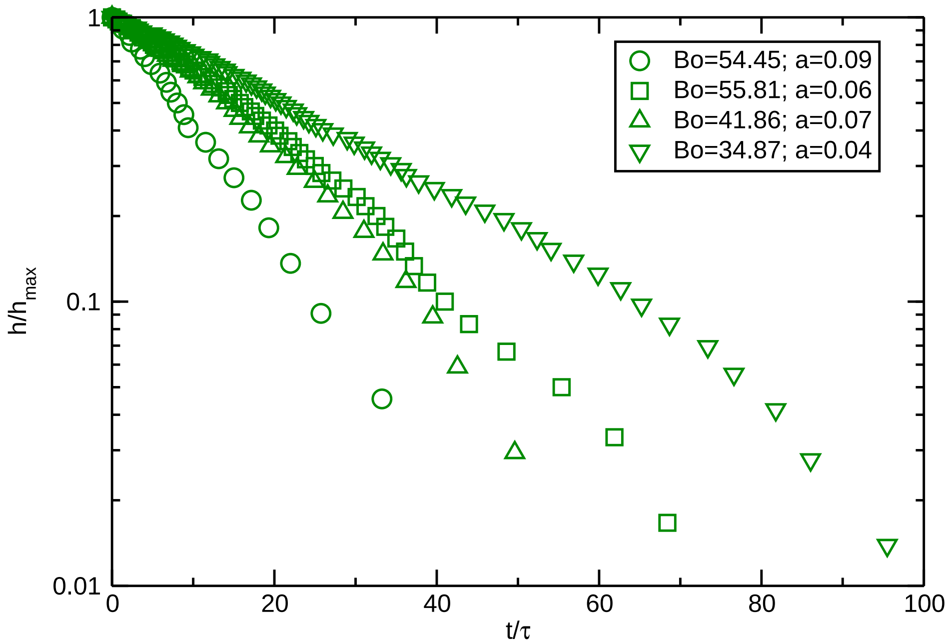

Figure G.20: Normalized evolution of thickness for various bubble size in soda-lime-silica glass with 1 wt% of B_2O_3 and temperature 1142°C.

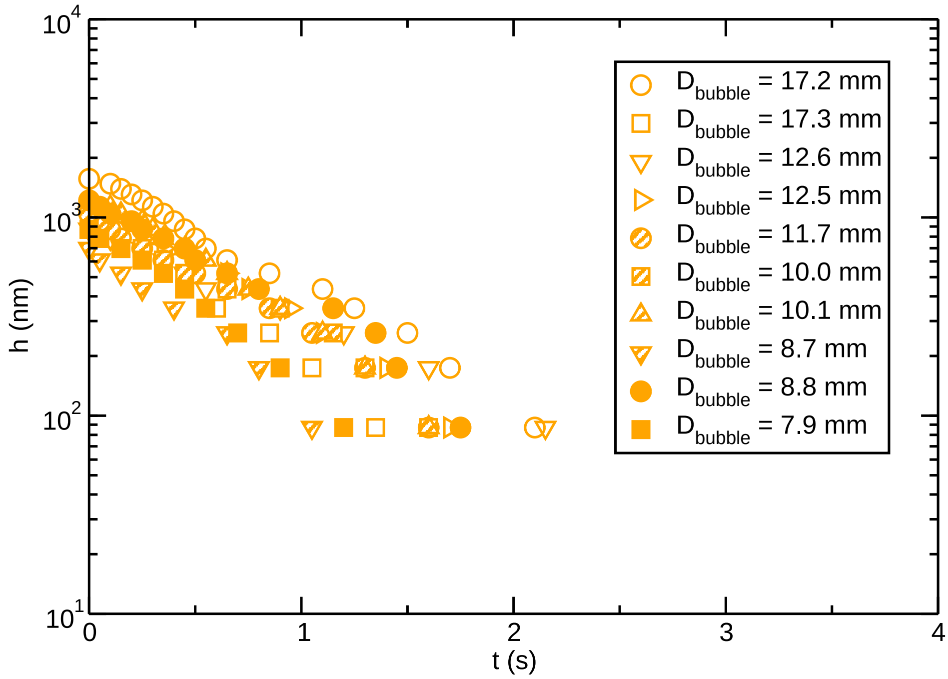

Figure G.21: Evolution of thickness for various bubble size in soda-lime-silica glass with 1 wt% of B_2O_3 and temperature 1228°C.

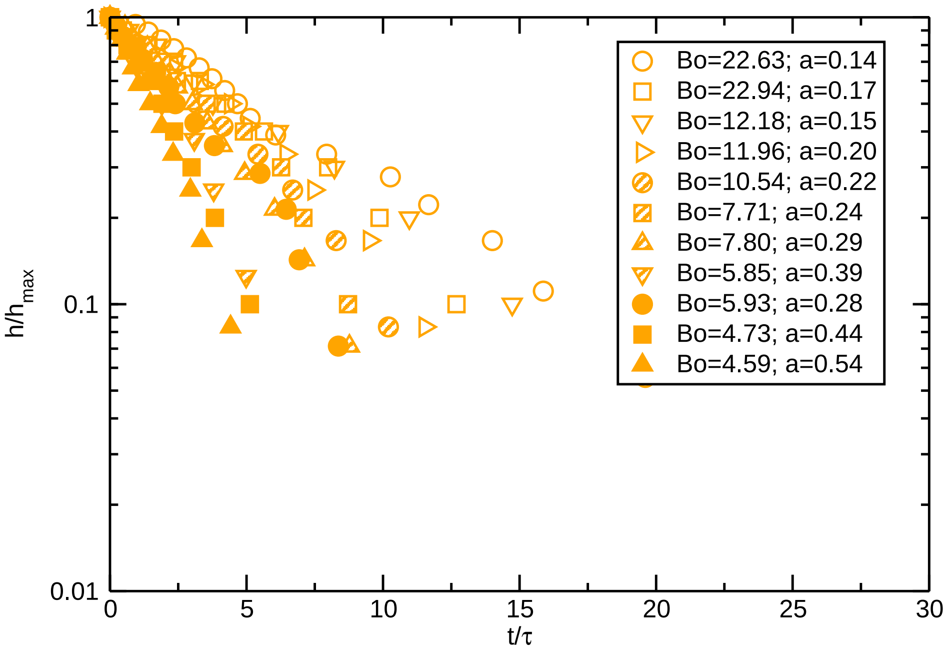

Figure G.22: Normalized evolution of thickness for various bubble size in soda-lime-silica glass with 1 wt% of B_2O_3 and temperature 1228°C.

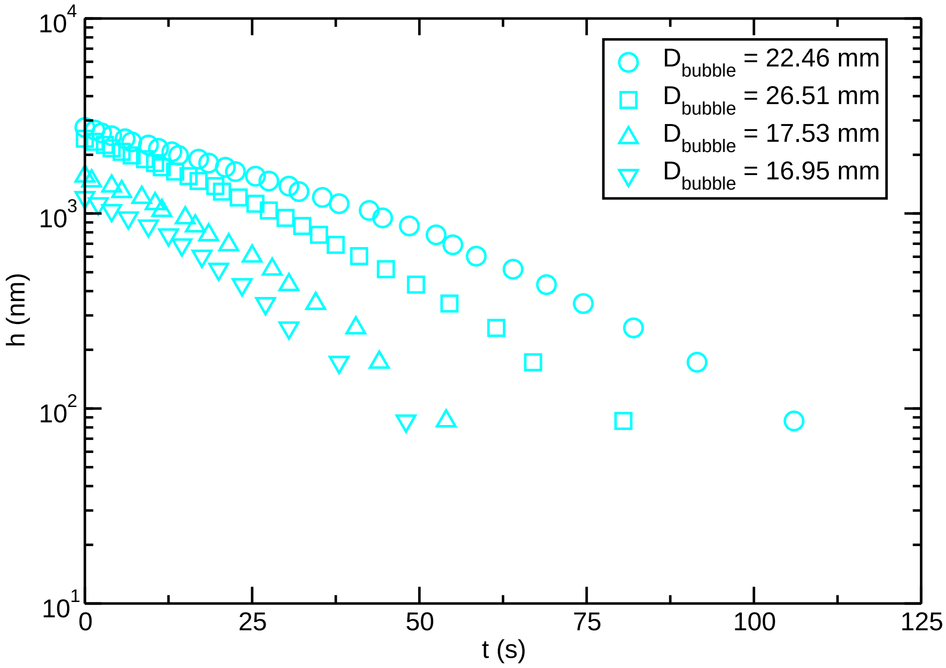

Figure G.23: Evolution of thickness for various bubble size in soda-lime-silica glass with 10 wt% of B_2O_3 and temperature 990°C.

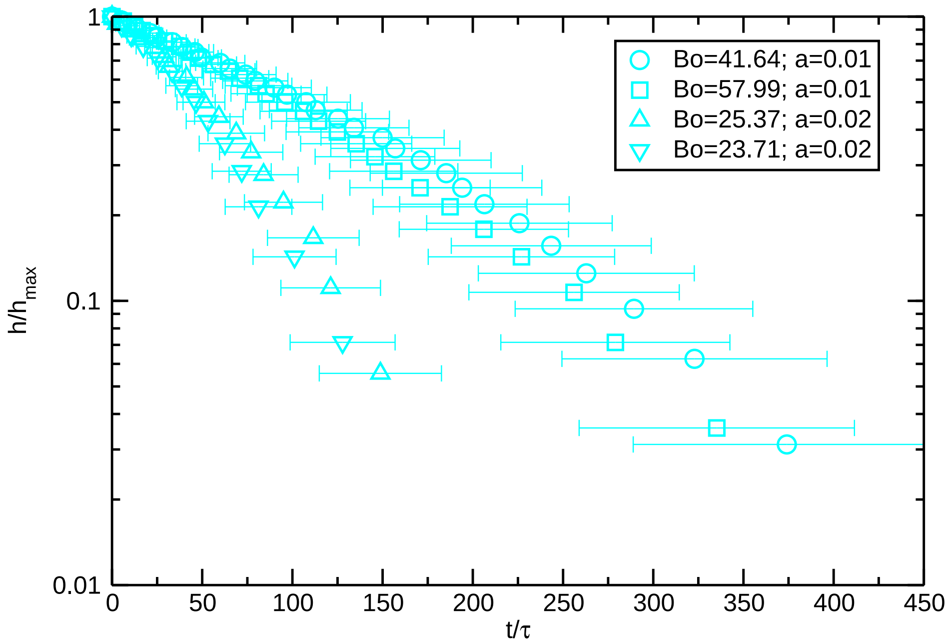

Figure G.24: Normalized evolution of thickness for various bubble size in soda-lime-silica glass with 10 wt% of B_2O_3 and temperature 990°C.

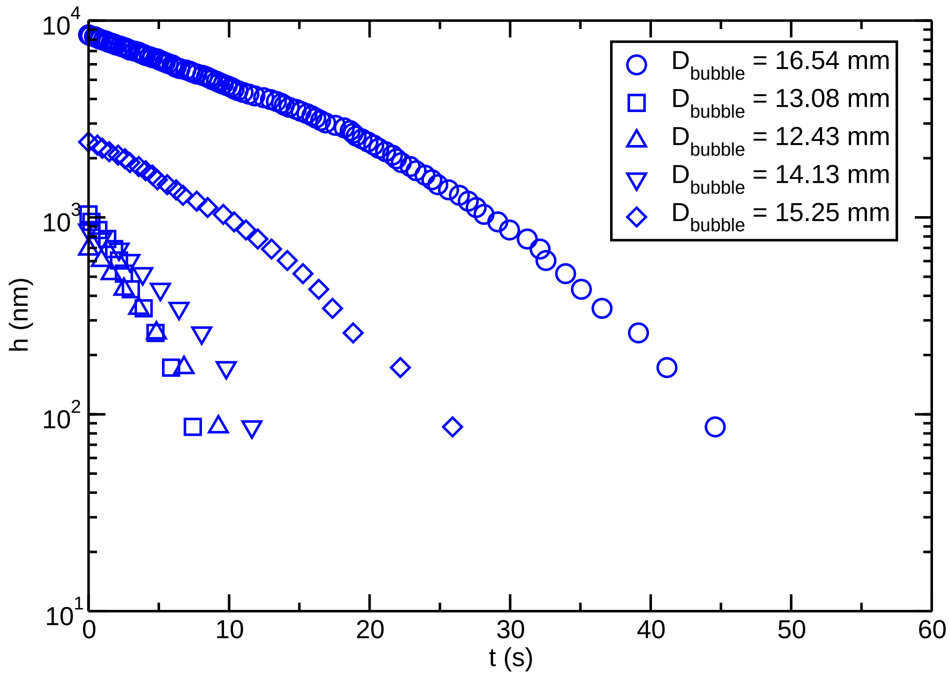

Figure G.25: Evolution of thickness for various bubble size in soda-lime-silica glass with 10 wt% of B_2O_3 and temperature 1044°C.

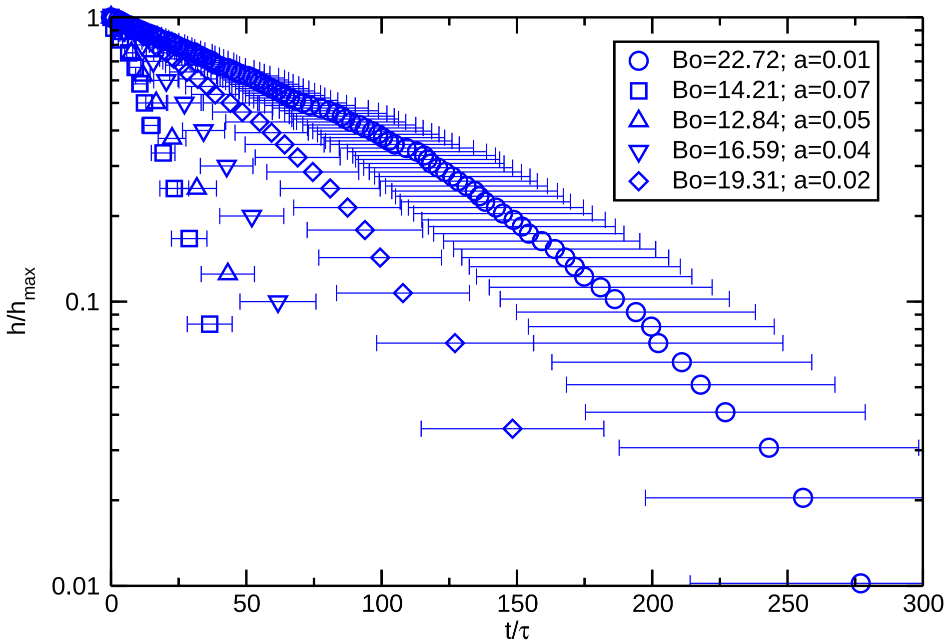

Figure G.26: Normalized evolution of thickness for various bubble size in soda-lime-silica glass with 10 wt% of B_2O_3 and temperature 1044°C.

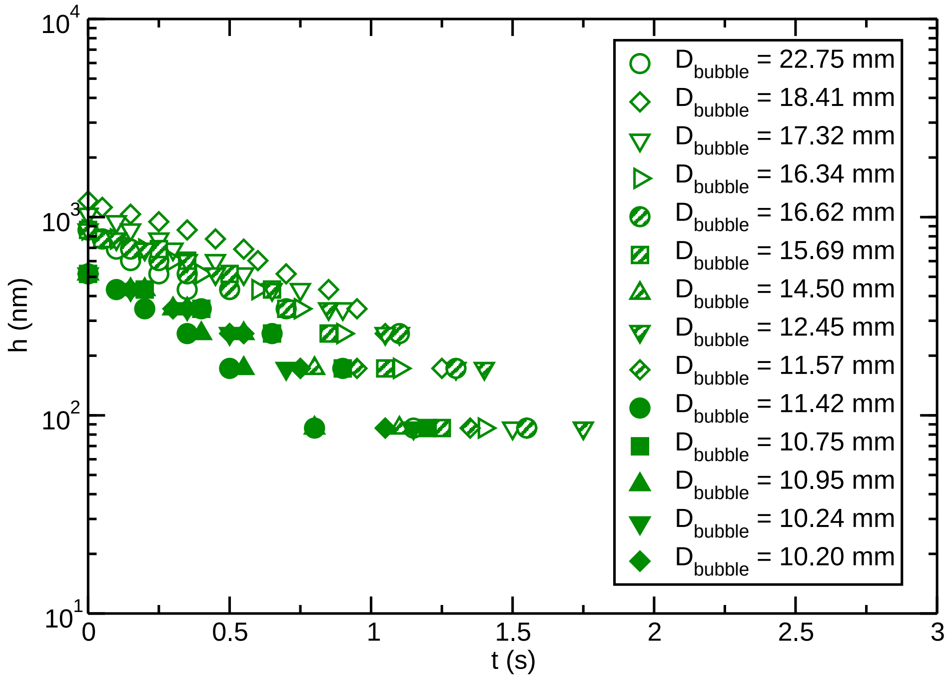

Figure G.27: Evolution of thickness for various bubble size in soda-lime-silica glass with 10 wt% of B_2O_3 and temperature 1142°C.

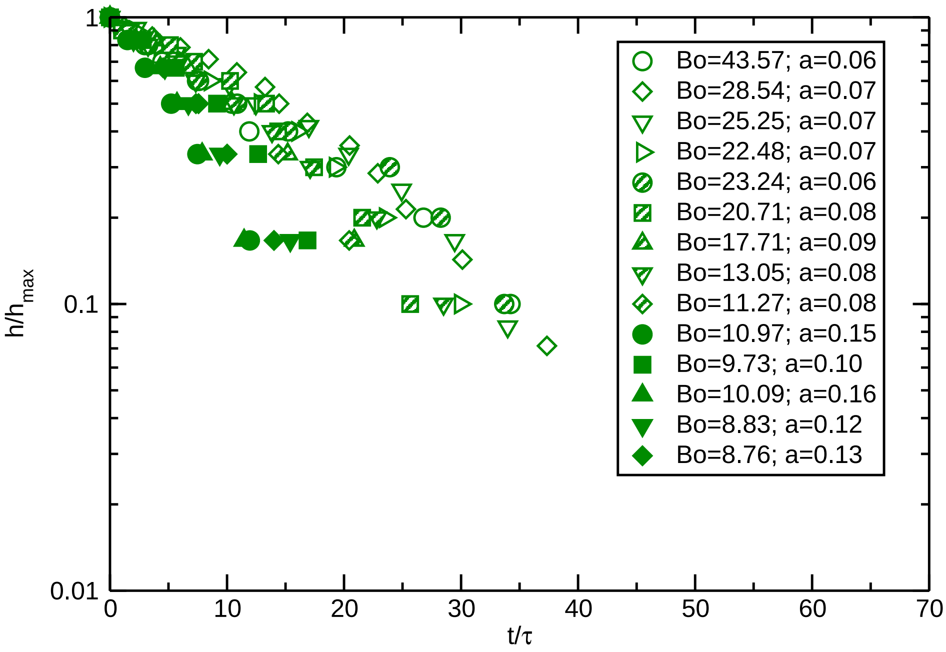

Figure G.28: Normalized evolution of thickness for various bubble size in soda-lime-silica glass with 10 wt% of B_2O_3 and temperature 1142°C.

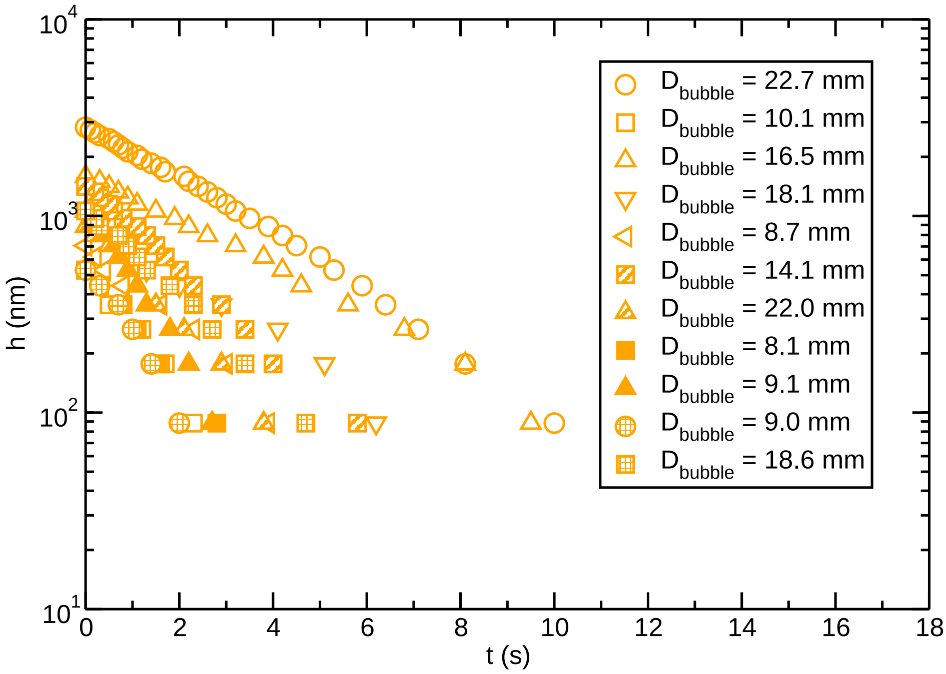

Figure G.29: Evolution of thickness for various bubble size in highly viscous AKM glass and temperature 1228°C.

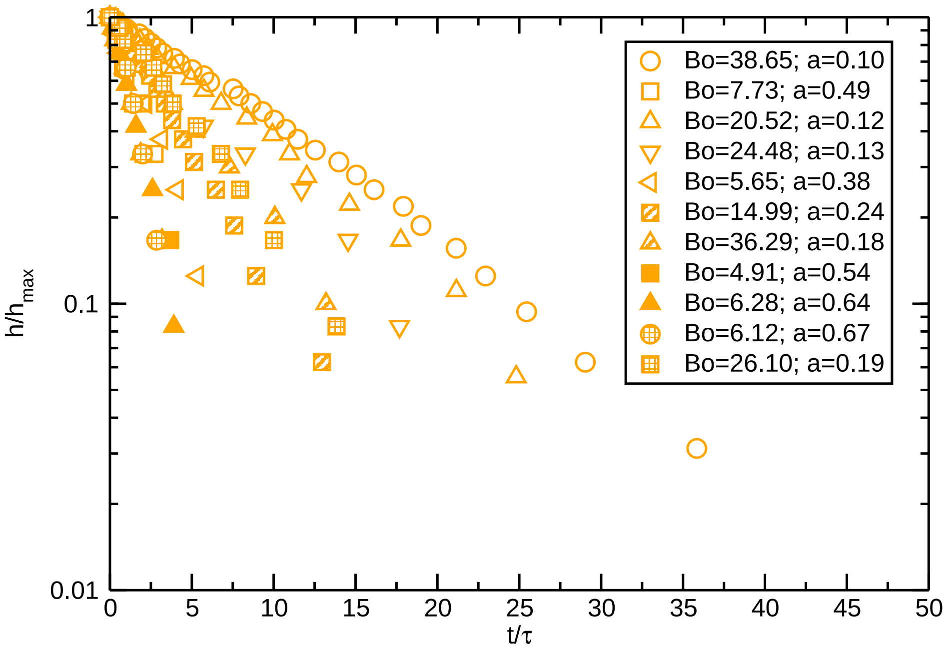

Figure G.30: Normalized evolution of thickness for various bubble size in highly viscous AKM glass and temperature 1228°C.

Appendix H

Tables related to bubble lifetime

Glass	gas	T_E (°C)	μ (Pa·s)	mean (s)	st. dev. (s)	min (s)	max (s)
0.01 wt% Fe_2O_3	N_2	1350	18	6.20	2.72	2.40	13.25
0.1 wt% Fe_2O_3	N_2	1350	22	6.13	2.31	2.55	15.23
0.1 wt% Fe_2O_3	O_2	1350	22	4.72	1.68	2.28	10.23
1 wt% B_2O_3	N_2	1350	15	4.06	1.33	2.25	9.70
10 wt% B_2O_3	N_2	1142	19	9.70	2.09	5.45	16.25
AKM	N_2	1350	42	9.09	2.81	5.87	22.40
AKM	N_2	1414	23	7.00	4.60	2.45	25.05

Table H.1: Summary of all results and experimental conditions related to lifetime of sequence of 100 bubbles.

Glass	gas	T_E (°C)	μ (Pa·s)	mean (s)	st. dev. (s)	min (s)	max (s)
0.01 wt% Fe_2O_3	N_2	1350	18	3.31	0.76	1.40	5.30
0.1 wt% Fe_2O_3	N_2	1350	22	3.35	0.56	2.00	4.55
0.1 wt% Fe_2O_3	O_2	1350	22	2.43	0.53	0.87	3.60
1 wt% B_2O_3	N_2	1350	15	2.90	0.50	1.65	4.64
10 wt% B_2O_3	N_2	1142	19	7.16	1.06	4.65	10.60
AKM	N_2	1350	42	6.03	0.95	2.67	8.10
AKM	N_2	1414	23	3.06	0.60	1.60	4.40

Table H.2: Summary of all results and experimental conditions related to RD of sequence of 100 bubbles.

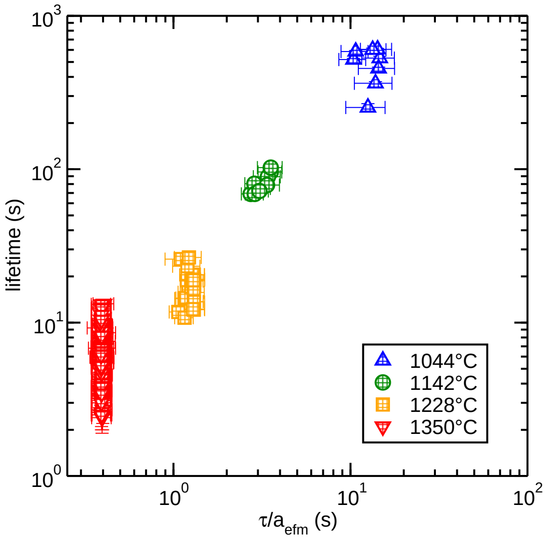

Figure H.1: Lifetime of nitrogen bubbles for glass with 0.01 wt% of Fe_2O_3 as a function of τ/a_{efm}.

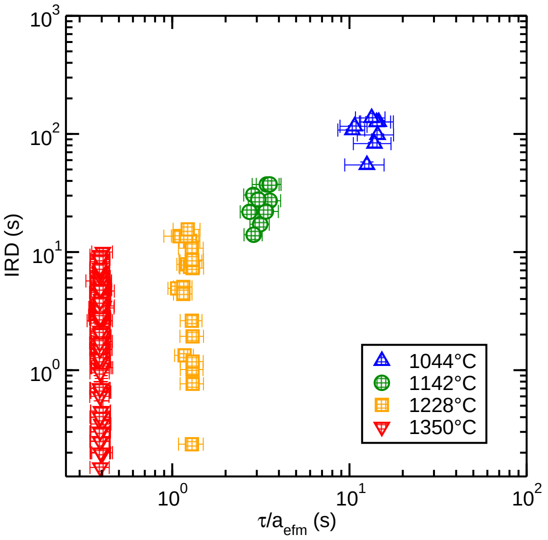

Figure H.2: IRD of nitrogen bubbles for glass with 0.01 wt% of Fe_2O_3 as a function of τ/a_{efm}.

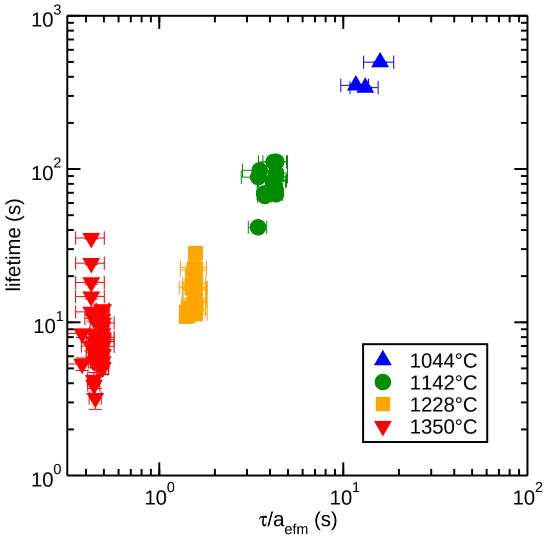

Figure H.3: Lifetime of nitrogen bubbles for glass with 0.1 wt% of Fe_2O_3 as a function of τ/a_{efm}.

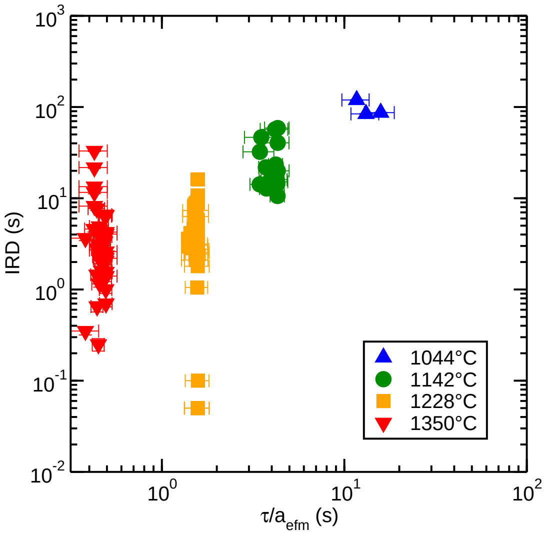

Figure H.4: IRD of nitrogen bubbles for glass with 0.1 wt% of Fe_2O_3 as a function of τ/a_{efm}.

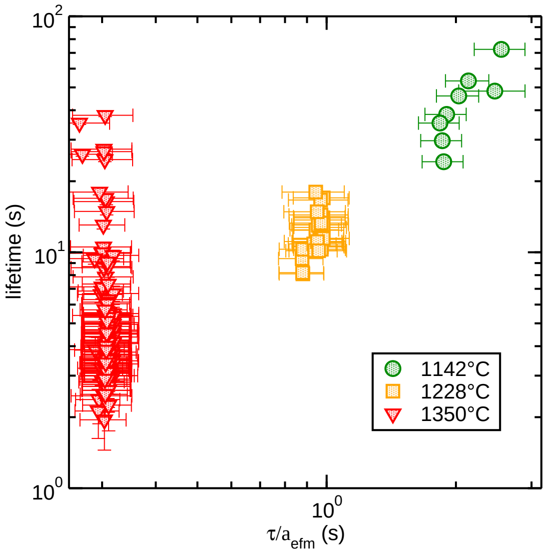

Figure H.5: Lifetime of nitrogen bubbles for glass with 1 wt% of B_2O_3 as a function of τ/a_{efm}.

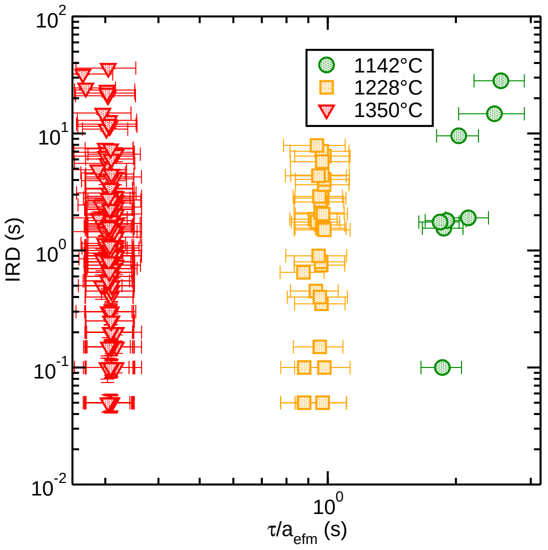

Figure H.6: IRD of nitrogen bubbles for glass with 1 wt% of B_2O_3 as a function of τ/a_{efm}.

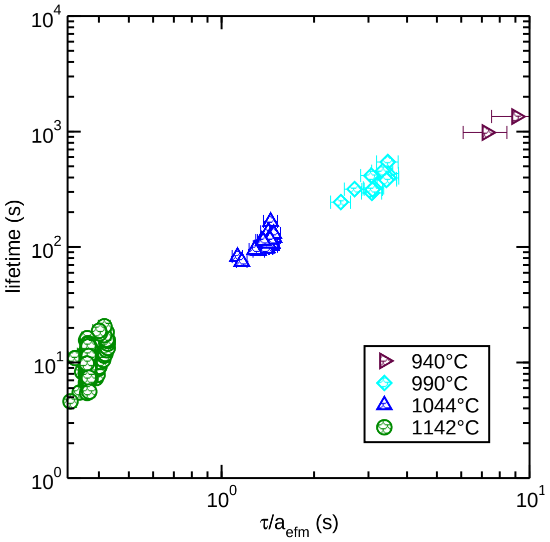

Figure H.7: Lifetime of nitrogen bubbles for glass with 10 wt% of B_2O_3 as a function of τ/a_{efm}.

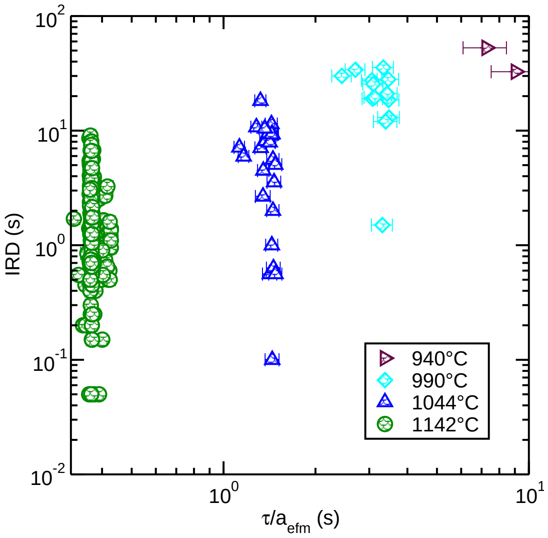

Figure H.8: IRD of nitrogen bubbles for glass with 10 wt% of B_2O_3 as a function of τ/a_{efm}.

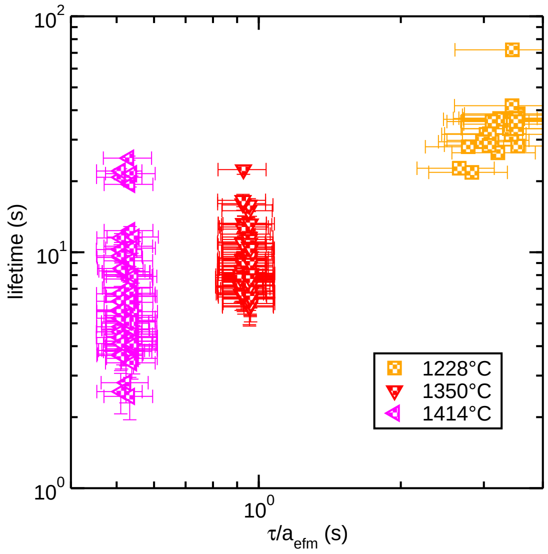

Figure H.9: Lifetime of nitrogen bubbles for highly viscous AKM glass as a function of τ/a_{efm}.

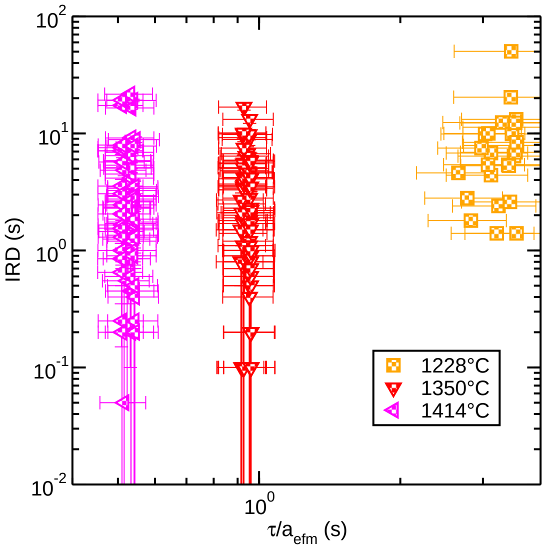

Figure H.10: IRD of nitrogen bubbles for highly viscous AKM glass as a function of τ/a_{efm}.

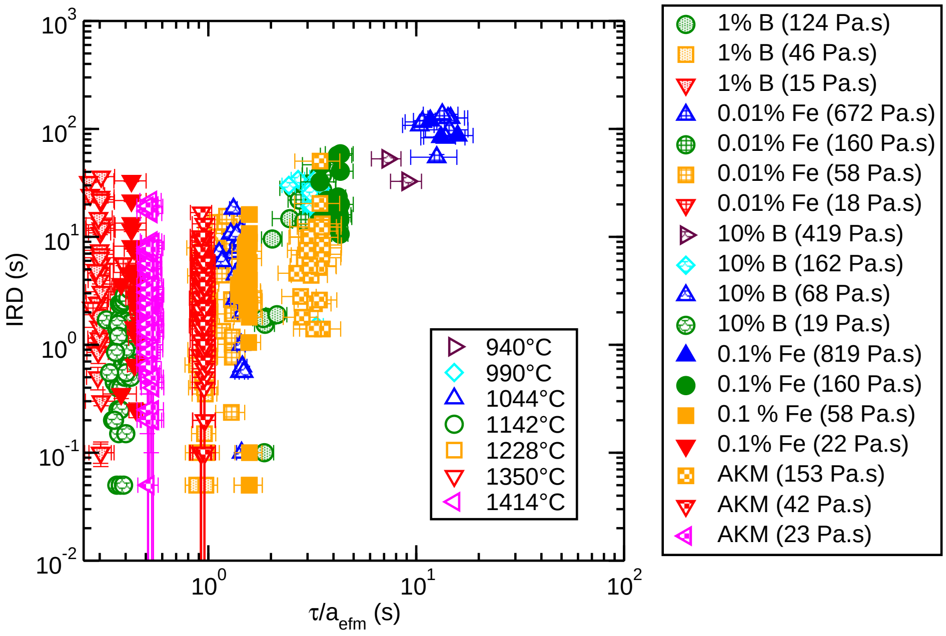

Figure H.11: IRD of nitrogen bubbles for all tested glass compositions as a function of τ/a_{efm}.

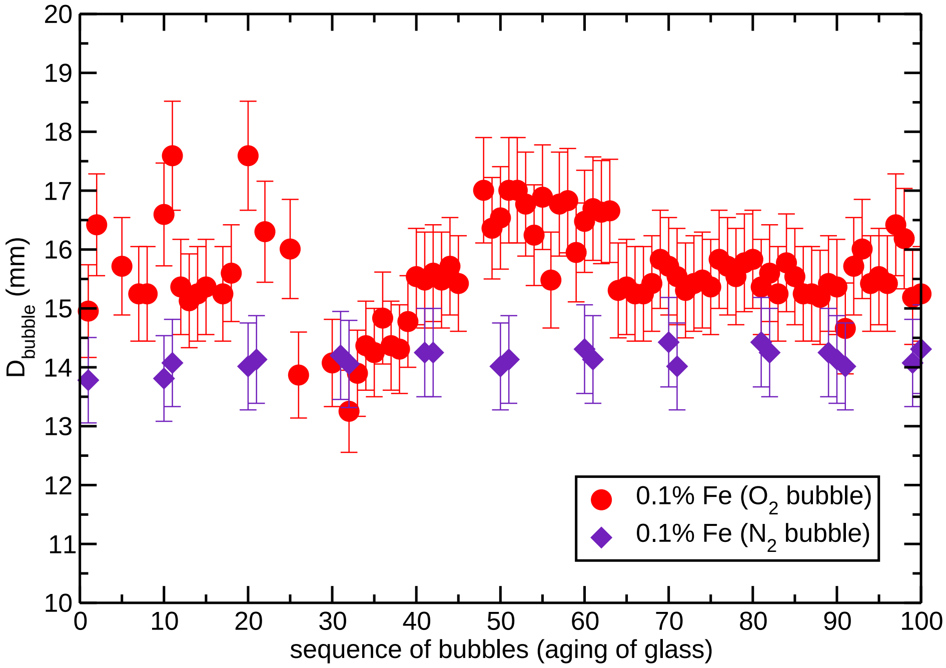

Figure H.12: Bubble diameter of sequence of 100 bubbles for glass with 0.1 wt% of Fe_2O_3 and various gas bubble.

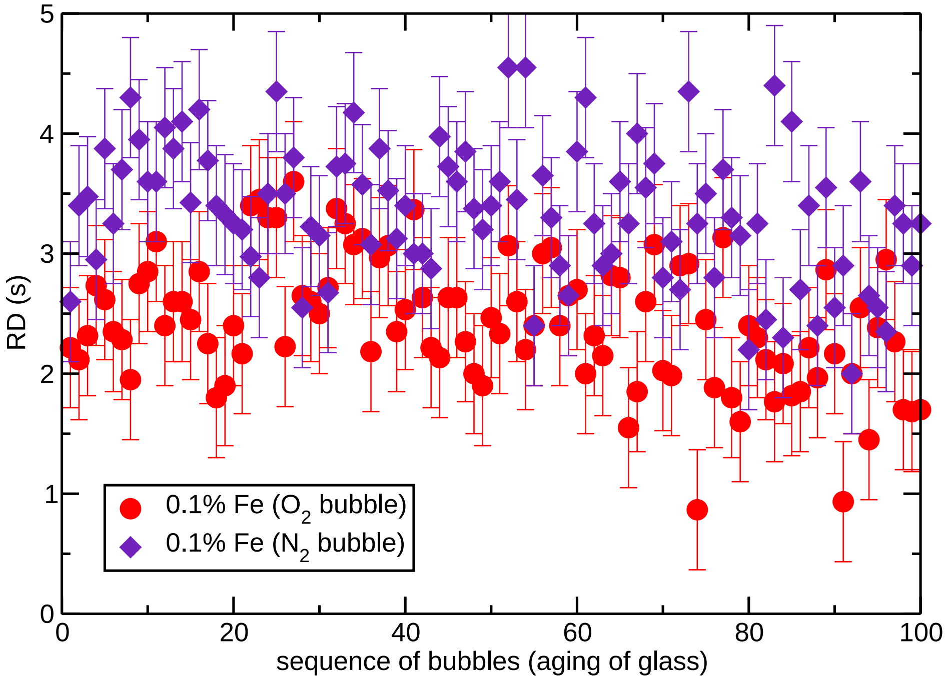

Figure H.13: RD of sequence of 100 bubbles for glass with 0.1 wt% of Fe_2O_3 and various gas bubble.

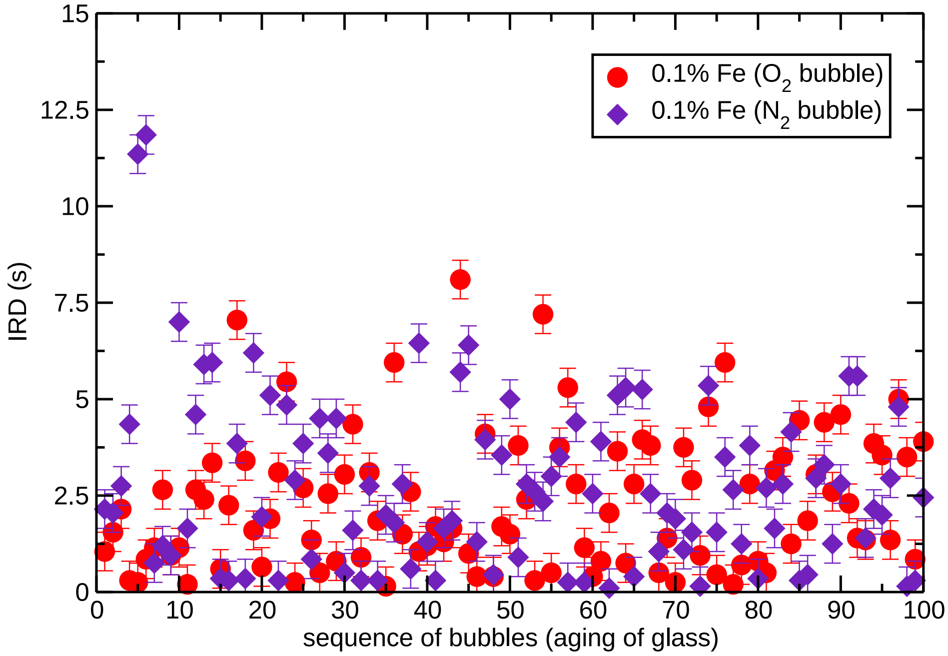

Figure H.14: IRD of sequence of 100 bubbles for glass with 0.1 wt% of Fe_2O_3 and various gas bubble.

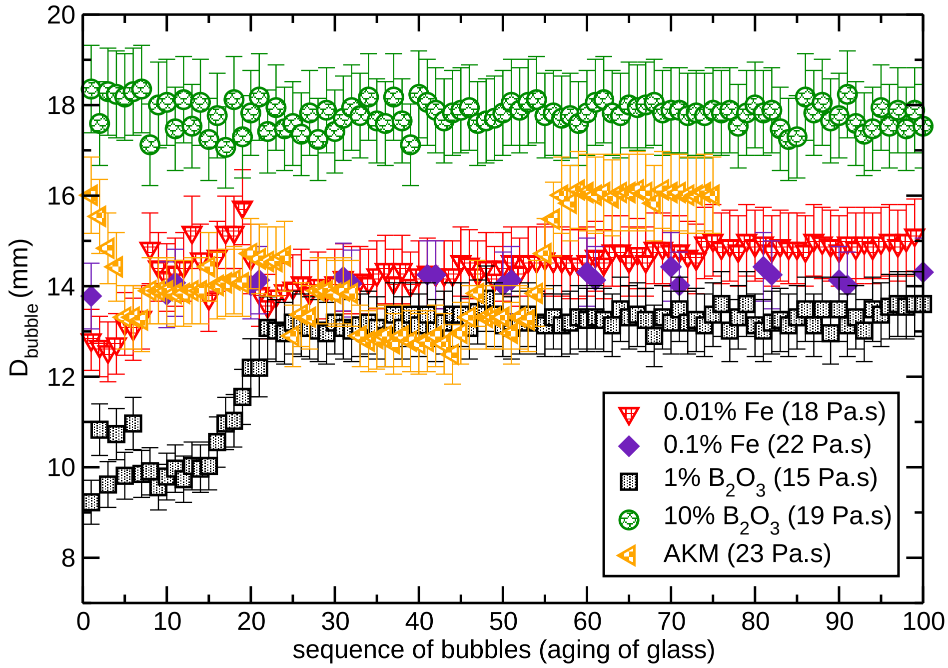

Figure H.15: Bubble diameter of sequence of 100 nitrogen bubbles for various glass composition and similar viscosity.

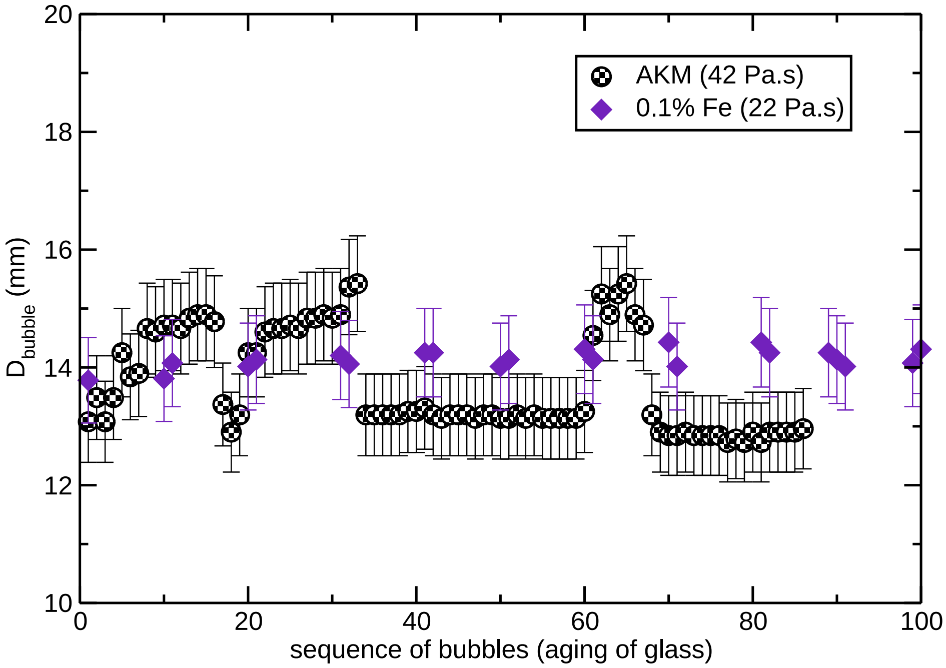

Figure H.16: Bubble diameter of sequence of 100 nitrogen bubbles for glass with 0.1 wt% of Fe_2O_3 and highly viscous AKM glass at temperature T_E=1350°C.

Glass	gas	T_E (°C)	μ (Pa·s)	mean (s)	st. dev. (s)	min (s)	max (s)
0.01 wt% Fe_2O_3	N_2	1350	18	2.89	2.60	0.15	10.00
0.1 wt% Fe_2O_3	N_2	1350	22	2.78	2.23	0.10	11.85
0.1 wt% Fe_2O_3	O_2	1350	22	2.30	1.74	0.15	8.10
1 wt% B_2O_3	N_2	1350	15	1.20	1.42	0.05	7.40
10 wt% B_2O_3	N_2	1142	19	2.55	2.07	0.05	9.05
AKM	N_2	1350	42	3.06	3.12	0.10	16.80
AKM	N_2	1414	23	3.93	4.64	0.05	21.65

Table H.3: Summary of all results and experimental conditions related to IRD of sequence of 100 bubbles.

Appendix I

FeO content

The transmission (T$_\lambda$) is measured for three wavelengths (λ=995, 1000 and 1005 nm). The content of FeO in the glass is computed as follows:

$$\mathrm{FeO(wt\%)} = \frac{1.1491}{ep(mm)} \log\left(\frac{1}{T_i}\right), \tag{I.1}$$

where $ep\,(mm)$ is thickness of the measured sample and T$_i$ is given in eq. below:

$$T_i = \frac{\sqrt{\left[(1-r)^2(1-r)^2 + 4T_\lambda^2 \cdot r^2\right]} - (1-r)^2}{2T_\lambda r^2}. \tag{I.2}$$

T_λ is the measured transmission and r is a coefficient that changes with the wavelength and is given in Tab. I.1.

λ (nm)	**r**
995	0.0413908850938441
1000	0.041381334812053
1005	0.0413718486508828

Table I.1: Constant r for various wavelength.

Appendix J

Velocity and temperature field inside the furnace

Temperature field inside a furnace can be determined experimentally (sec. 5.2.7) but it is not possible to measure velocity field inside a furnace under real conditions. As it is obvious from graph in Fig. 5.8, temperature close to the silica window which covers the furnace top is around 250°C for all T$_E$. For T$_E$=1044°C, this creates a temperature difference almost 800°C on a distance 500 mm between the window and the crucible with the glass sample. For higher T$_E$ the difference is even higher. This temperature difference can cause fluctuation of the surrounding atmosphere and influence the drainage in the bubble lamella as well as glass compounds evaporation.

In order to describe this issue, numerical simulation can be used. Gambit and Fluent are the commercially used programs. Model of a furnace with a crucible and glass sample is created in Gambit and imported to Fluent. Fluent enables computation of this issue thanks to additional data and boundary conditions. The accuracy of the numerical simulation can be verified by comparison of the computed temperature field inside the furnace with the experimentally measured values. Two different geometries were designed for the numerical solution. The first model consists of the alumina tube, column of refractory and Pt-Rh crucible with a glass sample (orange color in Fig. J.1 left). The temperature field is imposed by various temperature conditions on the alumina tube. Because several problems appeared during the computation in Fluent, second model with additional refractory was designed (Fig. J.1 right) in order to enable boundary conditions variation.

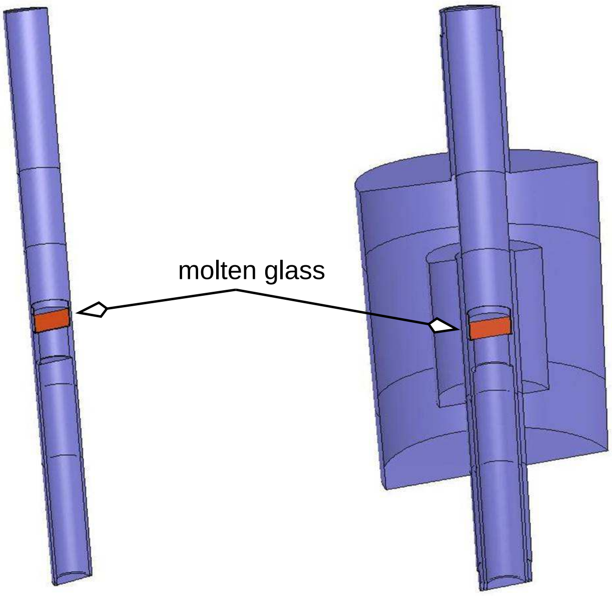

Figure J.1: Two models of the furnace with Pt-Rh crucible and molten glass. Left - model of alumina tube with Pt-Rh crucible and molten glass. Right - model of alumina tube with Pt-Rh crucible, molten glass and external refractory.